A Single-shot Nonlinear Autocorrelation Approach for Time-Resolved Physics in the Vacuum Ultraviolet Spectral Range

Dissertation zur Erlangung des Doktorgrades
an der Fakultät für Mathematik, Informatik und Naturwissenschaften
Fachbereich Physik
der Universität Hamburg

vorgelegt von

Dimitrios Rompotis
aus Athen, Griechenland

Hamburg
2015

Gutachter/in der Dissertation:	Prof. Dr. Markus Drescher Dr. Michael Meyer
Gutachter/in der Disputation:	Prof. Dr. Markus Drescher Dr. Michael Meyer Prof. Dr. Peter Schmelcher Prof. Dr. Ulrike Frühling Prof. Dr. Thorsten Uphues
Datum der Disputation:	16. 12. 2015
Vorsitzender des Prüfungsausschusses:	Prof. Dr. Peter Schmelcher
Vorsitzender des Promotionsausschusses:	Prof. Dr. Jan Louis
Leiter des Fachbereichs Physik:	Prof. Dr. Peter Hauschildt
Dekan der Fakultät für Mathematik, Informatik und Naturwissenschaften:	Prof. Dr. Heinrich Graener

Abstract

In this work, a single-shot temporal metrology scheme operating in the vacuum-extreme ultraviolet spectral range has been designed and experimentally implemented. Utilizing an anti-collinear geometry, a second-order intensity autocorrelation measurement of a vacuum ultraviolet pulse can be performed by encoding temporal delay information on the beam propagation coordinate. An ion-imaging time-of-flight spectrometer, offering micrometer resolution has been set-up for this purpose. This instrument enables the detection of a magnified image of the spatial distribution of ions exclusively generated by direct two-photon absorption in the combined counter-propagating pulse focus and thus obtain the second-order intensity autocorrelation measurement on a single-shot basis.
Additionally, an intense VUV light source based on high-harmonic generation has been experimentally realized. It delivers intense sub-20 fs Ti:Sa fifth-harmonic pulses utilizing a loose-focusing geometry in a long Ar gas cell. The VUV pulses centered at 161.8 nm reach pulse energies of 1.1 µJ per pulse, while the corresponding pulse duration is measured with a second-order, fringe-resolved autocorrelation scheme to be 18 ± 1 fs on average. Non-resonant, two-photon ionization of Kr and Xe and three-photon ionization of Ne verify the fifth-harmonic pulse intensity and indicate the feasibility of multi-photon VUV pump/VUV probe studies of ultrafast atomic and molecular dynamics.
Finally, the extended functionality of the counter-propagating pulse metrology approach is demonstrated by a single-shot VUV pump/VUV probe experiment aiming at the investigation of ultrafast dissociation dynamics of O_2 excited in the Schumann-Runge continuum at 162 nm.

Zusammenfassung

Im Rahmen dieser Arbeit wurde eine Apparatur zur Einzelschussmessung der Dauer von Lichtpulsen im extrem-vakuum-ultravioletten Spektralbereich entwickelt und aufgebaut. Die Intensitätsautokorrelation zweiter Ordnung für ultraviolette Pulse wurde in einer anti-kollinearen Geometrie realisiert, wodurch die Zeitinformation auf die Achse der Strahlausbreitungsrichtung abgebildet wird. Dafür wurde ein kombiniertes Ionen-Mikroskop und Flugzeit-Spektrometer mit einer Auflösung im Mikrometer-Bereich aufgebaut. Dieser Aufbau ermöglicht eine vergrößerte räumliche Abbildung der Ionen, die ausschließlich aus der direkten Zwei-Photonen-Absorption im gemeinsamen Fokus der gegenläufigen Pulse erzeugt werden. Dies entspricht der Einzelschuss-Intensitätsautokorrelation zweiter Ordnung.

Zusätzlich wurde eine intensive VUV-Lichtquelle aufgebaut, die auf der Erzeugung Hoher Harmonischer beruht. Durch eine Geometrie mit schwacher Fokussierung in einer längenvariablen Argon-Gaszelle, erzeugt diese Pulse der fünften Harmonischen des Ti:Sa-Lasers mit einer Pulsdauer unter 20 fs. Die VUV-Pulse mit einer mittleren Wellenlänge von 161.8 nm erreichen Pulsenergien von 1.1 µJ und eine Pulsdauer von 18 ± 1 fs, bestimmt mittels interferenzaufgelöster Autokorrelation zweiter Ordnung. Nichtresonante Zwei-Photonen-Ionisation von Krypton und Xenon, sowie Drei-Photonen-Ionisation von Neon bestätigen die hohe Pulsintensität der fünften Harmonischen. Dies ermöglicht Mehrphotonen-VUV-Pump/VUV-Probe-Studien an atomaren und molekularen Systemen mit ultraschneller Dynamik.

Zur Demonstration wurde diese Methode der Intensitäts-Autokorrelation mit gegenläufigen Pulsen für ein Einzelschuss-VUV-Pump/VUV-Probe-Experiment in der Untersuchung der ultraschnellen Dissoziationsdynamik von O_2 nach Anregung bei 162 nm im Schumann-Runge-Regime eingesetzt.

Contents

1 Introduction

Much of our understanding on the constituents of matter and the underlying fundamental natural phenomena has been provided by spectroscopy. Quantum mechanics, one of the most important scientific discoveries in the 20^{th} century, has been founded on the basis of spectroscopic observations. However, conventional spectroscopy cannot resolve the dynamics of fundamental processes on an atomic and molecular scale, which is only possible by time-resolved observation of their ultrafast evolution.

Time-resolved spectroscopy, typically follows a 'pump-probe' methodology for the investigation of processes occurring on a microscopic dimension and an ultrashort timescale. In this approach, a light pulse (pump) drives the system far from its equilibrium, initiating dynamics, while a second pulse (probe) is subsequently used to probe its temporal evolution. The information about the evolving dynamics is obtained by detecting changes on the probe light pulse or the interaction products, including photons, electrons, or ions, as a function of the delay between pump and probe pulses. In this way, a series of 'snapshots' of the evolving dynamics is obtained, which can be combined to reveal the complete temporal evolution of the process. The number of possible experimental schemes that can use this approach can be almost endless, while the attainable time resolution is determined by the duration of the employed light pulses.

Combined with femtosecond laser pulses the 'pump-probe' approach can follow molecular dynamics in their natural timescale, leading to the development of femtochemistry [1, 2]. Moreover, the energy localization in the focus of an ultrashort pulse, can be utilized in multi-photon time-resolved spectroscopy, giving access to otherwise non-allowed transitions. In addition to this, the same time-delay-scanning approach, when combined with spectrally-broad ultrashort light pulses, can deliver high-resolution spectroscopic information utilizing quantum-interference spectroscopy methods [3].

Typically, atomic and molecular electronic excitations lie in the deep-ultraviolet (DUV) to the extreme-ultraviolet (XUV) spectral region and in most cases the associated dynamics evolve in sub-picosecond timescales [4]. Therefore, light pulses with durations in the few-femtosecond scale are advantageous, or in some cases necessary, to follow ultrafast processes in this spectral regime.

The high peak intensities in the focus of infrared femtosecond laser pulses has given access to a plethora of non-linear optical phenomena, including the generation of high-order harmonic radiation of the fundamental laser frequency [5, 6]. The broad spectral bandwidth available via high-harmonic generation (HHG) in the DUV-XUV spectral range, leads to the formation of isolated pulses or pulse-trains in the few-fs or even sub-fs timescale, making possible to investigate ultrafast dynamics in their natural timescales [7–16].

However, VUV-XUV pulses obtained by HHG typically exhibit low pulse energies and conversion efficiency, limiting their applications in single-photon experiments. Recently, utilizing optimal generation schemes based in loose-focusing in dilute extended gas targets [17–19], HHG-based light sources have reached high-intensity levels, so far demonstrated in a limited number of laboratories worldwide and in the photon energy window between 13 eV up to 45 eV.

In addition to laser-based VUV-XUV light sources, Free-Electron Lasers (FEL) [20–23] deliver unprecedented peak brilliance in the XUV range, foreseen to revolutionize research in ultrafast dynamical and structural studies in nanoscale systems, coherent imaging and time-resolved spectroscopy. Their pulses have durations in the sub-ps, or in some cases fs range. With the exception of FEL's that operate in a 'seeded' mode, their pulses exhibit a complex spiky temporal profile that complicates time-resolved experimental result interpretation. The intensities attainable with both types of light sources in a focused beam, have facilitated a number of studies on sequential and direct multi-photon excitation of atomic and molecular ionization pathways [24–29], previously inaccessible, motivating the extension of non-linear time-resolved spectroscopy techniques to the VUV-XUV spectral regime.

Time-resolved spectroscopy in the VUV-XUV typically makes use of multi-photon ionization pump-probe schemes. During the past years, the lack of energetic VUV-XUV pulses resulted in an alternative approach, utilizing VUV-XUV pump/multi-photon IR probe schemes. In this approach the VUV-XUV pulse initiates dynamics which are probed by ionization, using an intense multi-photon IR probe transition. As pointed out before [30–32], a VUV-XUV-pump/VUV-XUV-probe scheme, is advantageous in order to avoid perturbations of the investigated dynamics, induced by the strong infrared field.

Following this approach, the ionization product yield is acquired as a function of the delay between the VUV-XUV pump and probe pulses, corresponding to the convolution of the intrinsic system time-constants with the finite instrument response, which are directly connected with the driving pulse temporal profile. In principle, information on the corresponding dynamics can be obtained by deconvolution, as soon as the driving pulse temporal characteristics are known. Consequently, the experimental determination of the pulse temporal profile is essential in order to conclusively deconvolve the characteristic time-constants and reconstruct the often complicated ionization pathway scenario.

Several successful temporal characterization approaches have been implemented in the VUV-XUV spectral regime over the past years, either based on cross-correlation or autocorrelation techniques. Most of them, rely on data acquisition over many successive pulses, typically tens of thousands to several millions, while scanning a temporal delay, incorporating the statistical properties of the light source in the measurement, with important implications in the case of light-sources with stochastic behavior. Additionally, even with a reproducible temporal profile, long-term operational stability using a light source with low-repetition rate, proves to be vital.

Free-Electron Lasers based on self-amplified spontaneous emission exhibit shot-to-shot spectral and temporal fluctuations, associated with the stochastic nature of their generation process and thus require single-shot diagnostics [33–35].

Intense HHG sources on the other hand, mostly driven by low-repetition rate laser systems, would benefit from techniques with decreased data acquisition time, enhancing the statistical significance of the experimental results.
Individual-pulse temporal metrology in this spectral range is therefore highly beneficial and has already been demonstrated in the femtosecond [36–38] and attosecond [8, 39–42] temporal regimes. Techniques targeting on attosecond pulse characterization either provide a constrained temporal detection window in the few-femtosecond timescale, sufficient though for attosecond applications, or when based on self-referencing spectral interferometry [40, 41], they require a spectrally shifted replica of the XUV pulse, restricting their applicability. On the other hand, THz streaking techniques operate in the femtosecond timescale, requiring an additional well-synchronized intense THz pulse have already delivered results related with the temporal structure and statistical behavior of individual FEL pulses [36–38] .
Ideally pulse temporal characterization techniques can incorporate the possibility to perform time-resolved spectroscopy and extract dynamical information combining pulse characterization and 'pump-probe' data. Moreover it would be of advantage if they can be self-contained, not relying on a second external light source and a jitter-free synchronization, operating in a broad range of experimental parameters and can avoid, to an extent that this is possible, assumptions related with the VUV-XUV light generation processes.
In the framework of this thesis, two steps have been made towards this research direction. In the first place, a light source based on HHG, delivering intense pulses in the VUV has been designed, implemented and characterized. Motivated by previous findings on high-harmonic energy scaling, the generation of intense Ti:Sa fifth-harmonic pulses, utilizing a loose-focusing geometry in conjunction with a long generating medium has been demonstrated, achieving the highest pulse energy reported so far, for a sub-20 fs pulse in the spectral region of 160 nm. Intense, ultrashort pulses in the vicinity of 160 nm are advantageous for a number of applications ranging from time-resolved studies of ultrafast molecular dynamics [30, 31, 43–46], to low-energy nuclear isomeric state excitation [47, 48], paving the way for a solid-state nuclear clock [49, 50]. Moreover, the ability to excite multi-photon transitions in this range gives reach to excitation schemes that can bypass selection-rules limitations. The energetic VUV pulse offers the possibility for extending nonlinear spectroscopy techniques into a range where many prototypical examples for ultrafast dynamics in organic and atmospherically relevant molecules can be found [30, 31, 44–46, 51, 52]. The high pulse energy combined with a sub-20 fs duration can bypass previous experimental limitations and investigate ultrafast molecular dynamics in the VUV, avoiding the influence of an additional intense IR probe-field.
In parallel, a novel experimental approach extending single-shot nonlinear autocorrelation methodology to the VUV-XUV spectral range has been demonstrated. In this approach, an all-reflective optical scheme geometrically encodes temporal delay information on a spatial coordinate in the focus of two counter-propagating pulses. The spatial distribution of the ions resulting from direct multi-photon absorption are then imaged onto a 2D position-sensitive detector, thereby revealing the time evolution of the investigated process in a single exposure. A dispersionless, all-reflective optical setup has been designed and optimized for use in three distinct spectral regions, ranging from the VUV to the XUV. Identifying a suitable non-resonant nonlinear process to provide an autocorrelation signal is not a trivial task in this spectral regime.

Competing ionization channels, being either at-wavelength or due to the always present accompanying ionizing radiation, can mask the desired autocorrelation signal. For this reason, a careful examination of the excitation possibilities has been performed and the corresponding excitation schemes have been matched with suitable optical components, avoiding such complications in all three variants. Operation in the VUV-XUV range results in a nonlinear autocorrelation signal obtained by multiphoton ionization, thus it requires single-shot charged particle imaging. For this purpose, an ion-imaging time-of-flight spectrometer, operating essentially as an ion microscope, has been implemented and characterized.

The individual-shot autocorrelation principle has been demonstrated in the VUV, aiming at characterizing the intense fifth-harmonic pulse at 162 nm. A complete series of benchmark measurements has been performed, thoroughly investigating the limitations imposed by imperfections in charged-particle imaging and associated charge-repulsion mechanisms.

The scope of the presented single-shot metrology approach has been additionaly extended to performing a single-shot VUV-pump/VUV-probe experiment, using the same delay-encoding concept. As a proof-of-principle experiment, the few-femtosecond dissociation dynamics of O_2, excited in the Schumann-Runge continuum at 162 nm, were investigated on a shot-to-shot basis.

Combining VUV-XUV pulse temporal characterization and time-resolved 'pump-probe' metrology in the same apparatus enables a reliable measurement, minimizing assumptions about the finite instrument response. This quantity is experimentally determined prior to the 'pump-probe' experiment following the presented approach and the combination of both datasets can lead to a high fidelity deconvolution. This approach enables one- or two-color excitation schemes and depending on the ion imaging resolution and the VUV-XUV pulse duration, it can deliver temporal information in a very wide temporal range from few fs to ps. The entire dataset, corresponding to a delay-line of approximately 4 ps, is acquired during every individual shot, remarkably enhancing the statistical significance of the experimental results. Several thousands of complete datasets can be collected in few minutes even with the low-repetition rate (25 Hz) laser system. The corresponding high data acquisition efficiency makes real-time monitoring and optimization of the experimental conditions trivial, constituting this approach considerably advantageous for performing multi-photon time-resolved experiments in the VUV-XUV spectral region.

2 Theoretical Background

2.1 Multiphoton Photoexcitation and Photoionization

An atom, or a molecule, interacting with the electromagnetic field can absorb the quantized photon energy $\hbar\omega$ in single or multiple absorption steps. As a result, electrons can be excited from an initial bound state at an energy level E_1 to a higher energy bound state at E_2, with $E_2 - E_1 = \hbar\omega$. For an atomic system, the lifetime associated with a bound excited state is related with its energy extent, or 'linewidth' via the Heisenberg uncertainty principle as:

$$\Delta t \cdot \Delta E \geq \frac{\hbar}{2} \text{ , or alternatively as: } \Delta t(\text{fs}) \cdot \Delta E(\text{eV}) \geq 0.659 \tag{2.1}$$

Considering a molecular system, the excited state lifetime depends on the particular structure of the considered system and the associated intramolecular processes that can be initiated upon excitation.
Alternatively when the photon energy exceeds the electron's binding energy, the atomic or molecular system will be ionized by single photon absorption, with the ejected electron carrying away the ionization excess energy as $E_{kin} = \hbar\omega - E_{ion}$, where E_{ion} denotes the atomic or molecular systems ionization energy. Additionally, given sufficient photon energy, an inner shell electron can be excited or ionized followed by subsequent electron re-arrangement within the system by means of the Auger effect.
Even if the photon energy is less than that required for the electronic transition, absorption of more than one photons can lead to excitation and/or photoionization in an intense electromagnetic field. In this case, multi-photon absorption may proceed through an excitation sequence of long-lived intermediate states (atomic or ionic), or in a non-sequential manner in a single quantum act. The latter mechanism, originally proposed by Maria Göppert-Mayer in 1931 [53] and observed during the first year after the invention of the laser by T. Maiman [54], relies on the concept of virtual absorption.
When the photon energy does not match or 'resonate' with any intermediate bound state of the system, the electron may absorb more than one photons 'simultaneously', in the time interval permitted by the uncertainty principle, to reach a final state that is inaccessible by single-photon excitation, or more generally, by a sequence of resonant excitation steps. Excitation or ionization proceeds, in this case, via intermediate 'virtual states' with lifetimes determined by the difference-energy between the virtual state and the nearest stationary state (Eq. 2.1). It should be noted, however, that there is no real population transfer in an intermediate virtual state, hence the name 'virtual', and its lifetime essentially reflects the probability of the multiphoton transition.

Time-Dependent Perturbation Theory

In the case of relatively weak electromagnetic fields, where the interaction with the field can be regarded as a small perturbation to the system under consideration, the transition probabilities can be derived within the framework of time-dependent lowest-order perturbation theory and Fermi's Golden Rule [55, 56].
A complete description of a quantum system can be provided in terms of its wavefunction $|\psi(t)\rangle$, which is the solution to the time-dependent Schrödinger equation:

$$i\hbar\frac{\partial}{\partial t}|\psi(t)\rangle = \hat{H}|\psi(t)\rangle \tag{2.2}$$

Considering that the interaction with the electromagnetic field can be treated within the electric dipole approximation, the Hamiltonian operator $\hat{H}$ describing the system can be written as:

$$\hat{H} = \hat{H}_{\mathrm{o}} + \hat{V}(t) = \hat{H}_{\mathrm{o}} + \vec{d}\cdot\tilde{E}\cos\omega t \tag{2.3}$$

where $\hat{H}_{\mathrm{o}}$ corresponds to the unperturbed system's Hamiltonian and $\hat{V}(t)$ describes the interaction between light and matter with $\vec{d} = -e\cdot\vec{r}$ being the electric dipole moment operator. Any state of the system can be expanded as a linear combination of its orthonormal, unperturbed and time-independent eigenfunctions $|n\rangle$ as:

$$|\psi(t)\rangle = \sum_n c_n(t)e^{-i\omega_n t}|n\rangle \tag{2.4}$$

The parameter ξ can be introduced at this point, in order to solve Eq. 2.2 systematically in terms of a perturbation expansion:

$$i\hbar\frac{\partial}{\partial t}|\psi(t)\rangle = (\hat{H}_{\mathrm{o}} + \xi\hat{V}(t))|\psi(t)\rangle \tag{2.5}$$

For the same purpose the wavefunction can also be expanded in the form of a power series in ξ:

$$|\psi(t)\rangle = |\psi(t)\rangle^{(0)} + \xi|\psi(t)\rangle^{(1)} + \xi^2|\psi(t)\rangle^{(2)} + ... \tag{2.6}$$

This form of the solution ensures that for any value of ξ, $\psi(t)^{(N)}$ will be the solution part which is of N$^{\mathrm{th}}$ order to the interaction $V(t)$. Introducing the expanded wavefunction in relation 2.5 and requiring that all terms proportional to ξ^N satisfy it separately, we obtain:

$$i\hbar\frac{\partial}{\partial t}|\psi(t)\rangle^{(0)} = \hat{H}_{\mathrm{o}}|\psi(t)\rangle^{(0)} \tag{2.7a}$$

$$i\hbar\frac{\partial}{\partial t}|\psi(t)\rangle^{(N)} = \hat{H}_{\mathrm{o}}|\psi(t)\rangle^{(N)} + \hat{V}(t)|\psi(t)\rangle^{(N-1)} \tag{2.7b}$$

For N=0, (Eq. 2.7a) the solution corresponds to Schrödinger's equation in the absence of interaction with the field. The higher orders can be iteratively determined once the preceeding solution is determined. At a next step, Eq. 2.7b can be expanded using relation 2.4. Projecting the resulting expansion on a final state $|f\rangle$ and utilizing the orthonormality condition $\langle m|n\rangle = \delta_{mn}$, we get for the probability amplitude $c_f(t)$:

$$\frac{\partial}{\partial t}c_f^{(N)}(t) = (i\hbar)^{-1}\sum_n c_n^{(N-1)}(t)\,\langle f|\,\hat{V}\,|n\rangle\,e^{i\omega_{fn}t}, \text{ with } \omega_{fn} = \omega_f - \omega_n \tag{2.8}$$

As becomes obvious from the above relation, once the probability amplitudes in the N-1 order are determined, the N$^{\text{th}}$ order probability amplitudes can be derived by time integration. The general form for the probability amplitude $c_f(t)$ in N$^{\text{th}}$ order can be written as:

$$c_f^{(N)}(t) = (i\hbar)^{-1}\sum_n \int_0^t dt' c_n^{(N-1)}(t')\,\langle f|\,\hat{V}(t')\,|n\rangle\,e^{i\omega_{fn}t'} \tag{2.9}$$

With the system found initially in the state $|i\rangle$, the probability amplitude can be calculated, here up to the second order, employing the initial condition $c_f^{(0)} = \delta_{fi}$ since the system is originally unperturbed:

$$c_f(t) = \delta_{fi} - \tag{2.10a}$$

$$-(i\hbar)^{-1}\int_0^t dt'\,\langle f|\,\hat{V}(t')\,|i\rangle\,e^{i\omega_{fi}t'} + \tag{2.10b}$$

$$+(i\hbar)^{-2}\int_0^t dt'\int_0^t dt''\sum_m \langle f|\,\hat{V}(t')\,|m\rangle\,\langle m|\,\hat{V}(t'')\,|i\rangle\,e^{i\omega_{fm}t'}e^{i\omega_{mi}t''} + \ldots \tag{2.10c}$$

The probability amplitude $c_f(t)$ is related with the transition from $|i\rangle$ to $|f\rangle$. Although a comprehensive analysis will not be provided here, it should be stated that the corresponding selection rules need to be satisfied for the transition from $|i\rangle$ to $|f\rangle$ in each case, depending on the number of photons absorbed [56, p.170]. The field induced perturbation appears once in each matrix element, denoting a single-photon interaction at each step. Thus, a single photon process is described in first order, whereas the second-order solution is interpreted as a two-photon transition from $|i\rangle$ to $|f\rangle$ described by a sum over all possible intermediate states. The corresponding transition probability can be obtained by $p_{i\to f} = |c_f(t)|^2$.
As the perturbing potential $\hat{V}(t)$ (2.3) is separable in terms of its space and time dependence, $\hat{V}(t) = V\cdot\cos\omega t = V\cdot(e^{i\omega t}+e^{-i\omega t})/2$[1], the probability amplitude in first-order can be written as:

$$c_f(t) = -(i\hbar)^{-1}\,\langle f|\,\hat{V}\,|i\rangle\int_0^t dt' e^{i\omega_{fi}}(e^{i\omega t}+e^{-i\omega t}) \tag{2.11a}$$

$$= \frac{-2i}{\hbar}\,\langle f|\,\hat{V}\,|i\rangle\left[\frac{e^{i(\omega_{fi}+\omega)t}-1}{i(\omega_{fi}+\omega)} + \frac{e^{i(\omega_{fi}-\omega)t}-1}{i(\omega_{fi}-\omega)}\right] \tag{2.11b}$$

[1]The division by a factor of 2 can be absorbed in a constant included in V for the sake of clarity, without sacrificing the description consistency.

Making use of the relation $e^{i\theta} - 1 = 2ie^{i\theta/2} \sin\frac{\theta}{2}$ and mainly considering the first term, as we are interested in photon absorption[2], we get:

$$c_f(t) = \frac{-2i}{\hbar} \langle f| \hat{V} |i\rangle \frac{e^{i(\omega_{fi}\pm\omega)t/2} \sin(\omega_{fi} \pm \omega)t/2}{\omega_{fi} \pm \omega} \tag{2.12}$$

and the associated transition probability can be written as[3]:

$$p_{i\to f} = |c_f(t)|^2 = \frac{1}{\hbar^2} \left|\langle f| \hat{V} |i\rangle\right|^2 \frac{4\sin^2\left[(\omega_{fi} \pm \omega)\frac{t}{2}\right]}{(\omega_{fi} \pm \omega)^2} \tag{2.13}$$

The transition probability per unit time, or the transition rate, for the one-photon process in that case, is obtained by evaluating the above expression at the limit $t \to \infty$, retaining energy conservation in the system and by additionally using the Dirac delta-function property $\delta(\omega) = (2/\pi) \lim_{t\to\infty} \frac{\sin^2(\omega t/2)}{t\omega^2}$:

$$\Gamma^{(1)}_{i\to f} = \frac{p_{i\to f}}{t} = \frac{2\pi}{\hbar^2} \left|\langle f| \hat{V} |i\rangle\right|^2 \delta(\omega_{fi} \pm \omega) \tag{2.14}$$

Alternatively, when the transition leads to a state continuum that can be described by a density of final states $\rho(E)$, Fermi's Golden Rule can be employed for the resulting transition rate:

$$\Gamma^{(1)}_{i\to f} = \frac{2\pi}{\hbar^2} \left|\langle f| \hat{V} |i\rangle\right|^2 \rho(E) \tag{2.15}$$

Keeping in mind that the dipole operator is proportional to the amplitude of the electric field, the transition rate in first-order $\Gamma^{(1)}_{i\to f} \propto \left|\langle f| \hat{V} |i\rangle\right|^2$ is proportional to the intensity and can be expressed as:

$$\Gamma^{(1)}_{i\to f} = \sigma^{(1)} I \tag{2.16}$$

where $\sigma^{(1)}$ denotes the single-photon cross section given in cm^2, or typically in Mb (10^{-18} cm^2) units. Along the same line of thought, the same type of evaluation can be generalized to higher-order terms, which effectively describe resonant or non-resonant multi-photon transitions [57]. In this case, a generalized form of Fermi's Golden Rule can be used, employing the higher order perturbation expansion of the interaction Hamiltonian in the transition matrix element while performing a summation over all the possible intermediate states [58]. The n^{th} order matrix element that describes an n-photon process, in which the interaction occurs n-times (Eq. 2.10c), can be written in a general form as [57, 59]:

$$\langle i| \hat{T}(n) |f\rangle = \sum_{\text{all j}} \langle f| V \frac{|j_{n-1}\rangle \langle j_{n-1}|}{E_i - E_{n-1}} V ... V \frac{|j_1\rangle \langle j_1|}{E_i - E_1} V |i\rangle \tag{2.17}$$

[2] The second term describes a photon emission process between the two states

[3] where the minus sign refers to photon absorption and the plus sign to photon emission.

where $\hat{T}(n)$ describes the n$^{\text{th}}$ order interaction, denoted also as transition matrix and can be combined with a generalized form of Eq. 2.15 to provide the n-th order transition rate as:

$$\Gamma_{i\to f}^{(n)} = \frac{2\pi}{\hbar^2} \left| \langle f | \hat{T}(n) | i \rangle \right|^2 \rho(E) \tag{2.18}$$

As it immediately becomes obvious, the n$^{\text{th}}$ order process transition rate, described in the n$^{\text{th}}$ order perturbative term expansion, will be proportional to the n$^{\text{th}}$ power of the intensity. This results in the famous I^n power-law, associated with multiphoton ionization for an intensity range within the validity of perturbation theory. It should be noted here that for very rapid processes, evolving in very short interaction times, the instantaneous transition probability, rather than the steady transition rate needs to be employed for adequately describing the process.

When the ionization signal emanating from an n$^{\text{th}}$ order process is plotted on a double logarithmic scale against the intensity, a straight line with slope given by the power n is obtained, as can be expected by:

$$\Gamma_{i\to f}^{(n)} = \sigma^{(n)} I^n \tag{2.19}$$

where $\sigma^{(n)}$ corresponds to the generalized multi-photon cross-section, expressing the transition probability independent from the intensity, as long as the interaction is adequately described under this assumption. Experimentally, the non-linearity order n, or the number of photons absorbed to generate an excitation/ionization signal $S^{(n)}$, can be determined by recording the intensity dependence of this signal. By plotting the intensity dependence on a double logarithmic scale, the slope determines the order of the process as previously described:

$$\log S^{(n)} \propto n \log I \tag{2.20}$$

Empirically, the atomic ionization generalized multi-photon cross-section value has been found to decrease as $\sigma^{(n)} = 10^{-33n} \text{cm}^{(2n)} \text{s}^{(n-1)}$ with the number of photons absorbed [7,60]. Already in the early multi-photon ionization experiments [7,61,62], the I^n power-law has been verified and its breakdown has been observed above a critical intensity level, mainly attributed to saturation effects [63] or non-perturbative phenomena [7].

Deviations compared to the anticipated slope value in such measurements can be also expected when the excitation proceeds through intermediate resonant states at high photon flux. In such conditions, the initial state might be significantly depleted, with a large part of the population excited in a resonant state within a very short time interval, even before the peak intensity of the pulse is reached. From this point on the dynamics may turn to be complicated, involving an extended set of excitation-ionization pathways, not neglecting the possibility of stimulated emission, driving the system back to its ground state. In such a case, especially when intensity-dependent non-resonant transitions are involved, the intensity dependent signal alone cannot tell the complete story [64] but also the time dependence of the pulse and/or the lifetimes of the states involved have to taken into account.

For example a less energetic but extremely short pulse will favor the non-resonant transitions and deliver less population to the resonant state, whereas a long energetic pulse with the same peak intensity may efficiently populate the resonant excited state, leaving a minor fraction of the population to experience the peak intensity.

Photoionization in the Focus of a Gaussian Beam

In a realistic laser experiment, due to the spatial dependence of the pulse intensity, the saturation behavior of the multiphoton signal as a function of peak intensity is different from the expected curve. The multi-photon signal continues increasing above the saturation intensity, typically with a decreased slope of 3/2 [65,66], contrary to the expected saturation behavior. This effect is mainly attributed to the spatially-dependent intensity profile of the laser beam, resulting in integration over an intensity distribution in the detected signal. For a steady increase in the peak intensity, a confined volume within the target will be driven into saturation, but at the same time atoms in the surrounding area experiencing the lower intensity wings of the beam will start contributing significantly, resulting in a non-monotonic non-linear signal increase.
In pulsed laser experiments, a Gaussian spatial profile is usually assumed, owing to the laser resonator mode that defines the intensity spatial distribution at the output. Leaving the temporal intensity distribution and related aspects for the next section of this chapter, the spatial intensity distribution of a Gaussian fundamental-mode (TEM_{00}) results from the solution of the the paraxial Helmholtz equation [67] and it is essentially defined by its minimum waist w_o (radius at $1/e^2$ of the Gaussian intensity distribution), wavelength and peak intensity value I_o. The spatial intensity distribution is given by:

$$I(r,z) = I_o \left[\frac{w_o}{w(z)}\right]^2 \mathrm{Exp}\left[-2r^2/w^2(z)\right], \text{ with} \tag{2.21a}$$

$$w(z) = w_o\sqrt{1+\left(\frac{z}{z_R}\right)^2}, \text{ and} \tag{2.21b}$$

$$z_R = \frac{\pi w_o^2}{\lambda} \tag{2.21c}$$

where r denotes the radial distance from the beam axis and z the axial distance from the minimum waist w_o position. The beam waist size as a function of the axial distance from the focal point is given by Eq. 2.21b and z_R (2.21c) corresponds to the Rayleigh length, being the distance within which the waist grows as $w(\pm z_R) = \sqrt{2}w_o$.
In the case of an n^{th} order non-linear signal, scaling with $I^n(r,z) \propto \mathrm{Exp}\left[-2nr^2/w^2(z)\right]$, the effective beam waist size will scale as $w_o^{(n)} = w_o^{(1)}\sqrt{n}$ within the range of validity of perturbation theory. This holds also for all the respective beam parameters that can be described by a Gaussian distribution, such as the beam angular distribution or the pulse spectral-temporal profile [68].
The total volume in the focal region that experiences an intensity in the finite interval between I_o and $I_o - \delta I$ is given by [69, 70]:

$$V(\delta I, I_o) = \pi z_R w_o^2 \left[\frac{4}{3}\left(\frac{\delta I}{I_o-\delta I}\right)^{1/2} + \frac{2}{9}\left(\frac{\delta I}{I_o-\delta I}\right)^{3/2} - \frac{4}{3}\tan^{-1}\left(\frac{\delta I}{I_o-\delta I}\right)^{1/2}\right] \tag{2.22}$$

This relation, used in combination with the respective multi-photon generalized cross section and the anticipated beam parameters, can calculate the intensity-dependent multi-photon ion yield in the focus of the Gaussian beam.

If the peak intensity I_o is much higher than the saturation intensity I_s ($\delta I = I_o - I_s$), the second term in 2.22 ($V(I_s, I_o)$) dominates, yielding the n = 3/2 volume increase behavior [65, 66, 70], where the focal volume contributing to the non-linear signal is defined by the total $V(I_s, I_o)$ minus the saturated volume in this case.
The discussion so far considers an intensity regime where the interaction between the electromagnetic field and the system can be considered as a small perturbation. For an increased intensity the states involved can no longer be considered as unperturbed since they couple to the strong electromagnetic field and dynamically shift in a manner which is dominated by the AC-Stark shift [71].
The interaction becomes non-perturbative and a wealth of new phenomena, such as above-threshold ionization [72–75], high-harmonic generation [5–7, 76] and light-induced atomic and molecular structure distortions [77–84], become prominent.
At very high peak intensities, reached in the focus of intense, ultrashort pulses, the electromagnetic field strength can become comparable to the Coulomb field within an atom, causing the valence atomic electron to experience the effect of the alternating combined potential. As a result, the atomic potential wall bends alternately in each half-cycle of the strong electromagnetic field, forming a permeable potential barrier through which the electron can tunnel, leading to 'tunneling' ionization. When the intensity is further increased, the atomic potential might be severely deformed and the electron can be released just by crossing the potential barrier when bent, leading to 'over-the-barrier' ionization.
For a quantitative comparison, consider the Coulomb electric field in a hydrogen atom which corresponds to $e/(4\pi\epsilon_o a_o^2) \simeq 5 \cdot 10^9$ V/cm. The equivalent intensity that defines the atomic unit of intensity can be calculated to be $I_{\text{atomic}} = (1/2)\epsilon_o c E^2 = 3.5 \cdot 10^{16}$ W/cm^2. Nowadays, this intensity level can be routinely reached in a femtosecond laser laboratory utilizing an amplified TW-level infrared laser system.
A way to systematically discriminate between the atomic ionization regimes in strong fields has been provided by L.V. Keldysh [85, 86] introducing the adiabaticity parameter γ:

$$\gamma = \sqrt{\frac{\text{I.P.}}{2\text{U}_\text{p}}} \tag{2.23}$$

where I.P. refers to the atomic ionization potential and U_p to the ponderomotive potential, being the quiver energy of a free electron in an oscillating electromagnetic field, defined as:

$$\text{U}_\text{p} = \frac{e^2 E^2}{4m\omega^2} \tag{2.24}$$

where E denotes the electric field of frequency ω and e, m refer to the charge and mass of the electron respectively. The adiabaticity parameter essentially compares the time that the system will take to ionize, with the oscillating period of the field which directly relates to the time the field bends the atomic potential to enable tunneling.
When the adiabaticity parameter value is in the range of $\gamma \gg 1$, ionization takes a longer time as compared to the field period and can be treated, to a certain extent, in a perturbative way. This regime is also called the 'multi-photon regime'. On the other hand, when $\gamma \ll 1$, or equivalently I.P. $< 2\text{U}_\text{p}$, atomic ionization is governed by the tunneling of the electron through the strongly suppressed atomic potential, corresponding to the optical field ionization regime, or alternately 'tunneling regime'.

Although the adiabaticity parameter does not provide a sharp demarcation line between regimes of different processes and has been the topic of intensive discussion in the literature, it sets nevertheless an intuitive criterion. Depending on the photon energy and pulse duration, the ionization dynamics have to be considered in detail, as the neutral atom might not get the chance of experiencing the peak intensity of the pulse [64, 87].

2.2 High-Order Harmonic Generation

Odd harmonics of the fundamental laser pulse frequency, reaching very high orders, are generated when atoms are exposed to a high intensity laser pulse. The generated high-order harmonic spectrum exhibits a generic shape, showing a sharp decline in the intensity of the first few lower-order harmonics, followed by a plateau where the intensity remains nearly constant for several orders and eventually ends at an abrupt spectral cut-off region.
The low-order harmonics, also referred to as below-threshold harmonics[4], follow a perturbative behavior in terms of their conversion efficiency and spatio-temporal characteristics. This tendency no longer holds in the 'spectral plateau', which makes a perturbative description of the process, predicting an exponential drop of the efficiency with the harmonic order, inconsistent. The typically achieved conversion efficiency, for the harmonics in the spectral plateau using atomic gas targets is low ($\sim 10^{-6}$), while it can be significantly increased with solid-state surface targets ($> 10^{-4}$) [88]. The following two sections, discuss the high-harmonic generation aspects in atomic gases. A brief description of the microscopic mechanisms involved in the generation process is followed by a more extensive discussion of the macroscopic effects that can enable the generation of intense high-harmonic radiation.

2.2.1 Microscopic Description: Individual Atom Response

High-harmonic generation (HHG) has been already proposed in [76], while it was initially observed experimentally by [5,6] and has been investigated later using a wide range of wavelengths, pulse durations and intensities. As the generation aspects in all the various regimes have been vastly discussed in the literature, mainly summarized in [7, 11, 13, 89, 90, and references therein], the discussion here is only intended to stay at a basic phenomenological description level.
The generation process evolves in a non-perturbative intensity regime and can be described using a semi-classical three-step model proposed in [91] and complemented later in a formulation known as the strong-field approximation (SFA) [92], providing a simple and intuitive picture of the underlying processes. According to this model, the electron tunnels through the suppressed atomic potential barrier to the continuum in the first step. Subsequently in a second step it is accelerated under the influence of the present strong electric field.

[4] Referring to the ionization threshold and the fact that the number of photons absorbed, that equals the respective harmonic order, is not sufficient to lead to ionization of the generating medium.

Finally it re-scatters or recombines with its parent ion with a certain probability, emitting the acquired kinetic energy during its excursion in the form of an energetic photon.
Although the atom can ionize at any instance in the strong field, the ionization probability is maximum near the electric field local maxima [7]. Immediately after being liberated, the electron is subject to the influence of the electric field being accelerated away from the core and gaining kinetic energy that amounts to a total of several tens of the photon energy. As the electric field rapidly changes sign, the electron is driven back towards the core direction. Within a fraction of half the laser pulse period, the electron may revisit the parent ion to recombine and emit a burst of XUV radiation. Quantum diffusion, that is dispersion of the electron wavepacket, during its excursion through the continuum, results in a decrease of the probability to encounter the core upon its return.
The high-harmonic generation process efficiency is very sensitive to the driving field polarization, as expected from the generation mechanism and a departure from linear polarization results in a dramatic decrease in the liberated electron recombination probability. An electron driven by an elliptically polarized field in the continuum has a finite probability to recombine with the parent ion, that decreases with increasing ellipticity [93–95]. In a classical description, no returning trajectory meets the core even for small ellipticity values, although due to its quantum nature, the electron can recombine with the core.
The process is repeated periodically every half cycle of the laser field and the emitted spectrum consists of a comb of the odd-order harmonics of the fundamental laser pulse frequency. In this case, only odd-order harmonics are observed, which is justified when taking into account the electric dipole selection rules, the symmetry in the repetition of the emission process and the symmetry of the atomic potential. This structured harmonic spectrum results from spectral interference of successive emitted bursts in every half-cycle of the laser field, resulting in a train of sub-fs pulses in the time domain [96–98], or a single, longer pulse when an individual harmonic order is spectrally chosen [99]. Confining the harmonic emission within a single revisit of the electron results in the emission of a spectral continuum, that supports an isolated pulse on the sub-fs timescale [100, 101, and references therein].
Following a simple classical analysis [91], the highest photon energy emitted as a result of the maximum kinetic energy accumulated by the recombining electron is given by:

$$E_{\text{cut-off}} = \text{I.P.} + 3.17\text{U}_\text{p} \tag{2.25}$$

where I.P. and U_p refer to the ionization and ponderomotive potential. The strong-field approximation (SFA) model [92] that takes into account the quantum nature of the process, while satisfying a set of assumptions that are valid when the ponderomotive potential is higher than the atomic ionization potential. It predicts that two dominant quantum paths are responsible for emission in the spectral 'plateau' region whereas a single quantum path contributes in emission in the 'cut-off' region. These two different quantum paths, associated with a long and a short electron return time, introduce an atomic dipole phase difference that modifies the spatio-temporal behavior of the generated harmonics.
It should be noted that the SFA model is not applicable in the first low-order, 'below-threshold' harmonics, which are assumed to follow a perturbative response [102].

Although most experimental and theoretical studies have focused so far on above-ionization-threshold harmonic generation, the emergence of vacuum-ultraviolet frequency combs based on below-threshold high harmonic generation [103–105] has revived research interest in this regime, mainly attributing the below-threshold harmonic generation mechanism in the long quantum path [106–109].

2.2.2 Macroscopic Description: Propagation and Phase-matching Effects

Experimentally, the macroscopic high-harmonic radiation field builds up as a coherent superposition of individual emission from a large number of atoms in the generation medium, typically supplied in vacuum by means of a nozzle or a gas cell. Therefore, propagation and more specifically phase-matching effects have a major influence on the generation efficiency and the spatio-temporal characteristics of the generated light.
In the gaseous harmonic generation medium, the macroscopic polarization density induced by the field is given by the single atom dipole moment $\vec{d} = \langle\psi|\,\vec{r}\,|\psi\rangle$, multiplied with the atomic number density as $\vec{P} = \rho \cdot \vec{d}$. The electric field, as well as the induced polarization can be written as a superposition of the driving fundamental and its higher harmonics as:

$$\vec{E}(r,t) = \sum_q \vec{E}_q(r) \cdot e^{-i\omega_q t} \tag{2.26a}$$

$$\vec{P}(r,t) = \sum_q \vec{P}_q(r) \cdot e^{-i\omega_q t} \tag{2.26b}$$

In the presence of the gas medium, the evolution of the electric field is described by the driven Maxwell's wave equation [110]:

$$-\nabla^2\vec{E} + \frac{1}{c^2}\frac{\partial^2\vec{E}}{\partial t^2} = \frac{4\pi}{c^2}\frac{\partial^2\vec{P}}{\partial t^2} \tag{2.27}$$

Inserting equations 2.26a and 2.26b in 2.27 leads to a set of coupled wave equations for each harmonic component:

$$\nabla^2\vec{E}_q(r) + \frac{\omega_q^2}{c^2}\vec{E}_q(r) = -\frac{4\pi\omega^2}{c^2}\vec{P}_q(r) \tag{2.28}$$

As previously mentioned, the macroscopic harmonic radiation field results as the coherent sum of radiation emitted by the individual atomic dipoles induced by the driving electric field. The coherent build-up of the harmonic radiation field, therefore depends on appropriately phase-matching these contributions throughout the generating medium. The linearly-polarized (z-direction) electric field can be written as a superposition of plane waves with varying amplitudes across the propagation direction x:

$$\vec{E}(r,t) = \hat{z}\sum_q A_q(x)e^{i(k_q x - \omega_q t)}e^{-a_q x} \tag{2.29}$$

with k_q and ω_q denoting the wavenumber and frequency corresponding to each harmonic order and a_q the respective field attenuation coefficient in the medium.

The field attenuation coefficient is directly related to the linear dielectric constant of the medium and can be expressed as a function of the respective photo-absorption cross section as $2a_q = \rho\sigma^{(1)}$. The field induced polarization can be separated into a linear and a non-linear part:

$$\vec{P}(x,t) = P^{(1)} + P^{(n-l)} = \sum_q \hat{z}(P_q^{(1)}(x) + P_q^{(n-l)}(x))e^{-i\omega_q t} \tag{2.30}$$

and inserting both expressions 2.29, 2.30 in 2.28 yields a set of coupled wave equations [110]:

$$\left(\frac{d^2A_q}{dx^2} + 2ik_q\frac{dA_q}{dx}\right)e^{(ik_q - a_q)x} = -\frac{4\pi\omega_q^2}{c^2}P_q^{(n-l)}(x) \tag{2.31}$$

Taking into consideration that the harmonic field amplitude A_q varies in a longer length scale than the corresponding wavelength, it becomes obvious that the first term in equation 2.31 is much smaller than the second and therefore can be neglected. This is also known as the slowly-varying-envelope approximation [110]. Under this approximation, equation 2.31 is reduced to:

$$\frac{dA_q}{dx} = \frac{2i\pi\omega_q^2}{k_q c^2}P_q^{(n-l)}(x)e^{(-ik_q + a_q)x} \tag{2.32}$$

As the macroscopic non-linear polarization in the medium is induced by the driving laser field, its phase is directly influenced by the phase of the driving laser pulse. According to the strong-field-approximation model [92] the phase of the induced non-linear polarization is given by:

$$\Phi_q = q\omega_o t_r - \frac{1}{\hbar}S \tag{2.33}$$

where ω_o denotes the fundamental driving field frequency, t_r is the exiting electrons classical trajectory return time with respect to a fixed phase of the laser field and S corresponds to the quasi-classical action integral describing the motion of the liberated electron in the driving laser field [111]. If the strong-field approximation is valid ($\gamma \ll 1$) the quasi-classical action integral can be approximated as $S \approx -U_p \cdot \tau_{cont}$, where τ_{cont} corresponds to the time spent in the continuum by the liberated electron between ionization and recombination.
While the laser pulse propagates in the x direction, the phase evolves as $\Phi(x) \approx \Phi_o + (d\Phi(x)/dx) \cdot x$ obtained by expanding relation 2.33 in series and keeping the first term. Performing the expansion, one obtains:

$$\Phi(x) = \Phi_o + \left[\frac{d}{dx}q\omega_o t_r + \frac{d}{dx}\frac{U_p}{\hbar}\tau_{cont}\right]x, \tag{2.34a}$$

$$\Phi(x) = \Phi_o + \left[qk_o + a_q^j\frac{dI}{dx}\right]x, \tag{2.34b}$$

where I denotes the laser field intensity and a_q^j refers to a coefficient that depends on the quantum path taken by the electron during the excursion in the continuum, dominating the single atom dipole [112, 113] and the spectral identity of the harmonic order.
Considering a more realistic case, the HHG driving pulse shows a Gaussian intensity profile, both in space and time. In this case, taking into account the Gouy phase shift [114] in the Gaussian focal region, will transform the first term in the bracket in equation 2.34a to: $k_o x \to k_o x - \tan^{-1}(x/x_R)$, where x_R corresponds to the Rayleigh length along the propagation direction x.

Making use of equation's 2.34b result, the wave-vector mismatch between the fundamental HHG driving field and the harmonics can be written as:

$$\Delta\vec{k} = (q\vec{k}_{\mathrm{o}} - \vec{k}_q) + a_q^j \frac{dI}{dx}, \tag{2.35}$$

differing from the phase mismatch relation valid in perturbative non-linear optics where the dipole phase does not show any intensity dependence.
Taking in addition into account that $\omega_{\mathrm{o}} t_r$ evolves together with the laser field phase, the right hand side part of equation 2.32 can be expressed as:

$$P_q^{(n-l)}(x) e^{(-ik_q + a_q)x} = \rho \left| \vec{d}(\omega_q) \right| e^{i\Delta\vec{k}x} \tag{2.36}$$

The phase factor $\Delta\vec{k} \cdot x$ denotes the phase difference between harmonic fields generated in the gaseous medium at two different positions at a distance x. Destructive interference between them occurs at a length defined by:

$$L_{\mathrm{coh}} = \frac{\pi}{\Delta\vec{k}} \tag{2.37}$$

referred to also as the high harmonic generation 'coherence length'. In the same manner, the length within which the harmonic field intensity will be reduced by 1/e by absorption in the medium, in the absence of non-linear polarization, is defined as the absorption length and expressed as:

$$L_{\mathrm{abs}} = \frac{1}{\rho\sigma^{(1)}} = \frac{1}{2a_q} \tag{2.38}$$

The electric field for each order can be derived by integrating equation 2.32 using as a boundary the generation medium length L_{med}.

$$\begin{aligned} E_q(L_{\mathrm{med}}) &= e^{-a_q L_{\mathrm{med}}} 2\pi i k_q \rho \left| \vec{d}_q \right| \int_0^{L_{\mathrm{med}}} dx e^{(i\Delta k + a_q)x} = \\ &= 2\pi i k_q \rho \left| \vec{d}_q \right| \frac{1}{i\Delta k + a_q} \left(e^{i\Delta k L_{\mathrm{med}}} - e^{-a_q L_{\mathrm{med}}} \right) \end{aligned} \tag{2.39}$$

Assuming loose focusing conditions and on-axis phase-matching, this result can be written in a more intuitive form, following the exact formulation as in [17]. In this case A_q and ρ can be considered to take constant values with no dependence along the x direction. Solving for the number of photons in a harmonic order q, following the derivation in [17], one gets:

$$\begin{aligned} &N_q = \\ &\frac{4\rho A_q^2 L_{\mathrm{abs}}^2}{1 + 4\pi^2 (L_{\mathrm{abs}}^2 / L_{\mathrm{coh}}^2)} \times \left[1 + \mathrm{Exp}\left(-\frac{L_{\mathrm{med}}}{L_{\mathrm{abs}}} \right) - 2\cos\left(\frac{\pi L_{\mathrm{med}}}{L_{\mathrm{coh}}} \right) \mathrm{Exp}\left(-\frac{L_{\mathrm{med}}}{2L_{\mathrm{abs}}} \right) \right] \end{aligned} \tag{2.40}$$

Both relations 2.39 and 2.40 are equivalent. When evaluated, it can be immediately realized that the harmonic yield rapidly decreases when Δk takes non-zero values as the harmonic field generated in different positions along the medium interferes destructively. In order to estimate Δk, the geometrical phase advance (Gouy phase contribution) has to be taken into consideration as well as the atomic dispersion for both the fundamental and harmonic fields.

At this point, all the terms that experimentally contribute to Δk can be shortly summarized. In a general form, Δk can be written as [115]:

$$\Delta k = \Delta k_{\text{geom}} + \Delta k_{\text{dipole}} + \Delta k_{\text{atomic}} + \Delta k_{\text{plasma}} \tag{2.41}$$

The first term Δk_{geom} corresponds to the geometrical phase difference within the Gaussian focus as a a result of the Gouy phase. The total Gouy phase mismatch between the fundamental and the generated harmonic beam can be expressed as $\Delta k_{\text{geom}} \approx -q/x_{\text{R}}$ [115], where x_{R} denotes the fundamental Rayleigh length. This term has a negative sign and can be minimized by the loose focusing generation condition where the fundamental Rayleigh length is significantly large.
The second term, accounts for the dipole-phase $\Delta k_{\text{dipole}} = a_q^j(dI/dx)$ introduced in Eq. 2.34b. This term depends on the intensity variation within the focal region, changing sign before and after the focal point where the peak intensity is reached, as well as on the electron quantum path in the continuum.
The third term Δk_{atomic} takes into account the atomic dispersion, or the phase mismatch between the harmonic and the generating field in the neutral atomic gas as a result of the frequency-dependent refractive index of the medium. This term is given by $\Delta k_{\text{atomic}} = q \cdot (\omega/c) \cdot (n(\omega_{\text{o}}) - n(\omega_q))$ and its role is small for a low atomic density.
Finally, the last term accounts for the wave vector mismatch due to dispersion in the plasma created by the ionizing pulse in the medium. The dispersion is mainly attributed to the free electrons as the formed ions exhibit a much lower polarizability. The free-electron plasma has a refractive index given by $n_p(\omega) = \sqrt{1 + (\omega_p^2/\omega^2)}$ where $\omega_p^2 = N_e e^2/m\epsilon_{\text{o}}$ corresponds to the plasma frequency and N_e denotes the free electron density. The corresponding phase mismatch is given by $\Delta k_{\text{plasma}} = q \cdot (\omega/c) \cdot (n_p(\omega_{\text{o}}) - n_p(\omega_q))$ taking negative values as the electron density increases, mainly affecting the generating fundamental [115].
Furthermore, even when perfect phase-matching is achieved, the absorption term starts playing an additional role for 'above-ionization-threshold' harmonics leading to re-absorption of the generated harmonics while traveling in the medium. After a certain medium length-density product there is no more gain and the optimization criteria defined in [17] are $L_{\text{med}} > 3L_{\text{abs}}$, $L_{\text{coh}} > 5L_{\text{abs}}$.
The overall macroscopic behavior as described above is illustrated in Fig. 2.1 based on Eq. 2.40, evaluated for different coherence-absorption length combinations as in [17].
As can be seen in Fig. 2.1, a longer 'coherence length' L_{coh}, meaning essentially optimized phase-matching conditions ($\Delta k \to 0$), results in an overall higher output, limited by re-absorption after a certain medium length. This is relevant for harmonic orders with photon energies exceeding the generation medium's ionization energy. In general, it can be shown using Eq. 2.40, that when the 'coherence length' is much longer than the absorption length and the medium length is much longer than the absorption length, the harmonic output flux scales as $N_q \sim A(PL_{\text{med}})^2$, where A is the focal spot size area and P is the gas pressure in the generating medium [12]. When re-absorption is negligible, as in the case of below-threshold harmonics, it is mainly the phase-mismatch value Δk that determines the harmonic flux output. A loose-focusing geometry or alternately, an optically guided beam geometry overcomes many of the limitations imposed by the phase mismatch factors discussed above [12].

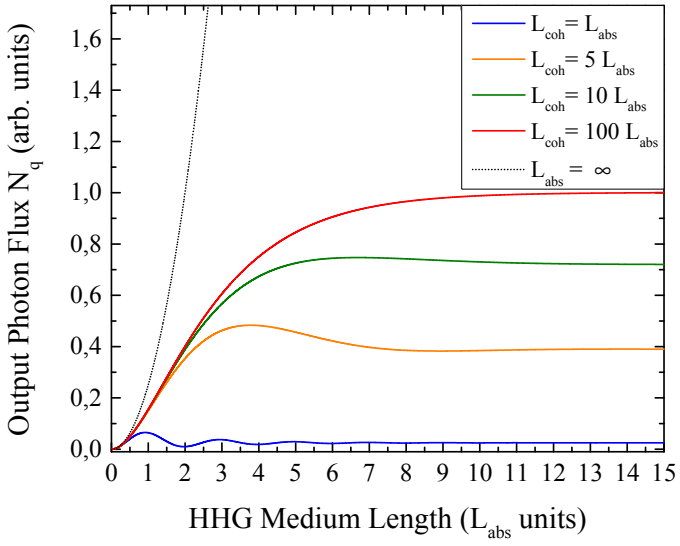

Figure 2.1: On axis phase-matching effects as described by Eq. 2.40. The number of emitted photons N_q is plotted as a function of the medium length for different phase-matching and absorption conditions. The black dotted line corresponds to the case of no absorption.

In order to achieve high-harmonic intensity scaling, utilizing an energetic driving pulse, the loose focusing geometry proves to be the most beneficial approach, avoiding the limiting optical wave-guide damage threshold. In this case the increased focal spot size results in an increased Rayleigh length which effectively reduces the geometrical phase mismatch. In order to retain phase-matching, the gas pressure is reduced and the interaction length can be increased, essentially keeping the pressure-length (PL) product constant. The decreased pressure minimizes the plasma effects on the beam profile and has proven to deliver harmonics with excellent spatial and temporal characteristics [18, 116, 117].

2.3 Ultrashort Light Pulses

The availability of light pulses in the femtosecond (fs) and in the recent years in the sub-femtosecond timescale, in a wide spectral range spanning the far-infrared (FIR) to the extreme ultraviolet (XUV) range, has allowed the investigation of ultrafast dynamics with unprecedented temporal resolution. This section is devoted to a general mathematical description of ultrashort laser pulses and their temporal properties. Although the definitions provided in this section are well-suited to describe an arbitrary temporal waveform, the analysis will focus on Gaussian temporal-spectral pulse profiles as they are commonly encountered in a femtosecond laser laboratory. Detailed discussion on fs/sub-fs light pulse generation, their properties and applications can be nowadays found in a number of excellent textbooks, as for example in [118–121]. The formation of an ultrashort light pulse requires a broad spectral bandwidth with phase-locked spectral components, according to the principles of Fourier synthesis.

Energy localization, both in space and time, emerges as a result of the superposition of mutually coherent monochromatic waves. Depending on their relative phase, the light pulse is synthesized via the interplay between constructive and destructive interference. The duration and spectral bandwidth of the pulse are Fourier conjugate variables and therefore they obey the uncertainty relation:

$$\Delta \mathrm{t} \cdot \Delta\omega \geq \frac{1}{2} \text{ , or alternatively: } \Delta \mathrm{t} \cdot \Delta\nu \geq \mathrm{K} \tag{2.42}$$

According to this relation, the broader the available spectral bandwidth, the shorter the duration that may be obtained, satisfying the equality condition. This condition refers to the case, where the pulse spectral components are perfectly phase-locked and the pulse is called bandwidth-limited or Fourier transform-limited (FTL), exhibiting the shortest duration which can be achieved, limited by the available spectral bandwidth.
The value that the constant K takes, in 2.42, depends on the pulse temporal shape and can be derived analytically in each case. Commonly, for a Gaussian pulse temporal profile, $\mathrm{K} = 0.441$ [118, 119], where $\Delta \mathrm{t}, \Delta\nu$ are defined as the respective time and frequency profile widths at their half-maximum value. In a more general case, the spectral components forming the light pulse can carry a time-dependent phase relation, due to chromatic dispersion for example, resulting in a longer duration than the bandwidth-limit (Eq. 2.42). Ultrashort light pulses can be mathematically expressed using their time and space dependent electric field and a complete description can be given both in the time or the frequency domain. The complex time-dependent electric field, neglecting its spatial dependence for the time being and assuming linear polarization, can be written as:

$$\tilde{E}(t) = \mathcal{E}(t) \cdot e^{i\phi(t)} \tag{2.43}$$

being the product of a slowly varying envelope function $\mathcal{E}(t)$ describing its temporal profile and an oscillatory term describing its temporal phase $\phi(t)$. The electric field is expressed here as a complex function for mathematical convenience. The real part of 2.43, is in principle a measurable quantity, while its intensity I(t) is proportional to the square of the real envelope function, $\mathrm{I(t)} \propto |\mathcal{E}(t)|^2$. A laser pulse is typically assumed to exhibit a Gaussian temporal profile:

$$\mathcal{E}_{\mathrm{Gauss}}(\mathrm{t}) = E_o \cdot e^{-\left(\frac{t}{\tau_\mathrm{g}}\right)^2} \tag{2.44}$$

where E_o is the peak electric field. The pulse duration, defined here and through the complete thesis at the intensity profile full-width-at-half-maximum (FWHM), is related with τ_g with:

$$\Delta \mathrm{t}_{\mathrm{FWHM}} = \sqrt{2\ln 2} \cdot \tau_\mathrm{g} \tag{2.45}$$

The electric field of the light pulse can be obtained in the frequency domain via the Fourier transform:

$$\tilde{E}(\omega) = \int_{-\infty}^{+\infty} \tilde{E}(t) \cdot e^{-i\omega t} dt \tag{2.46}$$

and vice versa an inverse Fourier transform results in a transformation back to the electric field in the time domain:

$$\tilde{E}(t) = \frac{1}{2\pi} \int_{-\infty}^{+\infty} \tilde{E}(\omega) \cdot e^{i\omega t} d\omega \tag{2.47}$$

The electric field in the frequency domain can be expressed in an analogous manner as that in the time domain:

$$\tilde{E}(\omega) = \mathcal{E}(\omega) \cdot e^{i\varphi(\omega)} \tag{2.48}$$

where $\mathcal{E}(\omega)$ corresponds to the pulse spectral amplitude and $\varphi(\omega)$ to the spectral phase. Both temporal and spectral phase terms, can be expanded in Taylor series as:

$$\phi(t) = \phi_o + \frac{\partial\phi(t_o)}{\partial t} \cdot (t - t_o) + \frac{\partial^2\phi(t_o)}{\partial t^2} \cdot (t - t_o)^2 + \sum_{n=3}^{\infty} \frac{\partial^n\phi(t_o)}{\partial t^n} \cdot (t - t_o)^n \tag{2.49a}$$

$$\varphi(\omega) = \varphi_o + \frac{\partial\varphi(\omega_c)}{\partial \omega} \cdot (\omega - \omega_c) + \frac{\partial^2\varphi(\omega_c)}{\partial \omega^2} \cdot (\omega - \omega_c)^2 + \sum_{n=3}^{\infty} \frac{\partial^n\varphi(\omega_c)}{\partial \omega^n} \cdot (\omega - \omega_c)^n \tag{2.49b}$$

Knowledge of the complete set of phase terms either in the time, or the spectral domain is sufficient to completely define the pulse, as the conjugate picture can be unambiguously obtained via Fourier transformation. Practically, the light pulse may hold an arbitrary initial phase distribution and the weight of each of those terms, is subject to change upon pulse propagation and interaction with matter. The physical interpretation assigned to each of the low-order terms of the Taylor expansion in both pictures, can be briefly discussed at this point.

The first constant term ϕ_o in the time-domain, corresponds to the carrier-to-envelope offset phase. This term determines the position of the peak electric field with respect to the peak of the pulse envelope, often of no practical importance for multi-cycle laser pulses where it can be neglected. Precise knowledge and control of the carrier-envelope phase becomes relevant in few-cycle pulse applications which rely on the exact pulse waveform, or, in ultra-precise frequency comb metrology where it is necessary for an absolute frequency calibration [122, 123]. In the time-domain (2.49a), the linear phase term gives rise to the pulse instantaneous frequency $\omega_{\text{inst}} = \omega_c + \partial\phi(t)/\partial t$, which equals the carrier frequency ω_c when the higher order terms are zero, i.e, when the pulse propagates in a non-dispersive medium. The quadratic temporal phase term corresponds to the linear rate of change in the instantaneous frequency as a function of time. This occurs upon propagation in a dispersive medium, typically in any transmissive optical component that exhibits a frequency-dependent refractive index. In this case, different frequency components forming the light pulse travel with different speed in the medium, exhibiting a linear change with wavelength in ordinary cases. As a consequence, they eventually separate in time as a function of their respective frequency, the pulse temporal profile gets broader and the pulse is said to be linearly-chirped.

Higher-order phase terms are responsible for asymmetric temporal distortions of the pulse shape, pre- or post-pulse formation and further pulse temporal broadening.

In the spectral domain, the linear spectral phase term describes the delay experienced by the pulse, described by its envelope, while propagating in an optical medium, also denoted as group delay (GD). The third term describes the group velocity temporal change as a function of wavelength, in direct correspondence to the linear chirp experienced by the pulse propagating in a dispersive medium, called also group velocity dispersion (GVD).

In summary, being broadband, ultrashort pulses experience temporal distortions when propagating through optical components. With prior knowledge of the initial pulse spectral or temporal phase, combined with the optical medium constants, the propagation effects on the pulse temporal shape can be determined and thus precisely tailored or compensated.

During the past years, a multitude of techniques have been developed, allowing for precise control of the pulse temporal/spectral phase. Routinely, temporally stretching and compressing a light pulse is achieved by taking advantage of the angular dispersion characteristics of optical elements like prisms or gratings, utilizing them in geometries that assign a defined optical path difference between different spectral components. In this way, mainly the 2^{nd} order phase term can be controlled with high precision and compensated accordingly. More advanced temporal shaping techniques using grating-prism combinations [124], dielectric aperiodic multilayer mirrors [125–127], acousto-optic programmable filters [128] and liquid crystal phase-masks [129] enable precise control of the pulse temporal shape and allow fine-tuning of higher-order phase terms [130]. A very detailed discussion about the above mentioned techniques and their applications is provided in [118] (Ch.2, Ch.8). The applicability of this pulse temporal shape tailoring technology is spectrally limited by the transmission characteristics of the utilized optical components. Beyond the ultraviolet spectral range, all-reflective approaches with limited transmission restrict the pulse-shaping capabilities significantly.

An illustrative example that showcases some of the concepts discussed above is presented in Fig. 2.2. The electric field and temporal intensity profile of a Gaussian pulse with a spectral bandwidth of $\Delta\lambda$ =100 nm is shown for two different spectral phase distributions. A flat spectral phase (2.2b) results in a bandwidth-limited pulse (2.2a) with a FWHM duration of 9.4 fs, while a modulated spectral phase (2.2d) results in a spectral redistribution within the pulse envelope and a longer, temporally distorted profile (2.2c).

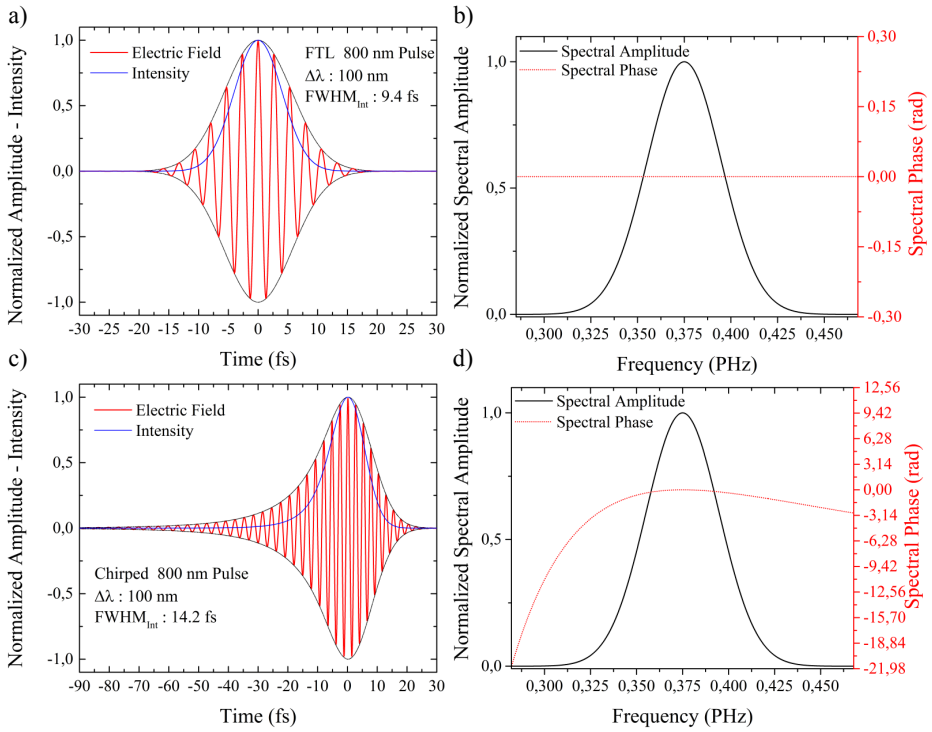

Figure 2.2: Gaussian infrared pulse electric field and intensity temporal profiles and corresponding spectral phase. In both cases a 100 nm bandwidth supports a bandwidth-limited duration of 9.4 fs at FWHM (a,b). For an arbitrary spectral phase distribution (d) the pulse stretches in time, its temporal profile changes and the instantaneous frequency varies along the pulse temporal profile (c).

In most practical experimental cases, an initially compressed pulse will propagate over a series of dispersive optical components before reaching the experimental target. Dispersive pulse broadening (linear chirp) is an unavoidable effect and can be compensated to a satisfactory level usually, using a grating or prism-pair optical compressor setup [130, 131]. An analytical expression providing the stretched pulse duration after propagation in a linear dispersive medium, assuming an initially bandwidth-limited Gaussian pulse is given below:

$$\Delta t_{D2} = \Delta t_{FTL} \cdot \sqrt{1 + \left(4 \cdot \ln 2 \cdot \frac{D_2}{(\Delta t_{FTL})^2}\right)^2} \tag{2.50}$$

with:

$$D_2 = \left(\frac{\partial^2 \varphi(\omega)}{\partial \omega^2}\right)_{\omega=\omega_c} \overset{\phi=k\cdot x}{=} x \cdot \left(\frac{\partial^2 k}{\partial \omega^2}\right)_{\omega=\omega_c} \overset{k\cdot c=\omega\cdot n}{=} \frac{x}{c}\frac{\partial^2}{\partial \omega^2}(\omega \cdot n(\omega)) \tag{2.51}$$

where D_2 corresponds to the group delay dispersion (GDD)[5] in the medium given in fs^2. As an example, one can consider a bandwidth-limited pulse centered at 162 nm with a duration of 20.0 fs at FWHM. Propagation through a CaF_2 window (GVD: 550.84 fs^2/mm at 20 °C, [132]) with 1 mm thickness will temporally stretch the pulse to 78.9 fs at FWHM. As a comparison, a second bandwidth-limited 162 nm pulse with a duration of 80.0 fs at FWHM, will only stretch to 82.2 fs at FWHM due to its reduced spectral width.
The amount of temporal broadening depends on the spectral bandwidth and initial spectral phase of the pulse as illustrated in the above example. Most optical materials will induce a positive chirp in the visible-infrared range ($n(\omega) > 0$, $\partial n(\omega)/\partial\omega > 0$), meaning that higher frequencies will be delayed with respect to lower frequencies and by using an optical material of appropriate type and thickness, residual phase can be compensated for an initially negatively chirped pulse.

2.4 Light Pulse Temporal Metrology based on Correlation Techniques

From the above analysis, it becomes obvious that the determination of the actual duration of the pulse by measuring its spectral width, using a spectrometer for example, is not sufficient when the corresponding spectral phase is not known. The information that one can obtain in that case would be the shortest possible duration supported by the given bandwidth described by Eq. 2.42.
Additionally, light pulses in the sub-100 fs temporal regime are by definition shorter than the temporal response of any electronic detector, thus it becomes impossible to perform a direct measurement that could determine their temporal profile [133]. The state-of-the-art technology that sets the temporal resolution limit in the case of electronic detectors, exhibiting an ultrafast response in the sub-picosecond timescale, is the streak camera [134]. Commercial streak cameras can reach nowadays a temporal resolution of 200 fs, while the theoretical limit lies just below 100 fs [135].

[5] Equal to to the group velocity dispersion mentioned before, multiplied with the medium length x

Ordinary electronic detectors have an infinitely slow response compared to the ultrashort light pulse duration and can be therefore considered to be time-integrating, simply measuring the average pulse power.
As a result, all-optical techniques that utilize statistical optics methodologies are necessary in order to access the pulse intensity temporal profile. All such techniques are basically variants of the cross-correlation or autocorrelation measurement principle. Advanced versions of those methods, mainly applied in the visible-infrared spectral range, are able to extract a considerable amount of temporal information, leading to a complete waveform reconstruction. The basic theoretical principles behind cross-correlation and autocorrelation-based temporal metrology will be discussed in the following section among their properties and implications. The discussion will eventually focus in 2^{nd} order non-linear autocorrelation, which is the technique experimentally investigated in the framework of the present thesis.

2.4.1 Autocorrelation - Cross Correlation Techniques

The temporal profile $I_s(t)$, describing the evolution of a time-dependent process, can be determined by using a narrow temporal gate that can progressively sample the evolution of this process at discrete time segments, by varying their relative timing.
This corresponds to measuring a convolution of the unknown signal $I_s(t)$ with a much shorter reference signal $I_{ref}(t)$. A convolution is a mathematical expression, describing the degree of overlap between two functions, when they are translated with respect to each other [136]. Practically, the reference signal either corresponds to the instrumental temporal response function or alternatively it can be obtained by an additional time-gate signal, when a time-integrating detection instrument is used. In both cases, the resulting convolution or cross-correlation[6] can be mathematically expressed as:

$$A_{conv}(\tau) = I_s * I_{ref} \equiv \int_{-\infty}^{+\infty} I_s(t) I_{ref}(t-\tau) dt \tag{2.52}$$

where A_{conv} is the signal cross-correlation function and can be obtained as a function of the temporal delay τ between the two time-dependent signals. In an ideal case the reference signal, or the instrumental response function, will be infinitely short compared to the unknown signal to be characterized and as such it can be described with the Dirac delta function in the time-domain. In that case the convolution function is written as:

$$A_{conv}(\tau) = I_s * I_{ref} \equiv I_s(t) * \delta(t) \equiv \int_{-\infty}^{+\infty} I_s(t)\delta(t-\tau)dt = f(\tau) \tag{2.53}$$

according to the Dirac delta function shifting property [137]. The relation 2.53 shows that with the availability of an infinitely narrow reference, the unknown temporal profile can be precisely determined by a cross-correlation measurement, as a function of the temporal delay between the two signals.

[6] Although the two terms mathematically differ by a time-reversal in one of the input signals, this difference has no practical implications in an experimental measurement where a time-reversal on the signals temporal profile or time-delay depends on the experimental implementation.

What also becomes obvious, is that in the unfortunate case where the reference signal has a broader temporal extent than the unknown signal, their roles will be reversed. As the reference signal duration increases, the resulting cross-correlation function will start to temporally smear and the instrumental temporal resolution will decrease (Fig. 2.3). With prior knowledge of the temporal shape of both signals, a deconvolution can extract the unknown time constant, corresponding to the unknown signal duration. The deconvolution process fidelity relies on the assumed temporal shapes and the degree that the reference signal is known.

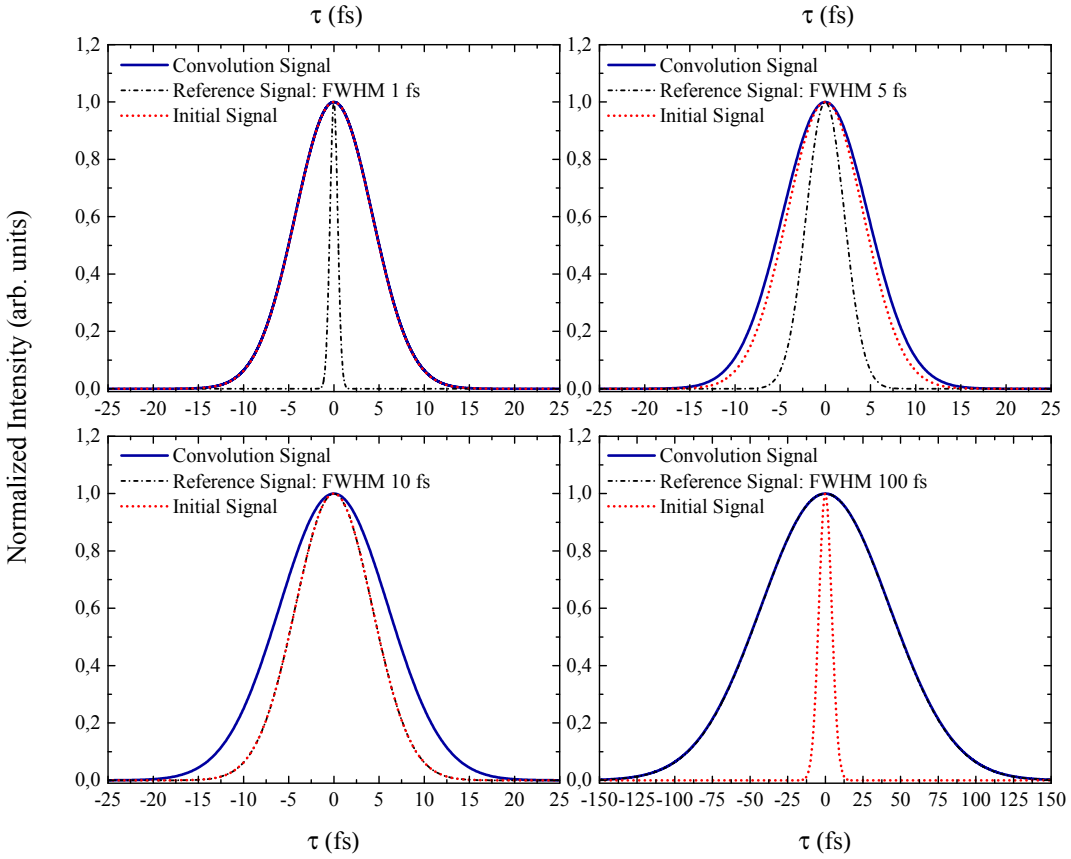

Figure 2.3: Simulated convolution signal between two pulses with Gaussian temporal profiles. With their duration defined at FWHM, the convolution of a 10 fs pulse with a reference pulse of 1,5,10 or 100 fs is presented, along with their corresponding intensity profiles centered at $\tau = 0$ as a visual guide. An effectively short reference pulse (1 fs) does not induce temporal smearing in the convolution signal which reproduces the initial pulse temporal shape. Using a broader reference pulse (5 fs, 10 fs) the resulting convolution signal is temporally smeared and deconvolution is necessary for initial pulse temporal shape retrieval. In the case of a broader reference pulse (100 fs) the roles of the two pulses are reversed.

The general principle described by the relation 2.52 is not limited in the temporal domain, rather it is a universal principle that applies to every case describing instrumental resolution. As an example, the spatial resolution associated with an imaging system is described by its point spread function [138] which is the intrinsic spatial reference function.

The point spread function describes the response of the imaging system to a point source, mainly accounting for diffraction phenomena. The image of each point in the object plane will result as a convolution of a spatial profile describing an ideally imaged point, with the optical systems point spread function, limiting the attainable spatial resolution.
The basic principles described above can be applied for the temporal characterization of an ultrashort light pulse. When a shorter optical pulse or temporal-gate signal is available, a cross-correlation measurement as described above can be performed. Practically, the reference pulse has to be considerably shorter than the pulse to be characterized and both pulses must be mutually synchronized in a robust manner, avoiding temporal jitter during the temporal delay scan. When the first condition cannot be fulfilled, accurate knowledge of the reference pulse is necessary for a high-fidelity deconvolution. Two very impressive examples of a cross-correlation measurements can be found in [36, 39]. In both works, a very narrow temporal gate offered by using an ultrashort XUV reference pulse, gave the ability to record the unknown pulses vector potential and thus to completely reconstruct the light waveform.
Frequently, a well characterized short reference light pulse is not available. In that case, the ultrashort light pulse can be temporally characterized by performing an auto-convolution or to be mathematically consistent, an autocorrelation measurement. An autocorrelation measurement, uses the complex conjugate of the unknown signal as the reference signal and can be obtained by superimposing two identical light pulse replicas on a time-integrating detector with a variable delay between them. Light pulse autocorrelation techniques typically employ an interferometric optical setup, used to split and delay two identical copies of the pulse with respect to each other in combination with a detection system based on photo-absorption. Depending on the detection process chosen, the measurement can obtain the n^{th} order correlation function of the radiation field, which describes its coherence properties [139–142]. When a light pulse is considered, relevant temporal information, such as the pulse duration and the temporal phase evolution can be extracted under justified assumptions.
The simplest variant of such a measurement is the linear field-autocorrelation (FAC) and can be experimentally realized, using a light interferometer, combined with a time-integrating detector such as a photodiode or a CCD camera, that possesses a linear response to the input pulse intensity. By varying the optical path length difference between the two interferometer arms, a time-delay can be introduced between the two resulting pulse replicas. The linear detector signal at the interferometer output would be:

$$S_{FAC}(\tau) \propto \int_{-\infty}^{+\infty} |[E(t) - E(t-\tau)]|^2 \, dt = \tag{2.54a}$$

$$= \int_{-\infty}^{+\infty} |E(t)|^2 + |E(t-\tau)|^2 - 2 \cdot \mathrm{Re}\left[E(t)E^*(t-\tau)\right] dt \tag{2.54b}$$

$$S_{FAC}(\tau) \propto 2 \cdot \int_{-\infty}^{+\infty} |E(t)|^2 \, dt - 2 \cdot \mathrm{Re} \int_{-\infty}^{+\infty} E(t)E^*(t-\tau) dt \tag{2.54c}$$

The resulting field-autocorrelation signal is composed by two main terms (2.54c). The first constant term is proportional to the pulse energy, describing the integrated intensity of each individual arm in the absence of the second and shows no interference effects.

The second oscillatory term gives rise to an interferogram which corresponds to the pulse 1st order correlation function. According to the fundamentals of statistical optics, when normalized, it describes the 1st order degree of coherence [140–142] of the considered light source. Being symmetric with respect to a delay sign change, $S_{FAC}(\tau) = S_{FAC}(-\tau)$ it cannot distinguish the time direction. Furthermore, it is straightforward to show that a field-autocorrelation measurement corresponds to a high-resolution measurement of the pulse spectrum. According to the Wiener-Khinchin theorem[7], the Fourier-transform of the 1st order field correlation function, provides the pulse spectral intensity distribution. As a result, the only temporal information obtained by a linear field-autocorrelation measurement, is the pulse coherence time, being the reciprocal of the pulse spectral width. This is connected with the shortest possible pulse duration attainable (2.42) but it does not provide useful information about the temporal phase terms. Therefore a linear field-autocorrelation measurement outcome of a temporally stretched pulse cannot be distinguished from that of its bandwidth-limited version.

Alternatively, by utilizing a detector at the interferometer output that exhibits an instantaneous, 2nd order, non-linear response to the input light intensity, will result in a 2nd order autocorrelation measurement. Experimentally, it can be realized by detecting a direct two-photon absorption signal, such as 2nd harmonic generation in a non-linear crystal, two-photon absorption fluorescence or direct two-photon ionization, as a function of the delay between the two pulse replicas. Such a measurement can be interpreted as a photon-photon coincidence experiment [143, 144], due to the fact that the two photons can be absorbed within an infinitesimal time interval, permitted by the time-energy uncertainty principle and thus it can provide time-dependent information. In the most general case, the outcome of a 2nd order autocorrelation measurement can be expressed as[8]:

$$S^{(2)}_{FRIAC}(\tau) = \int_{-\infty}^{+\infty} \left| [E(t) + E(t-\tau)]^2 \right|^2 dt = \tag{2.55a}$$

$$= \int_{-\infty}^{+\infty} I^2(t) + I^2(t-\tau) dt \tag{2.55b}$$

$$+ 4 \cdot \int_{-\infty}^{+\infty} I(t) I(t-\tau) dt \tag{2.55c}$$

$$+ 2 \cdot \int_{-\infty}^{+\infty} [I(t) + I(t-\tau)]\, E(t) E^*(t-\tau) dt + \text{c.c.} \tag{2.55d}$$

$$+ 2 \cdot \int_{-\infty}^{+\infty} E^2(t) E^{*2}(t-\tau) dt + \text{c.c.} \tag{2.55e}$$

where $I(t) \equiv |E(t)|^2$ and FRIAC stands for fringe-resolved intensity autocorrelation. The four different terms in the above expression represent different quantities. The first term (2.55b) is a delay-independent constant, corresponding to the non-linear signal generated individually by the two pulses. When the two pulses are collinear, the measurement output contains interferometric information represented by the oscillatory third (2.55d) and fourth (2.55e) terms and it corresponds to a fringe-resolved intensity autocorrelation. The third term oscillates with the fundamental frequency ω, whereas the fourth term oscillates with 2ω, as a function of the delay (τ).

[7] A mathematical proof is provided in Appendix A.1.

[8] A complete term expansion can be found in Appendix A.2.

When the interferometric information cannot be resolved these two terms vanish and the expression reduces to the first two terms:

$$S^{(2)}_{IAC}(\tau) = \int_{-\infty}^{+\infty} I^2(t) + I^2(t-\tau)dt \tag{2.56a}$$

$$+ 4 \cdot \int_{-\infty}^{+\infty} I(t)I(t-\tau)dt \tag{2.56b}$$

$$S^{(2)}_{IAC}(\tau) \propto 2 \cdot \int_{-\infty}^{+\infty} I^2(t)dt + 4 \cdot \int_{-\infty}^{+\infty} I(t)I(t-\tau)dt \tag{2.56c}$$

This expression is known as the intensity autocorrelation (IAC) of the light pulse and it corresponds to an intensity profile autocorrelation. Following the basic conceptual idea behind convolution techniques, the light pulse is used here as a reference to measure itself. In this case, a deconvolution is necessary in order to obtain the pulse duration as both reference and unknown signals have the exact temporal characteristics. Using an appropriate pulse temporal shape assumption, commonly a Gaussian shape, the pulse duration can be extracted from a 2nd order autocorrelation trace by deconvolution. When a Gaussian temporal profile is considered, it can be shown that the 2nd order autocorrelation width relates with the pulse intensity temporal width as:

$$\Delta\tau_{FRIAC} \equiv \Delta\tau_{IAC} = \sqrt{2} \cdot \Delta t_{pulse} \tag{2.57}$$

This results as a specific case of the general property of the convolution of two Gaussian functions, being also a Gaussian function [145] with $\sigma_{conv} = \sqrt{\sigma_1^2 + \sigma_2^2}$, where σ_{conv} represents the convolution signal width and σ_1, σ_2 the two initial Gaussian function widths respectively. Generally, the temporal conversion factor can be analytically derived for most of the anticipated temporal profiles and a long, although non-exhaustive list can be found in [118].

Second-order autocorrelation, both in its fringe-resolved variation, as well as an intensity autocorrelation, cannot distinguish the time axis direction and the resulting signal is completely symmetric around $\tau = 0$:

$$S^{(2)}_{FRIAC}(\tau) = S^{(2)}_{FRIAC}(-\tau) \equiv S^{(2)}_{2IAC}(\tau) = S^{(2)}_{2IAC}(-\tau) \tag{2.58}$$

The main implication in that case, is that a second pulse arriving either prior or after the main pulse, cannot be distinguished in a 2nd order autocorrelation trace. The trace will exhibit two equal satellite peaks, separated by the main peak by a delay-timescale distance that equals the original pulse temporal separation. In other words, a pre-pulse or a post-pulse with the exact temporal separation from the main pulse will result in the exact 2nd order autocorrelation trace (Fig. 2.4a). As the pulse temporal shape complexity increases, as in the case of an arbitrary femtosecond multi-pulse temporal structure, the pulse temporal shape reconstruction becomes increasingly complicated (Fig. 2.4b) and in even in trivial cases, a set of assumptions will have to be used .

The fringe-resolved autocorrelation trace contains temporal phase information [146] that can be extracted when a high signal-to-noise ratio condition is fulfilled [147, 148]. However, as a time-asymmetry insensitive method, it can not distinguish the sign of the pulse chirp, which in certain experimental cases can be predicted considering its physical origin.

The third FRIAC term, oscillating with the light pulse fundamental frequency ω, spectrally dominates in the measured interferometric trace and with previous knowledge of the pulse central frequency it provides an intrinsic temporal delay calibration scale or an intrinsic 'temporal ruler'. Alternatively when the delay scale is precisely determined, as for example in the case when a delay stage paired with an optical encoder is used or a second source with very well-defined spectral characteristics is used as a reference, the measured fringe pattern provides a very accurate measurement of the carrier frequency of the pulse obtained by the Fourier transform of the FRIAC trace.
In certain cases, a collinear interferometric measurement is not possible, as for example in spectral regions where a transmissive beam-splitter is not available. A non-collinear geometry has to be employed and the measured signal corresponds to a 2^{nd} order intensity autocorrelation (IAC) as mentioned above. The IAC signal does not provide specific information about the pulse temporal phase, but instead about the pulse intensity temporal distribution, always under a justified pulse temporal shape assumption as previously described.

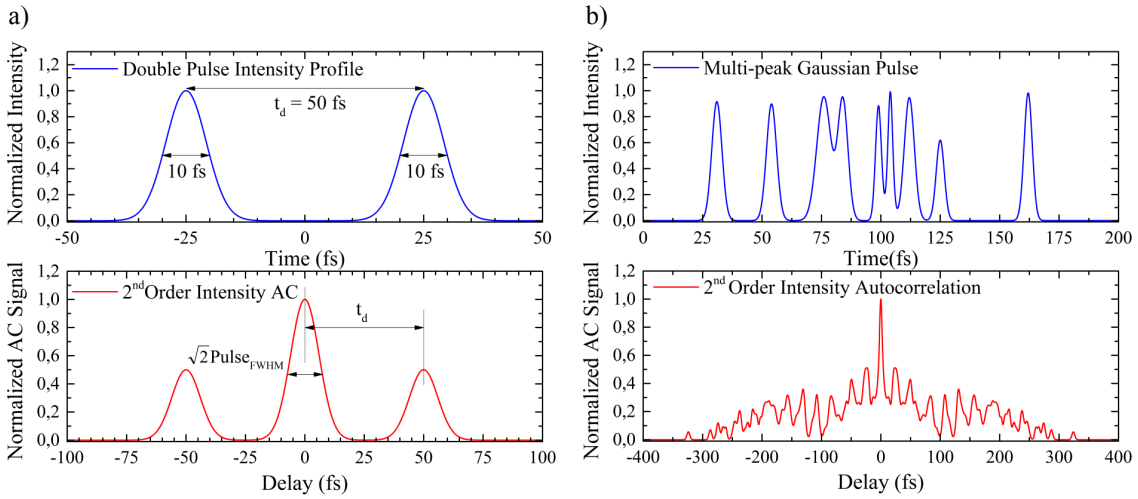

Figure 2.4: Simulated multi-pulse intensity autocorrelation traces: a) Double Gaussian pulse with FWHM: 10 fs duration and an inter-pulse temporal spacing of t_d = 50 fs. The resulting 2^{nd} order intensity autocorrelation trace exhibits a main and two satellite peaks with a spacing in delay units that equals t_d. b) Randomly-generated multi-Gaussian mode pulse. The resulting 2^{nd} order intensity autocorrelation trace increases in complexity, prohibiting an unambiguous deconvolution. The coherence spike at the delay origin relates with the pulse coherence time, or equivalently the pulse spectrum.

In an experimentally obtained signal, a quantity of interest is the maximum attainable peak-to-background autocorrelation signal contrast. The theoretically expected value can be calculated by evaluating both 2^{nd} order autocorrelation signal expressions at the limits $\tau \to 0$ and $\tau \to \pm\infty$.

For example, for the intensity autocorrelation signal contrast-ratio one obtains:

$$\lim_{\tau\to 0} \mathrm{S}^{(2)}_{\mathrm{IAC}}(\tau) = 6 \cdot \int_{-\infty}^{+\infty} I^2(t)dt \tag{2.59a}$$

$$\lim_{\tau\to \pm\infty} \mathrm{S}^{(2)}_{\mathrm{IAC}}(\tau) = 2 \cdot \int_{-\infty}^{+\infty} I^2(t)dt \tag{2.59b}$$

$$\mathrm{C}_{\mathrm{2IAC}} = \frac{\lim_{\tau\to 0} \mathrm{S}^{(2)}_{\mathrm{IAC}}(\tau)}{\lim_{\tau\to \pm\infty} \mathrm{S}^{(2)}_{\mathrm{IAC}}(\tau)} = \frac{3}{1} \tag{2.59c}$$

The resulting 3:1, 2$^{\mathrm{nd}}$ order intensity autocorrelation peak-to-background contrast ratio is an intrinsic property of a 2$^{\mathrm{nd}}$ order intensity autocorrelation function and it is independent on the pulse temporal shape. Following the same procedure it is trivial to show that the expected contrast ratio for a 2$^{\mathrm{nd}}$ order fringe-resolved intensity autocorrelation measurement (FRIAC) is $\mathrm{C}_{\mathrm{FRIAC}}$ =8:1.

It should be emphasized, that the measured contrast ratio provides a very important measurement consistency check and it can in addition provide important information about the light source coherence properties. In the case of an ideal mode-locked laser pulse, a different contrast ratio typically results due to poor spatial alignment or spatial-interference effects, as those associated with the 2$^{\mathrm{nd}}$ order volume-autocorrelation geometry in the focus of a spherical mirror [149–151], typically used in the vacuum-extreme ultraviolet spectral range. Nevertheless, a decreased peak-to-background contrast ratio (2:1, 1.5:1) is expected and has been observed in the past, in the 2$^{\mathrm{nd}}$ order autocorrelation traces when pulses originating from chaotic or partially-coherent light sources, like multi-mode free running lasers or stochastically generated radiation sources [152–155] are measured. The resulting autocorrelation trace, usually consists of a narrow temporal spike located at $\tau = 0$, sitting on a broader Gaussian temporal pedestal (Fig. 2.4b). The temporal spike is directly proportional to the pulse coherence time or the reciprocal bandwidth as mentioned before [140,142]. It is perhaps worth mentioning at this point that the coherence time associated with an incoherent, chaotic light source, such as a light bulb, can be also found in the fs-timescale and it is determined by the dominant line-broadening mechanism in the light source [140]. The temporal width associated with the temporally broader pedestal, corresponds to the average pulse duration, integrated over a set of pulses with varying temporal properties. According to each particular case, a pulse duration definition might not be possible anymore and the root-mean-square temporal width might be used in that case. Depending on the light source nature, a large number of temporal ambiguities associated with the autocorrelation technique [156] may hinder a robust deconvolution of the pulse temporal properties.

When the pulse intensity content is sufficient and a non-linear detector that exhibits an n$^{\mathrm{th}}$ order instantaneous intensity response available, an autocorrelation measurement of a higher-order n can be obtained. It has been theoretically shown, that a third-order autocorrelation measurement contains all the information that is present in higher autocorrelation orders [157]. Typically, a 3$^{\mathrm{rd}}$ order intensity autocorrelation measurement uses a non-resonant, three-photon transition in a direct analogy to the 2$^{\mathrm{nd}}$ order variant and the signal obtained in that case is:

$$\mathrm{S}^{(3)}_{\mathrm{IAC}}(\tau) = \int_{-\infty}^{+\infty} I(t)I^2(t-\tau)dt \tag{2.60}$$

The 3rd order autocorrelation signal is no-longer time-reversal symmetric $S^{(3)}(\tau) \neq S^{(3)}(-\tau)$. A 3rd order intensity autocorrelation measurement can therefore distinguish the temporal orientation of a satellite-pulse.
The resulting measurement contrast can be calculated in a similar manner as before (Eq. 2.59) when the complete expression is expanded, corresponding to 10:1 for a 3rd order intensity autocorrelation, or alternatively to 32:1 for a 3rd order fringe-resolved measurement. An important remark about the maximum attainable signal contrast should be made at this point. The calculated values mentioned above, both for 2nd and 3rd order autocorrelation measurements, consider that the autocorrelation measurement background corresponds to the non-linear signal generated by both pulse replicas individually in the medium. Taking advantage of an experimental geometry that poses phase-matching constraints such that the instantaneous non-linear signal, cannot be generated by each of the two pulses individually, a background-free, high-dynamic-range autocorrelation measurement can be obtained.
A typical example can be found in 3rd order autocorrelation signal obtained by sum-frequency generation, mixing the pulse to be characterized at frequency ω and its second harmonic at 2ω in a non-linear crystal. The resulting 3rd order autocorrelation signal, shows no contributions from the individual pulses due to phase-matching constraints and it may span over several (>7) orders of magnitude, depending only on the dynamic range of the time-integrating detector used [158]. In this way, not only the high intensity peak structure of the pulse is obtained, typically constrained to a 10^3:1 measurement dynamic range offered by a CCD detector for example, but also the lower intensity pulse pedestal, originating from amplified-spontaneous emission in the pulse amplification stage.
The Gaussian pulse duration can be obtained from a 3rd order autocorrelation by deconvolution as: $\Delta\tau_{3\mathrm{IAC}} = \sqrt{3/2} \cdot \Delta t_{\mathrm{pulse}}$ in this case. Additional deconvolution factors for most common temporal shapes, can be found in [158].

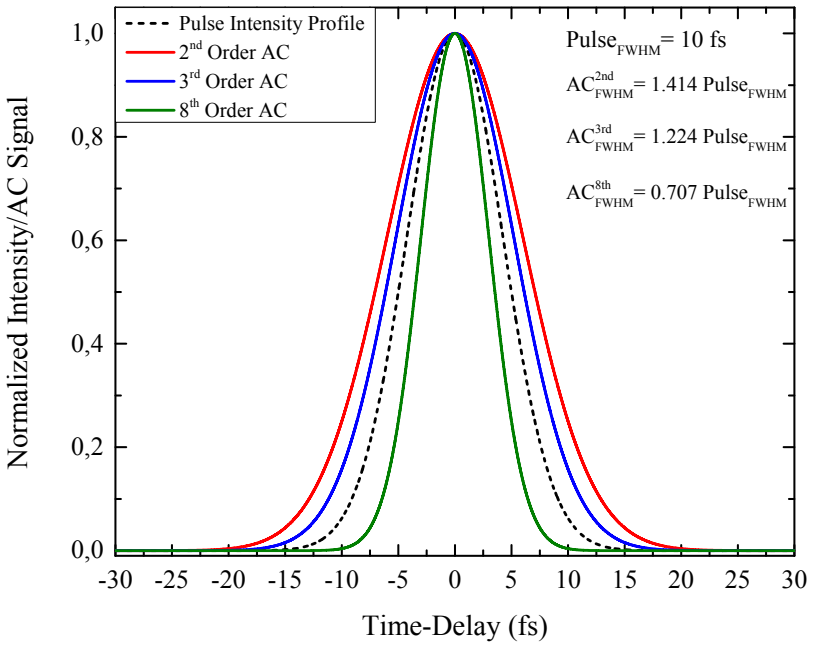

Figure 2.5: Simulated intensity autocorrelation traces and corresponding temporal deconvolution factors for a Gaussian pulse with 10 fs FWHM duration

.

Generally, the deconvolution factor decreases for increasing autocorrelation order, reaching values even below unity for higher orders. The deconvolution factor value depends on the particular non-linearity order sharing between the two optical branches, typically assumed to be equal, as it is in principle a high non-linearity cross-correlation measurement and depends on the respective pulse widths.
Following the same theoretical treatment as above, the deconvolution factor and peak-to-background contrast ratio can be obtained for any particular order. In order to provide a quantitative picture, the resulting intensity autocorrelation signal and corresponding temporal deconvolution factors have been numerically evaluated for three different orders, assuming a Gaussian pulse temporal profile and they are presented in Fig. 2.5.

2.4.2 Advanced Pulse Metrology Techniques

This section is dedicated to a brief description of some well-established, advanced pulse temporal characterization techniques. Although most of them are advanced autocorrelation or cross-correlation techniques and can provide more information on the pulse temporal characteristics, their implementation, especially in the short wavelength range, requires more complicated detection methods and data processing algorithms.
Starting with an advanced spectrographic variant of an intensity autocorrelation measurement, effectively dealing with most of the measurement ambiguities mentioned above, the frequency-resolved optical gating (FROG) technique [159–162] uses a spectrometer in the interferometer output. A frequency-resolved optical gating trace is obtained as a spectrally-resolved intensity autocorrelation signal, resulting in a spectrogram from which both pulse intensity and phase can be retrieved. The FROG trace inversion algorithm, relies on a two-dimensional phase retrieval problem, which is known to have a unique solution, in comparison to the one-dimensional phase retrieval problem of the intensity autocorrelation [163, 164]. An alternative, method that can retrieve the pulse spectral phase, based on spectral shearing interferometry, is the so called, SPIDER (spectral phase interferometry for direct electric-field reconstruction) technique [165]. In spectral shearing interferometry, two spectrally shifted copies of the pulse, usually one at the fundamental frequency ω_o and one shifted pulse replica at $\omega_o + \delta\omega$ interfere on a time-integrating detector, typically a spectrometer. The spectral phase at one frequency is referenced to the spectral phase at the different frequency separated by the spectral shift (shear). The pulse spectral phase can be retrieved from the resulting interferogram [166] when a calibration trace taken by measuring the spectrum of two time-delayed, non-frequency shifted replicas of the pulse, is available. Experimentally, the two spectrally shifted pulse copies are commonly obtained by sum-frequency generation of two time-delayed pulse replicas, with a third temporally-stretched pulse copy. Sum-frequency generation, occurs for each of the pulse replicas with a slightly different frequency portion of the original pulse in this case, as a result of their time-delay. Practically, although this method does not rely on non-linear optics, i.e. a multiphoton signal as with time-domain approaches, it effectively utilizes a multi-photon process to create the spectrally-sheared pulse pair.
Both FROG and SPIDER techniques are able to retrieve the pulse temporal shape, with limited ambiguity as compared to intensity autocorrelation measurements. Nowadays,

they are both routinely used in femtosecond laser laboratories, utilizing visible, infrared or ultraviolet light, for pulse characterization and optimization purposes. However, for shorter wavelengths, beyond the ultraviolet regime, the implementation of both pulse temporal characterization methods becomes extremely challenging with limited applicability, that for the time being relies on the particular light source properties [40, 41, 167–174].
On the one hand, frequency-resolved optical gating, depends on spectrally-resolved detection of an instantaneous non-linear signal, usually obtained by means of direct multi-photon ionization. The required spectral resolution is provided by means of high-resolution, energy-resolved photo-electron detection, which is experimentally demanding and sensitive to space-charge repulsion mechanisms.
On the other hand, a SPIDER measurement requires a spectrally sheared replica of the pulse to be characterized. Although, a spectral shear is a trivial task in the visible-infrared regime, using sum-frequency generation in a non-linear crystal, in the VUV-XUV it has limited applicability [156] to sources that can offer such a spectrally-shifted pulse pair [40, 41, 174].
A very successful alternative technique, mainly used with XUV light pulses and based on photo-electron spectroscopy is light-field streaking [8, 10, 36, 38, 39, 175–177]. In a conventional streak camera, an electron bunch is released from a photo-cathode hit by the light pulse, inheriting its temporal structure. This electron bunch is accelerated towards a position-sensitive detector, being transversally deflected at the same time, by a fast varying electric field. In this way the pulse temporal structure is spatially encoded on the electron distribution mapped on the detector image. As previously mentioned, the temporal resolution achieved with such an apparatus is limited to approximately 200 fs.
Light-field streaking, employs an intense long-wavelength electromagnetic light field instead, in order to streak photoelectrons released by the XUV pulse that reproduce its temporal structure. Following this approach, the streaking speed is significantly increased and thus the achievable temporal resolution. The pulse to be characterized, is typically an isolated XUV pulse with sub-fs or fs duration and the streaking field originates from a well-synchronized, co-propagating fs infrared or sub-ps far-infrared pulse, depending on the anticipated XUV pulse duration. Being essentially a cross-correlation spectrographic technique, temporal sampling (by a temporal gate or reference function) is realized by the steep gradient of the streaking fields vector potential, acting as a sub-fs or fs phase gate respectively. The XUV pulse temporal shape can be retrieved by deconvolution, comparing the resulting photoelectron peak width detected parallel to the streaking field when the XUV pulse coincides with a zero crossing of the streaking field vector potential, with and without the streaking field. The temporal resolution mainly depends on the streaking speed, which is experimentally determined by scanning the delay between the two pulses and evaluating the resulting photoelectron peak spectral shift. The measurement temporal window is determined by the streaking field period, being in the sub-fs timescale at 800 nm and reaching the 100-fs timescale when single-cycle THz radiation pulses are employed. One very important prerequisite for such a measurement is a temporal-jitter-free synchronization between the two pulses, ensuring that the XUV pulse stays within the zero-crossing of the vector potential curve, in a linear-slope regime. By tuning the delay between the two pulses, reconstruction of the streaking pulse waveform can be achieved, using the resulting spectrogram [36, 38, 39], as the roles of the two pulses are exchanged and the short XUV pulse is used in this case as the reference signal.

A longer XUV pulse or an XUV pulse train, spanning over one cycle of the long wavelength field will result in satellite photoelectron peaks, or 'side-bands', spaced by integer multiples of the long-wavelength field photon energy, with respect to the main photoelectron peak [10, 178, 179].
Pulse trains resulting from a high-harmonic spectral comb, can be temporally characterized using the resulting sideband spectrum. If the sideband intensity is measured as a function of the delay between the XUV and dressing infrared laser fields, it will appear modulated with a period equal to twice the phase of the dressing laser field and with a relative offset equal to the phase difference between the adjacent high-harmonics. If this phase offset is obtained for a number of different sidebands, then it is possible to obtain the phase difference between multiple harmonics, and thus determine whether they are phase locked and form an attosecond pulse train [9, 180].
When individual fsec XUV pulses are considered, the sideband intensity as a function of the delay between the XUV and dressing pulses can provide an accurate estimate of the temporal jitter between the two pulses and depending on the pulse length, an estimate of the XUV pulse duration resulting as a cross-correlation measurement [26, 181–183].
As a closing remark, it is important to stress the fact that each of the above techniques provides reliable results, depending on the validity of the theoretical assumptions used in each case, the implementation and the signal limitations that are always present in real experimental datasets. This is also reflected in the number of experimental [184–186] and theoretical studies [148, 156, 187–190] aiming to benchmark these techniques and identify possible reconstruction ambiguities. Depending on the pulse generation conditions, the existence of a well-synchronized reference pulse and the corresponding spectral and temporal characteristics, certain approaches become more attractive than others.
For example, an experiment using a high-intensity multi-TW fs laser pulse would benefit from a high-dynamic range measurement, offered for example by a 3^{rd} order autocorrelation [191]. In such a case the ps amplified-spontaneous emission (ASE) pedestal surrounding the main peak, formed during amplification, can be measured and subsequently suppressed. On the other hand, the compression of a broadband few-cycle laser pulse, temporally fragile due to its sensitivity to chromatic dispersion, can be optimized using a pulse characterization technique capable of handling such a broad bandwidth and can reliably reconstruct the spectral phase profile of the pulse [192].

2.4.3 Single-shot Pulse Temporal Characterization

An autocorrelation or cross-correlation measurement obtains a signal recorded as a function of the delay between two pulse copies or two different pulses respectively. Therefore, the resulting trace typically integrates over many consecutive pulses, incorporating the light source statistical properties. Amplified, mode-locked laser systems are known to exhibit very good pulse-to-pulse stability, which is typically also inherited by the light source based on high-harmonic generation, driven by such systems. The pulse temporal profile variation is usually negligible and a multi-pulse integrated autocorrelation trace reflects the individual pulse temporal properties in this case.

On the contrary, free running multi-mode lasers [153, 193], or Free-Electron Lasers based on self-amplified spontaneous emission [35, and references therein] where the amplified radiation generation starts from shot-noise, exhibit strong shot-to shot fluctuations both in their spatial, spectral and temporal properties.
In such cases, the measured autocorrelation trace incorporates the light sources statistical behavior, which manifests itself as reduced pulse-to-pulse coherence. The resulting autocorrelation trace exhibits a coherence spike (also denoted as coherent artifact in the literature) peaked when the two pulse replicas are synchronized, sitting on a broader pedestal that corresponds to the average pulse envelope duration. In other words, the autocorrelation trace in this case reflects not the individual pulse temporal properties, but rather the averaged coherence properties of the light source. Individual-shot pulse diagnostics are indispensable in this case, providing the possibility to post-process the retrieved experimental data and sort them accordingly.
A single-shot autocorrelation, or cross-correlation measurement can be obtained, by encoding the temporal delay information in space. Instead of scanning a temporal delay over consecutive pulses, the two pulse replicas can be geometrically superimposed in a way, such that the delay between them is encoded on a spatial coordinate. In this manner the complete autocorrelation measurement is performed during each shot by spatially resolving the resulting instantaneous non-linear signal with an imaging detector.
Such a measurement can be obtained, utilizing either a co-propagating pulse geometry with a small angle between the two pulses [194], or alternatively a counter-propagating pulse arrangement [195]. A fringe-resolved intensity autocorrelation or alternately an intensity autocorrelation trace can be obtained depending on the spatial resolution of the utilized detection system. In the visible-infrared spectral region, the single-shot autocorrelation measurement is commonly obtained by recording the non-linear signal resulting from semi-collinear frequency mixing in a non-linear crystal, with the temporal delay being encoded on the axis along the beam intersection plane. Nevertheless, a multitude of alternative, suitable non-linear processes can be also utilized, as for example two-photon conductivity in semiconductors [196, 197] or direct multi-photon ionization [198, 199] in the gas phase.
A similar geometrical analysis can be applied in both cases and a thorough description of the counter-propagating pulse geometry, experimentally utilized within the framework of the present thesis, will be given in the following chapter. Without loss of generality, the spatial delay-encoding principle will be discussed here for the case of a semi-collinear pulse propagation geometry (Fig. 2.6) [194, 199–202].
As shown in Fig. 2.6a, two synchronized pulses cross under a small angle θ. In such a geometry, the two pulses exhibit a continuously increasing arrival time difference along the x-axis, corresponding to an increasing mutual time-delay with respect to the intersection point (x=0) where they are synchronized. Additionally, it is evident that the delay $\tau(x)$ on a fixed x axis position, grows with an increasing angle θ, while $\tau(x) = 0$ at every point x when $\theta = 0$. Following a simple geometrical analysis, the resulting temporal delay encoded along the x-axis, can be expressed as:

$$\tau(x) = \frac{2nx}{c} \sin\frac{\theta}{2} \tag{2.61}$$

where n is the refractive index of the medium where the light propagates, c refers to the speed of light and θ is the angle between the two co-propagating pulses.

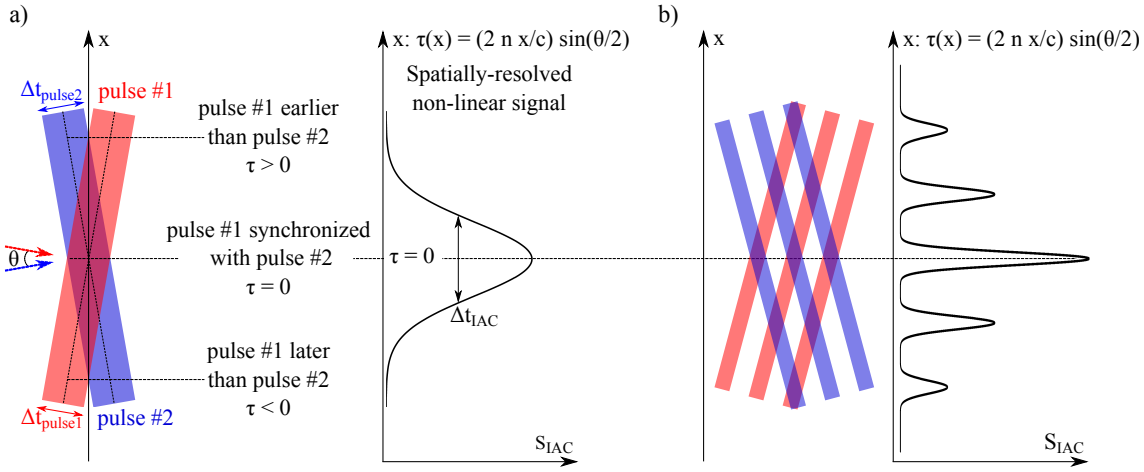

Figure 2.6: Spatial delay-encoding principle for single-shot temporal metrology. a) Two pulses cross at a small angle θ. Their arrival-time difference, corresponding to a spatially-dependent time-delay $\tau(x)$, increases in each position x away from their intersection point (x=0) as $\tau(x) = (2nx/c)\sin\theta/2$ (2.61). The corresponding intensity autocorrelation trace is obtained in every individual shot by imaging the resulting non-linear signal. b) Single-shot multi-pulse autocorrelation example using the exact principle.

The corresponding autocorrelation measurement can be therefore performed on a single-shot by imaging the resulting non-linear signal. The autocorrelation signal delay dependence is encoded in the x-direction and can be directly retrieved from the non-linear signal image. Depending on the spatial resolution offered by the detection system, a fringe resolved autocorrelation can be obtained in the same manner.
The case of a multi-pulse autocorrelation measurement is schematically depicted in Fig. 2.6b. A delay-time symmetric multi-peak autocorrelation curve will result for a triple pulse, in a similar manner as it would for a delay-scanning autocorrelation measurement. The non-linear signal emanates from the two pulse overlap regions and the delay encoding principle previously described, can be clearly demonstrated visually in this example. A detailed discussion and thorough theoretical analysis of a single-shot autocorrelation in the XUV range, using such a geometry is provided in [42].
It should be additionally noted at this point that the relation 2.61 implies that a temporal-delay smearing will be always present in a non-collinear delay-scanning autocorrelation measurement. Each point on the autocorrelation curve will integrate over a range of temporal delay values. For reasonable beam profile dimensions though and for small angles between the two pulses, this introduced time-delay axis uncertainty turns out to be smaller than the typical experimental uncertainty in most cases.
Generalizing this spatial delay-encoding concept, the same principle can be used for the complete range of experiments that exhibit a time delay-dependence. This applies to pulse metrology techniques, such as, frequency-resolved optical gating [202] for example, or more generall,y to experiments based on the cross-correlation methodology designed to follow ultrafast dynamics of an evolving process [203].

As final remark, it should be mentioned here that both techniques based on spectral phase interferometry for direct electric-field reconstruction (SPIDER), as well as light-field streaking, also provide individual-shot temporal information. Their applicability relies mainly on the availability of an additional well-synchronized streaking field or the possibility to experimentally realize a spectrally-shifted copy of the pulse to be characterized, in addition to the particular pulse temporal and spectral properties.

2.4.4 Time-resolved Ultrafast Dynamics: The Pump-Probe Approach

The pump-probe technique is a well-established method utilized to follow dynamical processes that evolve in ultrashort timescales. Its principles in combination with femtosecond laser pulses form the methodological backbone of femtochemistry [1].
In a pump-probe experiment, a pump pulse prepares a molecular system in a time-dependent transition state, initiating dynamics and defining the time origin for its subsequent evolution. The pump pulse is followed by a second pulse (probe) with a variable time-delay, which promotes the time-dependent excited population from the transition state to a final state resulting in a signal which is recorded as a function of the delay between the two pulses. The resulting delay-dependent pump-probe signal encodes information about the dynamics in the excited state which can be usually retrieved by deconvolution.
Essentially, according to the thorough analysis performed in [204], the pump-probe signal results as a cross-correlation between the molecular response function $M_c(t)$, describing the temporal evolution of the population in the excited state, and the cross-correlation signal between pump and probe pulses, also known as the finite instrument response function. In the special case where pump and probe pulses are replicas of the same pulse, the pump-probe signal results from the cross-correlation of the molecular response function, with the intensity autocorrelation function of the light pulse.
Following the derivation presented in [204], an example of a simple pump-probe experiment can be discussed. A molecular system, initially at its ground electronic state $|a\rangle$ is excited to a dissociative state $|b\rangle$ by a pump pulse. In absence of coherent effects, the excited state population will decay exponentially with a rate t_d+f, with t_d and f being the non-radiative and fluorescence decay rates respectively:

$$\frac{d}{dt}n_b(t) = -(t_d + f)n_b(t) \tag{2.62a}$$

$$n_b(t) = n_b(t_0) \cdot \mathrm{Exp}\left[-(t_d + f) \cdot t\right] \tag{2.62b}$$

where $n_b(t)$ denotes the population in $|b\rangle$, t_0 corresponds to the time-origin for the experiment defined by the pump pulse temporal profile peak and t in 2.62b evolves after t_0 such that $t > t_0$. Following the excitation, a probe pulse arrives at a later time, ionizing a part of the population in $|b\rangle$. Repeating this experiment for a sequence of delay times between pump and probe pulses, results in a delay-dependent ion signal, from which the decay constant t_d+f can be extracted. The total number of photons impinging in the interaction region can be defined as:

$$a_{\mathrm{pu/pr}} = \frac{E_{\mathrm{pu/pr}}/(\hbar\omega_{\mathrm{pu/pr}})}{\pi R_{\mathrm{pu/pr}^2}} \tag{2.63}$$

where R corresponds to the photon beam radius and the index pu/pr differentiates between the pump and the probe beam. Considering that the light-matter interaction can be described by perturbation theory, the population excited from $|a\rangle$ to $|b\rangle$ will be $\sigma_{ab}^{(1)} \cdot a_{\mathrm{pu}} \cdot n_a$, where $n_a = N$ and N is the number of molecules in the interaction volume. All molecules are initially at $|a\rangle$ and $\sigma_{ab}^{(1)}$ is the respective single-photon cross section. Equivalently, for the transition from the excited dissociative state $|b\rangle$ to the continuum $|c\rangle$ we have $\sigma_{bc}^{(1)} \cdot a_{\mathrm{pr}} \cdot n_b$. The time evolution of the population in the each state, is in principle described by a system of coupled differential rate equations. Away from saturation, the total ion signal ($t \to \infty$) will be given in the form of the molecular response function $M_c(t)$ written as [204]:

$$M_c(t) = N \cdot \sigma_{ab}^{(1)} \cdot a_{\mathrm{pu}} \cdot \sigma_{bc}^{(1)} \cdot a_{\mathrm{pr}} \cdot \mathrm{Exp}\left[-(t_d + f) \cdot t\right] \tag{2.64}$$

The fluorescence decay rate, typically in the ns timescale, can be neglected when considering ultrafast dissociation dynamics in the few-10 fs timescale. Taking into account the theoretical analysis preceding this section, it is obvious that the resulting delay-dependent pump-probe ion signal results as a convolution of the molecular response function with the cross-correlation, or autocorrelation, of the pump and probe pulses.
Consequently, the experimental temporal resolution is determined by the finite instrument response function and the time constants connected with the molecular response function. Depending on their relation the molecular time-constants can be obtained by deconvolution under the appropriate assumptions. This requires that the pulse cross-correlation, or intensity autocorrelation has been also measured prior to the pump-probe experiment. For the considered case, the convolution function that can fit the experimental pump-probe data is given by the following analytical expression:

$$C(\tau) = \mathrm{Exp}\left[\frac{-2\tau t_d + \sigma^2}{2t_d^2}\right] \times \\ \times \sigma\sqrt{\pi/2}\left(1 + \mathrm{Erf}\left[\frac{\tau t_d - \sigma^2}{\sqrt{2}\sigma}\right] + \mathrm{Exp}\left[\frac{2\tau}{t_d}\right] \cdot \mathrm{Erfc}\left[\frac{\tau t_d + \sigma^2}{\sqrt{2}\sigma}\right]\right) \tag{2.65}$$

where σ refers to the Gaussian autocorrelation function waist, t_d to the exponential decay constant and τ to the delay between pump and probe pulses. As already discussed [Fig. 2.3], when the finite instrument response function is temporally narrower or equally long with the molecular response function, the latter can be obtained by deconvolution from the pump-probe ion signal. When the finite instrument response function is considerably shorter than the molecular response function, such that it can be considered as a temporal δ-function, the measurement yields directly the molecular response function as described by Eq. 2.53.
An instructive example is shown in the simulation results of Fig. 2.7. A numerical simulation of a pump-probe experiment is performed using two identical Gaussian pulses for both pump and probe steps with a duration of 10 fs at FWHM shown in Fig. 2.7a. The molecular response function is modeled with a bi-exponential decay function, as the roles of pump and probe pulses are symmetrically interchangeable in the considered case. Three different cases are considered related with the assumed decay-constant. In the first case, shown in Fig. 2.7b the decay constant $\mathrm{t}_d = 500$ fs, is considerably longer than the intensity autocorrelation temporal extent, resulting in a convolution signal that is identical with the bi-exponential decay function, showing no effects from the pulse temporal profile on the pump-probe signal

and yielding the exact decay behavior without any deconvolution assumptions. When the decay constant $t_d = 50$ fs, becomes comparable to the intensity autocorrelation temporal width, the convolution signal starts to deviate from the bi-exponential decay function profile, Fig. 2.7c, including effects from the pulse temporal profile and deconvolution is necessary to obtain the exact time-constant.
Finally, it can be shown that even when the finite instrument response is longer than the molecular response, the decay constant can still be obtained by deconvolution when the assumption for the decay and pulse temporal profiles is justified. Such a case is shown in Fig. 2.7d where the assumed decay constant is $t_d = 5$ fs. The pump-probe signal resulting as a convolution, inherits the Gaussian shape of the intensity autocorrelation function, while it is broader than the intensity autocorrelation trace including the decay rate information. By measuring both the convolution (pump-probe) and intensity autocorrelation traces experimentally, enables obtaining the decay-constant by deconvolution. In the particular case this can be accomplished by fitting the experimental data with Eq. 2.65.

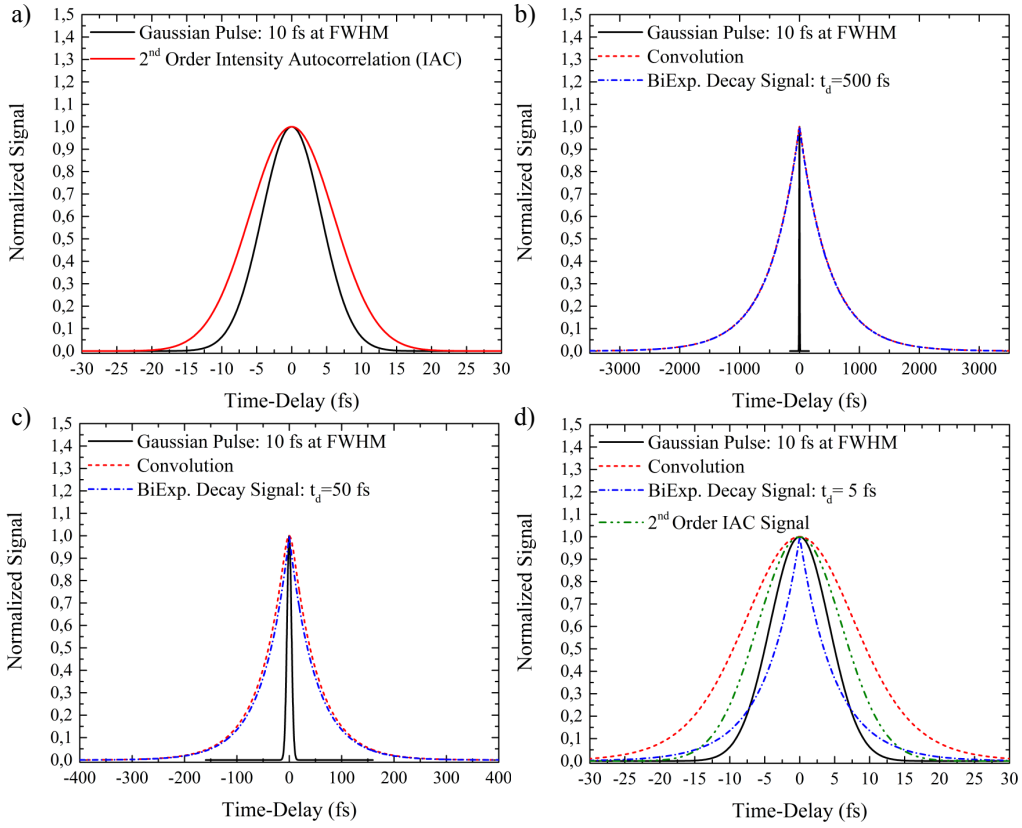

Figure 2.7: Simulated pump-probe signal resulting as the convolution between the molecular response function and the intensity autocorrelation function of a Gaussian pulse (refer to the text for more details).

Although the measurement principle is straightforward, difficulties may arise with the assumed temporal shapes both for the pulse intensity profile, as well as for molecular response function. This analysis applies when an exponential decay for the intermediate state population is a valid assumption.

Even more complicated dynamics involving two subsequent decay channels with two different decay constants involved can also be treated in the same spirit, as shown in [204].
Finally, it is the temporal shape of the finite instrument response function that determines the experimental temporal resolution in a pump-probe experiment. In two-photon pump-probe experiments that utilize two identical pulses both for the pump and probe steps of the experiment, the role of the finite instrument response function is taken by the pulse intensity autocorrelation function. Being able to directly measure this quantity, in the way described in the previous sections permits a deconvolution that can extract time-constants and follow atomic and molecular dynamics evolving in the timescale of the pulse duration. This fact has, in addition, important implications in ultrafast metrology using partially coherent pulses. It was not until recently that has been realized and experimentally proven, that the temporal resolution of a molecular multiphoton pump-probe experiment is dominated by the width of the intensity autocorrelation coherence spike [205, 206], or indirectly by the pulse coherence time, rather than the average pulse duration envelope. As has been shown in [205, 206], the observed dynamics would need a far better temporal resolution in order to be observed, than that indicated by the average pulse duration envelope. In this case, the reduced temporal coherence enables high temporal resolution experiments using partially coherent pulses such those delivered by Free-Electron Lasers operating in a self-amplified spontaneous emission mode.

3 Counter-propagating Pulse Single-Shot Autocorrelation

A dispersionless, single-shot temporal metrology optical scheme that utilizes a counter-propagating pulse geometry, operating from the near-infrared (NIR) to the extreme-ultraviolet (XUV) spectral range, is introduced in the present chapter. Although an all-reflective approach ensures applicability in a broad spectral range, the discussion in this chapter will be devoted to the vacuum-extreme ultraviolet (VUV-XUV) range, in correspondence with the scope of this thesis.

The employed anti-collinear propagation geometry, encodes temporal delay information between two pulses on their common propagation axis. The two pulses coincide in a common focus, where they interact with a medium that transmits the incoming radiation. Mainly due to transmission restrictions, gaseous targets are used in the VUV-XUV range. Non-resonant multiphoton transitions are typically associated with low excitation probabilities in this spectral regime, rendering beam focusing necessary for reaching sufficient intensity levels. Depending on the optical transition nature, a non-linear autocorrelation, or alternatively a pump-probe measurement, can be obtained by imaging the interaction products and spatially resolving their delay-dependence.

Temporal resolution in the fs timescale is directly associated with micrometer imaging resolution with the proposed anti-collinear approach. In the visible-NIR range, well-established microscopy techniques are used to spatially resolve the resulting multiphoton fluorescence [195, 207–211] or second-harmonic light generated with rather exotic phase-matching schemes [212]. In the VUV-XUV however, non-resonant multiphoton fluorescence emission lies beyond the visible spectrum, excluding ordinary microscopy. All-reflective imaging in this spectral range is wavelength-specific and suffers from low reflectance and detection efficiency. The dominant multiphoton excitation pathway results in ionization of the system in the VUV-XUV range. Consequently, imaging the ionization products with micrometer resolution can substitute multiphoton fluorescence detection and extend this approach in the VUV-XUV spectral region. For this purpose, an ion-imaging time-of-flight spectrometer has been realized within the framework of the present thesis and will be described in detail in the following chapter.

The present chapter describes the utilized anti-collinear optical scheme and its experimental implementation. Three optical component variants, designed to fulfill experimental requirements in three separate spectral regions will be described in detail. Finally, characterization results obtained as the 2^{nd} order intensity autocorrelation of a NIR fs laser pulse will be presented and discussed.

3.1 Delay Encoding Principle - Experimental Design

According to the analysis presented in the previous chapter, a single-shot autocorrelation can be measured using a carefully designed experimental geometry. Owing to the absence of transparent solid-state targets in the VUV-XUV spectral region, a non-linear process in the gas phase is commonly used. In this case, the nonlinear signal is provided by atomic or molecular direct multiphoton ionization, as it has been demonstrated in delay-scanning, co-propagating pulse autocorrelation approaches, both in the femtosecond and attosecond timescales over the past years [98, 99, 170, 205, 213–220]. Most of these approaches utilize a bisected spherical mirror, to introduce a variable delay between two pulse copies that result after pulse wavefront division. The delay dependence of a direct multiphoton optical transition, leading to ionization of a gaseous target in the focal volume provides the autocorrelation signal. Although this experimental geometry is associated with reduced measurement contrast resulting from spatial interference in the focal volume and possible temporal distortions in the fs timescale with tight-focusing conditions [149–151, 221], it has been successfully utilized both with laboratory light sources based on high-harmonic generation [98, 99, 213, 214, 216, 217, 219], as well as with free-electron lasers pulses [215, 218]. An approach that bypasses the contrast limitations of the spherical split mirror has been realized using a custom comb-like plane mirror, employed as an all-reflective beamsplitter, delivering a Michelson-interferometer type intensity autocorrelation [220]. A second-order fringe-resolved intensity autocorrelation (FRIAC) measurement of a 5^{th} harmonic pulse at 162 nm has been performed, exhibiting a contrast ratio of 8:1, as predicted by the previously discussed, theoretical considerations. The development of this novel technique has been performed by Dr. Thomas Gebert within the framework of his doctoral work [222] and the present author has contributed both in the conceptual and experimental work. The results obtained by this experimental setup, situated in the same laboratory and using the same light source, have been utilized in order to benchmark and calibrate the results presented in this thesis.

It must be noted that obtaining an autocorrelation measurement in the considered wavelength range, is not a trivial task and the direct extension of the visible-infrared methodology is not possible in most cases. Complete absence of transmissive optical components, as well as reflectivity limitations on the existing optical components, constitute the task of creating two pulse replicas with a variable delay extremely challenging. High absorption of almost all materials in the XUV range, dictate the use of grazing incidence angles or alternatively wavelength-specific multilayer coated optics for operation at normal incidence. Even in this case, their reflectance is limited and the overall amount of optical components must be minimized in order to ensure a satisfactory reflectance, necessary to provide sufficient intensity on target.

Additional attention must be paid in attenuating the residual synchronized, co-propagating harmonic radiation, which can give rise to the same signal (i.e, ions), as that from the multiphoton optical transition chosen to deliver the autocorrelation signal.

Furthermore, limitations associated with the low multiphoton excitation probabilities, in addition to competing ionization channels, significant above a certain photon energy, impose further challenges in identifying a suitable multiphoton signal.
The present approach relies on a conceptual extension of the well established single-shot autocorrelation technique, in the VUV-XUV range. An all-reflective, counter-propagating pulse geometry is employed, mapping the temporal delay between two pulse copies along their propagation coordinate. The two pulse replicas, created by wavefront division, propagate in an anti-collinear manner and temporally coincide in a common focus. Subsequently, each of them symmetrically propagates on the exact optical path used by the oppositely propagating pulse. In this fashion, temporal delay information between the two partial pulses is encoded along their common propagation axis with the focal point being the delay axis origin as:

$$\tau(\mathrm{x}) = \frac{2 \cdot n \cdot \mathrm{x}}{\mathrm{c}} \tag{3.1}$$

where x corresponds to the distance from the origin $\tau(\mathrm{x_o})$=0, where both pulses are synchronized, n to the refractive index of the medium where the pulse propagates and c refers to the speed of light in vacuum. Exhibiting sufficient spatial resolution, an imaging detector recording the signal originating from direct two-photon ionization, can provide an intensity autocorrelation measurement on a shot-to-shot basis.
As previously mentioned, this approach can be easily generalized to deliver a cross-correlation measurement when two different pulses propagate in each optical branch, or alternatively, to be utilized as a single-shot pump-probe method, also in a single or two-color excitation scheme. The pump-probe picture describes the delay encoding principle in a comprehensive manner. At any point on the propagation axis found at a distance $\mathrm{x_1}$ from the focal point, where both pulses are synchronized $\tau(\mathrm{x_o})$=0, the incoming pulse (pump) initiates the dynamics of interest at a time $\mathrm{t_o}$. The evolving system, is subsequently probed by the counter-propagating pulse, coming from the opposite optical branch, upon its arrival at this point $\mathrm{x_1}$, at a later time $\mathrm{t_o} + \tau(\mathrm{x_1})$. Taking into account the inherent optical path symmetry, the probe pulse will travel twice the distance ($2\mathrm{x_1}$), in order to reach the oppositely symmetric position with respect to $\tau(\mathrm{x_o})$=0 as illustrated in Fig. 3.1 and in accordance with relation 3.1.

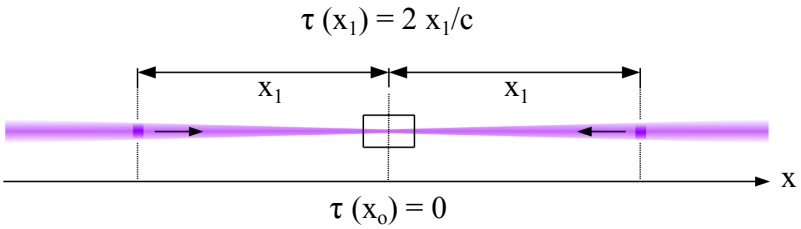

Figure 3.1: Counter-propagating pulse, single-shot temporal metrology principle: The delay between the two pulses is encoded on the common propagation axis according to Eq.3.1. With the focal point $\mathrm{x_o}$ as a center of symmetry, dynamics that are initiated by the first pulse at a distance $\mathrm{x_1}$ from the origin, will be subsequently probed at a later time $2\mathrm{x_1}/\mathrm{c}$ by the oppositely propagating pulse. The black frame encircles the signal detection area.

Employing a nonlinear medium that exhibits an instantaneous response and spatially resolving the corresponding nonlinear signal along the x-axis, can therefore deliver a single-shot nonlinear autocorrelation measurement. Additionally, once the autocorrelation measurement has been performed, the same apparatus can be used to perform a pump-probe experiment according to the measurement concepts described in the previous chapter. Furthermore, two pulses with different central wavelength can be used in each optical branch, enabling a two-color pump-probe measurement. In that case, their cross-correlation serves as the finite instrument response function and can be obtained in a similar manner. The achievable temporal resolution directly relies on the spatial resolution offered by the utilized imaging detection system. As an example, according to Eq. 3.1, in order to resolve two temporal events separated by 10 fs in delay-time units, a spatial resolution of approximately 1.5 µm is required.

An additional geometrical advantage offered by the proposed anti-collinear geometry, is the long temporal detection window offered even in tight-focusing conditions, necessary to reach the intensity needed for direct multiphoton excitation in the VUV-XUV. Although the imaging detection system will finally influence the single-shot temporal window, it may be neglected for the sake of a quantitative example.

We may assume a VUV pulse possessing a Gaussian spatial and temporal profile, centered at 162 nm, with a duration of 20 fs at full-width-at-half-maximum (FWHM), a beam diameter of 2 mm at $1/e^2$ and focused using a spherical mirror with f=50 mm. Neglecting spherical aberrations, the resulting diffraction-limited focal spot diameter is calculated to be in the order of 5 µm at $1/e^2$ and the corresponding Rayleigh length 128.9 µm. In order to avoid spatial distortions, the temporal window is defined as twice the Rayleigh length, a region where the pulse wavefronts do not exhibit a considerable curvature. Using relation 3.1, a long temporal window of 1.72 ps is calculated, even for this short focal length. Depending on the wavelength and the available pulse intensity, the temporal window can be further scaled together with the corresponding Rayleigh length using a longer focal length.

Staying with the values obtained in the example above, a complete dataset equivalent to a delay scan spanning to ±858 fs is obtained on every individual shot, boosting the statistical significance of the experimental results. Even for a low-repetition rate light source, as commonly most high-intensity VUV-XUV light sources (i.e. 10 Hz), several thousands of individual datasets can be collected within few minutes. This is a beneficial feature, not only minimizing the statistical uncertainties associated with the measurement, but in addition avoiding the influence of short and long-term drifts that commonly obstruct long-delay scan measurements. Establishing a well aligned beam path and synchronizing the two pulses in a common focal point, constitutes a stable, advantageous delay-scanning alternative compared to opto-mechanical stage delay-scanning, typically subject to external influence or misalignment issues.

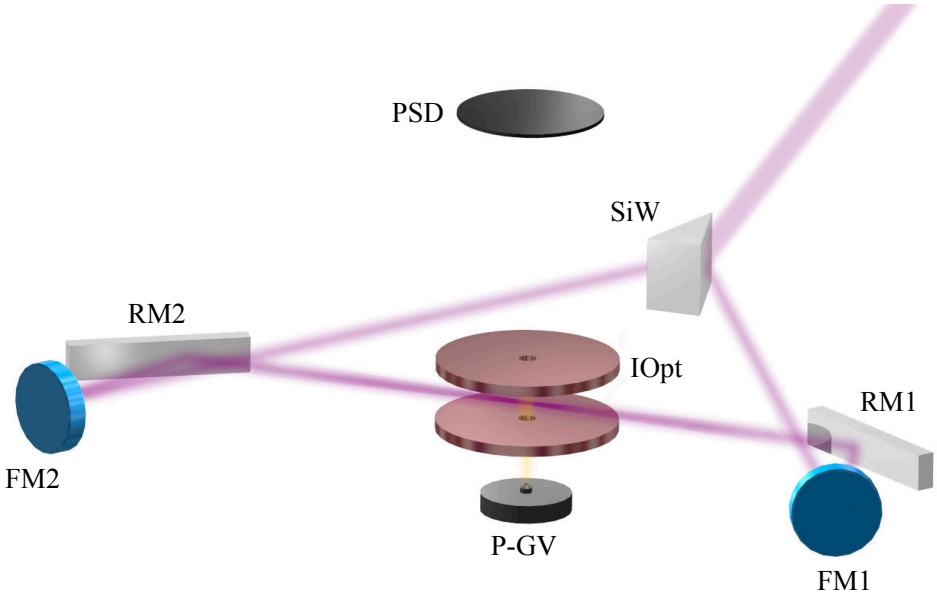

Figure 3.2: Single-shot autocorrelation experimental setup scheme: SiW: Si-Wedge beam-splitter mirror, FM1, FM2: Identical spherical mirrors with f=150 mm, RM1, RM2: plane mirrors, IOpt: Electrostatic lenses - ion imaging optics, P-GV: Pulsed gas valve, PSD: Position-sensitive detector.

The experimental realization of the described concept, is illustrated in Fig. 3.2. The optical setup is designed to operate under ultrahigh-vacuum (UHV) conditions, with light in the VUV-XUV spectral range, in combination with the aforementioned ion microscope detection system.

The pulse to be characterized, or to initiate and subsequently investigate dynamics on a gas-phase target, is initially split and symmetrically reflected in two equal parts using a super-polished Si wedge-shaped mirror (SiW). Acting as a wavefront divider, it bisects the beam profile into two equally intense parts. It is specified to exhibit a surface flatness better than $\lambda/20$ and an optical surface roughness of $< 1\,\text{nm}$. The Si-wedge is cut such that the two partial beams are reflected at a grazing incidence angle of 15^{o}, providing a spectrally broadband high-reflectance profile in the VUV-XUV range, while it additionally matches the Brewster angle for light at 800 nm. This is beneficial for experiments that utilize high-harmonic radiation, avoiding the influence of the intense, naturally-synchronized, co-propagating IR pulse [117]. Taking advantage of the fact that the HHG-driving IR pulse is linearly p-polarized, the Si-wedge mirror acts as a spectral filter, suppressing light at 800 nm to approximately 10^{-4}, while exhibiting high-reflectance at high-harmonic radiation wavelengths. The calculated Si wedge-shaped mirror reflectance profile, taking into account the presence of the Si native oxide layer [223] is shown in Fig. 3.3. The calculation has been performed using the IMD extension [224] for the European Synchrotron Radiation Facility XOP software package with the provided collection of optical constants both for Si and SiO_2.

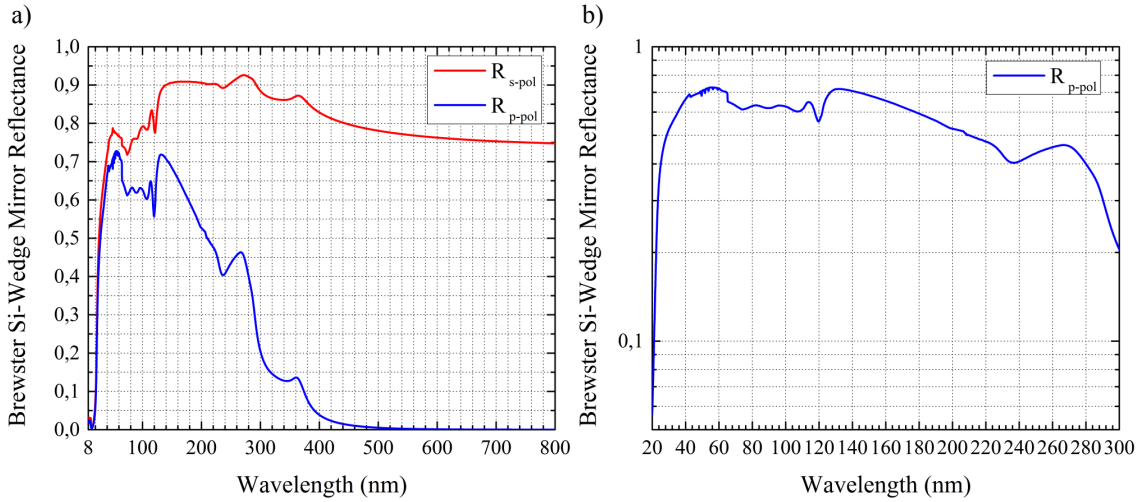

Figure 3.3: Calculated Si-wedge wavefront divider mirror reflectance profile: a) linear scale, b) logarithmic scale DUV-XUV spectral range, p-polarization results. The calculated curves [224] correspond to a grazing incidence angle of 15° and additionally take into account the native oxide on the mirror surface (1.5 nm SiO_2). For p-polarized light, the Si-wedge mirror exhibits high reflectance across a broad spectral bandwidth in the DUV-XUV spectral range, while it effectively suppresses the strong infrared pulse at 800 nm.

Leaving the Si wedge-mirror, the two reflected beams encounter two symmetrically placed identical spherical mirrors (FM1, FM2) with f=150 mm, used for focusing both pulses and are subsequently back-reflected under a mirror-tilt angle of 2°. Two additional plane mirrors (RM1, RM2) are used to direct the two pulses in a common focal point (x_o) in a counter-propagating manner. The two partial beams spatially overlap over the complete focal region and temporally as soon as both pulses arrive at the focal point x_o.
The optical layout has been optimized using both the Optica software extension package for Mathematica and ZEMAX. Ray-tracing simulations have been performed, taking into account practical constraints imposed by the utilized vacuum chamber space, the ion-imaging detector footprint as well as geometrical constraints imposed by the optical mounts. The Si-wedge mirror reflection angle has been kept fixed in this case, satisfying the 800 nm Brewster angle criterion, while exhibiting a broadband high-reflectance profile in the complete spectral range of interest. A set of different focal lengths and optical path combinations have been considered, taking into account the reflectance profiles of possible, normal (FM1,FM2) and grazing (RM1,RM2) incidence optics in the VUV-XUV range with the aim to achieve the highest intensity in the interaction region and minimize imaging aberrations. The resulting optimized geometry, uses the shortest possible focal length (f = 150 mm) with the smallest possible spherical mirror reflection angle (2°). An alternative optical scheme with a f=275 mm spherical mirror has been designed and experimentally realized, exploiting to a full extent the space possibilities offered by the experimental chamber.

The intensity requirements, especially in the case of the experiments performed at Free-Electron Lasers (FEL), favored the short focal length optical setup variation.
The experimental setup permits easy exchange of optical components, or installation of bandpass thin-filters in one or both branches according to the particular experimental demands, enabling two-color (VUV-pump - XUV-probe or vice versa), as well as broadband operation (attosecond pulses), being compatible with different types of sources of VUV-XUV radiation. The experimental work presented in this thesis uses three different mirror sets, assigned to three separate spectral regions. The reflective optics have been chosen in order to provide the highest possible reflectance in each case, while suppressing undesired spectral contributions. A detailed description for each set will be given in the following section, in connection with the corresponding experimental prerequisites.
Both spherical mirrors are fixed on motorized high-precision linear translation stages offering a travel range of $\pm 10\,\mathrm{mm}$. Furthermore, both spherical mirror mounts, as well as one plane mirror mount (RM1), provide horizontal/vertical mirror tilt control using picomotor actuators. These controls are necessary, in order to optimize the spatial and temporal overlap of the two optical branches under vacuum conditions. Although the experimental setup is aligned prior to evacuation of the hosting chamber using a He-Ne alignment laser, further optimization adjustments can be performed at-wavelength using the motorized mirror mounts. Furthermore, the temporal overlap in the common focus is established under ambient pressure conditions, using a NIR fs laser pulse and performing a 2^{nd} order intensity autocorrelation using CdSe quantum dots in solution as the non-linear medium. This has proven to be a very successful pre-alignment technique, simplifying the exchange of the focusing and redirecting reflective optics. Detailed description of the technique and corresponding results will be presented in the final section of the present chapter.
Although the optical setup is carefully aligned prior to evacuation, a difference in divergence between the NIR pulse and the VUV-XUV pulse causes a symmetric shift in the two optical branch focal positions. In that case, the two focal positions are symmetrically shifted and matched using the motorized mirror mounts in combination with the ion-imaging spectrometer image as a feedback under vacuum conditions.

3.2 Experimental Case Studies

From the discussion so far, it becomes evident that a judicious choice of the autocorrelation non-linear process is necessary. The corresponding non-linear target must exhibit a broadband, spectrally flat response to the incident radiation, avoiding any resonance with intermediate long-lived states.
In this section, the selection criteria for a non-linear process suitable to deliver an intensity autocorrelation measurement in the VUV-XUV range will be discussed. Without loss of generality, the analysis will focus on the acquisition of a 2^{nd} order autocorrelation signal delivered by two-photon absorption, leading to ionization of an atomic gas target.

Although any non-resonant multiphoton signal is suitable to deliver a non-linear intensity autocorrelation measurement, multiphoton atomic ionization is advantageous in this spectral region, mainly due to the high atomic ionization barriers and the simple energy level structure, which avoids complicated intermediate state dynamics.
Charged-particle imaging favors the detection of ions. They are less sensitive to space-charge mechanisms and imaging limitations imposed by initial-momentum distributions compared to photoelectrons, evident by their relative mass ratio (e.g. $m_{Kr^+}/m_{e^-} \approx 1.5 \cdot 10^5$).
It is important to note, in connection with the analysis performed in Ch.2, that an intermediate resonance with a long-lived state in one of the multiphoton absorption steps, will lead to a convolution signal of the corresponding autocorrelation function with the intermediate state temporal-decay profile. According to typical atomic state natural line-widths, the associated lifetime lies typically in the ns-ps timescale, prohibiting any delay-dependence in the resulting signal for fs light pulses.
In the VUV-XUV spectral range, the photon energy (6 eV - 124 eV [225]) is sufficient to lead to ionization already in one of the intermediate multiphoton absorption steps. Nevertheless, depending on the available intensity, single or multiphoton absorption may further proceed stepwise to generate highly-charged ionic states [87, 226–228]. In that case, the ionizing pulse temporal profile together with the corresponding optical transition probabilities, will decide on the temporal evolution of the ionization scenario. In any case, an effective lifetime can be assigned to the intermediate ionic states, corresponding to the time that ions typically spend within the focal volume. This time lies typically in the ns range, even when very high particle extraction fields are applied.
Taking into account that the multiphoton absorption probability drops with the number of photons involved, we will only consider the simplest case of direct two-photon absorption as 2^{nd} order autocorrelation process in the VUV-XUV. Nevertheless, the following discussion addresses the basic multiphoton excitation possibilities applied also to higher-order processes.
Two-photon absorption in the VUV-XUV spectral regime may lead to a number of excitation possibilities, depending on the photon energy and the particular atomic energy level structure. The possible two-photon ionization pathways are summarized in Fig. 3.4.

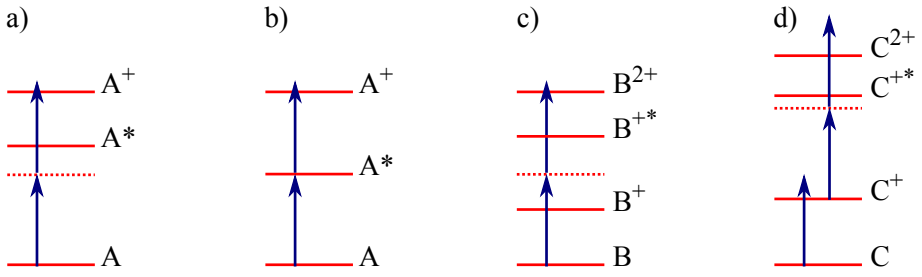

Figure 3.4: a) Two-photon, direct (non-resonant) ionization, b) Two-photon, resonance-enhanced ionization - the resulting signal is a convolution of the pulse intensity autocorrelation function with the intermediate state (A^*) temporal decay profile (Fig. 2.7), c) Two-photon, direct (non-resonant), double ionization, d) Three-photon (1+2), sequential, double ionization.

In the simplest case, the photon energy lies below the atomic ionization energy and away from any selection-rule allowed excited state of the system (3.4a). Ionization proceeds via direct two-photon absorption ($A \xrightarrow{2\cdot\hbar\omega} A^+$) and the delay-dependence of the resulting singly-charged ion signal can provide a 2^{nd} order autocorrelation measurement.
If instead, the photon energy is resonant with an intermediate excited state (3.4b), the resulting signal ($A \xrightarrow{\hbar\omega} A^* \xrightarrow{\hbar\omega} A^+$) will be a convolution of the instruments response function, the second-order autocorrelation function in this case, with the states population decay temporal profile (Fig. 2.7). When the pulse second-order autocorrelation measurement is available, the time constant associated with the corresponding decay mechanism can be obtained by deconvolution.
An alternative scenario arises for a photon energy larger than the first ionization threshold (3.4c). In this case, single-photon absorption leads to photoionization ($B \xrightarrow{\hbar\omega} B^+$). As already concluded in Ch.2, the singly-charged ion signal, originating from single-photon absorption, cannot deliver sufficient temporal information. When the photon energy is such that 2 photons can directly reach the second ionization threshold, without exciting any intermediate resonance ($B \xrightarrow{2\cdot\hbar\omega} B^{2+}$), the doubly-charged ion signal serves as a 2^{nd} order autocorrelation signal. Direct multiphoton double ionization is mediated by electron-electron correlation effects, as the two photons are 'simultaneously' absorbed by a single electron, sharing its excess energy and both electrons are ejected in the continuum.
Finally, a longer pulse will eventually transfer a significant part of the initial population in the singly-charged ionic state ($C \xrightarrow{\hbar\omega} C^+$). Depending on the photon energy and the ionic energy level structure, a single, or two additional photons might be needed to doubly ionize the system (3.4d). The first case ($C \xrightarrow{\hbar\omega} C^+ \xrightarrow{\hbar\omega} C^{2+}$), reduces to the excited state discussion (3.4b), although in this case there is no interesting information to obtain. The second case ($C \xrightarrow{\hbar\omega} C^+ \xrightarrow{2\cdot\hbar\omega} C^{2+}$), assuming that it is based on a non-resonant transition, provides a delay-dependent signal that contains pulse temporal information. One must be careful with the result interpretation though, as a significant portion of the light pulse might be consumed to prepare this 'new ground state' for the autocorrelation measurement. Depending on the pulse duration and intensity distribution [25,228,229], this might not pose severe limitations, but it will certainly introduce severe ambiguities in the autocorrelation measurement interpretation.
A similar theoretical treatment, can be found in [230], where two-photon double ionization of He is evaluated as a 2^{nd} order autocorrelation nonlinear process in XUV spectral region.
In the discussion above, effects associated with core-hole formation and subsequent Auger decay have not been included. Typical single-photon Auger-process lifetimes spanning the fs timescale, will result in a convolution with the autocorrelation function and thus deliver a broader cross-correlation signal.
As a final remark here, it needs to be stressed that purely sequential processes, although 'multiphoton', do not deliver a pulse intensity autocorrelation measurement. The reason is that they do not depend on the time of arrival of the second pulse. As long as the excited atom or ion, lies within the focal volume, the second pulse can always excite the final sequential step of the ionization process. A mixture of sequential and non-sequential steps, can in principle provide a delay-dependent signal, although a significant part of the pulse might be needed to excite sufficient amount of population in the first excited state, leading to the measurement of a shorter duration (Fig. 3.4d).

Keeping the above considerations in mind, a suitable combination of non-linear process and corresponding reflective optical components has been optimized for three distinct experiments, differing in both their anticipated pulse temporal and spectral characteristics. These three different variations utilize the previously described counter-propagating pulse experimental setup (Fig. 3.2), varying only in terms of the focusing (FM1,FM2) and re-directing (RM1,RM2) mirror coatings. Pulse splitting is achieved by the same Si wedge-mirror (SiW) in all cases, which was chosen to suite experimental demands over a broad spectral range (Fig. 3.3).
Switching between these three spectral regions, is a matter of few hours, only by exchanging the respective mirrors one-at-a-time while maintaining the previously established alignment. A re-alignment strategy has been developed, using a 2^{nd} order autocorrelation signal obtained by two-photon fluorescence. Utilizing this signal under ambient pressure conditions, allowed the precise optimization of both spatial, as well as temporal degrees of freedom.

2^{nd} Order Autocorrelation at 162 nm

The vacuum-ultraviolet experimental variant, utilizing direct, two-photon, single ionization of Kr or alternatively Xe as a non-linear autocorrelation process will be described first.
The experimental setup has been optimized for use with an intense VUV pulse, centered at 161.8 nm (7.66 eV photon energy), delivered by a self-implemented, laboratory-based high-harmonic generation (HHG) light source, described in detail in Ch. 5. The energetic VUV pulse, generated as the 5^{th}-harmonic of a Ti:Sa laser pulse, offers the possibility for extending nonlinear spectroscopy techniques into the vacuum-ultraviolet range, where many prototypical examples for ultrafast dynamics in organic and atmospherically relevant molecules can be found.
Exhibiting no intermediate resonances at this wavelength, being considerably detuned from any selection-rule allowed transitions, both Kr and Xe are suited to provide a 2^{nd} order autocorrelation signal at 161.8 nm (Fig. 3.5). The autocorrelation measurement can be obtained by recording the delay dependence of the singly-charged ion signal. The same autocorrelation excitation scheme has also been utilized in [30], using Kr as a non-linear target, with similar experimental conditions.

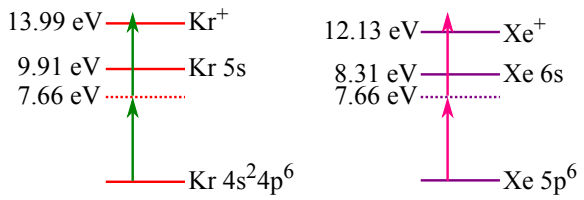

Figure 3.5: Energy level schematic depicting non-resonant, two-photon ionization of Kr, or alternately Xe with 7.66 eV photon energy.

The naturally synchronized, co-propagating IR pulse (800 nm/1.55 eV), as well as the residual high-harmonic radiation generated at the same gas target, have to be attenuated so that they no longer contribute to the non-linear ion signal.

The infrared p-polarized HHG driving pulse is primarily attenuated by the Si wedge-mirror, set to reflect both partial beams at the Brewster angle for 800 nm. In addition, a significant portion of the highly diverging infrared beam is excluded by a 15 mm diameter aperture at the setup entrance.
The two spherical mirrors (FM1,FM2) with f=150 mm are coated with a multilayer dielectric stack (Layertech GmbH), optimized to reflect the Ti:Sa 5^{th} harmonic ($R_{160\pm4\text{ nm}} > 90\%$), with excellent dispersion specifications (GDD $< 20\text{fs}^2$) and additionaly separate it from residual fundamental and harmonic radiation ($R < 4 \times 10^{-2}$).
Finally, the two re-directing plane mirrors are Al-coated, covered with an additional thin protective coating, transparent to VUV radiation (Layertech GmbH). The optical component reflectance profiles ensure sufficient attenuation of undesired spectral contributions, while exhibiting high throughput for the 5^{th}-harmonic pulse. The dispersion optimized multilayer optics can accept broadband VUV pulses down to a duration above 10 fs without inducing significant temporal distortions. Indicatively, a bandwidth-limited Gaussian pulse with 15 fs duration, will be stretched to 15.4 fs at the dispersion maximum of GDD = 20 fs^2 (Eq.2.50). Dispersion-free operation needs metallic mirror coatings, missing however the necessary bandpass spectral filtering characteristics. The reflectance characteristics of the 162 nm counter-propagating pulse, single-shot autocorrelation optical setup are summarized in the table below:

Optical Component	$R_{\text{p-pol}}$ (7.66 eV)	$R_{\text{p-pol}}$ (1.55 eV)	$R_{\text{p-pol}}$ HHG
Si-Wedge Beam-splitting Mirror	0.65	$1.2 \cdot 10^{-4}$	$0.33 - 0.69$
5^{th} H. Spherical Mirror	0.9	$< 4 \cdot 10^{-2}$	$< 10^{-2}$
Al-coated Plane Mirror	0.82	0.74	$0.86 - 3 \cdot 10^{-3}$
Total Reflectance	0.48	$< 3 \cdot 10^{-5}$	$< 6 \cdot 10^{-3}$

Table 3.1: Optical component reflectance and total setup transmission for operation at 7.66 eV. The values correspond to the 5^{th} harmonic (7.66 eV/161.8 nm), fundamental (1.55 eV/800nm) and high-order harmonic radiation (up to the observed 33^{rd} order) considering p-polarized light.

Taking into account the 5^{th} harmonic beam divergence of 0.45 mrad [222], in addition to a rough estimate for the source size of 180 µm and the distance to the dedicated experimental chamber of approximately 11.7 m, the estimated 5^{th} harmonic beam diameter at the entrance of the experimental setup is calculated to be approximately 5.4 mm FWHM. Using this value, the focal intensity distribution in a single branch of the counter-propagating pulse optical setup has been simulated using the physical optics ray-tracing capabilities offered by ZEMAX. The wavelength-specific simulation takes into account the propagation distance within the optical setup, the wavefront division imposed by the Si wedge-mirror, as well as the spherical mirror tilt-angle. Astigmatism is expected in the spherical mirror focus, due to the non-zero incidence angle. Furthermore, additional focal spot shape distortion is expected as a result of diffraction effects originating from the steep edge of the Si-wedge mirror used for wavefront division.

Choosing the plane of observation exactly at the theoretical focal point, as dictated by the spherical mirror radius-of-curvature and defining an ideal Gaussian beam (M^2=1) with a diameter of 5.4 mm FWHM, the intensity spatial profile at the focus has been simulated using ZEMAX. The simulation result is presented in Fig.3.6, together with the corresponding horizontal and vertical line-out profiles, obtained in each direction at the maximum peak intensity.

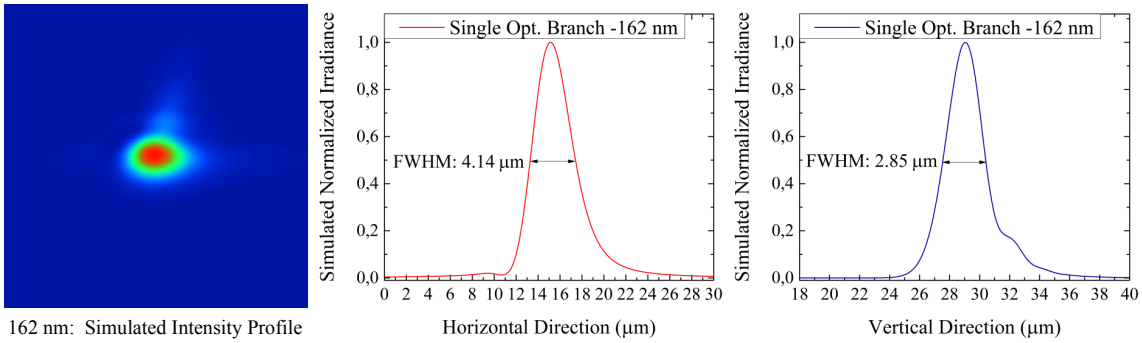

Figure 3.6: Single optical branch, simulated intensity spatial profile at the focal point for the 162 nm optical setup variant.

The simulated focal spot shows non-negligible spatial distortion, although overall it retains a smooth Gaussian-like profile with a beam diameter of approximately 4.1 µm along the horizontal direction and 2.85 µm along the vertical direction. The associated Rayleigh length corresponds to 240 µm in the horizontal and 113.7 µm in the vertical direction, respectively. This asymmetry is expected, in analogy to the asymmetry imposed by division of the incoming beam wavefront.
It also worths pointing out that the simulated focal spot dimensions are not significantly larger than those expected for a perfect Gaussian beam, assuming M^2=1. As a comparison, the calculated diffraction limited Gaussian spot size is 3.97 µm FWHM, considering an initial beam diameter of 2.7 mm FWHM (half of the initial 5^{th} harmonic beam size). Note further that the simulation results for the beam propagating on the opposite optical branch are exactly the same.

2^{nd} Order Autocorrelation at 62 nm

Entering the extreme-ultraviolet spectral range, with experiments both at free-electron lasers (FEL), or with HHG radiation, the operation parameters at 62 nm (20 eV) have been optimized.
Delay-scanning intensity autocorrelation measurements have been previously reported at this wavelength range, both in the attosecond regime utilizing phase-locked high-harmonic radiation [98, 150, 170, 217], as well as for femtosecond FEL pulses [218].

The most favorable non-linear process that can obtain a 2nd order autocorrelation signal in this spectral range, is direct two-photon single ionization of He. Being in a spectral regime, where every atomic or molecular system gets ionized by single-photon absorption, He exhibits the highest single-ionization energy threshold, combined with a simple energy level structure, avoiding resonant excitation complications.

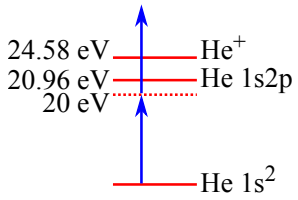

Figure 3.7: Non-resonant, two-photon, single ionization of He at 62 nm (20 eV).

The non-resonant, two-photon ionization window spans a photon energy range between 12.3 eV to just below 20.9 eV, providing the possibility to characterize extremely broadband and short XUV pulses. Spectral overlap between the pulse spectral profile and a near-resonance atomic state linewidth must be avoided to ensure an instantaneous non-linear response and avoid any delay-independent signal background.
The resulting delay-dependent He ion signal can deliver a 2nd order autocorrelation measurement. Nevertheless, at a lower photon energy, a three or four-photon transition can also deliver a higher-order autocorrelation measurement, when the pulse intensity content is sufficient, as reported in [231].
The corresponding set of optics delivers the highest possible throughput at 62 nm, while effectively suppressing spectral contributions below 31 nm and in the vicinity of 800 nm (by means of the Si-wedge mirror at Brewster angle, Fig. 3.3).

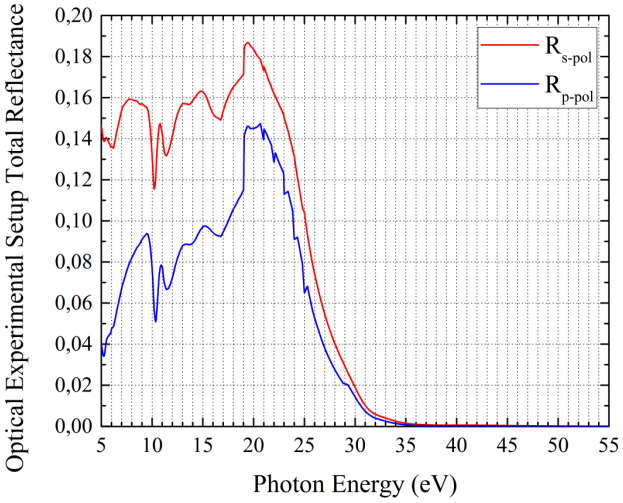

Figure 3.8: Calculated [224] total reflectance for the the complete 62 nm (20 eV) setup for both polarization states. Experiments with FEL pulses at FERMI utilize light in s-polarization, while the HHG experiments are performed in p-polarization, effectively suppressing the strong infrared pulse at 800 nm (1.55 eV - not shown in this graph).

For a 2nd order autocorrelation measurement of seeded-FEL pulses, centered at 62 nm at the free-electron laser FERMI [21], the mirror coatings were chosen so that they can effectively suppress FEL-harmonic radiation, occurring at the undulators. Although theoretically only the odd harmonic orders are expected [232], with the 3rd harmonic order to be the most prominent, the 2nd harmonic order can also be present depending on the generation conditions [233]. In this case, both the 2nd and the 3rd harmonic can lead to ionization of He by single-photon absorption and thus this competing background signal can completely mask the direct two-photon contribution.
The super-polished spherical mirrors (FM1, FM2) are coated with a 50 nm Mo layer, sealed by a 2 nm B_4C capping layer, whereas the plane redirecting mirrors (RM1, RM2) use a Si coating. The overal reflectivity (including the Si-wedge mirror) is shown in Fig. 3.8. Furthermore, the 62 nm s-polarization reflectance values for the FEL experiment are summarized in Table 3.2.

Optical Component	$R_{s\text{-pol}}$ (20 eV)	$R_{s\text{-pol}}$ (40 eV)	$R_{s\text{-pol}}$ (60 eV)
Si-Wedge Beam-splitting Mirror	0.76	0.57	$8.8 \cdot 10^{-2}$
Mo-coated Spherical Mirror	0.40	$2.6 \cdot 10^{-2}$	$1.8 \cdot 10^{-2}$
Si-coated Plane Mirror	0.59	$2.4 \cdot 10^{-2}$	$2.6 \cdot 10^{-3}$
Total Reflectance	0.18	$3.5 \cdot 10^{-4}$	$4.1 \cdot 10^{-6}$

Table 3.2: Calculated reflectance for 20 eV (62 nm). The values correspond to the FEL fundamental, second and third harmonic photon energies for s-polarized light.

The optical set has a broadband reflectance profile, with a peak value of 0.19 at around 19.5 eV. Furthermore, it effectively suppresses FEL harmonic radiation, while for experiments using HHG radiation, additional spectral filtering using thin metallic bandpass filters [234, 235] can be realized. It should be noted, that similar collinear experimental arrangements, utilizing a Brewster angle Si-plate combined either with a spherical Au-coated mirror [150], or a bulk SiC mirror in normal incidence [219], reach at 20 eV a calculated [224] reflectance of 0.08, or 0.24 respectively. Although a bulk (or CVD-coated) SiC mirror would offer a higher overall reflectance, it was not accessible within the timescale of the present thesis.
Following the simulation approach as previously with the 162 nm setup, the focal intensity spatial distribution has been simulated using ZEMAX and presented in Fig. 3.9.
The incoming 62 nm beam diameter at FERMI almost matches the 162 nm laboratory beam diameter[1] and for this reason the same simulation parameters (besides wavelength) were used for the 62 nm simulation allowing a qualitative comparison.

[1] The rough estimation of the beam diameter at FERMI for 62 nm was 9-10 mm at $1/e^2$, in comparison to 9.2 mm for the 162 nm in the laboratory case.

As expected for a shorter wavelength, astigmatism and diffraction effects become more pronounced, as can be observed in the simulation results in Fig. 3.9.

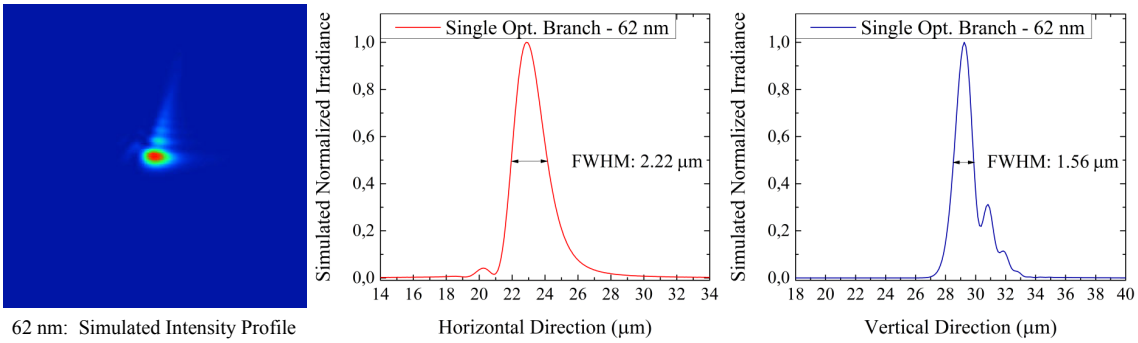

Figure 3.9: Single optical branch, simulated intensity spatial profile at the focal point for the 62 nm optical setup. The simulation uses the same parameters as in Fig.3.6, apart from the new wavelength of 62 nm.

Neglecting either the spherical mirror tilt angle, or the Si-wedge beam-splitter edge, the same simulation has been performed in order to provide insight on the origin of the observed spatial distortion. The vertical spot shape deformation is mainly caused due to astigmatism, whereas the horizontal is attributed mainly to edge-diffraction.
Although a fraction of the intensity is distributed in the periphery of the main spot, the multiphoton signal is expected to originate directly from this central intense part of the beam. The simulated spot diameter corresponds to 2.2 µm FWHM in the horizontal direction and approximately to 1.6 µm FWHM in the vertical direction. The associated Rayleigh length corresponds to 180.1 µm and 88.9 µm in the horizontal and vertical directions, respectively. As a benchmark, a perfect Gaussian beam (M^2=1) at the same wavelength and half the beam diameter (corresponding to the horizontally divided beam) would focus to a diffraction-limited spot of 1.5 µm FWHM, or alternately to 0.76 µm at FWHM when the complete beam diameter is taken into account.

2nd Order Autocorrelation at 28.2 nm

The third optical component variant has been designed for 28.2 nm (44 eV FEL pulses), intending to perform pulse temporal characterization measurements at FLASH in Hamburg [20, 236].
In this photon energy range, a single-photon absorption already exceeds the first ionization threshold of any atomic or molecular system. Identifying a suitable non-resonant, multiphoton ionization process that can provide an intensity autocorrelation measurement as a delay-dependent ion signal, becomes a non-trivial task. According to the preceding analysis, a direct multiphoton process resulting in a multiply-charged ion, exhibiting no intermediate resonances with atomic or ionic states, is suitable to provide such a signal.

At this wavelength, a non-linear process that has been theoretically considered [230] and utilized [215, 237] to obtain a 2nd order intensity autocorrelation is the two-photon, direct double-ionization of He. The autocorrelation can be obtained through the delay-dependent detection of doubly-charged He^{2+} ions. The non-resonant, two-photon double-ionization mechanism and the corresponding ionization probability has received significant theoretical [238–246, and references therein] and experimental [226, 247–250] attention, since it is a prototypical process for dynamical three-body interaction. The corresponding autocorrelation ionization scheme is outlined in Fig 3.10.

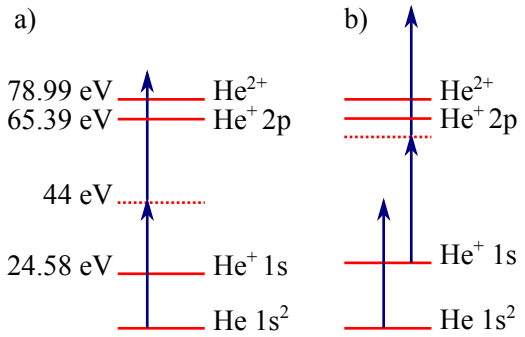

Figure 3.10: a) Non-resonant, two-photon, double ionization of He at 28.2 nm (44 eV photon energy), b) Sequential, three-photon (1+2), double ionization of He at 28.2 nm.

At 44 eV, non-resonant two photon absorption can lead to direct double ionization. In direct two-photon double ionization, the two electrons are simultaneously ejected, sharing the excess energy above the double-ionization threshold (Fig. 3.10a). As a non-resonant 2nd order nonlinear process, the doubly-charged ion signal can be used for a 2nd order autocorrelation.
Alternately, sequential double ionization of He would require at least three-photons at 28.2 nm, involving a non-resonant, two-photon absorption process in the second step (Fig. 3.10b). Using this ionization pathway, the delay-dependent measurement incorporates time-constants that depend on the ionization dynamics and potentially introduce deconvolution ambiguities. However, the probability for this three-photon ionization pathway is reduced, taking also into account that the two-photon ionization cross-section for the step $He^{+} \rightarrow He^{2+}$ exhibits a local minimum at 28.2 nm [230].
Nevertheless, the ionization scenario depends on the XUV pulse duration and intensity profile. A long energetic pulse will transfer a significant part of the He ground state population to the singly-charged ion state with high probability, before the atoms in the ground state can 'see' the peak intensity of the pulse, favoring the sequential mechanism [64]. On the contrary, a weaker short pulse, exhibiting the same peak intensity, will efficiently drive the direct double-ionization process and drive less population in the singly-charged ionic state. This case is experimentally advantageous, avoiding space-charge repulsion effects, typically degrading the performance of the utilized ion detection scheme. For the FEL pulse experiment operating at 28.2 nm, additional attention must be taken, so that the FEL harmonic radiation able to generate the doubly-charged He^{2+} signal by single-photon absorption, is sufficiently attenuated.

The number of reflective optics utilized in the counter-propagating arrangement and the normal incidence refocusing geometry impose reflectance limitations with increasing photon energy. An optimum wavelength-specific multilayer coating has to be used for the normal incidence spherical mirrors (FM1, FM2) and additionally the plane mirror (RM1, RM2) coating shall exhibit optimum reflectance at the same wavelength.
The spherical mirrors use a Mg/SiC or alternately a Mg/SiC/Al multilayer coating, exhibiting a peak reflectance at 28.2 nm [251–254], with no considerable competitor at this wavelength range [255].
The initially utilized Mg/SiC coating showed severe reflectivity degradation accompanied with a shady XUV beam footprint on the mirror surface, after the first experimental attempts. Carbon surface contamination has been excluded and the possible cause has been attributed to photochemical oxidation mechanisms on the Mg layer [255]. An improved version of the multilayer system utilizing additional Al-Mg barrier layers [253, 254] has been used, although without considerable improvement. The plane re-directing mirrors are coated with a thin B_4C layer, exhibiting the highest reflectivity at 28.2 nm for the utilized angle of incidence.
The optical component individual reflectance characteristics are summarized in Table 3.3.

Optical Component	$R_{\text{p-pol}}$ (44 eV)	$R_{\text{p-pol}}$ (88 eV)	$R_{\text{p-pol}}$ (132 eV)
Si-Wedge Beam-splitting Mirror	0.49	$4.4 \cdot 10^{-3}$	$2.3 \cdot 10^{-2}$
Mg/SiC ML Mirror (1)	0.46	$1 \cdot 10^{-2}$	$6 \cdot 10^{-4}$
Al-Mg/SiC ML Mirror (2)	0.32	$3.7 \cdot 10^{-4}$	$2.6 \cdot 10^{-7}$
B_4C-coated Plane Mirror	0.21	$1.5 \cdot 10^{-3}$	$2.5 \cdot 10^{-5}$
Total Reflectance (1)	0.047	$6.6 \cdot 10^{-8}$	$3.4 \cdot 10^{-10}$
Total Reflectance (2)	0.033	$2.4 \cdot 10^{-9}$	$1.5 \cdot 10^{-13}$

Table 3.3: Calculated optical component and total setup reflectance for 44 eV (28.18 nm). The values correspond to the FEL fundamental, second, and third harmonic photon energies for p-polarized light.

As the beam parameters where not precisely specified for 28.2 nm radiation at FLASH and the estimated beam diameter is expected to be in the same range as that used in the previous ZEMAX simulations, the focal spot intensity profile has been simulated using the same parameter set apart from the corresponding wavelength. The simulated intensity distribution at the focal spot is presented in Fig. 3.11.
In accordance to the previously observed behavior, the beam spot distortion further increases at a shorter wavelength. A more pronounced fringe pattern forms in this case, especially along the horizontal direction. The simulated spot diameter in the horizontal plane is approximately 1.6 µm FWHM, far from its calculated diffraction limit of 0.69 µm FWHM. This increased focal spot distributes a certain amount of intensity in the fringe pattern and thus leads to a peak intensity decrease. The observed distortion can be minimized with a smaller incidence angle or a longer focal length. The corresponding Rayleigh length is calculated to be 200.6 µm in this case.

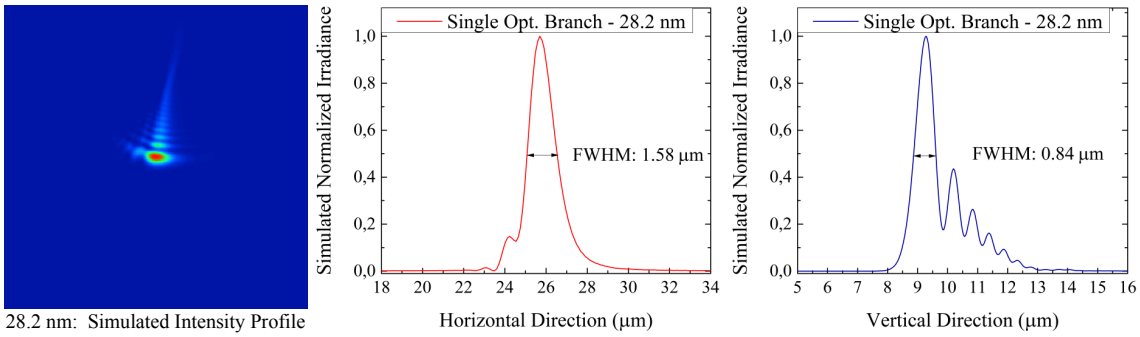

Figure 3.11: Single-optical branch simulated intensity profile at the focal point. The simulation takes into account wavefront division and the spherical mirror tilt angle.

It should be noted that the simulated peak intensity drops by approximately 4.96 times, in comparison to the perfect normal incidence geometry. Additionally, as pointed out before, the intensity-dependence of the nonlinear signal is expected to confine the origin of the doubly-charged ions in the central most intense part of the focal spot.

3.3 Two-photon Fluorescence Autocorrelation

The optical experimental setup has been initially aligned and characterized under ambient conditions. The 62 nm mirror set has been used at the beginning, replaced by the other two sets successively. A He:Ne laser has been employed to properly adjust the positions and angles of the optical components and establish a spatial alignment. The optical components are mount on an optical breadboard, used to introduce the complete pre-aligned setup in the experimental chamber.
In a second step, a femtosecond near-infrared (NIR) laser pulse, following the exact optical path of the He:Ne beam has been used to establish the temporal overlap between the two counter-propagating pulses in their common focal spot. The NIR fs laser pulse is provided by a commercial laser system (Light Conversion PHAROS 06-200-PP), seeded by a diode-pumped ytterbium doped potassium gadolinium tungstate (Yb:KGW) laser oscillator. The laser system delivers pulses with a tunable repetition rate between 1-200 kHz, at 1024 nm ± 5 nm (1.2 eV), a pulse duration in the range of 290-302 fs, and an average output power of approximately 6 W.
Utilizing two-photon induced fluorescence in the liquid phase as a non-linear signal, the temporal overlap could be established and the counter-propagating pulse geometry could be optimized. The two-photon fluorescence light generated by each partial beam, originating from two-photon excitation of CdSe quantum dots[2] solved in hexane, is imaged using a microscope objective on a CCD camera. The two-photon transition is non-resonant at 1.2 eV and well below the first excited state of the system [256–258] being suitable for an intensity autocorrelation.

[2]Provided by Prof. Dr. H. Weller, Institute of Physical Chemistry, University of Hamburg.

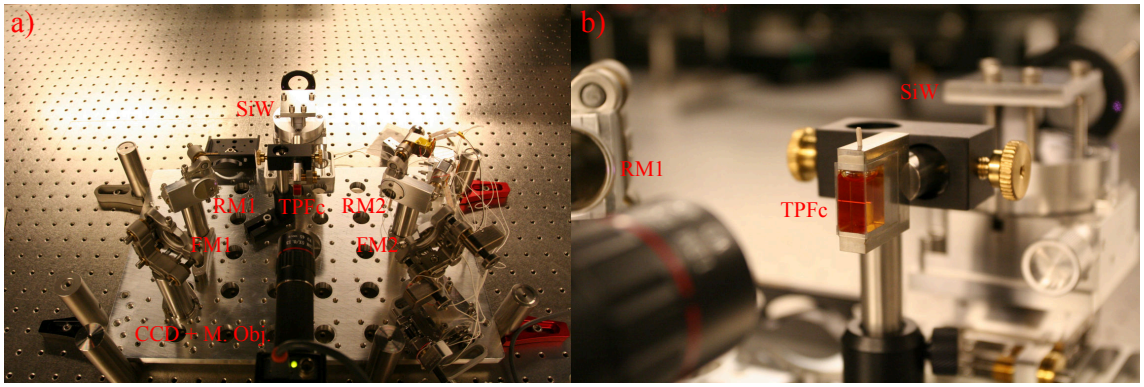

Figure 3.12: Single-shot counter-propagating pulse optical setup pre-aligned and characterized in ambient conditions. A He:Ne laser beam in combination with an NIR fs laser pulse have been used to align the experimental setup prior to the experiments in vacuum.

The CdSe quantum dot solution is contained in a transparent optical-grade cuvette (Hellma Analytics) and placed in the focal region. The complete experimental setup is shown in Fig. 3.12a. The cuvette is marked as TPFc and the remaining components use the labels previously defined in Fig. 3.2.
The magnified two-photon fluorescence distribution image, originating from both counter-propagating pulse foci in the CdSe cuvette (Fig. 3.12b), allows for spatially overlapping the two partial beams.
Furthermore, by equalizing the optical path lengths, an enhanced two-photon fluorescence signal can be observed at their temporal overlap region. This is accomplished by linearly translating both spherical mirrors (FM1, FM2), such that the two pulses temporally coincide exactly in the focus.
An image of the spatially and temporally overlapping counter-propagating pulses is shown in Fig. 3.13. The resulting two-photon fluorescence light distribution, spatially encodes a 2^{nd} order autocorrelation of the NIR fs pulse, according to the delay-encoding principle. The refractive index of hexane at 1024 nm corresponds to n=1.36 [259]. Taking into account the CCD pixel size and the measured optical magnification, a temporal delay scale can be assigned along the beam propagation axis, according to $\tau(\mathrm{x}) = 2 \cdot n \cdot \mathrm{x}/\mathrm{c}$ (Eq.3.1).
The optical magnification has been measured by displacing the CCD camera, using a µm-precision linear translation stage, along the axis parallel to the propagation axis and monitoring the temporal overlap position shift. For an observed temporal-overlap position difference of (22.5 ± 0.8) pixels/50 µm and a pixel size of 4.65 µm, the measured magnification value corresponds to $\mathrm{M_{TPF}} = 2.09$ (Fig B.1). Taking these facts into account, the temporal delay scales along the propagation axis with 20.2 fs/pixel.
The resulting second-order intensity autocorrelation trace, obtained as an average measurement over multiple laser pulses, inseparable with the utilized CCD camera due to the high repetition rate, is presented in Fig. 3.13. The autocorrelation trace exhibits a Gaussian profile with a temporal width of $\tau_{\mathrm{AC}} = 503.9 \pm 20.9$ fs FWHM. Assuming a Gaussian pulse temporal profile and using the corresponding deconvolution factor ($\sqrt{2}$) this corresponds to a pulse duration of $\tau_{\mathrm{p}} = 356.3 \pm 18$ fs FWHM.

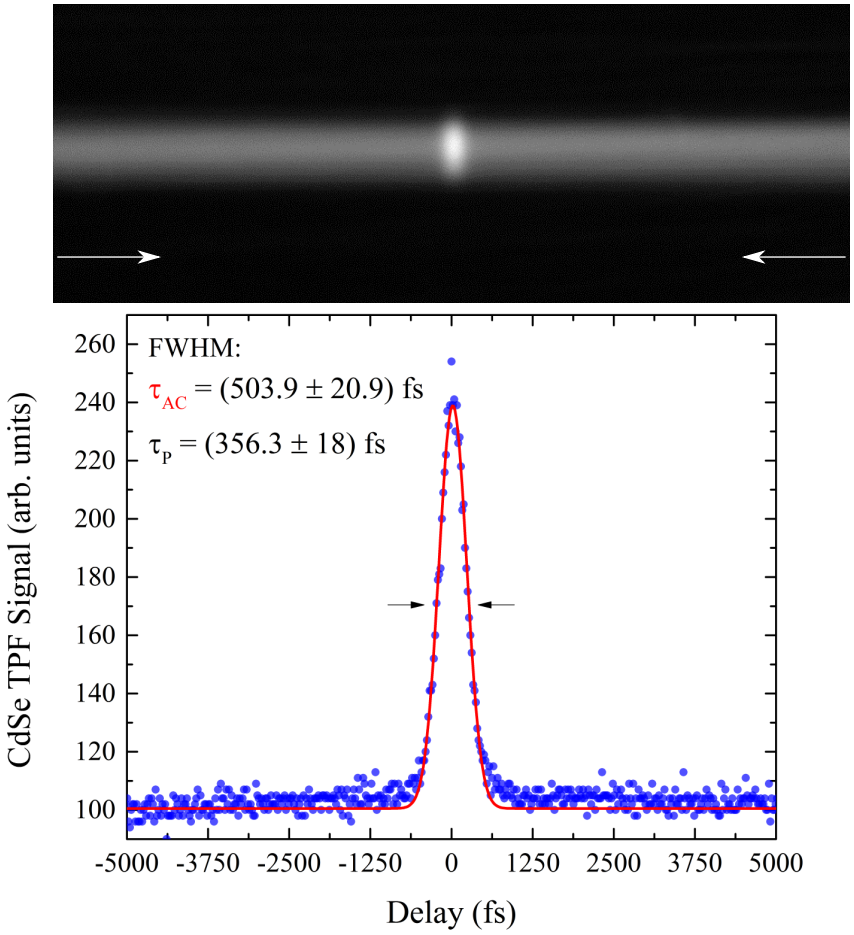

Figure 3.13: Counter-propagating pulse 2nd order intensity autocorrelation obtained by two-photon fluorescence, emitted by CdSe quantum dots in solution.

The measured duration is in good agreement with the anticipated value. It should be stressed, that the measurement has been obtained parasitically during a period where the pulse compression has been optimized for second-harmonic generation in the laser system accompanying harmonic generation module (HIRO). The pulse was utilized by a different experiment and therefore its compression has not been tuned in order to achieve the manufacturers specified values.
Nevertheless, according to the compression calibration chart [260], the measured 356.3 ± 18 fs pulse duration appears to be in very good agreement with the expected value of 370 ± 10 fs at the utilized compressor setting.
The effects of chromatic dispersion, due to propagation through the cuvette, on the pulse duration are negligible in this case. With the use of Sellmeier's equation provided in [259], the group velocity dispersion (GVD) in hexane at 1024 nm, is calculated[3] to be 56.75 fs^2/mm. The pulse travels through 1.25 mm quartz (cuvette wall thickness, GVD=23.39 fs^2/mm) and subsequently through 2.5 mm in hexane until it reaches the temporal overlap position. With the above values, the accumulated group delay dispersion is 171.11 fs^2.

[3] GVD$=\frac{\lambda^3}{2\pi c^2} \cdot \frac{d^2 n(\lambda)}{d\lambda^2}$, here λ=1024 nm.

Considering a bandwidth-limited pulse of 290 fs FWHM duration, the shortest reported duration, the pulse stretches after propagation to 290.005 fs FWHM, resulting in a non-observable change. Longer pulses with narrower bandwidth are influenced even less and in the case of an initial negative chirp the pulse will be slightly compressed. Nevertheless, due to the pulse's narrow spectral bandwidth the changes induced in the cuvette will be infinitesimal, not influencing the autocorrelation measurement outcome.
In summary, a counter-propagating pulse optical arrangement designed to deliver a single-shot intensity autocorrelation in the VUV-XUV range has been presented. This approach encodes the required non-linear signal delay dependence in space, such that it can be spatially resolved using an imaging detector on an individual-shot basis.
Limitations related with the multiphoton ionization mechanisms delivering the intensity autocorrelation signal have been discussed and three different second-order processes spanning from the VUV to the XUV range have been considered.
The corresponding optical sets associated with each of the proposed experiments have been described along with their simulated optical properties and resulting focal intensities.
Finally, the implementation of the counter-propagating arrangement, together with the first characterization results have been presented. Non-resonant two-photon fluorescence, emitted by CdSe quantum dots in solution, excited in the NIR has been used to optimize the pulse temporal overlap in their common focus and additionally provide a first benchmark intensity autocorrelation measurement. The two-photon fluorescence light distribution has been spatially resolved in the common focus of two counter-propagating NIR pulse replicas, providing a spatially-encoded intensity autocorrelation measurement.
Extending the described methodology in the VUV-XUV spectral regime requires an equivalent multiphoton microscopy detection scheme and for this purpose an ion-imaging time-of flight spectrometer, or an 'ion microscope', has been designed and realized. The following chapter describes the design and implementation of this instrument.

4 Ion Imaging Spectrometer: Mass-Charge Selective Ion Microscopy

Focusing intense ultrashort pulses on a gas target and recording the ionization product yield has allowed the study of atomic and molecular ionization dynamics down to sub-femtosecond timescales from the visible to the x-ray spectral range. In a typical experiment, the ionization products are collected as a function of the pulse intensity or the delay between two consecutive pulses, delivering information on the ionization pathways and the intrinsic time-constants associated with the system under study.

In most cases, the ionization process intensity-dependence is obtained using an ion/electron time-of-flight (TOF) spectrometer. The acquired signal is originating from an extended volume within the focal region, with dimensions which depend on the instruments detection solid angle. This signal is a convolution of the intensity-dependent ionization product yield with the corresponding focal intensity distribution within the detection volume. Although a Gaussian intensity profile is commonly assumed, observationally inaccessible effects on the focal intensity distribution, originating from diffraction, beam quality imperfections and optical aberrations can significantly alter the particle yield in realistic experimental conditions.

The ability to resolve the ion/electron yield spatial distribution with sufficient resolution can give access to such information [70, 261–264]. In many cases this is necessary for meaningful comparison between experimental results and theoretical predictions, while it can further enable elaborate experimental techniques, previously not feasible.

In the context of this experimental work, a spatially-resolving detection technique is is required in order to record the spatial distribution of the multiphoton ionization yield in the focal region of the counter-propagating pulse optical scheme. For this purpose, an ion-imaging TOF spectrometer, which provides a magnified image of the ion distribution in the focus of an ionizing light pulse in a mass-charge selective manner, has been experimentally realized. The ion microscope design and operation concept and has been presented in a previous work [265]. The current design is a simplified, adapted version of the previous instrument using minor modifications that resolve previous practical limitations and match the specifications relevant to the experiments described in this thesis.

This chapter discusses the design and experimental implementation of an ion-imaging time-of-flight spectrometer, or an 'ion microscope'. A schematic overview of the instrument is presented, followed by a detailed description of each section of the instrument. Furthermore, a collection of simulation results obtained using SIMION [266], related with the expected performance, specifications and practical limitations of the ion imaging system is presented. In the final section, a set of basic characterization measurement results is presented and discussed.

4.1 Ion Microscope General Layout

The ion imaging time-of-flight spectrometer consists of four main sections illustrated in Fig. 4.1. From the left to the right hand side these are, the ion optics section responsible for the ion image formation, the ion flight tube where ions drift in a field-free region towards the detector, the position-sensitive detector unit where the ion image is projected and transformed to an optical image and finally the external data acquisition unit. The three first sections are kept under ultrahigh vacuum conditions (typically below 10^{-7} mbar), whereas the data acquisition unit is external to the hosting experimental vacuum chamber. The complete instrument is mounted on the main experimental chamber via a three-axis linear positioning stage (VAb PM 112), allowing adjustment of the ion microscope position with respect to the ionizing light beam with 10 µm precision.
A magnified image of the ion distribution formed after the interaction of a focused light pulse with a gas target, can be obtained for every individual shot in combination with the corresponding ion time-of-flight (TOF) spectrum. Taking advantage of the fact that ions with different mass/charge ratio exhibit different flight times, the ion microscope additionally provides the possibility to image ions in a mass-charge selective manner by applying a precisely timed temporal gate on the detector gain.

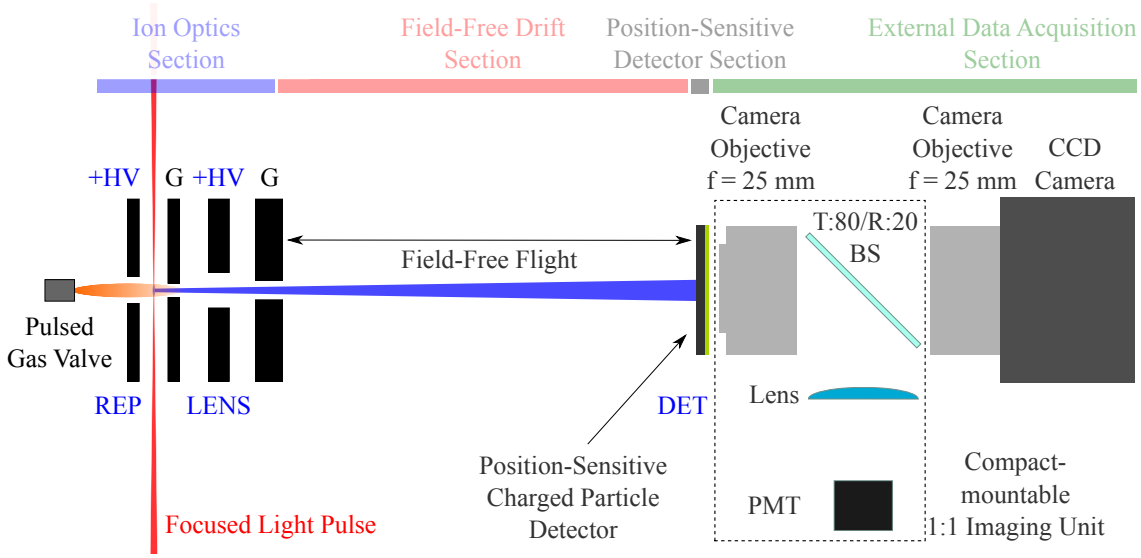

Figure 4.1: Ion Microscope general layout illustrating the main sections of the instrument and the general operation principles.

A brief description of the instruments general operational principle will be given here as an introduction to the detailed discussion of each respective section in the following parts of this chapter. Beginning from the left-hand side on Fig. 4.1, a gas target, supplied with an integrated pulsed valve (Parker Series 9) is ionized in the focus of a light pulse. The valve is synchronized with the light pulse and its opening time can be adjusted using a dedicated commercially available controller (Parker IOTA One).

A set of cylindrically symmetric electrodes, the ion optics system, form a magnified image of the ion distribution generated within the light pulse focal volume on the surface of a position-sensitive detector. Ions that are created between the two first electrodes, are first extracted in a homogeneous electric field in the order of several kV/mm, created by applying a positive high voltage on the first electrode (REP). In a second step, the ions propagate through the successive three electrodes which constitute an electrostatic lens, controlled by a second positive high voltage (LENS) and a high resolution magnified image of the ion distribution is projected on the detector surface (DET). The position-sensitive detector consists of a microchannel plate stack (MCP) paired with a thin YAG:Ce crystal scintillator. On ion impact the MCP stack releases a confined electron cloud which is accelerated towards the surface of the YAG:Ce crystal scintillator, emitting fluorescence light at the point of electron impact. In this way the ion image formed on the MCP detector surface is converted to an optical image and it is subsequently recorded with a CCD camera (Allied Vision Pike) located externally to the experimental vacuum chamber.
The optical arrangement paired with the CCD camera is modular and consists of two different parts, either providing the possibility to acquire a non-magnified image (1:1 imaging) utilizing an optical relay imaging system, or alternatively, directly image the scintillator crystal surface using an objective lens coupled to the CCD camera. In the latter case, the image is obtained with an additional measured demagnification of 0.48. The 1:1 imaging unit consists of two identical camera objectives (Voigtländer Nokton 25 mm), one of which is attached on the CCD camera and utilized also for direct imaging and a beam-splitter plate (Edmund Optics 68-375) which transmits 80% of the light to the CCD camera and reflects 20% to be collected on a photo-multiplier tube cathode (PMT) with a second lens, providing the ion time-of-flight spectrum in an optical manner. Alternatively, the 1:1 imaging unit is removed and the CCD camera with a single objective is used for direct imaging. Transmission losses and imaging distortions favor the direct imaging option, delivering an overall sharper and brighter image. In that case, the ion TOF spectrum can be acquired by electrically decoupling the high-frequency signal from the scintillator surface using a high-pass RC circuit. The YAG:Ce crystal is coated with a thin Al layer on the front surface, effectively acting as a collection anode electrode in that case.
Ions with different mass-over-charge (m/q) ratio arrive at the detector at different times, in well separated intervals in the microsecond timescale, permitting selective detection of different ion species. By using an adjustable temporal gate on the detector gain, realized with a fast high-voltage switching module, ions of an individual mass/charge state can be selectively imaged. This is a very important feature, assisting in background ion signal suppression, or alternatively, providing the possibility of performing mass/charge resolved imaging studies. The temporal separation between ion TOF spectra corresponding to successive light pulses allows operation up to a 100 kHz pulse repetition rate without ion TOF peak overlap, although the overall instruments capabilities are limited by the current high-voltage switching module to 1 kHz and additionally by the utilized CCD camera to approximately 30 Hz.
A three-dimensional CAD model of the ion microscope as it has been experimentally realized is shown in Fig. 4.2. The four main instrument sections, namely the ion optics section, the field-free flight tube, the position-sensitive detector and the location where the external imaging system is mount are explicitly indicated.

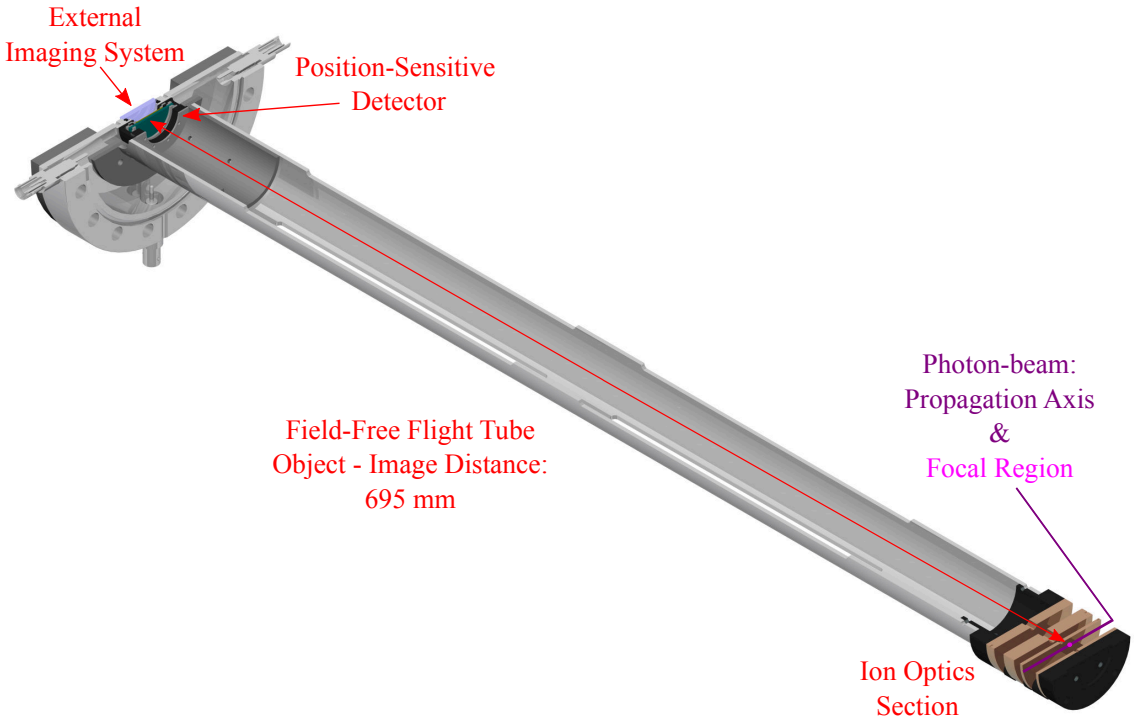

Figure 4.2: Ion Microscope 3D CAD model cross-section as it has been experimentally realized. The four main instrument sections, namely the ion optics section, flight tube, position-sensitive detector and external imaging system are explicitly indicated. The external imaging system and the pulsed gas valve are not shown here for illustration simplicity.

The pulsed gas valve is fixed on the bottom-side of the demountable ion-optics assembly in a specially designed insulating (PEEK) cylindrical spacer plate which ensures centering and isolates electrically the valve from the first electrode (REP). The pulsed operation reduces the overall gas load and the gas target reaches the interaction region through the first electrodes aperture. The influence of mechanical vibrations originating from the pulsed valve operation has been investigated and no visible effects have been found on the ion image.

4.2 Time-Gated Position Sensitive Detector

The magnified image of the ion distribution must be converted to an optical image in order to be acquired and evaluated. For this purpose, a self-assembled, charged-particle position-sensitive detector (PSD) has been designed and realized (C.1).
The complete detector is assembled and mounted in a dedicated insulating housing which is designed such that all the detector parts are efficiently insulated, shielded, pumped and optimally positioned with respect to each other, in order to minimize spatial resolution degradation. The resulting optical image is transmitted through an optically flat ($\lambda/10$), anti-reflection coated window and imaged with the optical arrangement described above, which is fixed on a dedicated optical breadboard on the top of the detector vacuum flange.

A specially designed metallic ring (not-shown here) acts both as a mount for the first camera objective, minimizing light loss and ensuring sharp imaging of the YAG:Ce screen, as well as a clamp for the vacuum-window. The detector consists of a microchannel plate (MCP) stack, using two MCP plates in a Chevron arrangement, paired with a thin YAG:Ce scintillator crystal. A schematic of the complete detector assembly and its position when mounted on the ion microscope flight-tube is shown below (Fig. 4.3).

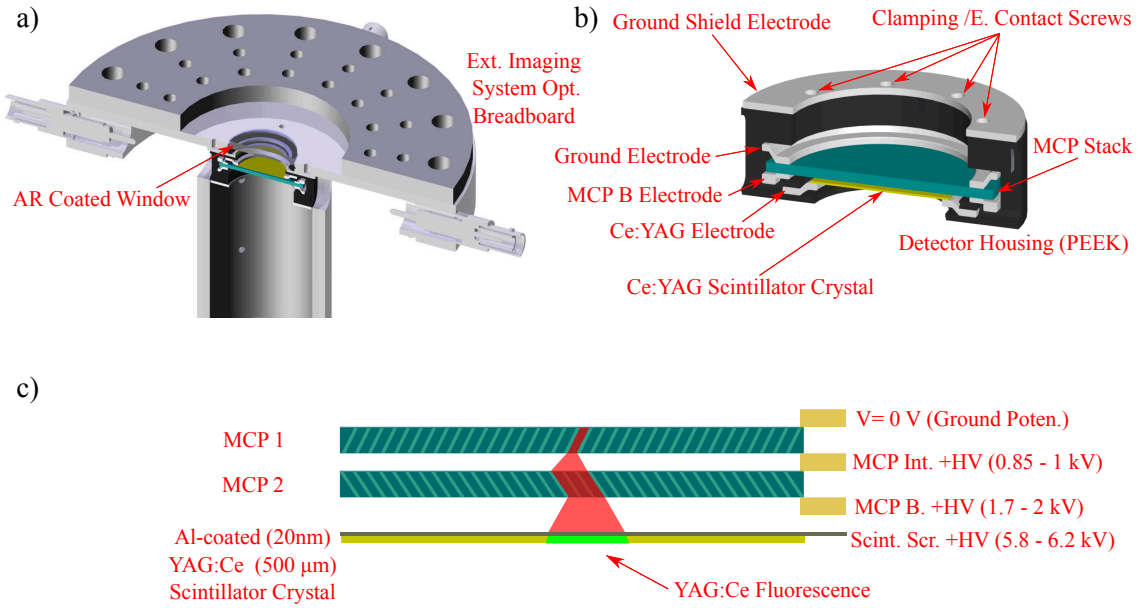

Figure 4.3: a.) Three-dimensional CAD model of the position-sensitive detector (PSD) section. b.) Cross-section view of the assembled detector unit. c.) Schematic of the PSD operation principle along with the relevant experimental parameters.

A microchannel plate [267,268] is a thin high-resistance glass plate hosting a two-dimensional array of 10^4-10^7 secondary-electron multiplier channels (microdynodes), contacted in parallel with a metallic coating on the plates surface. Typical channel diameter and inter-channel spacing dimensions are in the order of 10 µm and the channels are usually biased at a small angle ($\pm 8^o$) to the plate surface, increasing the probability for secondary emission. Energetic particles (photons, electrons, ions) impacting on a channel create secondary electrons and a single MCP plate typically exhibits an electron multiplication factor (or gain) in the order of 10^4. The detection efficiency of an MCP plate for positive ions, relevant to this work, lies between 50% -60% [269, 270] at the typically reached 5 keV electron impact energy. In a Chevron MCP arrangement the two plates are oriented such that their channels form a V-shape configuration, increasing the detectors gain to approximately 10^7 [267, 268], while avoiding ion feedback effects.
The MCP plates that were available for the particular detector are of 25 mm diameter and specified with a channel diameter of 10 µm and a center-to-center channel spacing of 12 µm. The two plates are electrically contacted using a 100 µm thick, gold-plated ring electrode, providing a stable intermediate voltage. This is important in order to avoid high-voltage afterpulse (ringing) effects when the detector is operated in a time-gated mode.

The MCP pair is operated below saturation (nominal voltage: 850 V per plate) in a linear amplification range. The electrons exiting the stack are accelerated in a strong homogeneous electric field towards the scintillator surface, located approximately 500 µm away from the second MCP, in order to minimize their spread.
The YAG:Ce scintillator crystal is 500 µm thick, polished on both sides and coated with a 20 nm Al layer on the front surface. The Al coating serves as a high-voltage electrode as well as a charge collection anode for ion TOF signal decoupling as discussed above. The YAG:Ce scintillator emits at 550 nm upon excitation, exhibiting a fast decay time of approximately 70 ns [271], while it shows a high radiation-damage resistance [272]. A thin crystal is used for an improved spatial resolution, expected to be better than 10 µm according to the results presented in [273]. Alternatively a YAP:Ce crystal has been also considered, exhibiting a higher light output at the expense of an inconvenient emission wavelength at 370 nm. This option was experimentally investigated, using a 370 nm light-emitting diode, which was found not to transmit over the external imaging system.
The high spatial resolution offered by the MCP channel pattern, together with an excellent time resolution (< 100 ps), constitutes an MCP detector ideal for charged-particle time-of-flight spectroscopy and imaging applications. Typically, an MCP-based imaging detector employing a single MCP plate, assisted with centroid analysis software, can reach a spatial resolution in the order of the MCP pore separation distance (10 µm). In a stacked Chevron MCP detector the spatial resolution is expected to deteriorate due to the fact that signal from one channel in the first plate will inevitably spread to more channels in the second plate [267], as illustrated in Fig. 4.3c. Additionaly, the increased gain can lead to an increase in electrostatic repulsion at the second MCP plate exit. For this reason, a high voltage applied between the MCP detector back surface and the scintillator screen is used in order to minimize space-charge broadening effects. After optimizing the MCP-scintillator spacing and voltage difference, as well as the MCP applied voltages, it is the size of the resulting fluorescence spot on the scintillator screen originating from a single channel in the front plate, that determines the spatial resolution of the detector. The measured scintillator fluorescence spot size for the described detector corresponds to 76 µm ± 15 µm.
As mentioned above, the detector can be operated in a time-gated gain mode providing the ability to selectively image ions of an individual mass/charge state. In this case a high-voltage pulse with a controllable temporal width and timing is applied on the second plate, effectively switching the detector gain on for a short time interval in the 10-ns scale. Matching the timing of the high-voltage pulse with the desired mass/charge ion time-of-flight, allows for exclusively imaging the particular ion species. The fast high-voltage pulse is provided by a commercial switching module (Photek GM-MCP-2) which can deliver a pulse as short as 9 ns at full-width-at-half-maximum (FWHM) in up to 1 kHz repetition rate.
A trigger signal, provided in the laboratory by a fast-photodiode installed close to the laser beam output port, is used together with a delay generator for defining the high-voltage gate-width and timing. Due to the fact that the acquired ion time-of-flight spectrum is directly connected to the ion image obtained, the temporal gate tuning can be effectively performed in real time and the desired ion peak can be selected, ensuring that no undesirable ionic species will contribute to the final ion image.

4.3 Ion Imaging: Ion Optics and Simulation Results

High-Resolution Ion Imaging

The ion optics section has been designed such that it can accommodate a light beam of up to 10 mm in diameter without clipping, providing the possibility for refocused beam experiments using normal incidence focusing optics.
The ion optics set consists of four cylindrical electrodes, precisely spaced in a concentric arrangement. Ions are generated in the light beam focal volume which is adjusted to lie exactly in the middle between the first and second electrode. This position, which is the design ion starting position, will be from this point on denoted as x_{nom}. The first electrode is set to a positive high voltage (typically 10 kV, maximum 20 kV) whereas the second electrode is kept at ground potential. The ions generated between the first two electrodes are accelerated in a strong homogeneous static electric field towards the detector. The second, third and fourth electrode are forming an electrostatic immersion lens which is adjusted by a positive high voltage applied on the third electrode (schematically shown in Fig. 4.1). The electrodes are made of oxygen-free high conductivity (OFHC) copper and a lapping finishing process ensured a high degree of planarity and a very low surface roughness. Spacing and centering is achieved with a very high degree of accuracy by precision insulating (PEEK) spacers. Together with the two additional insulating cylindrical mounting plates they form a compact demountable assembly that is fixed on the bottom part of the field-free flight tube (Fig. 4.2, Fig. C.2).
The ion imaging properties of the system rely on the ratio between the two positive high voltages, the electrode aperture dimensions and the distance between the consecutive electrodes. A detailed description and optimization of the ion optical system can be found in [265] and the basic charged particle optics principles underlying the ion imaging system design, are thoroughly discussed in a wide variety of excellent textbooks and journal articles, as for example in [274–277] to list a few. Two minor differences in the new design compared to that discussed in [265], are the distance between the first two electrodes and the electrode size. An increased electrode diameter ensures a homogeneous electric field at the extraction area, avoiding any electrode edge effects. Furthermore, the larger spacing between the electrodes allows an incoming light beam of larger diameter (up to 10 mm) to pass through the electrode before being refocused and it only affects the voltage ratio providing a sharp image on the detector surface (DET). For the current ion optical system parameters, the optimized voltage ratio corresponds to:

$$V_{LENS}/V_{REP} = 0.3717 \tag{4.1}$$

The ion imaging properties of the ion microscope have been simulated using SIMION and additionally a set of tolerance studies, corresponding to the relevant and anticipated experimental parameters has been performed. SIMION is a well established ion optics simulation program that uses finite difference methods together with a fourth order Runge-Kutta numerical integration algorithm. It can simulate electric fields and the trajectories of charged particles propagating in those fields for a given configuration of electrodes and particle initial conditions [266].

A generalized schematic of the simulation parameters used for computing and optimizing the main imaging properties of the system, namely the ion image magnification and spatial resolution and their dependence on the relevant experimental parameters is shown in Fig. 4.4. The numerical grid unit size used corresponds to 10 µm, while choosing a smaller grid size did not show any deviations in the results presented below.
In order to develop an intuitive understanding, the presented set of simulations makes use of homogeneous cylindrical ion distributions defined by their radius R and length L. Using a cartesian coordinate system, the ions propagate towards the detector in the x-axis and the detector plane is parallel to the z-y plane. The cylinder axis is coincident or parallel with the light beam propagation axis (y) and the light pulse polarization direction is along the z-axis as experimentally realized. The ions are assigned with a specific mass, charge, initial starting position and velocity and are subsequently propagated in the electric field created by the ion microscope electrodes. As a result, the final ion properties of interest are recorded when they encounter the detector surface. The ion initial kinetic energy is considered to be thermal (38 meV at 21 °C, according to the equipartition theorem of energy) with directions in a spherical homogeneous distribution with the ion channel dimensions, unless otherwise stated. Additionally, in order to evaluate the spatial resolution of the system, a set of cylindrical disk pairs were defined in a direct analogy to line-pairs used in optics. The individual cylindrical disks are defined by their radius R and length T (or thickness in that case, as L is used for defining the total distribution length), whereas the disk-pair separation is given by the parameter s and the separation between two consecutive pairs by D as illustrated in Fig. 4.4.

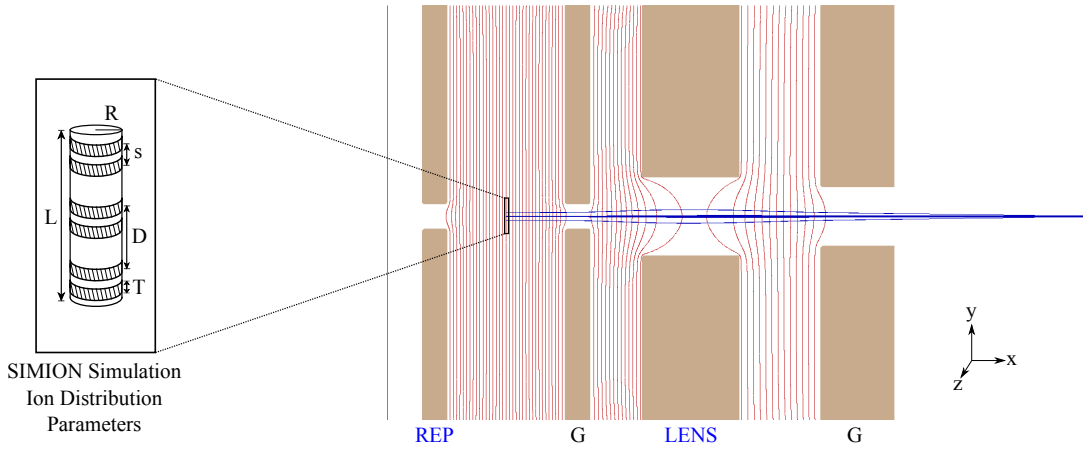

Figure 4.4: SIMION Simulation: Electrodes and ion definition parameters. The red lines depict an equipotential map in the area between the electrodes. The ion distribution is described by a cylindrical distribution. The light propagation axis is matching with the y-coordinate, the ion optical axis with the x-coordinate (the ions propagate in the x direction towards the detector) and the light polarization vector in the actual experimental implementation is directed along the z-coordinate.

A sharp magnified image of the ion distribution, starting at x_{nom}, is formed on the detector surface located at $x_{nom} + 695$ mm in the x-axis coordinate, when the optimized voltage ratio $V_{LENS}/V_{REP} = 0.3717$ is used.

The ion image magnification depends on the voltage ratio, or equivalently, on the ions starting position as shown in Fig. 4.6. The magnification design value corresponding to the sharpest image on the detector for this system is:

$$M_{theor.} = 24.5 \tag{4.2}$$

A simple imaging simulation example is illustrated in Fig. 4.5. A distribution of seven individual Kr^+ ion cylinders (10000 particles/cylinder) with their axis oriented parallel to the y-axis, located at x_{nom} in the x-axis direction (Fig. 4.4) has been defined. The ion cylinders have an individual diameter of $2\times R = 10\,\mu m$ (x,z-axes), length of $L = 734\,\mu m$ (y-axis), matching the actual 18 mm detector active diameter (taking into account Eq. 4.2) and are mutually spaced by 100 µm along the z-coordinate. The voltages used are in accordance with Eq. 4.1 and $V_{REP} = 10$ kV. As soon as the ions reach the detector, their final position (z, y) is registered and the resulting distribution is presented in Fig. 4.5b.

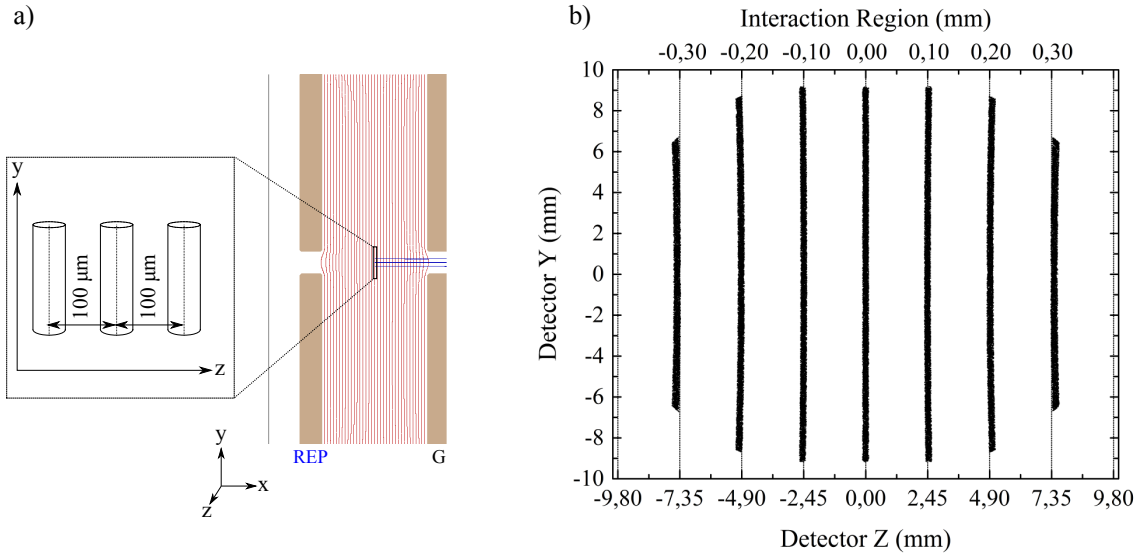

Figure 4.5: Simulated Kr^+ ion image on the detector plane (detector diameter: 18 mm). The circular ion image cut is due to the detector shape. The ion image is magnified by $M_{theor.} = 24.5$. A minor imaging distortion effect (pincushion) is observable at the detector edges. 4.5a) The initial ion distribution for the SIMION simulation corresponds to seven Kr^+ ion cylinders with $R = 5\,\mu m$, $L = 734\,\mu m$ (y-axis), placed at x_{nom}, spaced by 100 µm per cylinder along the z-axis and their axis oriented parallel to y-axis. 4.5b) Simulated ion image on the detector plane.

An ion cylinder image spacing of 2450 µm on the detector plane, per 100 µm initial displacement in the interaction region, is in accordance with Eq. 4.2. Imaging distortion is evident at the detector ion image edge, although the resulting magnification deviation shows only 2% maximum difference with the nominal value at the detector edge. Taking into account that the most important information is expected in the central part of the ion image this aberration is not expected to exert significant imaging restrictions (abberation specific simulation results are shown in Fig. C.5). Furthermore, when of importance, the ion microscope may successively obtain a series of images that can be later combined utilizing

the higher quality central part of the image. Varying the ion channel diameter between 1 µm - 30 µm and using the same simulation parameters, did not show any deviations from the results presented in 4.5, apart from the anticipated line thickness increase according to the simulated magnification value. The results presented above are valid when the ion cylinder-axis, or the center-of-mass of the ion distribution, is located exactly in the middle between the two first electrodes at $x=x_{nom}$. As mentioned before the ion imaging system magnification depends on the ion initial position and a set of simulated magnification values can be found below (Fig. 4.6).

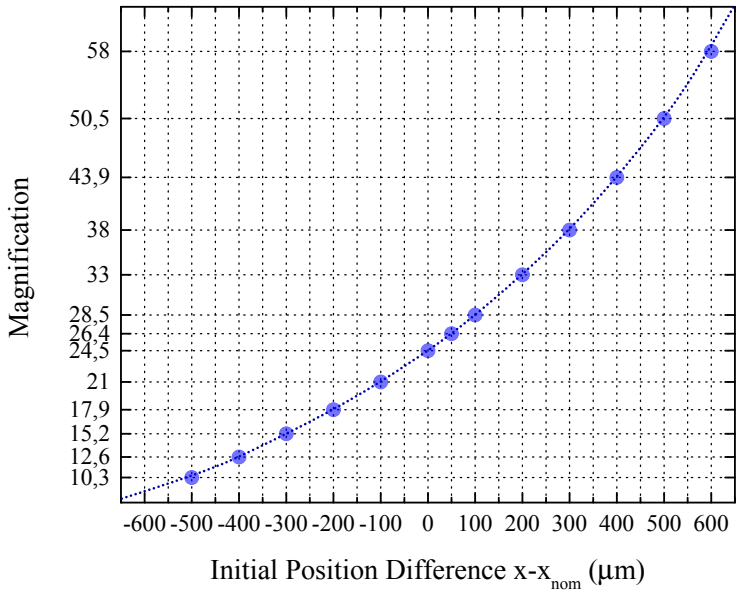

Figure 4.6: Variation of the ion image magnification as a function of the ions starting position along the ion optical axis x, referenced with respect to the design position x_{nom}.

It is worth noting at this point, that as the initial position difference from the x_{nom} grows, the simulated imaging aberrations enhance and as a result the resolution drops. This tendency enhances towards the repelling electrode direction (minus sign in the position difference) where the magnification decreases. The imaging quality does not show an observable change for ion starting positions within ± 100 µm around x_{nom}, although an ion distribution with a wide x-axis extent will experience a broad range of magnification values, compromising the ion imaging resolution as will be discussed in detail below.
In connection to the initial x-axis position imaging properties dependence, the depth-of-focus of the ion imaging system has been found to depend on the ions initial velocity, both in terms of its absolute value, as well as its direction. The ion optics depth-of-focus is defined in this context as the position interval Δx along the x-axis, in which ions that originate from, will end up in a well-defined circular area (spot) on the detector surface. Without loss of generality, this can be defined by the spacing between two MCP pores (here 12 µm), ensuring that ions starting within Δx, sharing the same z,y coordinates, will end up in a single MCP pore on the z,y detector plane. By applying a higher repelling voltage (REP), while satisfying the V_{LENS}/V_{REP} condition (4.1), the depth-of-focus of the ion microscope grows due to the relative increase of the x-axis acceleration vector component.

The corresponding simulation results are illustrated in Fig. 4.7 and supplementary results are contained within Appendix C. A cylindrical ion distribution (500 ions), defined in a similar manner as previously, with R=L=0.4 µm and the cylinder-axis coinciding with the y-axis, is imaged on the detector plane. The ions y-position standard deviation (identical results obtained in the z-direction) is recorded as a function of their initial starting position along the x-axis. The cylinder length L (y-axis) is chosen such, that one ion cylinder does not impinge in more than a single MCP channel, when starting at x_{nom}.

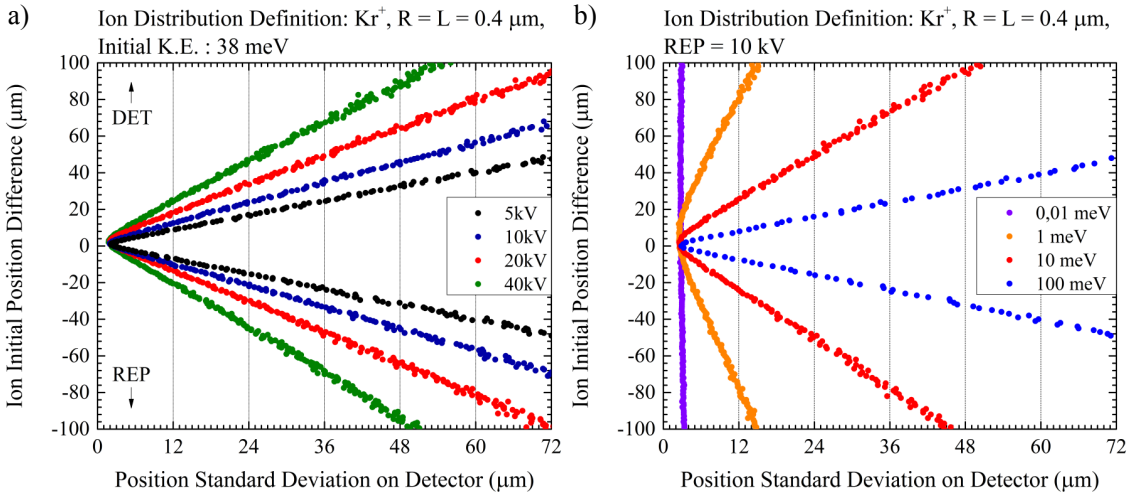

Figure 4.7: Ion Microscope Simulated Focusing Properties: Ion optical system focal properties as a function of the repelling electrode (REP) voltage. Simulation parameters: Kr^+ ions, R=4 µm, L=4 µm, K.E.=38meV, (x,y,z)=(var.,0,0). The ion position standard deviation on the detector increases with the ion starting position along the ion optical axis (x). Higher repelling electrode voltages, while satisfying the optimal imaging voltage ratio, lead to a depth-of-focus increase. Horizontal lines: integer multiples of the utilized MCP plate channel spacing (12 µm).

The y-position standard deviation minimum shown in both plots of Fig. 4.7 corresponds to the focal position of the ion optical system, exhibiting the highest spatial resolution, which for the given voltage ratio (0.3717) corresponds to x_{nom}. The y-axis on both plots scales with the ions initial position difference with respect to x_{nom}. As a guide to the eye, the multiples of the MCP channel spacing are marked with dashed lines. As shown in both plots, only ions that start within a finite distance Δx from x_{nom} will end up in the same MCP channel (generally, same location on the detector surface), depicting the ion optics depth-of-focus dependence as a function of the repelling electrode voltage (4.7a) and ions initial kinetic energy (4.7b) respectively.

In Fig. 4.7a, the depth-of-focus dependence on the repelling electrode voltage (REP) is shown, for Kr^+ ions with a thermal initial kinetic energy (38 meV) and directions in a spherical distribution as defined above. The results are ion mass independent and a comparative benchmark simulation has been performed using He^+ ions, presented in Appendix C. As described above, a higher repelling voltage corresponds to a broader depth-of-focus as clearly visible in Fig. 4.7a. A practical limitation to the maximum voltage that can be experimentally applied in that case is imposed by the presence of the target

gas which at a critical density will promote an electrical discharge between the electrode and the surrounding surfaces at ground potential.
The depth-of-focus as a function of the absolute initial ion kinetic energy for REP at 10kV is illustrated in 4.7b. A lower ion initial kinetic energy will result in an increased depth of focus. This can be achieved experimentally by means of a cold gas target supplied by a skimmed supersonic molecular beam at the expense of target density [278], neglecting for the time being the case where molecular dissociation will result in energetic ionic fragments. As mentioned above, the direction of the momentum vector plays an important role and when aligned with the ion propagation axis (x) the effects presented in Fig. 4.7 become negligible. This has also been verified by performing an additional benchmark simulation with a well defined directional (x) initial momentum (App. C, Fig. C.4).
The results illustrated above describe the case where the ion distribution starts at x_{nom}, where the V_{LENS}/V_{REP} voltage ratio (4.1) is optimized for the highest resolution as will be discussed in detail in the next paragraph. For an ion distribution formed at a different position along the x-axis, sharp ion imaging can be achieved by tuning the V_{LENS}/V_{REP} voltage ratio as shown in Fig. 4.8.

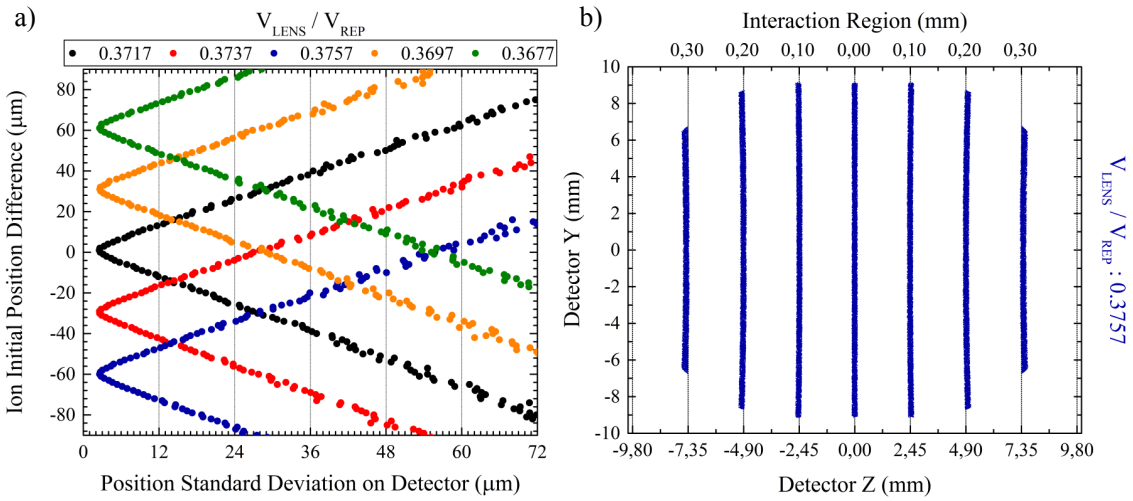

Figure 4.8: a) Fine tuning of the ion optics focal plane can be achieved by changing the V_{LENS}/V_{REP} voltage ratio while retaining the ion imaging properties of the system. The simulation parameters are identical to those in 4.7a for REP: 10kV. b) Ion imaging simulation with the exact simulation conditions to the results shown in Fig. 4.5 but with ions starting 60 µm closer to the REP electrode and $V_{LENS}/V_{REP} = 0.3757$ providing identical results.

As previously mentioned, efficient positioning of the ion microscope with respect to the photon beam can be achieved with 10 µm precision using the VAb 3-axis positioning stage. Fine adjustment of the ion optics focal plane (x-axis) in order to experimentally match the ions starting position, can be achieved by tuning the V_{LENS}/V_{REP} voltage ratio as shown above (4.8). When the voltage ratio is chosen such that the standard deviation minimum coincides with the ion channel x-coordinate position, the ion imaging quality is retained, exhibiting the exact characteristics as if the ion channel would be located at x_{nom}. A simulated example is illustrated in Fig. 4.8b showing the Kr^+ ion image on the detector

plane for such a matched x-axis starting position / voltage ratio combination. The ion distribution cylinder axis is set to be 60 µm below x_{nom}, closer to the REP electrode surface (-60 µm). The remaining simulation parameters are exactly the same as those used for the simulation shown in Fig. 4.5 in order to allow a direct comparison. By choosing the LENS electrode voltage as $V_{LENS}/V_{REP} = 0.3757$ being the ratio that is shown to provide the sharpest image for this position (Fig. 4.8a), a sharp ion image is formed on the detector surface exhibiting the exact magnification (24.5) and ion imaging quality as shown before (Fig. 4.5b).

One aspect of high importance to the envisioned experimental applications of the ion microscope, is the achievable spatial resolution. As already discussed, charge spread and repulsion mechanisms in the PSD detector are expected to impose limitations on the ultimate spatial resolution defined by the MCP pore spacing. The external optical detection system exhibits a spatial resolution better than 10 µm, characterized with a transmissive calibration scale plate (Pyser-SGI) and thus does not compromise the instruments resolution. It is therefore important to assess to which degree the native ion imaging systems spatial resolution depends on experimental parameters, such as the initial ion channel dimensions, position and initial velocity distribution. An additional set of dedicated SIMION simulations has been performed, mainly in order to provide an intuitive understanding of the influence of each of those parameters in the ion optical imaging system performance. A cylindrical disk-pair Kr^+ initial ion distribution is used, as illustrated in detail in Fig. 4.4. Briefly, a set of cylindrical disk-pairs is defined along the light propagation axis y, in a direct analogy to line-pairs in optics. The ability to spatially resolve the disk-pair ion image on the detector surface has been evaluated for pairs spaced in a range between 1 µm - 3 µm. The simulation results reported below correspond to a REP: 10 kV / LENS: 3.717 kV voltage combination as this was commonly used during the experiment. A higher repelling electrode voltage did not show significant improvement apart from the already reported initial kinetic energy compensation effects.

A typical simulation input and output, illustrating both a fraction of the ion initial distribution, as well as the corresponding detector-plane ion image (y-z plane), is shown below (Fig. 4.9). The ion disk-pair distribution, set to begin in the interaction region (nominal ion starting position), is shown in Fig. 4.9a. The Kr^+ ion disk-pairs with R=5 µm, T=0.1 µm, D=5 µm, L=370 µm (See Fig.4.4), separated here by s=1 µm along the y-axis, begin with no initial kinetic energy with their axis parallel to y and centered at $x=x_{nom}$. The resulting ion image on the detector plane is shown in Fig. 4.9b, exhibiting a radial spatial resolution variation (here on y-axis for simplicity). This is interpreted as a combined effect of imaging aberrations, distortion but mainly ion imaging depth-of-focus limitations. A systematic study was performed with a series of simulations as that shown in Fig. 4.9, varying the initial ion cylinder radius, velocity, or starting position while keeping the remaining parameters constant. The ion cylinder radius has been identified as the most influential parameter. Ion distributions with a broad x-axis extent (Δx) will experience a range of magnification values depending on the respective ion starting position.

A representative example is shown in Fig. 4.10, combined together with Fig. 4.9b, as both utilize the exact simulation parameters apart from the ion cylinder radius. For an increasing radius, the 1 µm spatial resolution is attained for a shorter distance from the origin (y=z=0), as it becomes apparent from the corresponding disk-pair ion detector images.

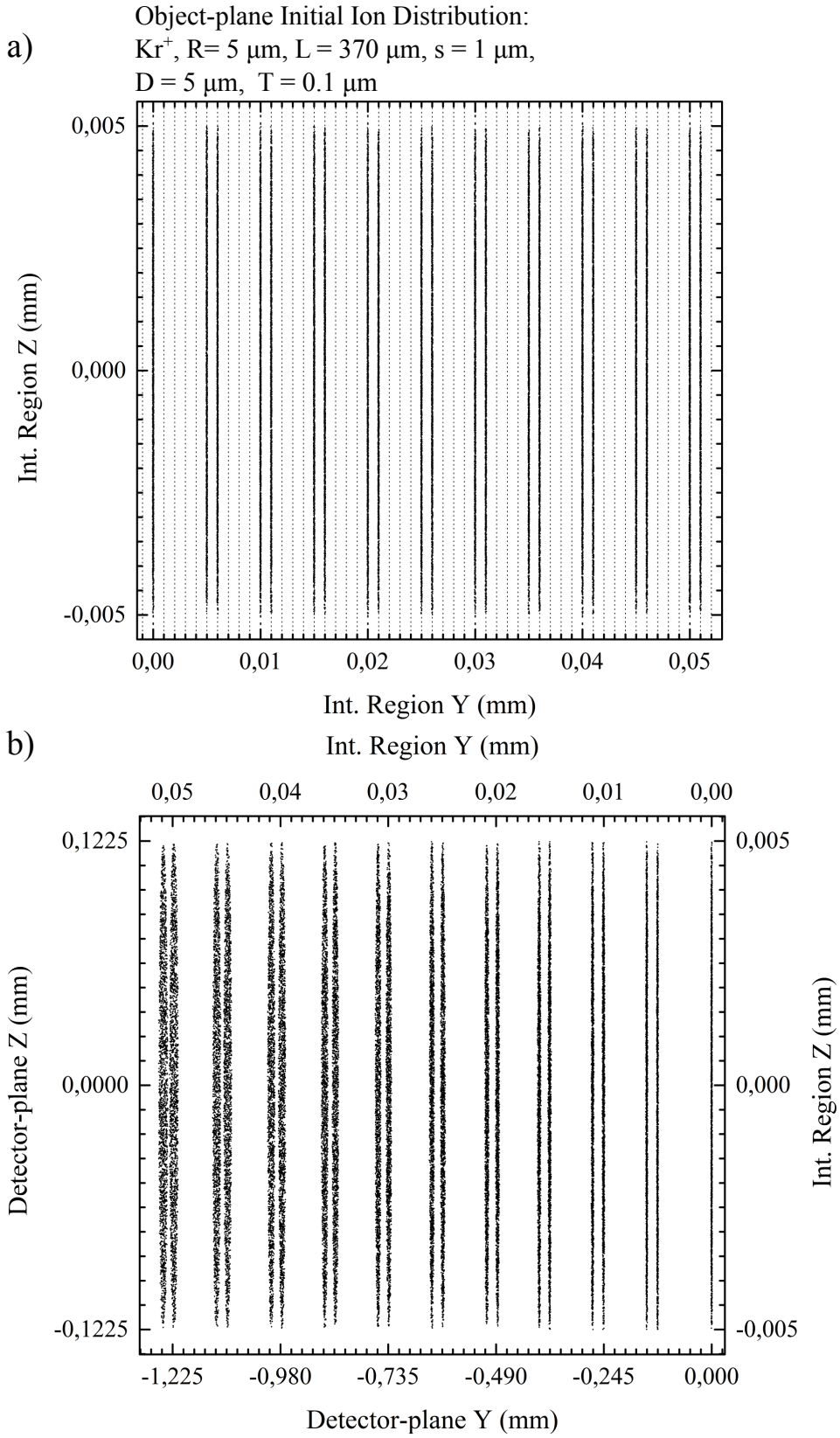

Figure 4.9: Spatial resolution simulation: 1 µm spaced Kr^+ ion line-pairs along the light-propagation axis (y). Simulation parameters: REP = 10 kV, LENS= 3.717 kV, ion cylinders with R=10 µm, T=0.1 µm, s=1 µm, D=5 µm, no initial kinetic energy, according to Fig. 4.4 definitions. a) Initial ion distribution defined at the interaction region ($x=x_{nom}$), b) Simulated ion distribution on the detector surface.

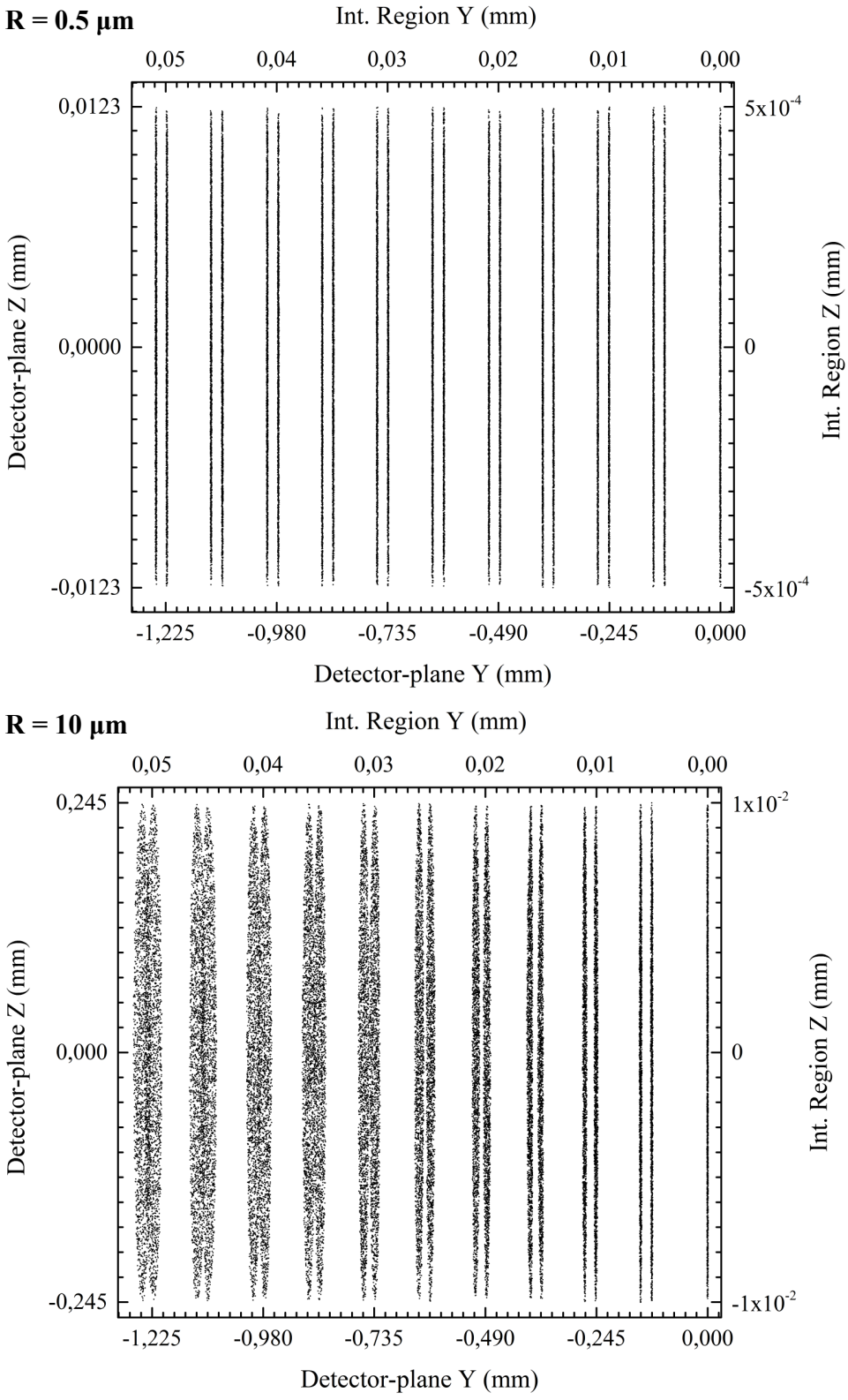

Figure 4.10: 1 µm cylinder-pair resolution simulation as a function of the initial ion cylinder radius (a: R=0.5 µm, b: R=10 µm, detector-plane ion distributions). Apart from the cylinder radius, the simulation parameters are identical to the one shown in Fig. 4.9. As previously described, the spatial resolution deteriorates as the ion distribution extent grows along the x-direction.

In the case of an ion cylinder with R =0.5 µm, the disk pairs can be resolved even when they begin at a 370 µm radial distance (here y-direction) corresponding to the complete detector active area radius ($L_{DET} \approx 9$ mm, Eq. 4.2). On the contrary, in the case of an ion distribution with R=10 µm, the ion image spatial resolution deteriorates and the disk-pair image can only be resolved in a radial range up to roughly ± 25 µm from the origin (Fig. 4.10b). Alternately, for an ion disk-pair spacing of s=2 µm with the R=10 µm ion distribution, the corresponding distance where the pair can be spatially resolved in the ion image plane extends to ± 120 µm or to ± 180 µm in the case of a s=3 µm ion disk-pair spacing (not shown here). A table summarizing the spatial resolution simulation results performed for a range between 1 µm - 3 µm, as a function of the ion cylinder radius R, attained in the same manner to that described in the previous example can be found below (Tab. 4.1).

Ion Cylinder Radius	Radial Spatial Resolution Extent (y-axis)		
	Cylinder-Pair Spacing		
R	s =1 µm	s =2 µm	s =3 µm
R=0.5 µm	± 370 µm*	± 370 µm*	± 370 µm*
R=1.5 µm	± 200 µm	± 370 µm*	± 370 µm*
R=2.5 µm	± 115 µm	±250 µm	± 370 µm*
R=5 µm	± 55 µm	± 120 µm	± 180 µm
R=10 µm	± 25 µm	± 55 µm	± 80 µm
R=15 µm	± 15 µm	± 30 µm	± 50 µm

Table 4.1: Simulated spatial resolution radial dependence as a function of the ion cylinder radius. The radial extent (here along the y-axis) from the origin (z=y=0) that an ion cylinder disk-pair can be spatially resolved on the detector surface is provided as a function of the disk-pair spacing and disk radius. Values with an asterisk are limited by the utilized detector active diameter (∼ 18 mm).

The initial ion velocity distribution has an additional influence on the ion optical systems spatial resolution, in accordance with the results presented in Fig. 4.7. Although the origin of the ion initial velocity influence on the final spatial resolution has been previously discussed, the relative contribution of this effect in comparison with the ion distribution radius dependence results was investigated. For this purpose a simulation identical to the example described above (Fig. 4.9) has been performed. An initial ion disk-pair set with the exact parameters as those used in Fig. 4.9 (R=5 µm, s=1 µm) has been defined, with the only difference that the ions were assigned with an initial kinetic energy and direction in a homogeneous spherical distribution. In this case, the radial extent (y-axis) that 1 µm spatial resolution is retained, remains constant at ± 55 µm between 10^{-5} meV to 1 meV and shows a gradual degradation to ± 40 µm at 100 meV initial kinetic energy (Table C.1). Therefore, the resolution limitations imposed due to the particles initial kinetic energies, considering for example the kinetic energy distribution in a thermal gas target ($E = 3/2 k_B T$, distributed over all directions homogeneously, 38 meV at 21 °C), are not as severe as those posed by the ion distribution extent in the x-direction.

Finally, an additional tolerance study investigating the effect of the ion distribution starting position mismatch, with respect to x_{nom}, along the x-coordinate has been performed. Using the exact simulation parameters as before (Fig. 4.9), the 1 µm spatial resolution radial extent in the z-y plane is found to first show a decrease from ± 55 µm to ± 50 µm when ions begin at $\Delta x = \pm$ 200 µm from the nominal ion optics focal plane position x_{nom} with $V_{LENS}/V_{REP} = 0.3717$. This change is accompanied with the expected increase/decrease in magnification as previously shown in Fig. 4.6. In any case, as it will be described below, the absolute instrument positioning can be in principle determined and corrected with much higher precision.
In addition to a high-resolution image of the focal ion distribution, the ion microscope provides the ion time-of-flight spectrum on a single-shot basis. The dependence of the ion time-of-flight on the ion mass/charge state and the utilized repelling electrode (REP) voltage (with $V_{LENS}/V_{REP} = 0.3717$), is presented below (Fig. 4.11).

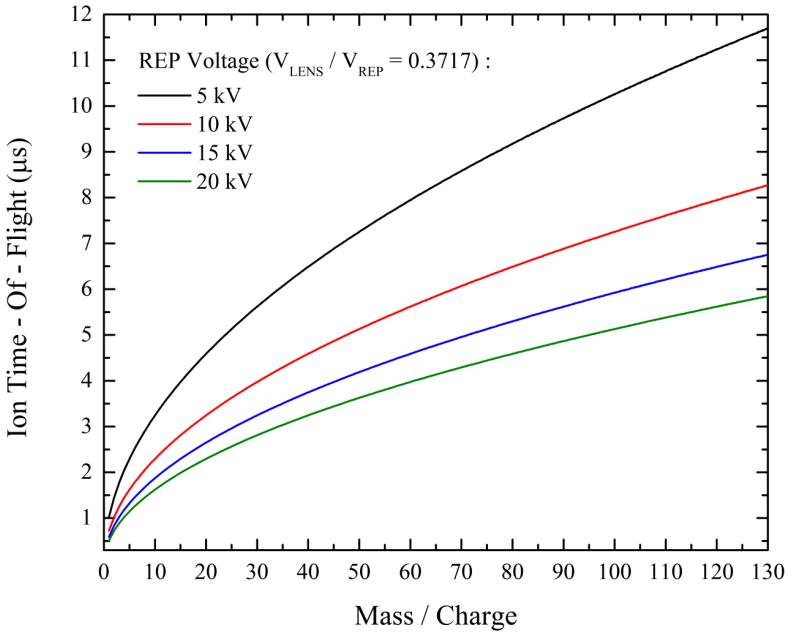

Figure 4.11: Ion time-of-flight as a function of the ions mass/charge ration for different repelling electrode (REP) voltage.

Using the above simulated curves, the ion time-of-flight spectrum can be routinely calibrated in the laboratory. This can be performed by comparing the time difference between two ion peaks corresponding to two different ionic species within the same TOF spectrum. An excellent agreement has been found between the simulated curves and the experimentally observed ion TOF peak difference in a multitude of experiments using different gas targets. Furthermore, the TOF spectrum information is instrumental in accurately positioning the ion microscope along the x-axis, with use of the three-axis linear positioning stage. This is achieved by tuning the ion microscope x-axis position and matching the observed ion peak time-of-flight difference between two distant ion peaks with the simulated time-of-flight difference obtained for an ion distribution starting at the design position $x=x_{nom}$.

When this is achieved, the measured magnification ($M_{exp.} = 25.08 \times \pm 0.67\times$, Fig. 4.15) is found to be in excellent agreement with the simulated theoretical value ($M_{theor.} = 24.5\times$), verifying the validity of the SIMION simulated ion trajectories and the related simulation results presented in this chapter.
While the experimentally observed ion TOF peak width for a heavy ion (Xe^+), is 10 ns measured at FWHM with a 2 GHz digital storage oscilloscope, a displacement from the nominal ion channel position of $|x - x_{nom}|$=5 µm results in a simulated ion TOF peak shift of approximately 5 ns when using a REP: 10 kV-LENS: 3.717 KV ion optics voltage set. The ion time-of-flight is very sensitive on the ions x-axis starting position, providing the possibility to position the ion microscope with respect to the ion distribution with a precision of at least ± 5 µm in the x-direction.
Complementing the two-dimensional spatial information, the time-of-flight spectrum can be additionally used in order to align the ionizing light beam position along the x-axis coordinate. This feature has been particularly beneficial for the counter-propagating pulse optical setup alignment under vacuum conditions. The two foci, corresponding to each optical branch, can be first matched in the y-z plane, taking advantage of the two-dimensional ion image information and subsequently matched in the x-direction, by temporally matching the two TOF ion peaks corresponding to each of them. This can be realized by blocking the first optical branch, acquiring a TOF spectrum from the second focus and subsequently blocking the second arm and matching the TOF peak corresponding to the ion distribution created by the first focus, changing the beam position with the motorized mirror mount. This has been a very effective alignment strategy, especially during the periods when the experiment was repeatedly transfered to Free-Electron-Laser facilities and back to the laboratory on a monthly basis.

Ion Initial Momentum Imaging Mode

As illustrated both in Fig. 4.7b and Fig. C.4, the optimal performance of the ion optical system described in this section, relies on the ions initial velocity, both in terms of magnitude and direction. When the ions initial velocity vector is non-parallel to the ion optical axis (x), the depth-of-focus (Δx) decreases together with the achievable spatial resolution, with increasing initial ion kinetic energy. This 'chromatic' dependence is further enhanced when the ion optics voltage ratio is detuned from its nominal value. Taking advantage of this limitation in a constructive way, this dependence can be utilized for estimating the ions initial kinetic energy, when the anticipated velocity vector direction is constrained by the physical process under investigation. It should be however noted that this is mainly applicable in cases where the ions initial kinetic energy originates from kinetic energy release following molecular dissociation where the resulting ionic fragments fly along a defined linear axis.
In such a case, molecular photo-absorption leads to dissociation and the excess energy absorbed above the dissociation limit, is converted into kinetic energy release, shared amongst the molecular fragments. In a very simple but illustrative example, the two fragments of a dissociating homo-nuclear diatomic molecule, will equally share the excess energy, flying in two opposite directions.

Optical excitation of the dissociation transition in a randomly-oriented gas sample with linearly-polarized light, will favor molecules whose bond-axis lies parallel to the light-polarization direction if the transition moment lies along the bond axis ($\Delta\Omega = 0$), or alternatively it will favor molecules with their bonds lying perpendicular to the polarization direction, for a perpendicular transition ($\Delta\Omega = 1$). In each case, the resulting fragments will fly with oppositely directed initial velocities, parallel or perpendicular to the light polarization axis. If the two fragments are ionized and the recoil direction is non-coincident with the ion optical axis (x), they will arrive on the ion microscope detector forming two separated ion channel images, with an inter-channel spacing that depends on their initial velocity and the utilized ion optics voltage ratio. This effect can be already predicted by examining the results presented in both Fig. 4.7b, C.4, although they refer to homogeneously, spherically distributed initial velocity directions.
A dedicated set of simulations, using well-defined realistic initial conditions has been performed and the possibility of accessing kinetic energy release information by direct ion imaging has been evaluated. Two sets of singly-charged oxygen atomic ions, originating from a common cylindrical distribution in the interaction region, with an ion cylinder radius of R=3 µm and length L=100 µm, centered at x=x_{nom} and oriented along the light propagation axis (y) have been initially set. The two groups possess an initial kinetic energy of 300 meV each and only differ in their initial velocity direction which is set in the positive z-axis direction (+z) for the first group and the negative z-direction (-z) for the second. The parameter set used in this simulation is not randomly chosen, but rather experimentally adjusted to the anticipated conditions resulting from excitation of the $B^3\Sigma_u^-$ dissociative state of O_2 [279] with a linearly-polarized pulse at 162 nm and subsequent fragment ionization. An in-depth analysis of the excitation scheme and the corresponding experimental details is provided in Chapter 7.

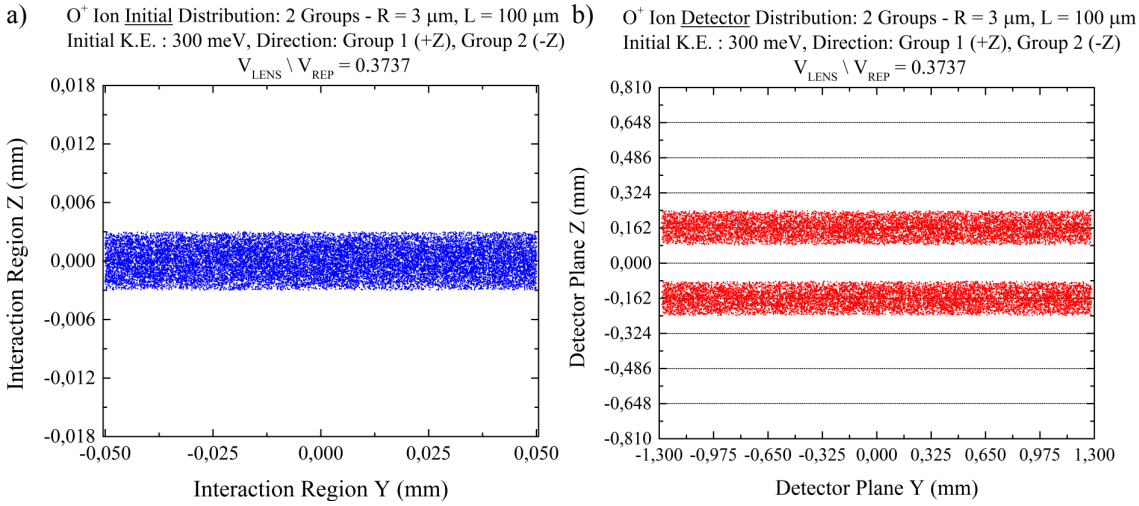

Figure 4.12: Simulated Ion momentum imaging mode: A minor V_{LENS}/V_{REP} ratio detuning (0.3737), results in a spatially separated ion image on the detector plane. Fig. 4.12a) Initial O^+ ion distribution, consisting of 2 equal ion groups, with 300 meV initial kinetic energy directed in two opposite directions in the z-axis (+Z) and (-Z) respectively. Fig. 4.12b) Simulated resulting ion distribution on the detector plane. The ion image appears separated, with the separation distance being proportional to the ions initial kinetic energy.

As a result of the initial velocity distribution, the resulting ion image on the detector plane appears separated along the z-direction, while retaining its initial cylindrical shape. Using the optimal voltage ratio of $V_{LENS}/V_{REP} = 0.3717$, the two ion groups displacement is minute, resulting in a slight, barely observable, broadening in the resulting ion image. By slightly detuning the voltage ratio, to $V_{LENS}/V_{REP} = 0.3737$, facilitating a slight magnification increase, the two ion groups observably separate on the ion image plane (Fig. 4.12). It should be noted that the resulting double ion cylinder image still retains the original ion group cylindrical shape with no additional imaging distortions apart from the slight magnification increase. For the anticipated total kinetic energy release of 600 meV, equally distributed in the two atomic oxygen fragments, an ion channel separation of approximately 324 µm is predicted, when V_{LENS}/V_{REP}=0.3737.
In view of this result, an additional parametric study has been performed, varying either the atomic ions initial kinetic energy at $V_{LENS}/V_{REP} = 0.3737$ or keeping the initial kinetic energy fixed at 300 meV and varying the ion optics V_{LENS}/V_{REP} voltage ratio. The corresponding results are illustrated below (Fig. 4.13).

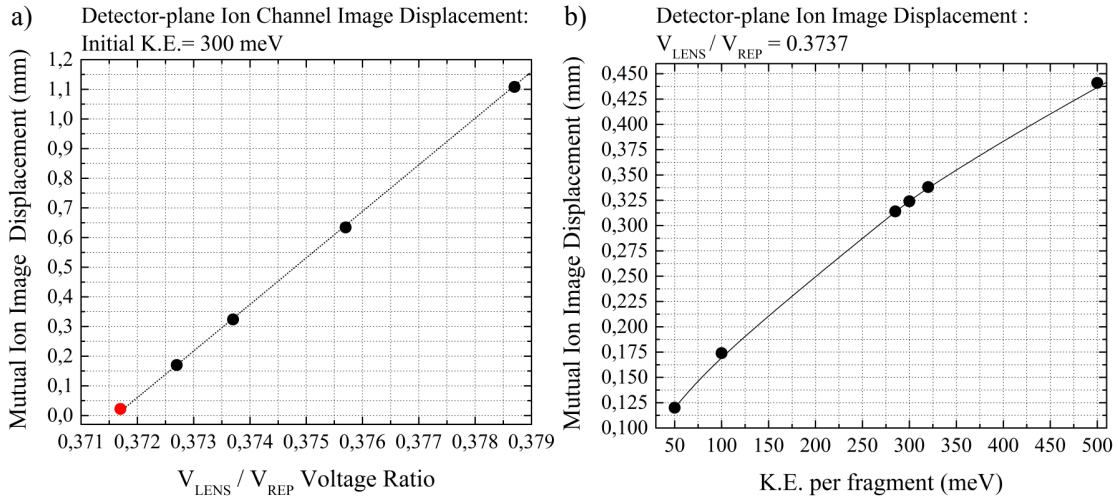

Figure 4.13: Ion momentum imaging mode parametric study results: Ion image separation dependence as a function of a) V_{LENS}/V_{REP} ion optics voltage ratio and b) ion fragment initial kinetic energy. The initial ion distribution definitions are the same as in Fig. 4.12.

The ion image separation increases with higher ionic fragment initial kinetic energy, for a fixed $V_{LENS}/V_{REP} = 0.3737$ ratio (Fig. 4.13b). The achievable kinetic energy resolution, relies on the ability to resolve the two spatially separated ion images and depends on the initial ion distribution dimensions and the spatial resolution of the position sensitive detector. Using the current simulation parameters defined above and using the MCP pore spacing of 12 µm as the ion imaging resolution limit, the kinetic energy resolution reaches ±20 meV in the vicinity of 300 meV, corresponding to the two neighboring points in the plot of Fig. 4.13b.
Furthermore, as evident by the results presented in Fig. 4.13a, further increase in the V_{LENS}/V_{REP} ratio detuning, results in an ion channel image separation increase. The lowest red point, depicts the nominal voltage ratio (0.3717) showing the minimum separation value.

Although a higher voltage detuning results in a larger displacement, pointing to a higher energy resolution, the resulting ion image starts to eventually deform due to ion imaging aberrations. The optimum voltage ratio can be chosen in each particular case, taking into account the specific experimental conditions.
This result, further implies that the voltage set accuracy as well as the voltage stability are extremely important to experimentally utilize this operation mode. Ultra-stable high-voltage power supplies (ISEG CPS Series), have been chosen to charge both electrodes, specified to typically exhibit a 400 mV peak-to-peak voltage ripple, which is not expected to influence the results presented above. Additionally, the control voltage supplied as a regulating input to the high-voltage power supplies is set with an accuracy of 10^{-4} V, monitored with a microvolt digital multimeter, finally resulting in a high-voltage accuracy in the 1 V level. This ensures that the utilized V_{LENS}/V_{REP} ratio can be set with high precision.
As a final remark, it should be stressed that the presented results are specific to this case study, comprising of a specific well-defined two-particle ion fragment recoil geometry. When more complicated ion momentum distributions result from a larger system, a velocity map imaging spectrometer [280], optimized to provide a high-resolution measurement of the ion or electron velocity distribution, is indispensable.

4.4 Data Acquisition and Characterization Results

In this part, a brief description of the ion microscope data acquisition and synchronization system will be given, followed by a series of selected characterization experimental results obtained during the commissioning phase of the instrument, as well as during the main experimental work of this thesis.
As described above, the YAG:Ce scintillator surface where the optical image of the focal ion distribution is formed, is being imaged using a CCD camera (Allied Vision Technologies PIKE - pixel size: 7.4 µm). The CCD camera supports hardware pixel binning (2×, 4× or 8×), which has been utilized in low signal conditions. The CCD data are acquired with a dedicated software suite, developed in National Instruments LabVIEW, which allows for individual-shot data-tagging, incorporating a communication interface to pulse ID data offered both at the free-electron lasers FLASH in Hamburg, Germany and FERMI at Trieste, Italy. An additional LabVIEW routine is used for image data post-processing. As beam-pointing jitter has been present in virtually all the experiments performed, this routine has been developed in such a way that single-shot data could be evaluated individually and sorted according to the particular experimental needs.
Image data acquisition can be performed up to a tested repetition rate of 25 Hz and a proper software synchronization with the trigger signal has been checked and verified, relevant in single-shot experiments when pulse ID tagging is necessary.
The ion TOF spectrum signal is decoupled from the YAG:Ce surface Al coating using an high-pass RC circuit in the direct-imaging mode, or optically retrieved using a photomultiplier tube (Fig. 4.1) in the optical relay-imaging mode. Both the oscilloscope used for the display and storage of the ion TOF spectrum, as well as the CCD camera for imaging

the ion distribution, operate in a triggered mode using a fast electronic trigger signal synchronized with the incoming light pulse. Additionally, a fast TTL pulse trigger signal in combination with a stable pulse/delay generator is used for the synchronization of the pulsed gas valve and the fast high-voltage switching module used for the position-sensitive detector time-gated mode.
As previously described, the detected ion TOF spectrum provides direct information on which specific ion mass/charge states are imaged, as it is obtained directly from the scintillator plate, which is located after the time-gated MCP plate, in both cases. This is an extremely useful feature when operating the detector in a time-gated mode, ensuring that the correct ion species are imaged, by choosing the desired ion peak using the TOF spectrum information online. An example of this kind of operation is shown in Fig. 4.14.

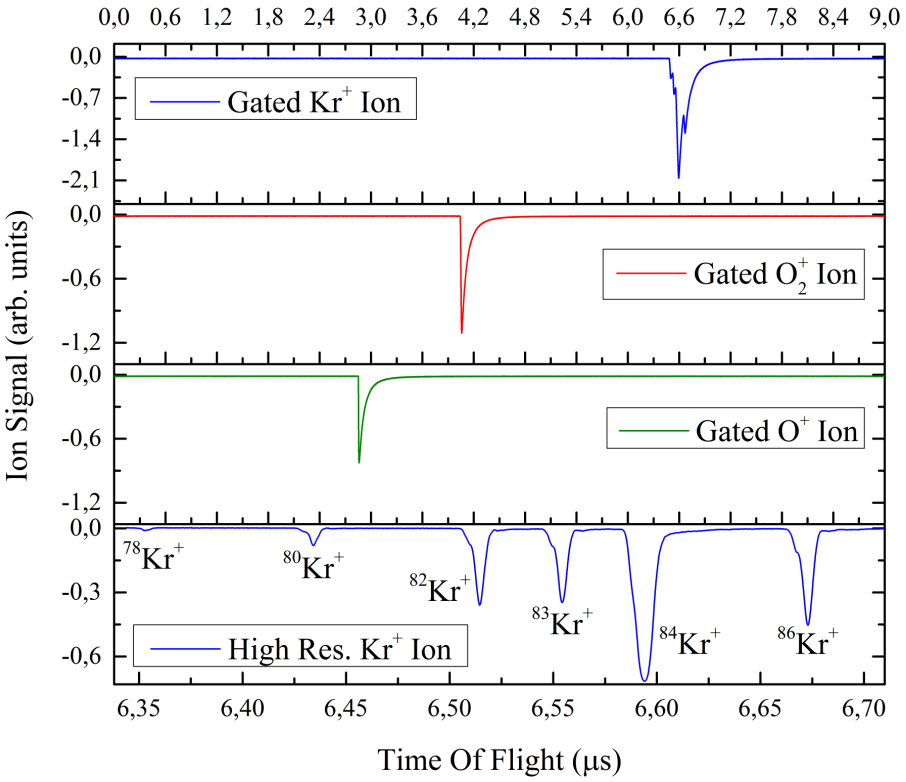

Figure 4.14: Experimentally obtained ion time-of-flight spectrum with a time-gated detector operation at REP: 10 kV. The TOF spectra shown on the three first graphs have been optically acquired using the 1:1 imaging setup with the installed photomultiplier tube whereas the high-resolution Kr spectrum by electrically decoupling the signal from the YAG:Ce crystal surface.

The top three graphs show a TOF spectrum obtained with the photomultiplier tube on the 1:1 imaging optical setup (Fig. 4.1), while the last graph on the bottom shows a TOF spectrum obtained by electrically decoupling the fast signal from the scintillator surface. In this experiment, Kr and O_2 where provided as a gas mixture with the pulsed gas nozzle and have been ionized in a single optical branch of the counter-propagating optical setup, using a short intense pulse at 162 nm. The detector has been operated in a time-gated mode allowing selective Kr^+, O_2^+ and O^+ ion detection by tuning the high-voltage pulse timing

with respect to the time origin, defined by the light-pulse induced electronic trigger signal. Comparing Fig. 4.14 top and bottom graphs, the YAG:Ce light decay time is convoluted with the detector response as can be clearly seen on the obtained TOF spectrum. By directly decoupling the electronic signal from the YAG:Ce crystal surface, the individual isotopes of Kr can be identified in direct correspondence to the information that can be found in the literature [281]. According to the specifications of the fast high-voltage switching module (HV pulse min. width: 9 ns) selective imaging of individual Kr^+ isotopes is possible when this would be desirable, showcasing the mass/charge selectivity capabilities of the detection scheme. This is important for selectively imaging ions with small TOF difference, as for example molecular ionic fragments with difference of one proton mass.
As already discussed, when the position of the ion microscope is set such that the experimentally determined ion TOF is in accordance to the calculated values, the measured magnification is also in very good agreement with the theoretical value. Typically the ion microscope magnification is experimentally determined prior to any measurement that is presented in this thesis and the experimentally determined value is used for further data analysis. The deviation in the daily obtained magnification value is small and it mainly originates from slight deviations in the incoming beam path. A typical example of a magnification measurement is shown below (Fig. 4.15).

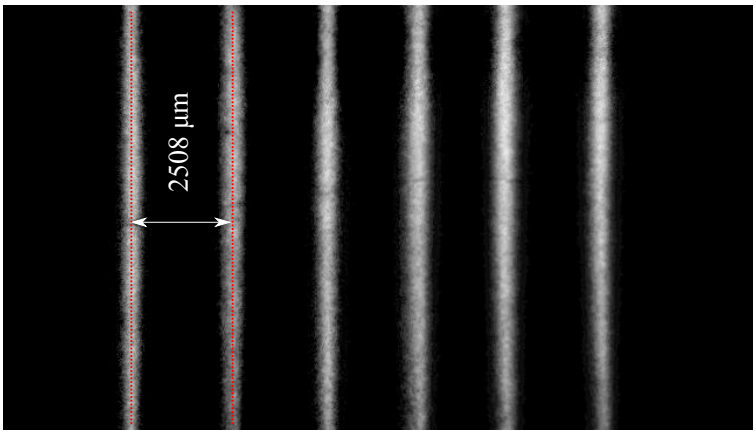

Figure 4.15: Experimental ion microscope magnification determination. The ion microscope is displaced along the z-axis in 100 μm steps using the 3-axis linear position manipulating stage. The ion channel position difference on the detector corresponds to 2508 μm per 100 μm displacement, or equivalently to a magnification factor of $M_{exp.} = 25.08\times \pm 0.67\times$ for the displayed dataset.

The ion microscope magnification is measured by advancing the ion microscope position with respect to the ionizing light beam, using the linear positioning stage (VAb PM 112), in 50 µm or 100 µm steps along the z-axis (measurements along the y-axis give the exact results) and recording the ion image position. A combined Kr^+ ion image, where the ion microscope is moved in 100 µm steps, is shown in Fig. 4.15. The distance per 100 µm displacement step is 2508 µm, taking into account the CCD pixel size (7.4 µm) and the measured demagnification imposed by the camera objective (0.48×), corresponding to a measured ion microscope magnification of $M_{exp.} = 25.08\times \pm 0.67\times$. This value is in excellent agreement with the SIMION simulation result of 24.5× (Eq. 4.2).

The magnification uncertainty is dominated by the ion microscope absolute position uncertainty. The fitting and statistical errors are insignificant in this case, however the reported uncertainties are calculated by adding all the fractional uncertainties in quadrature. The magnification measurement presented above has been performed using a single optical branch of the 162 nm counter-propagating pulse experimental setup, exciting a direct two-photon ionization transition in Kr with an intense VUV pulse at 162 nm[1]. The generation and optimization aspects of the intense VUV light source based on high-harmonic generation, will be described in the following chapter in detail.
The ion imaging behavior of the ion microscope has been investigated initially using a dilute Kr gas target, supplied with a precision gas dosing valve (Pfeiffer Vacuum), homogeneously filling the vacuum chamber. A single optical branch of the 162 nm counter-propagating pulse optical setup was used to ionize the Kr gas, 3.2. The measured pulse energy on target, taking into account the corresponding optical transmission characteristics [3.2], was (92.4±9.6) nJ. The resulting focal ion distribution image, obtained for different ambient pressure values is illustrated in Fig. 4.16. The presented images correspond to position-sorted averaged datasets over 1000 pulses. Position-sorting is necessary to avoid beam position jitter effects on the average image and it is achieved by fitting a Gaussian curve on the vertically-summed horizontal image profile. The beam axis is defined by the fitted Gaussian curve peak. Subsequently, an average image is formed by matching the respective fitted beam propagation axes. The jitter in this case was minute and the single-shot fitted Gaussian curves showed the exact characteristics as the sorted average image. A single-shot dataset is also presented here (a1) as a reference.

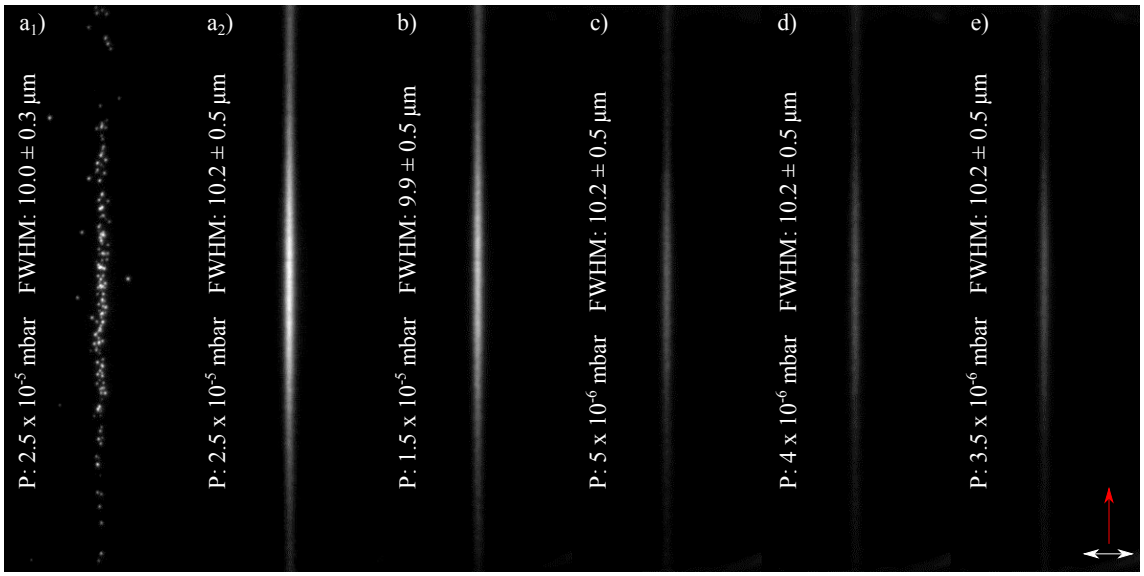

Figure 4.16: Kr^+ ion channel recorded using a single optical branch of the counter-propagating autocorrelation optical setup as a function of the vacuum chamber ambient pressure. The pressure is precisely adjusted using a gas dosing valve (Pfeiffer Vacuum). The measured ion channel width of: 10.2 µm ± 0.5 µm at FWHM shows no variation within this pressure range. Red arrow: propagation direction, white arrow: polarization direction.

[1] A detailed description is given in Section 3.2

The measured magnification, obtained in a similar manner as in 4.15, corresponds to $M_{exp.}=(24.1 \pm 0.6)$. The data were obtained in an ion time-of-flight gated mode, although no residual background gas contributions were noticeable in the TOF spectrum.
The reported gas pressure values, refer to the measured ambient pressure, obtained with a Bayard-Alpert type sensor (Leybold Ionivac ITR 90), after being corrected with the manufacturers calibration factor (0.5) for Kr gas [282]. The experimental vacuum chamber base pressure was at 5×10^{-8} mbar prior to external gas supply.
The measured Kr^+ ion channel width corresponds to 10.2 µm ± 0.5 µm measured at FWHM and does not deviate in the pressure range between $3.5 \cdot 10^{-6} - 2.5 \cdot 10^{-5}$ mbar. Thus any possible space-charge effects, connected with the varying ion density, are excluded in this pressure range. The channel width is obtained by fitting a Gaussian curve on the intensity line-out at the most intense part of the focal distribution. For the presented dataset the same value is also obtained when fitting a Gaussian over the complete image horizontal average profile.
Assuming a Gaussian beam profile and taking into account that the signal results from a two-photon process (Fig. 5.8), the actual beam diameter (FWHM) is expected to be $\sqrt{2}$ times wider than the measured channel width[2]. This results to an actual beam diameter of 14.4 µm ± 0.7 µm, being approximately 3.5 times larger than the simulated value of 4.14 µm (3.6).
A possible ion image broadening due to the position-sensitive detector resolution must be assessed in that case. Although the detector was not characterized using a known reference pattern during the presented experimental work, an estimation can be given by measuring the spatial extent of a single event on an individual shot dataset, as for example in $4.16a_1$. Choosing the region away from the beam waist, where individual events can be isolated, a series of fit evaluations has been performed for a sequence of images, resulting in an average imaged spot diameter of 76 µm ± 15 µm per individual event. Taking into account the ion microscope magnification, this value results in a spatial resolution of 3.1 µm ± 0.6 µm in the ion imaging object plane, or the interaction region. Thus, the imaged width of an ion distribution with an actual width of 4.14 µm (FWHM) will be [3] $d_{\text{im}} = \sqrt{(4.14\,\mu\text{m})^2 + (3.1\,\mu\text{m})^2}$=5.17 µm which is not the case here. The observed channel width is not influenced by resolution limitations posed by the position-sensitive detector, which only contribute to a change within the stated uncertainty for a 10.2 µm ion distribution width. Finally, averaging effects can be also excluded in this case, as the single shot image has the exact width. The measured width is considered to be the actual beam width attributing the difference with the simulated value to the 162 nm beam quality.
In summary, an ion-imaging time-of-flight spectrometer has been designed, implemented and characterized utilizing an intense VUV pulse and a low-density noble gas target. The validity of the simulation results is verified by the well-behaved ion image, exhibiting a measured magnification in excellent agreement to the simulated value combined with an ion time-of-flight accuracy within few ns. The ion microscope, when desired, can operate in mass/charge selective imaging mode enabling ion charge-state selective imaging, thus fulfilling the detection prerequisites for a single-shot autocorrelation measurement in the VUV-XUV spectral range.

[2] Detailed discussion in Ch.2.1
[3] In direct analogy to the results discussed in Fig. 2.3.

5 Intense Vacuum-Ultraviolet Pulse Generation

Within the framework of this thesis, a light-source based on high-harmonic generation (HHG) utilizing a Ti:Sapphire driving laser pulse, has been designed and implemented. The experimental apparatus has been designed, such that the HHG source parameters can be easily adapted and optimized for different spectral regions and that future development changes can be easily accommodated. Aiming in the investigation of ultrafast atomic and molecular dynamics in the vacuum-ultraviolet (VUV), the optimal experimental parameters for generating an intense 5^{th} harmonic pulse at 161.8 ± 0.3 nm (7.66 ± 0.15 eV) has been investigated.

Typically, molecular electronic excitations lie in the deep-ultraviolet to vacuum-ultraviolet (DUV-VUV) spectral region and in many cases the corresponding dynamics evolve in the sub-picosecond timescale [4]. Intense, ultrashort pulses in the vicinity of 160 nm are advantageous for performing time-resolved studies of ultrafast molecular dynamics, where many prototypical examples of ultrafast dynamics in organic and atmospherically relevant molecules can be found and typically evolve within few tens of femtoseconds [30, 31, 44–46, 51, 52]. Furthermore, the availability of short, energetic pulses in this spectral region enables the extension of multiphoton spectroscopy [3] in the VUV.

Considerable effort has been directed towards generating intense short pulses in the 160 nm range over the past years. Below 200 nm, frequency conversion using non-linear crystals becomes inefficient due to transparency and phase-matching limitations [283]. Using noble gases as the generating medium, a variety of different approaches, based on four-wave difference-frequency mixing (FWDFM) or high-harmonic generation have been followed. Employing near- and off-resonance FWDFM schemes, the obtained VUV pulse durations evolved from 450 fs at 155 nm [284], to 160 fs at 161 nm [285], while more complicated arrangements led to energetic 43 fs pulses [285] and recently sub-20 fs, 410 nJ pulses [286]. Utilizing a short-pulse Ti:Sa laser system delivering 12 fs IR pulses, 11 fs 5^{th} harmonic pulses at 162 nm were generated, although their energy content was limited to 4 nJ [287]. In this work, motivated by previous findings on high-harmonic energy scaling [17–19], a loose-focusing geometry in conjunction with a long gaseous medium has been utilized for generating an ultrashort, intense 5^{th} harmonic pulse.

A detailed description of the experimental apparatus for the generation and characterization of the intense 5^{th} harmonic pulse is provided in this chapter together with the experimental results.

5.1 Femtosecond Laser System

The infrared (IR) femtosecond pulse driving the high-harmonic generation process is supplied by a commercial laser system (Amplitude Technologies - Pulsar), based on the chirped pulse amplification principle [288]. Briefly, an ultrashort laser pulse from a laser oscillator gets temporally stretched, in order to avoid nonlinear damage mechanisms in the amplifying solid-state medium, where it gets amplified by several orders of magnitude and finally it gets temporally compressed again, ideally back to its initial duration.
The solid-state gain medium for both laser oscillator and optical amplifiers described here, is a titanium-doped sapphire crystal (Ti:Al_2O_3 or Ti:Sa). As a lasing medium, it exhibits a very broad amplification spectral profile centered at 800 nm, combined with excellent thermal conductivity and a long upper level lifetime [289]. This features make Ti:Sa a favorable gain medium for generation and amplification of extremely short and intense laser pulses, nowadays enabling commercial systems to deliver sub-10 fs laser pulses reaching petawatt peak power.
The Ti:Sa laser system utilized in this work, delivers horizontally-polarized (p-polarized) IR laser pulses at a 25 Hz repetition rate. The pulse carrier wavelength is at 805 nm and its spectral width reaches approximately 28-30 nm at FWHM (Fig. 5.1a), mainly limited by gain-narrowing during amplification. The pulse duration is 43 ± 3 fs at FWHM, although recently shorter pulses in the order of 35 fs have been obtained using the same spectral output. The difference lies in the pulse compression as will be explained later. The individual pulse energy reaches 15 ± 0.3 mJ and the beam diameter is measured to be about 15 mm at $1/e^2$ of the Gaussian profile.
The laser system consists of a commercial laser oscillator (Femtolasers Synergy) [290], operating at a repetition rate of 75 MHz, pumped by a frequency-doubled, continuous-wave Nd:YAG laser (Coherent Verdi). It delivers pulses with a spectral width of 90 ± 5 nm FWHM, corresponding to a bandwidth-limited duration of 10 fs FWHM and a pulse energy typically in the range of 5 ± 1 nJ per pulse. The oscillator pulses are first temporally stretched, using an all-reflective Öffner triplet optical stretcher configuration [291] and subsequently propagate through an acousto-optic programmable dispersion filter (Fastlite Dazzler), which is used for dispersion compensation.
The stretched pulses enter a Ti:Sa regenerative amplifier operating at 1 kHz repetition rate, pumped by a Q-switched, frequency-doubled, diode-pumped Nd:YAG (Photonics Industries) laser and are amplified to approximately 0.7-0.8 mJ per pulse. At a second stage, 25 pulses/s are picked and further amplified in a Ti:Sa multi-pass amplifier, pumped by a Q-switched, frequency-doubled, flashlamp-pumped Nd:YAG (Big Sky) laser. The remaining pulses are amplified in a second multi-pass amplifier, sharing the same Nd:YAG pump laser with the regenerative amplifier, reaching 3 mJ at 1 kHz with approximately the same duration. The 1 kHz branch of the laser system will not be further discussed, as it has not been utilized in this work.
After amplification, the pulses in the 25 Hz branch, are temporally compressed with a diffraction grating pair to typically 43 ± 3 fs FWHM, reaching a pulse energy of 13-15 mJ with a measured energy fluctuation in the order of ± 0.3 mJ.

Optionally, an achromatic $\lambda/2$ retardation plate (with $< \lambda/100$ retardation deviation over the complete bandwidth) is used prior to the grating compressor, taking advantage of the diffraction efficiency difference between s and p polarization, as the most effective way to attenuate the p-polarized IR pulse without any measurable effect on the pulse temporal characteristics.

The laser system is accompanied by a commercial pulse temporal characterization system (APE SPIDER), based on self-referencing spectral interferometry [165], used for pulse temporal characterization and optimization. The spectral phase information obtained by the SPIDER measurement is fed as an input to a dedicated software suite, supplied by the laser system manufacturer, that provides an optimized waveform to the acousto-optic programmable dispersion filter (AOPDF). Residual chromatic dispersion accumulated during the amplification process can be compensated using the SPIDER apparatus feedback iteratively, in order to reach an almost bandwidth-limited pulse duration at the compressor exit. Although, group-delay dispersion (GDD) can be effectively compensated with the grating-pair compressor, third and higher order dispersion terms are only minimally influenced, requiring an optimized AOPDF operation for reaching an optimally compressed pulse at the systems output.

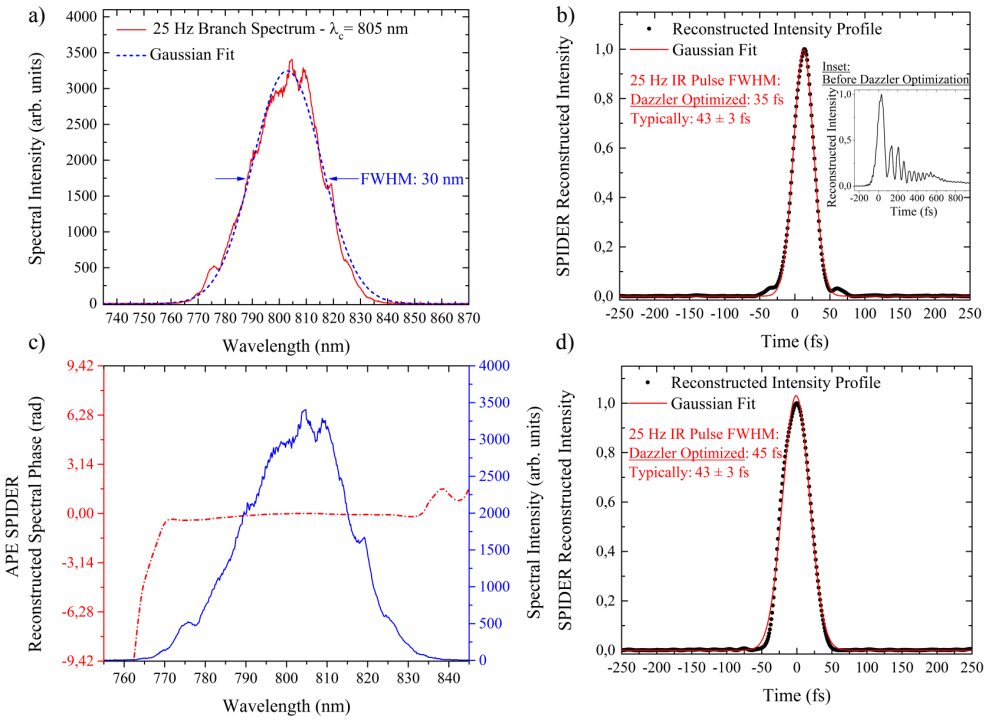

Figure 5.1: Compressed IR pulse spectrum and SPIDER reconstructed intensity profile:
5.1a) Spectrum measured at the 25Hz compressor output - central wavelength: 805 nm, spectral bandwidth: 28-30 nm FWHM,
5.1b) APE SPIDER reconstructed temporal intensity profile after optimization using the Dazzler AOPDF providing a 35 fs FWHM pulse, inset graph: before optimization
5.1c) Spectrum and APE SPIDER reconstructed spectral phase corresponding to a 45 fs FWHM shown in d
5.1d) APE SPIDER reconstructed temporal intensity profile after optimization using the Dazzler AOPDF providing 45 fs FWHM.

As illustrated in Fig.5.1b, use of the pulse compression algorithm in combination with the Dazzler AOPDF can result in a pulse duration reaching 35 fs FWHM, almost as expected at the bandwidth limit (Gaussian FWHM - 34.04 fs for 28 nm bandwidth). Nevertheless, the pulse duration typically obtained on a daily basis, has been in the range of 43 ± 3 fs. The output SPIDER reconstructed spectral phase is similar in both cases, indicating an appropriately compressed pulse. This misbehavior is mainly attributed to the limited SPIDER apparatus dynamic range resulting to incomplete information in the spectral wings, possible AOPDF optimization algorithm issues, or possible undetected SPIDER calibration spectrum issues [188]. Due to the fact that the pulse compression optimization relies on the SPIDER output spectral phase, which is fed as an input in the corresponding AOPDF algorithm, the spectral phase reconstruction quality directly influences the laser pulse temporal characteristics.
Two different measurement examples are illustrated in Fig. 5.1b, 5.1c, and 5.1d. In the first case (5.1b), the reconstructed intensity temporal profile, given as a SPIDER measurement output, corresponds to an optimized 35 fs pulse, exhibiting an almost flat spectral phase distribution (not shown). The reconstructed intensity profile shown in the graph inset is obtained prior to optimization with the dedicated Dazzler AOPDF software algorithm.
Following the same optimization procedure on a different instance and obtaining again a flat spectral phase distribution as a SPIDER measurement output (Fig.5.1c), the reconstructed pulse temporal profile exhibits a temporal width of 45 fs FWHM (Fig.5.1d) although it exhibits a similar spectral intensity distribution. Trying to further compress the pulse, using the AOPDF optimization algorithm does not provide any change in the reconstructed profile.
As commonly experienced when operating multi-component, TW-class, femtosecond laser systems, the overall system performance is subject to the laboratory environment influence, as for example the laboratory climate stability. Although, the external influence has been minimized to a large extent, frequent maintenance and daily fine alignment in each sub-part of the laser system was necessary in order to daily achieve optimal performance. These tasks have been carried out by the author over the period of the reported experimental work.

5.2 High-Harmonic Generation

The experimental setup for generation and characterization of high-harmonic radiation (HHG), driven by the femtosecond laser pulse described in the previous section comprises of three distinct segments, all under vacuum conditions, separated by differential pumping stages. The three different segments correspond to three separate vacuum chambers that enclose the corresponding instrumentation and each of those will be described in detail separately.
The complete experimental layout is presented in Fig. 5.2. The red section shows the Ti:Sa laser system footprint, described in detail in the preceding section and the part entitled as ExpChamb corresponds to the single-shot metrology apparatus.

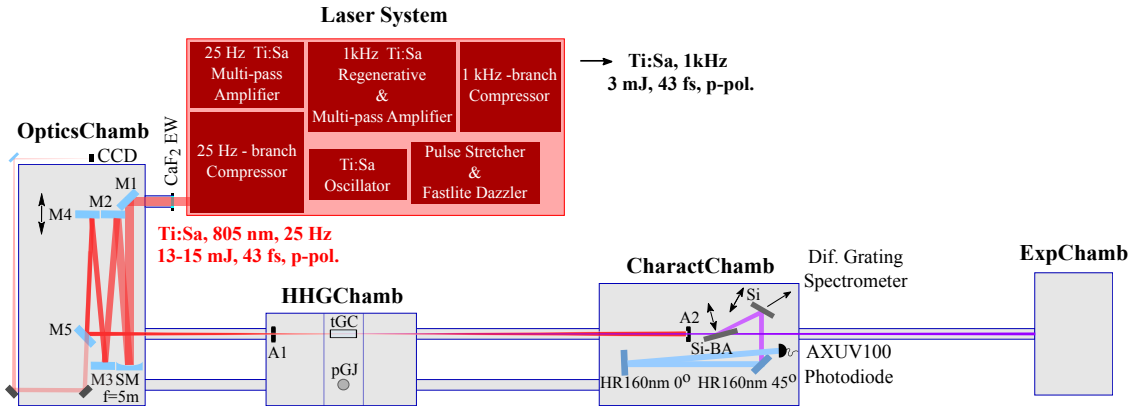

Figure 5.2: Complete experimental setup.

The first segment, devoted to steering and focusing the intense IR pulse beam in the high-harmonic generation area, is hosted in a vacuum chamber (Fig.5.2: OpticsChamb, Fig.5.3) enclosing the required optical components. This part of the experimental setup needs to be evacuated due to the fact that the IR pulse is already reaching a high intensity level prior to the focal region, inducing nonlinear effects in air which are expected to spoil the spatio-temporal pulse profile. The vacuum requirements are relaxed, with the pressure kept in the range of 10^{-4} mbar. The compressed IR pulse propagates for less than 2 m in air before entering the vacuum chamber through a 1.5 mm thick, anti-reflection coated, CaF_2 window (CVI-Melles Griot). The material choice and thickness of the entrance window is very important in order to avoid effects associated with the nonlinear refractive index of the material, such as Kerr-induced self-focusing and self-phase modulation. CaF_2 was chosen due to its low nonlinear refractive index in the minimum thickness possible, being constrained by the force applied on the window by the 1 bar pressure difference.
After entering the chamber, the pulse first encounters a 45° dielectric folding mirror (M1) and it is further directed on a f = 5000 mm spherical mirror (SM) used for focusing the beam in the high-harmonic generation area. A set of 4 dielectric mirrors (M2-M6) are used after the spherical mirror for folding the beam path before the focal position due to space restrictions. The horizontal/vertical tilt degrees of freedom for two of them are accessible under vacuum conditions, with the use of rotational vacuum-feedthroughs coupled to an improvised rotational motion control system based on tachometer cable, transferring motion to the mirror mount control knobs. In this way, daily fine-alignment of the IR beam path can be accomplished and long-term position and pointing drifts can be compensated without having to vent the system. One of the normal-incidence dielectric mirrors (M4) in the folding set is fixed on a vacuum-compatible linear translation stage (MOVTEC L60), providing focal position adjustment over 150 mm. Both the folding mirrors, as well as the spherical mirror are specified (Laser Components GmbH) for high reflectivity at 800 ± 40 nm ($R > 0.99\%$) combined with a very high damage threshold (0.5 Joule/cm^2 for a 150 fs pulse). The experimental transmission factor, over the complete optical system, was measured to be $T = 0.87 \pm 0.02$.

The measurement has been repeated for different IR pulse power, in order to exclude any systematic uncertainties and no deviations have been observed. The transmission factor is lower than the theoretical value of T = 0.94, due to the slight incidence angle deviations, being nevertheless within the manufacturer specifications tolerance margin.
A minute infrared light leakage through the dielectric coating of the last folding mirror (M5), is propagated to an external CCD camera, over a set of two silver coated mirrors (M6-M7) and a glass wedge-shaped plate (GW) serving as a reflective attenuator. By matching the optical path length to the spherical mirror focal distance, the focus of the IR pulse is available on a shot-to-shot basis, providing a real-time monitor utilized for beam alignment under vacuum conditions. It is also currently planned to be used as a beam-pointing feedback for implementing an automatized positioning system by motorizing the mirror mount.

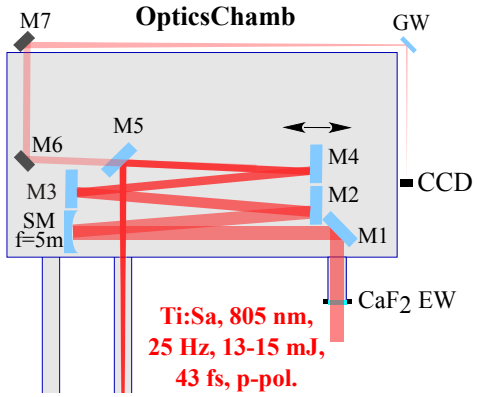

Figure 5.3: Optical component vacuum chamber: CaF_2 EW:1.5 mm thick Calcium-fluoride entrance window, M1-M5: 800 nm high-reflectivity dielectric mirrors, M4 mirror fixed on MOVTEC L60 linear translation stage, SM: spherical mirror(f=5 m), M5-M6: Al-coated mirrors, GW: wedge-shaped plate, CCD: focal-point imaging CCD camera.

Taking into account a Gaussian beam and the measured transmission factor of 0.87, the calculated intensity in the focus corresponds to 3×10^{14} W/cm^2 with a $\sim 342\,\mu$m FWHM beam diameter and a confocal length of approximately 22.7 cm.
The focal spot position is located in the second experimental segment, located in the second vacuum chamber (Fig.5.2: HHGChamb, Fig.5.4: HHGChamb), in the center of a length and position tunable, statically filled gas cell (tGC). The gas cell provides the medium where high-harmonic generation takes place. The experimental parameters that directly influence the macroscopic aspects of the high-harmonic generation process in the gas medium, such as the medium length and density can be precisely tuned, in order to achieve optimal phase-matching. The gas cell has a tunable-length (0-150 mm) tube with laser-pulse drilled pinholes on both sides and an additional cylindrical enclosure which provides a first differential pumping stage. Length variation is achieved by two tightly fitting concentric tubes, enclosing the cell volume, sliding within each other by means of a linear translation stage. The concentric tube system is made leak-tight with a thin layer of vacuum-compatible lubricant (Fomblin PFPE) applied between the tubes. In this way, the cell length can be continuously tuned under vacuum, providing the possibility to optimize the high-harmonic generation conditions in-situ.

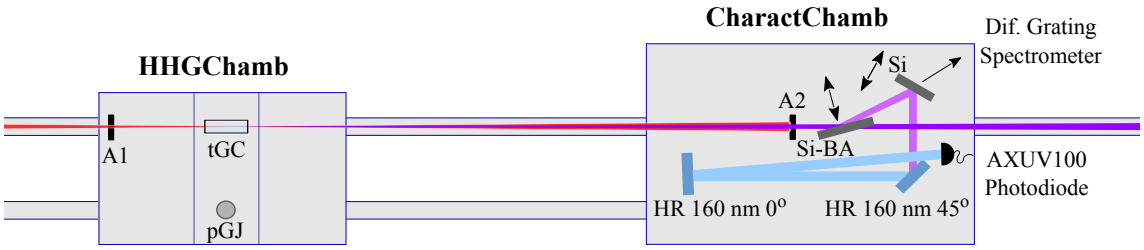

Figure 5.4: High-harmonic generation and characterization chambers: A1, A2: Alignment assisting apertures, A2 used also for blocking residual IR light after HHG, tGC: Position and length (0-150 mm) tunable gas cell, SiBa: Si Mirror at Brewster's angle, Si: Si mirror (incidence $\sim 30°$), HR160nm: dielectric mirrors $R(160 \pm 4)\text{nm} > 0.9$, AXUV100: IRD AXUV 100G calibrated XUV photodiode.

The cell pressure can be set by means of a gas dosing valve and monitored with an implemented pressure gauge. The gas cell area, which handles a considerable gas load, is efficiently separated from the surrounding vacuum system. The chamber is split in three parts which are linked by sub-mm pinholes drilled by the propagating intense IR pulse on aluminum foils in the same manner as at the gas cell ends. The windowless differential pumping scheme, effectively separates the three distinct experimental areas maintaining high-vacuum conditions in the area behind the gas cell. At typical operation conditions, the pressure in the optics area (OpticsChamb) is kept below 5×10^{-4} mbar, whereas the area in front of the gas cell is maintained to below 3×10^{-1} mbar. Behind the gas cell, the pressure values do not exceed 10^{-6} mbar both for maintaining safe conditions for high-voltage instrumentation used in the experimental area (ExpChamb) as well as for minimizing light reabsorption by the generation medium.
After exiting the cell, the co-propagating fundamental and high-harmonic beams reach the third experimental segment (Fig.5.2, Fig.5.4: CharactChamb), devoted to high-harmonic radiation diagnostics. In this chamber both beams first encounter a limiting aperture (A2) where the outermost part of the more divergent fundamental beam is blocked and subsequently they can either continue propagating to the final experimental chamber (Fig.5.2:ExpChamb), located approximately 11.6 m downstream after the HHG gas cell, or reflected within the chamber for characterization purposes. This is accomplished by inserting a movable Si mirror (Si-BA) fixed on a precise linear translation stage. The copropagating fundamental and high-harmonic beams are separated by a silicon mirror aligned at the Brewster's angle for the fundamental (Fig.5.4: Si-BA), in addition to the aforementioned limiting aperture (A2) blocking the outermost part of the more divergent fundamental beam, at a distance of ~ 2.7 m from the cell. The reflectivity of the Brewster's Si mirror, taking into account the native oxide layer, is calculated using the XOP-IMD software [224] to be in the order of 1×10^{-4} for the fundamental, 0.65 for the 5^{th} harmonic, and between 0.33 - 0.69 for the rest odd harmonics, as described previously (Fig. 3.3), including the observed 33^{rd} order which corresponds to the cut-off frequency.
The 5^{th} harmonic pulse energy is determined using an XUV calibrated photodiode (IRD AXUV-100G).

Two multilayer dielectric stack mirrors (HR160nm), optimized to reflect the 5th harmonic (Layertech GmbH, $R_{160\pm4\ nm}$ >90%, GDD <20 fs^2) are used to separate it from residual fundamental and harmonic radiation ($R < 5 \times 10^{-2}$). In combination with a Si (Fig.5.4: Si) mirror fixed in a linear translation stage, the spectrally purified 5th harmonic pulse is directed to the XUV photodiode, with an overall transmission of 0.33 at 162 nm and $<2 \times 10^{-6}$ for the residual radiation.
The XUV calibrated photodiode signal is recorded with a digital storage oscilloscope triggered by the rising slope of a fast IR photodiode signal. The IR photodiode is located in the laser compressor and detects stray light providing a stable fast-rising signal which is used as a global trigger for all the detectors that are used in this experimental work. The XUV calibrated photodiode quantum efficiency corresponds to QE = 0.93 according to the specification sheets provided by the distributor (http:/optodiode.com/library.html, [292]) and combined with the optical transmission factor can provide the 5th harmonic pulse energy. This value can be directly derived from the area (nVs) of the corresponding signal peak recorded with the oscilloscope as follows:

$$E_{5^{th}H}(nJ) = T_{5^{th}H} \cdot \left(\frac{nVs}{50\Omega}\frac{1}{e} \cdot \frac{1}{QE}\right) \cdot \left(\frac{7.66\ eV}{photon}\right) \cdot e \cdot \frac{Joule}{eV} \tag{5.1a}$$

$$E_{5^{th}H}(nJ) = 0.5747 \cdot \text{ Oscilloscope Peak Area (nVs)} \tag{5.1b}$$

The first term in 5.1a ($T_{5^{th}H}$) takes into account the optical transmission over the mirrors used to steer the beam to the XUV photodiode. The second and third terms describe the conversion of the peak area to number of electrons, which are subsequently converted to number of photons using the quantum efficiency of the XUV photodiode, along with the photon energy at the 5th harmonic measured wavelength of 161.8 nm (7.66 eV) and the oscilloscope input impedance (50 Ω). Finally, the last term converts this value to eV and finally to nJ. The scattered infrared radiation background signal is minimized by protecting the XUV photodiode detection area using a long anodized tube equipped with an adjustable entrance aperture, restricting the light collection angle to the highly-directional 5th harmonic beam path. The infinitesimal residual signal from scattered infrared light is measured with an evacuated gas cell and gets subtracted from the final measurement.
Alternatively, when removing the Si mirror from the beam path, the high-harmonic beam is directed towards a diffraction grating spectrometer. The spectrometer has been set-up and commissioned by F. Karimi during his M.Sc. thesis work [293] related with spectral characterization of the high-harmonic beam, but as it has not been utilized in the reported experimental work, it will not be discussed in more detail here.

5.3 Intense Fifth-Harmonic Pulse Generation

The optimal generation conditions leading to an intense sub-20 fs 5th harmonic pulse have been investigated. Additionally, the ion microscope and the 162 nm counter-propagating pulse optical setup have been employed for complete characterization of the 5th harmonic pulse properties.

The experimental results, connected with a complete parametric study performed for defining the most favorable 5^{th} harmonic pulse generation and investigating the intensity scaling behavior of the experimental scheme will be described in this section.
Using Ar as a high-harmonic generation medium and by optimizing the cell length and gas pressure (tGC), up to 1.1 μJ per pulse has been obtained at the source, corresponding to 9×10^{11} photons/pulse, and a conversion efficiency of 10^{-4} reaching the highest peak power reported in the literature so far for a sub-20 fs 160 nm pulse. The pulse energy was measured using the IRD AXUV-100 photodiode, taking into account the corresponding calibration characteristics as discussed above and by subtracting the infinitesimal residual signal from the fundamental beam measured with an evacuated cell. The optimum cell length was 5.5 cm and the corresponding gas pressure $\sim$ 50 mbar.
While maintaining identical experimental parameters for all the cases discussed below, a gas cell pressure and length study has been performed, using Ar or alternatively Xe gas as a generating medium. For each different cell length, the gas cell pressure was varied continuously and the corresponding 5^{th} harmonic pulse energy has been recorded. The results of the gas cell pressure dependence on the obtained 5^{th} harmonic pulse energy for two different representative cell lengths, namely 5.5 cm and 10 cm for both the cases of Ar and Xe are presented in Fig. 5.5.
Using Ar as a generating medium, the maximum output flux is observed with a 5.5 cm cell, following a constantly increasing trend. The maximum gas cell pressure attainable is limited by the current pumping capabilities. The decreased output flux observed for a longer cell is attributed to loss of phase-matching due to dispersion in the longer generating medium. Absorption at 162 nm is negligible as the photon energy is below the ionization threshold of Ar and away from any possible resonance.

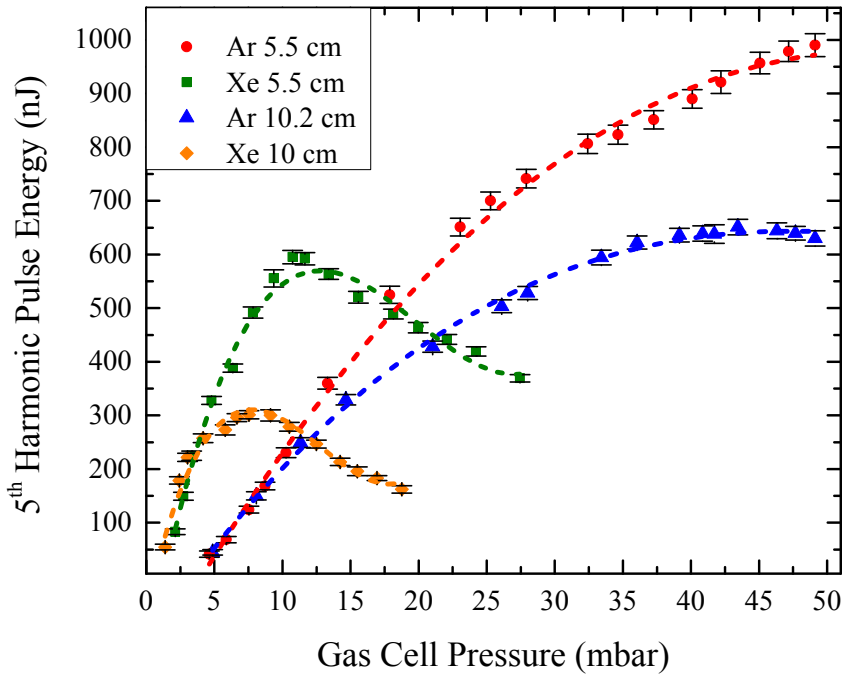

Figure 5.5: Fifth-harmonic pulse energy as a function of gas cell, length and pressure for Ar and Xe. As shown in [294].

When Xe gas is used, the 5th harmonic pulse energy first increases at a lower gas cell pressure compared to Ar and subsequently drops as a result of excessive ionization in the medium, altering the phase-matching conditions significantly. A combination of parameters employing a shorter cell or a reduced-intensity driving pulse were not found to deliver a 5th harmonic pulse energy content comparable to that obtained with Ar at 5.5 cm cell length in both cases. It is also worth mentioning that the 5th harmonic pulse duration obtained as a function of the gas cell pressure in the case of Ar showed no variation within the corresponding uncertainty interval.
Furthermore, the intensity dependence of the 5th harmonic pulse as a function of the driving laser pulse intensity is presented in Fig. 5.6 on a logarithmic scale. For all the measurements reported here, the Ti:Sa fundamental pulse duration was monitored and found to remain constant with varying pulse energy. The 5th harmonic pulse energy grows with the 5th power of the driving pulse intensity as expected in the perturbative limit, although at higher intensities the slope gradually decreases, showing saturation effects.

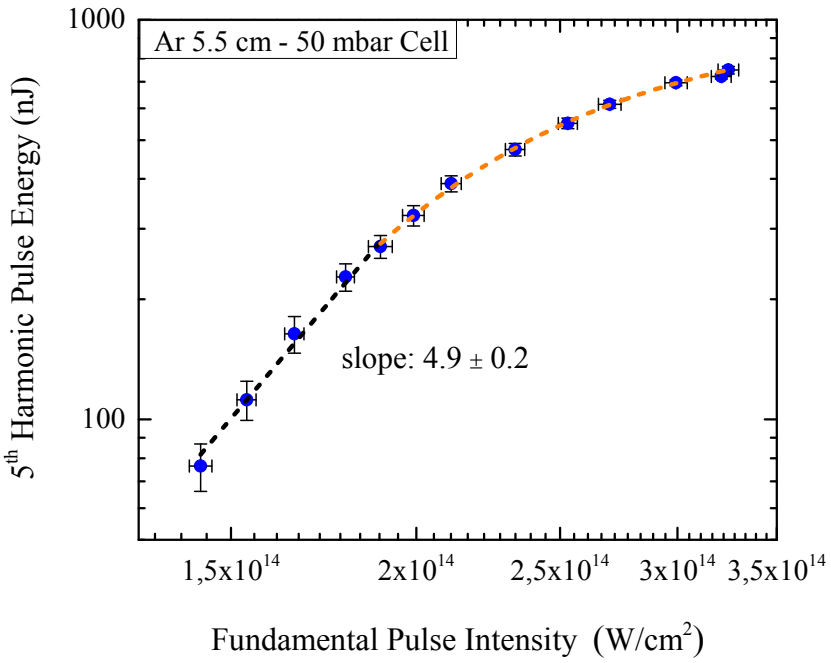

Figure 5.6: Fifth-harmonic pulse energy as a function of the driving Ti:Sa pulse intensity for a 5.5 cm-50 mbar Ar cell. Graph, as shown in [294].

While, 1 μJ, 5th harmonic pulses are available on a daily basis, it has been observed that the pulse energy attainable continues increasing when a more energetic driving Ti:Sa pulse is used. This has been confirmed by increasing the pump-pulse energy in the 25 Hz multi-pass amplification stage up to the safety limit, in order to prevent damage on the multi-pass Ti:Sa crystal. In this case, the maximum pulse energy was slightly above 1.1 µJ indicating that the 5th harmonic pulse energy can be further scaled. The same holds when the gas cell pressure is further increased, although limited by the pump system capabilities presently, verifying the pulse energy scaling trend, emerging in both Fig.5.5 and Fig.5.6 graphs.

The 5^{th} harmonic pulse has been initially temporally characterized utilizing a novel, all-reflective, interferometric autocorrelation scheme, by Dr. T. Gebert during his doctoral thesis work [222], with contribution from the author of the present thesis. Non-resonant two-photon ionization of Kr is employed as the nonlinear process that delivers a second-order interferometric autocorrelation measurement of the 5^{th} harmonic pulse. The resulting autocorrelation trace, apart from the pulse duration, additionally provides a very precise measurement of the pulse carrier frequency, obtained by Fourier transform. Details about the interferometric technique, the relevant theoretical aspects and the pulse properties information extraction can be found in [220, 222].
To provide a benchmark for the results presented in the following chapter, a 5^{th} harmonic pulse second-order fringe-resolved intensity autocorrelation (FRIAC) dataset, measured by Dr. T. Gebert is presented here with his permission, in Fig. 5.7.

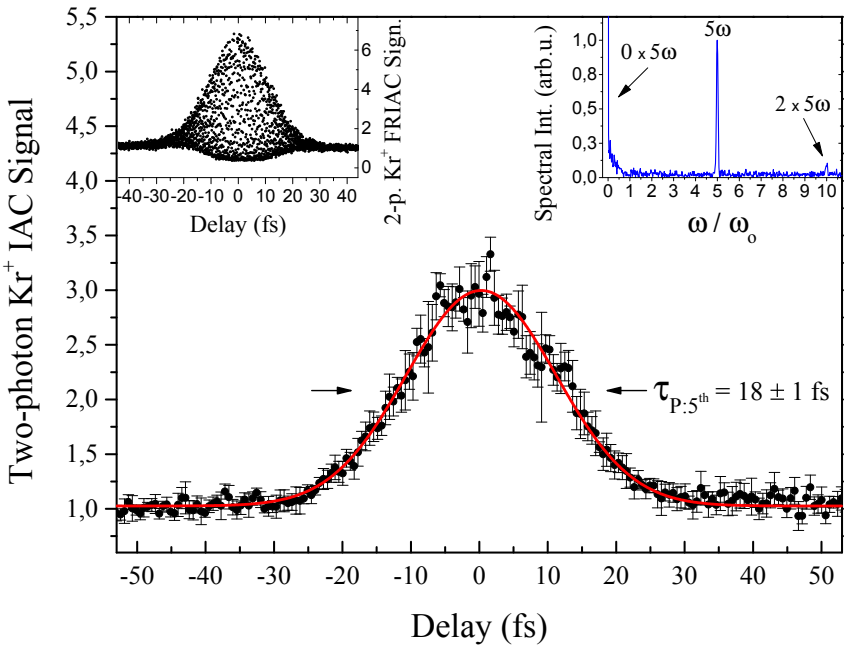

Figure 5.7: Second-order intensity autocorrelation of the 5^{th} harmonic pulse, extracted from the interferometric measurement shown in the left inset by low-pass filtering, taken from [220,222,294]. The pulse carrier frequency, corresponding to a carrier wavelength of $\lambda_c = 161.8 \pm 0.3$ nm, is obtained from the Fourier transform of the interferometric trace, shown on the right inset. Graph, as it appears in [294].

The 5^{th} harmonic pulse duration, as extracted from the interferometric autocorrelation shown in Fig. 5.7, corresponds to 18 ± 1 fs FWHM, very close to the value expected in the perturbative limit, that is, $\sqrt{5}$ shorter than the fundamental, assuming a Gaussian temporal profile. At a later time, using an optimized IR driving pulse duration, a measured 5^{th} harmonic pulse duration reaching approximately 15 fs has been established, with a slightly reduced pulse energy content though. The information about the pulse carrier frequency is contained in the Fourier-transformed non-linear interferometric trace [222] and in this case the carrier wavelength measured is 161.8 ± 0.3 nm.

The high-intensity content of the focused 5th harmonic pulse is confirmed by its ability to ionize Xe, Kr, and Ne via non-resonant, two and three-photon absorption, respectively. Utilizing the previously described, ion-imaging time-of-flight spectrometer combined with the 162 nm counter-propagating pulse optical setup, the distributions of Xe^+, Kr^+, and Ne^+ ions have been recorded in the focus of a single optical branch. The intensity-dependence of the ion yields has been measured by normalizing the corresponding ion time-of-flight spectra to the XUV photodiode signal.

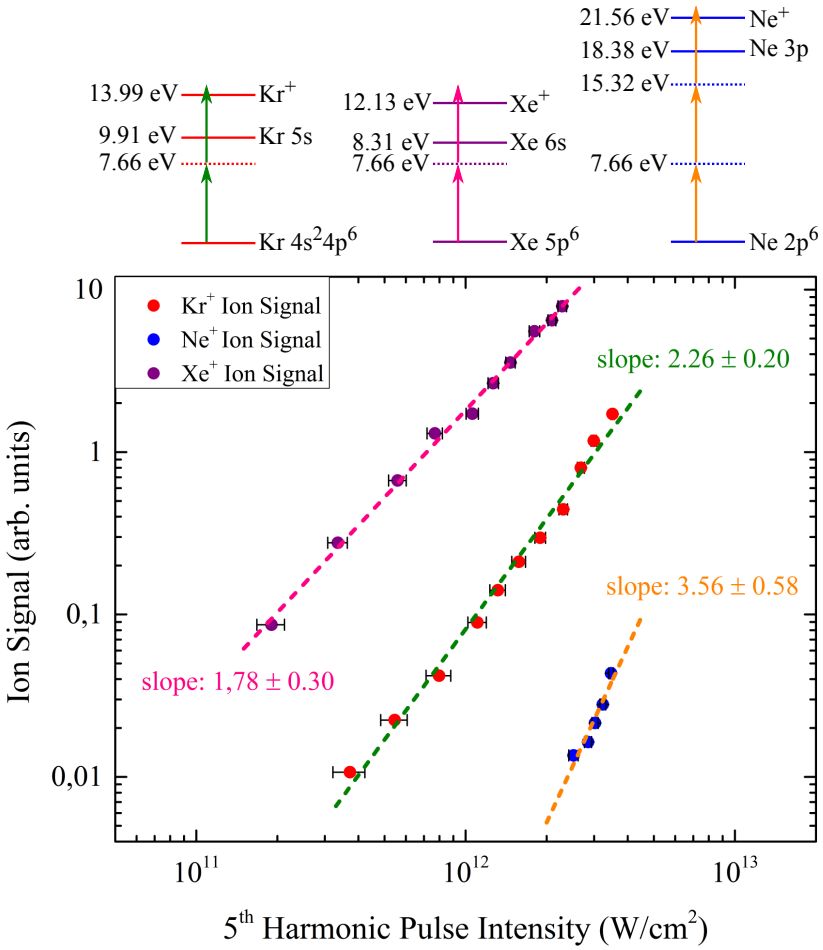

Figure 5.8: Multiphoton, non-resonant ionization of Xe, Kr and Ne. The ion yield intensity dependence has been measured using a single branch of the counter-propagating pulse optical setup. Ionization proceeds with non-resonant absorption of 2 and 3 photons in each case, verified by the measured slopes in the logarithmic intensity dependence graph.

The 5th harmonic pulse intensity was varied by tuning the generating fundamental pulse energy and ensured that none of the other pulse properties were affected. The corresponding results are presented in Fig. 5.8 together with the multiphoton excitation schemes. A fitted slope of 2 for Kr^+ or Xe^+ and 3 for Ne^+ in a logarithmic scale plot, verifies that ionization proceeds via non-resonant, two or three-photon absorption in each case and the multiphoton transition is solely induced by the 5th harmonic pulse.

Obtained with a single optical branch of the 162 nm counter-propagating setup, these results experimentally verify the chosen optical component spectral purification properties, showing no influence from the accompanying spectral components, which would manifest itself with a different slope connected with a different excitation scheme. Additionally, they justify the choice of the Kr^+ or alternatively Xe^+ ion signal as a suitable non-resonant multiphoton ionization process for obtaining a 2^{nd} order intensity autocorrelation measurement of the 5^{th} harmonic pulse and demonstrate its feasibility with the current setup. The much weaker Ne^+ signal did not allow a reliable 3^{rd} order intensity autocorrelation measurement.
Taking into account the optical reflectivity, as well as the measured focal spot size of 14.4 µm ± 3 µm FWHM, the 5^{th} harmonic pulse intensity on target is calculated to be $3 \pm 2 \times 10^{12}$ W/cm^2. An optimized geometry employing a shorter focal length mirror, could deliver intensity on target reaching the 10^{15} W/cm^2 level.
The focal spot size is determined by the imaged ion distribution, taking into account the respective non-linearity factor. The absolute intensity scale uncertainty is mainly influenced by the precise knowledge of the focal spot size. A spot size measurement uncertainty attributes a constant scale shift to the x-axis intensity values in Fig. 5.8, lying within the reported intensity uncertainty interval ($3 \pm 2 \times 10^{12}$ W/cm^2). Nevertheless, the absolute peak intensity value does not affect the presented results, which depend only on the relative ion yield difference.
In summary, a laboratory-based light source delivering 1.1 μJ, 18 fs VUV pulses at 162 nm based on HHG has been experimentally realized. The driving 15 mJ IR pulse supports a loose-focusing geometry, allowing efficient phase-matched harmonic generation in a long statically-filled Ar gas cell. The optimal generation conditions using Ar, or alternately Xe, as a generating medium have been investigated and compared. It has been shown that when using Ar as a generating medium, the 5^{th} harmonic pulse intensity follows an increasing trend that can be further scaled using higher laser energy and gas target density. The high intensity of the 5^{th} harmonic pulse, verified by the observation of non-resonant two- and three-photon absorption in the focus of a relatively long focal-length focusing mirror, overcomes low multiphoton cross section limitations enabling versatile multiphoton excitation schemes in the vacuum-ultraviolet spectral region. Additionally, the high pulse energy, avoids the necessity of the typically used tight-focusing geometries in VUV multiphoton experiments, allowing large focal dimensions that overcome technical pump-probe limitations [221] and can result in an exceptional signal-to-noise ratio.

6 Single-Shot Autocorrelation in the Vacuum-Extreme Ultraviolet

In this chapter, the experimental results obtained both in laboratory experiments, utilizing the intense 162 nm pulse, as well as in two free-electron laser facilities, FLASH in Hamburg and FERMI in Trieste, that mainly benefit from the individual-shot operation of the presented counter-propagating pulse technique, will be discussed.
The experimental apparatus and measurement methodology has been described in detail in Ch. 3 and Ch. 4, where the reader is referred for instrumentation details and specifications, as well as for the complete discussion of the respective excitation schemes. In the present chapter, a detailed analysis of the results obtained in each of the three experimental variants will be given separately in each dedicated section.

6.1 Second-Order Single-Shot Autocorrelation at 162 nm

The first section is devoted to a thorough discussion of the experimental results obtained using the counter-propagating pulse approach in the vacuum ultraviolet (VUV) spectral region. Combining the 162 nm optical setup [Ch. 3], with charge-state selective ion microscopy [Ch. 4] and direct two-photon single ionization of Kr or Xe as an instantaneous non-linear process [Ch 5.3], a 2^{nd} order, single-shot intensity autocorrelation (IAC) of the 5^{th} harmonic pulse at 162 nm can be measured.
The two pulse replicas are synchronized in the focal point in a counter-propagating geometry, with the temporal delay between them encoded on the propagation axis [Eq. 3.1]. The resulting spatially-resolved Kr^+ or Xe^+ ion distribution, can be interpreted as a delay-dependent non-linear signal, resulting directly in a 2^{nd} order IAC measurement of the VUV pulse. Owing to the high 5^{th} harmonic pulse intensity, the two counter-propagating pulse replicas were able to individually deliver a substantial amount of non-sequential two-photon ion signal [Fig. 5.8], demonstrating the feasibility of a single-shot measurement.
The availability of a pulse duration reference measurement, obtained earlier than this experimental work employing a novel fringe-resolved intensity autocorrelation (FRIAC) technique, presented in Fig. 5.7 and in [220, 222, 294], combined with the imaging specifications of the ion microscope, allow for an estimation of the anticipated IAC signal characteristics. As previously stated [Ch. 2], the temporal extent of the 2^{nd} IAC measurement as compared to the initial pulse duration, is given by $\Delta\tau_{\text{IAC}} = \sqrt{2} \cdot \Delta t_{\text{pulse}}$ [Eq. 2.57].

In the present case, the measured 5$^{\text{th}}$ harmonic pulse duration was 18±1 fs FWHM [Fig. 5.7]. This results in a 2$^{\text{nd}}$ order IAC trace FWHM of approximately 25.4 fs. As the delay is spatially encoded along the propagation axis via Eq. 3.1, this results in a IAC spatial width of $\Delta x = (1/2n) \cdot (c\Delta\tau) \approx 3.8\,\mu\text{m}$ FWHM, where n=1 considering a dilute gas medium.
Recalling that the position-sensitive detector offers a comparable spatial resolution ($\sim 3.1\,\mu\text{m}$ [Ch. 4.4]), the imaged extent of the IAC signal will result from the convolution between these two quantities as $\sqrt{(3.8\,\mu\text{m})^2 + (3.1\,\mu\text{m})^2} = 4.9\,\mu\text{m}$ FWHM, when Gaussian profiles are considered [Fig. 2.3]. As a result of this additional broadening, the autocorrelation width will be 32.7 fs FWHM and the pulse duration obtained by temporal deconvolution 32.7 fs/$\sqrt{2}$ = 23 fs FWHM, resulting in a predicted error of 5 fs. Although anticipated and possible to subtract, this error lies in an uncertainty range that is commonly stated in measurements performed in this spectral range [30, 31, 51, 52]. A position-sensitive detector with higher resolution, not available during the time of this work, could easily overcome this issue, while with the existing detector, the error will be in the 1 fs range when pulses over 40 fs are used.
Furthermore, the combination of the ion microscope magnification (24.5) with the measured camera objective magnification (0.48), results in a total combined magnification of $M_{\text{combi}} = M_{\text{IM}} \cdot M_{\text{Obj}} \approx 11.76$. The directly-imaged IAC width is thus expected to extend on the CCD chip on 4.9 µm×11.76 ≈ 57.6 µm. Taking into account the CCD pixel size of 7.4 µm, the IAC FWHM will therefore correspond to 7.8 pixels. When the CCD is operated in hardware-binning mode, this value will have to be divided by the corresponding binning factor (2×, 4× or 8×), compromising imaging resolution and thus fitting reliability, in favor of a higher signal-to-noise ratio.

6.1.1 Experimental Results

Keeping the above analysis under consideration, the two 162 nm counter-propagating pulse replicas were brought to overlap spatially, as well as temporally, in a common focus, at the center of symmetry of the optical arrangement. Non-resonant two-photon ionization of Kr served as the non-linear autocorrelation process in this case.
The coarse pre-alignment has been performed using the NIR autocorrelation measurement, as described in Ch. 3.3, while fine optimization has been accomplished under vacuum conditions, employing the motorized mirror mounts. The main optimization step concerned matching the two focal positions, which had to be re-adapted as the 162 nm beam exhibited a different divergence than the NIR beam. For this task, the areas of higher ion density (as shown in Fig. 4.16), corresponding to the focal region of each optical branch, were brought to an optimum spatial overlap using both the ion image and time-of-flight information offered by the ion microscope, as described in Ch. 4.
An average image of the resulting TOF-gated, Kr^+ delay-dependent ion distribution, after optimization, is shown in Fig. 6.1. The recorded IAC trace resembles that obtained in the visible two-photon fluorescence measurement with the NIR pulse [Fig. 3.13].

A pronounced Kr^+ ion density enhancement is observed at the region where the two counter-propagating pulses overlap both temporally and spatially. The ion signal enhancement additionally extends in the vertical direction as a result of the increased intensity experienced locally by the neutral Kr atoms, leading to a local increase in Kr^+ ions [Eq. 2.19].
Referring to the theoretical analysis presented in Ch. 3, the Kr^+ ion distribution along the propagation direction directly results in a 2^{nd} order IAC measurement of the VUV pulse (Fig. 6.1, 6.2). At a later stage a similar dataset has been obtained using Xe as the non-linear gas target showing the exact features, while providing an overall higher signal, according to expectations [Fig. 5.8].
The measured magnification has been in this case $M_{combi} = M_{IM} \cdot M_{Obj} = 10.23 \pm 0.11$, while no CCD pixel binning has been used. This value results in a conversion factor of 0.72 µm/pixel or equivalently 4.825 fs/pixel in delay-time units, via Eq. 3.1. The data presented in Fig. 6.1 correspond to a position-sorted average over 800 pulses, whereas a single-shot dataset is shown in Fig. 6.2.

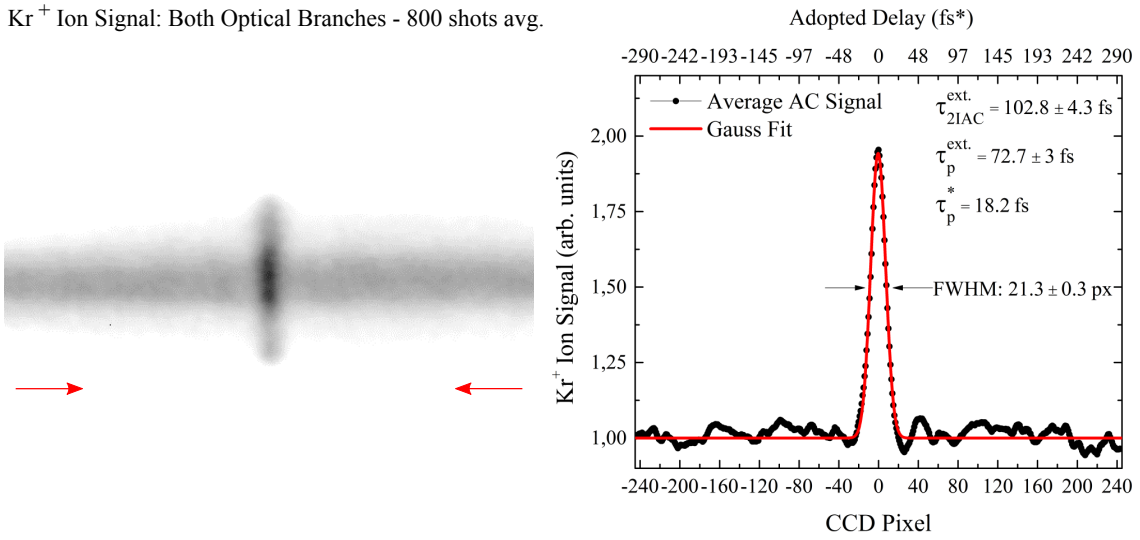

Figure 6.1: 800-shots Average, Delay-dependent Kr^+ signal delivering a 2^{nd} order intensity autocorrelation measurement at 162 nm.

The horizontal profile, taken here from the complete-image horizontal average, depicts the Kr^+ delay dependence that directly translates to the 2^{nd} order IAC measurement. The attained peak-to-background contrast ratio matches the theoretically expected 3:1 [Eq. 2.59] in the single-shot case, while it decreases to ∼2:1 on the 800-shot average dataset. It was observed that the decreased contrast ratio results from beam-pointing deviations, leading to a spatial overlap mismatch and decreased autocorrelation signal for a number of shots. A Gaussian fit, results in similar autocorrelation widths for both presented traces, corresponding to 21.3 ± 0.3 pixels in Fig. 6.1 and 22.1 ± 1 pixels in Fig. 6.2. Using the conversion factor originating from the ion-imaging magnification measurement, these values result in an autocorrelation trace FWHM of $\tau_{ACavg} = 102.8 \pm 4.3$ fs and $\tau_{ACs} = 106.6 \pm 11.7$ fs respectively. Assuming a Gaussian pulse temporal profile, the pulse duration can be obtained by deconvolution [Eq. 2.57], corresponding to $\tau_{Pavg} = 72.7 \pm 3$ fs and $\tau_{Ps} = 75.4 \pm 8.3$ fs.

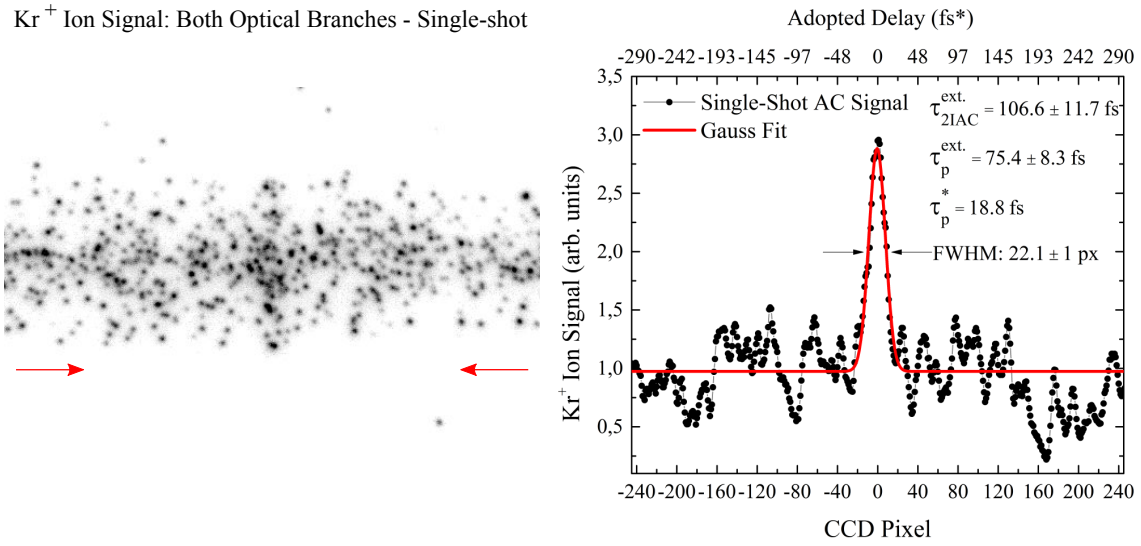

Figure 6.2: Single-shot, Delay-dependent Kr^+ signal providing a single-shot 2^{nd} order IAC measurement at 162 nm.

The stated uncertainties result after error propagation, taking into account the measured ion microscope magnification uncertainty, the Gaussian fit uncertainty, as well as the statistical uncertainty for multi-shot datasets.

The obtained pulse duration is in disagreement with the previous measurement [Fig. 5.7], used as a reference here, while it even exceeds the pulse duration of the infrared HHG-driving pulse [Fig. 5.1]. Even though the same measurement has been performed during a period of several months, varying a multitude of experimental parameters, including both the HHG generation as well as the instrumentation operational parameters, the obtained results did not show any significant variation beyond the stated uncertainty range. Being highly-efficient in terms of data acquisition and corresponding statistics, a set of several-thousands of single-shot measurements can be obtained over few minutes with the 25 Hz repetition-rate laser system, permitting real-time parameter tuning and ensuring stable experimental conditions in the comparative studies performed.

The 162 nm pulse duration, measured utilizing the counter-propagating pulse autocorrelation apparatus, varied between approximately 62 fs - 82 fs FWHM over a period of 4 months, stabilizing at approximately 64±8 fs FWHM during the last month, connected with a laser system performance optimization delivering shorter HHG-driving infrared pulses. When measured in sequence, using both the fringe-resolved intensity autocorrelation (FRIAC) apparatus and the counter-propagating pulse setup, the apparent discrepancy in the obtained duration remained. An interesting fact is that the pulse duration extracted from the counter-propagating pulse IAC is always approximately 4 times broader than that extracted from the FRIAC measurement.

Two consecutive measurements performed recently, within few minutes difference using the exact experimental conditions by A. Baumann and O. Schepp, nowadays responsible for the two experiments, resulted in a ratio between the retrieved pulse durations of $\tau_{\mathrm{CPIAC}}/\tau_{\mathrm{FRIAC}} = 3.8 \pm 0.4$, where τ_{CPIAC} denotes the counter-propagating IAC width and τ_{FRIAC} the FRIAC width, respectively.

The apparent difference can be attributed either to a systematic error introduced by the experimental apparatus, or to an unidentified mechanism that results in a longer pulse at the counter-propagating pulse setup common focus. The influence of the imaging resolution offered by the position-sensitive detector/external imaging setup has already been shown not to significantly contribute, as discussed in the beginning of this chapter.
It should be also noted that the FRIAC measurement [Fig. 5.7] possesses an intrinsic temporal calibration scale provided by the temporal fringe pattern which comprises mainly of the VUV pulse carrier frequency, as can be seen in the inset graph in Fig. 5.7. This ensures that the time-delay scale used in the FRIAC measurement is extremely accurate. Furthermore, the high peak-to-background contrast and the consistency with expectations in the perturbative-limit, that is a $\sqrt{5}$ scaling for the 5^{th} harmonic pulse duration compared to the fundamental, constitute the fringe-resolved intensity autocorrelation results a reliable reference beyond dispute.

6.1.2 Benchmark Measurement Results

In order to identify the origin of this discrepancy, a number of benchmark/comparative measurements has been performed. The dependence of the 2^{nd} order IAC trace width on the pulsed gas valve duration, non-linear target gas, VUV pulse energy, and position-sensitive detector gain has been studied. The corresponding results are summarized in a compact form within this section.
Prior to these measurements which mainly aim in identifying instrumentation flaws, temporal distortions on the pulse temporal shape or delay-time scale calibration errors have been checked. In a first step, the calibration accuracy of the time-delay axis has been verified. This was accomplished by introducing a well-defined optical path difference in one of the two optical branches of the counter-propagating optical setup. One pulse replica was delayed by a linear displacement of the FM1 spherical mirror [Fig. 3.2], employing the picomotor-controlled linear translation stage where the spherical mirror mount is fixed. The utilized picomotor actuator is specified with a thread pitch of 80 turns-per-inch, resulting in a d=317.5 µm linear displacement per revolution. By performing exactly one revolution, the temporal overlap location is translated in a neighboring position along the propagation axis, at a distance equal to d [Fig. D.1]. The measurement has been repeated several times yielding a self-consistent result, with $d_{exp} = 313\,\mu m \pm 5\,\mu m$ [results shown in Fig. D.1]. The experimental value is in very good agreement with the expectation, verifying the delay-encoding principle and the experimentally determined ion imaging magnification.
In a second step, a 1 mm±0.1 mm thick CaF_2 window has been used to controllably introduce chromatic dispersion to the 5^{th} harmonic pulse. The optical properties of CaF_2 have been extensively studied in the VUV, as it is excessively used for optical components related with VUV lithography applications. It exhibits a group velocity dispersion of GVD=550.84 fs^2/mm at 161.8 nm (20 °C) [132], a transmission cut-off at 125 nm and does not show any significant birefringence [295].

Taking into account the measured CaF_2 optical constants [132], apart from stretching the 162 nm pulse due to linear dispersion, the CaF_2 window is expected to suppress the odd-harmonic radiation above the 5^{th} order and additionally introduce a delay between the 5^{th} harmonic and the transmitted fundamental (805 nm) and 3^{rd} harmonic (268 nm) pulses, due to their group velocities difference in the material. For a 1 mm thick CaF_2 window, the calculated propagation time-differences are $t_{161.8\,nm}$-$t_{268\,nm}$=1257.1 fs and $t_{161.8\,nm}$-$t_{805\,nm}$=1587.2 fs, respectively. A Gaussian bandwidth-limited 161.8 nm pulse with a duration of 20 fs FWHM, will be stretched to 78.9 fs FWHM upon propagation [Eq. 2.50] and thus exhibit a ratio of $\tau_a/\tau_b = 3.94$ between its duration after propagation though the window τ_a and its duration before τ_b. Equivalently, a pulse with an initial duration of 80.1 fs FWHM will stretch to 82.3 fs FWHM, corresponding to a pulse duration ratio of $\tau_a/\tau_b = 1.03$ defined in the same manner as before. The fundamental and 3^{rd} harmonic pulses, although calculated not to transmit over the optical setup [Ch. 3.2], are expected to be minimally influenced, as they experience significantly less dispersion ($GVD_{268\,nm} = 126.83$ fs^2/mm, $GVD_{805\,nm} = 27.56$ fs^2/mm) and have a longer duration.
The CaF_2 window has been installed in the 5^{th} harmonic beam path prior to the Si wedge-mirror [Fig. 3.2]. Two measurements have been obtained, one before installing the CaF_2 window and one afterwards. The measured 5^{th} harmonic pulse duration before propagating through the CaF_2 window was 80.1 ± 4.8 fs FWHM, obtained by deconvolution from an autocorrelation width of 6 pixels, using pixel-binning 4× and a measured $M_{combi} = 10.45 \pm 0.56$. The corresponding pixel to delay-time conversion factor results as 18.88 fs/pixel for this dataset.

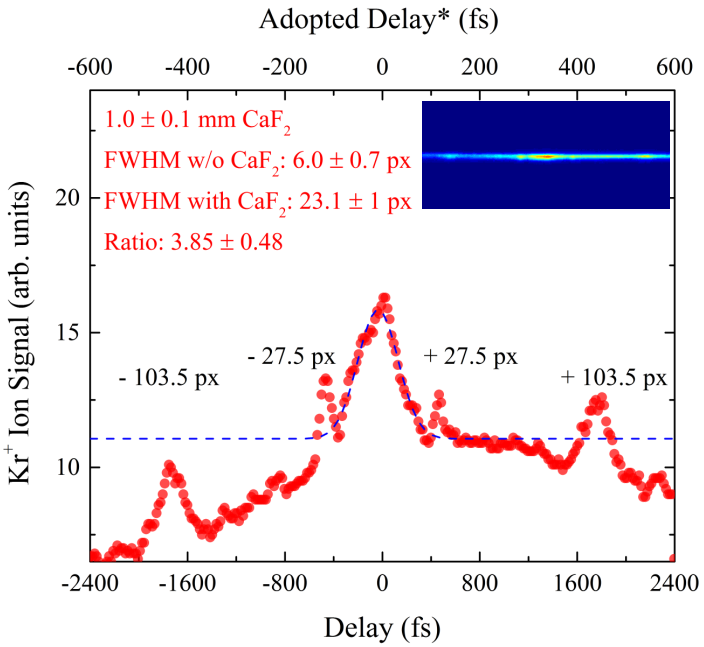

Figure 6.3: 1 mm CaF_2 window dispersion characterization.

Insertion of the CaF_2 window in the beam path prior to the experimental setup results in a decrease of the Kr^+ ion signal and an autocorrelation width broadening as shown in Fig. 6.3. The asymmetry observed in the Kr^+ distribution is mainly due to poor statistics.

Moreover, two pairs of satellite peaks appear symmetrically with respect to the main peak, denoting a multi-pulse structure. The autocorrelation width is 435.6 ± 9.6 fs FWHM corresponding to a pulse duration of 308 ± 6.8 FWHM considering a Gaussian temporal shape. This is a quite puzzling result as a 80.1 fs FWHM pulse is expected to stretch only up to 82.3 fs FWHM as stated before.
Going one step further, one may assume that the initially short pulse (20 fs) stretches, not only due to propagation through the CaF_2 window, but also due to dispersion accumulated within the optical setup, thus explaining the initially observed long duration of 80.1 ± 4.8 fs FWHM as compared to the FRIAC result of 18 ± 1 fs FWHM. Although counter-intuitive, since the optical setup comprises of all-reflective components and a multi-layer mirror with specified dispersion characteristics, this possibility must be evaluated. The second-order dispersion needed to temporally stretch a 20 fs FWHM pulse to 80.1 fs FWHM would result from group-delay dispersion (GDD) of ± 559.5 fs^2. When combined with the dispersion induced by the CaF_2 window, it results in GDD_{tot}=1110.3 fs^2, considering the +559.5 fs^2 case, or in GDD_{tot}=-8.66 fs^2 in the -559.5 fs^2 case. In the first case (GDD_{tot}=1110.3 fs^2), the pulse would stretch to 155.2 fs FWHM, corresponding to an IAC trace width of 219.5 fs FWHM. The pulse duration ratio, after and before propagation through the CaF_2 window would be τ_a/τ_b=(155.2 fs/80 fs)=1.94, which is not the case here. In the second case though (GDD_{tot}=-8.66 fs^2), the initially negative GDD is almost completely compensated by that induced after propagation through the CaF_2 window, resulting in an non-measurable change in the initial pulse duration (20 fs FWHM $\rightarrow$ 20.03 fs FWHM). This scenario is also not compliant with the experimental observations.
The experimental τ_a/τ_b pulse width ratio can be directly obtained by the measured widths in pixel units, avoiding any assumed or measured pre-factors. The experimentally determined ratio corresponds to $(23.1 \pm 1$ pixel$)/(6 \pm 0.7$ pixel$)=3.85 \pm 0.48$. This result is in very good agreement with the $\tau_a/\tau_b = 3.94$ ratio expected for a 20 fs FWHM pulse propagating through 1 mm CaF_2 and being stretched to 78.9 fs FWHM, as described above. Indeed, if the pixel size is neglected and the IAC width is cross-calibrated to the FRIAC measurement width, an adopted delay-time scale can be established. When this adopted delay-time scale is used instead, the results presented in this and the following chapter are in accordance to expectations. Moreover, as described in the following chapter, pump-probe measurements aiming at disclosing molecular dissociation constants are in very good agreement with values reported in the literature.
The origin of the satellite peaks in Fig. 6.3 can be also briefly discussed here. The 2nd order IAC of a double pulse is expected to exhibit symmetrically spaced satellite peaks with respect to the main peak, with a spacing equal to the time delay between the two pulses [Fig. 2.4]. This concept can be generalized for a pulse triplet, resulting in a similar autocorrelation pattern with a pair of satellite peaks spaced by their respective delays. The observed spacing here is ± 27.5 pixels and ± 103.5 pixels, corresponding to delay times of 519.2 fs and 1954.1 fs, respectively, or equivalently 129.8 fs and 488.5 fs in the adopted time-delay scale. The observed delay times, rule out the assignment of the satellite peaks to the fundamental or the 3rd harmonic pulse, an argument which is also reinforced by the fact that their contribution would alter the measured slopes in Fig. 5.8. Their contribution in the non-linear ion signal would result to larger slopes as the number of photons needed to reach the ionization threshold would increase.

The origin of the satellite peaks is not completely understood and it is assumed that they might result due to the presence of an unidentified thin-film coating on the window surface. The findings presented so far, rule out temporal distortion effects and point to an instrumentation-induced broadening of the autocorrelation FWHM. The spatial resolution limit imposed by the position-sensitive detector and external imaging setup does not explain an imaging distortion resulting in a factor of 4 broadening. As a complementary characterization measurement, a set of IAC measurements have been performed in the same manner as presented in Fig. 6.1, 6.2, while varying the detector gain. Operating in a TOF-gated mode, an IAC measurement was obtained by recording the Kr^+ ion distribution image and varying the front MCP voltage, while keeping the rest of the applied voltages fixed. This effectively changed the gain of the front MCP, in order to investigate whether saturation or space-charge effects, within the detector, influence ion imaging and therefore the obtained IAC width. The IAC measurement information has been extracted in the same manner as described above and the results are summarized in Table 6.1.
By tuning the front MCP voltage within its complete range, from 0.65 kV to 1.00 kV, no deviations have been observed in the obtained IAC FWHM, excluding detector saturation effects. It should be noted, that different voltage combinations, by tuning the second MCP and scintillator screen voltages did not show any deviations from the reported results. Also, operating the detector in a non-TOF-gated mode, resulted in the exact IAC width, since the chamber base pressure (5×10^{-8} mbar) ensures that there are hardly any contributions in the recorded ion image besides from Kr^+ ions.

Front MCP Voltage	IAC FWHM Spatial Ext.	Adopted Delay Scale 5^{th} H. Duration	Experimental Delay Scale 5^{th} H. Duration
0.65 kV	12.6 µm	(14.9 ± 1.1) fs	(59.4 ± 4.5) fs
0.70 kV	12.8 µm	(15.1 ± 1.1) fs	(60.4 ± 4.5) fs
0.75 kV	13.3 µm	(15.7 ± 1.1) fs	(62.8 ± 4.5) fs
0.80 kV	13.3 µm	(15.7 ± 1.1) fs	(62.8 ± 4.5) fs
0.85 kV	13.5 µm	(15.9 ± 1.2) fs	(63.6 ± 4.9) fs
0.90 kV	13.0 µm	(15.3 ± 1.1) fs	(61.2 ± 4.5) fs
0.95 kV	12.7 µm	(15.0 ± 1.1) fs	(60.0 ± 4.5) fs
1.00 kV	13.2 µm	(15.6 ± 1.2) fs	(62.4 ± 4.9) fs

Table 6.1: Fifth-harmonic second-order autocorrelation temporal overlap extent as a function of the front MCP voltage. Kr^+ ions were detected in a time-gated mode with the second MCP operating at 1.37 kV in addition to the 0.5 kV gating HV pulse. The temporal overlap extent shows no voltage dependence or saturation effects.

Excluding reduced resolution or saturation effects in the charged-particle detection system, indicates that the IAC width broad extent should be associated with ion imaging defects. So far, the experimental observations have been in excellent agreement with the SIMION simulations results presented in Ch. 4.

As stated earlier, when the position of the ion microscope is tuned in relation to the ionizing beam in a way that the ion TOF matches the simulated values, the measured magnification matches exactly with the simulated M=24.5 within the measurement uncertainty. This fact indicates that the trajectories that the particles actually follow within the instrument, should be matching those simulated. Nevertheless, the SIMION simulation results presented in Ch. 4 do not take into account charge repulsion effects. The main reason for this is that SIMION has limited capabilities in handling such a problem as explicitly stated in its user's manual.
When operating in low-pressure conditions, no ion-imaging distortions appear within a certain pressure range [Fig. 4.16]. However, single-shot operation demands a higher local gas density in order to enhance the non-linear ion yield. The single-shot IAC measurements reported in this chapter were mainly conducted using a pulsed gas valve, which delivers a much higher gas density on target. For this reason a second characterization measurement, employing the pulsed gas valve has been performed in the same way as the one shown in Fig. 4.16, introducing only the pulse from a single optical branch in the focal region. In order to verify the previous results and exclude systematic uncertainties, some measurements were performed initially using the gas dosing valve, as before. The pulse energy in the interaction region was (145.9±3.4) nJ and the measured ion microscope magnification $M_{exp.}=(24.3 \pm 0.63)$. The corresponding results are presented in Fig. 6.4.

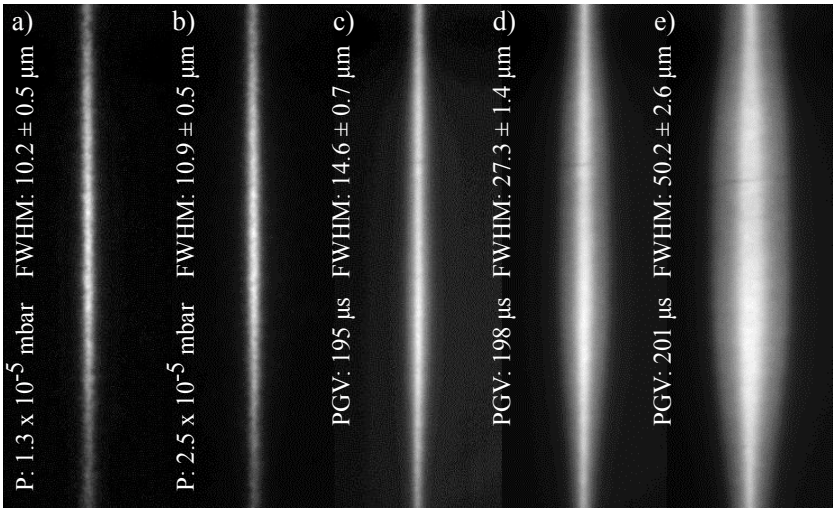

Figure 6.4: Kr^+ ion channel recorded using a single optical branch of the counter-propagating autocorrelation optical setup. The gas is provided in the interaction region with a pulsed gas valve (Parker Series 9). a) and b) where obtained as in 4.16 using the gas dosing valve. The measured ion channel width increases with longer valve opening times, showing hints of charge repulsion effects due to space-charge. The ion image retains its shape while it becomes broader. It should be stressed, that the local gas density on target scales non-linearly with the gas valve opening time.

The first two datasets obtained with the gas dosing valve are in excellent agreement with the previous measurements, shown in 4.16. When the pulsed gas valve is used, the ion image appears broader as a function of the gas pulse duration, set using the IOTA One driver unit.

It should be noted that the stated duration does not necessarily correspond to the actual gas pulse duration but rather to the supplied HV pulse, responsible for opening and closing the valve. As observed in the average Kr^+ ion distribution images 6.4c, 6.4d, 6.4e, the ion channel appears broader and brighter, reaching an unphysically large size with longer opening times. Nevertheless, the ion channel retains its shape although with increased dimensions. The black defect line observed in all images, is a minor MCP detector crack, appearing displaced as the position of the ion microscope has been slightly adapted between measurements. The ion imaging magnification has been verified to remain constant in this case, by performing intermediate measurements. The conclusion that can be reached from the results shown in 6.4, is that above a certain ion density the imaging properties of the ion microscope are modified. In addition to this, the radial ion distribution width at the pulse temporal overlap region is found to be broader than that in the neighboring areas, where the two pulses do not overlap temporally, verifying the charge repulsion effect hypothesis. An additional series of single-shot measurements was performed, in order to rule out external influences to the measurement results, such as vibrations from the gas valve operation, beam pointing instabilities and vibrations from the scroll pre-vacuum pump. During data acquisition the scroll pre-vacuum pump is turned off and an intermediate buffer volume is connected with the turbo-molecular pump ports. In this way the scroll-pump only switches on for a short time to evacuate this volume, after the data acquisition is complete.
The pulsed valve operation has been also found not to influence the measurement. A series of datasets have been obtained as in 4.16, using the gas dosing valve to provide the gas target, while operating the pulsed valve evacuated. No deviation from the reported results has been observed during this set of measurements. Finally, although beam pointing instabilities have been always present, mainly connected with laser system instabilities and partly with vibration sources external to the building, the position-sorting algorithm described before has been very successful in sorting the single-shot datasets after the experiment was concluded, circumventing any position averaging effects. The averaged ion distribution image exhibits the same characteristics as the single-shot data.
The results shown in Fig. 6.4, support the argument that the IAC width should be also influenced by space-charge effects in this gas density regime. Furthermore, the IAC width would be expected to grow as a function of the pulsed gas valve opening time, as observed in the single optical branch datasets. In order to investigate the influence of the gas valve opening time on the IAC results, a series of single-shot IAC measurements have been conducted, using either Kr^+ or alternatively Xe^+ ion signal to obtain a counter-propagating IAC measurement. The pulsed gas valve opening time was varied between 194 µs and 203 µs and the IAC data were analyzed following the same procedure as before. The corresponding results are summarized in Table 6.2.
While the ion distribution radial width is observed to expand with increasing pulsed gas valve opening time, the same way as in Fig. 6.4, the IAC width remains invariant to this change. The measurements have been performed using either Xe, or Kr gas, within few minutes difference and no deviations have been found.
Charge-repulsion effects are obvious when comparing the ion distribution radial width for increasing gas density and explain the difference between Kr and Xe datasets, as the Xe^+ yield is way higher than that of Kr^+ in the same experimental conditions.

Pulsed Gas Valve Opening Time	IAC FWHM Spatial Ext.	NL Target	Adopted Delay Scale 5^{th} H. Duration	Exp. Delay Scale 5^{th} H. Duration	Radial Width FWHM
203 µs	13.9 µm	Kr^+	(16.5 ± 1.1) fs	(66.0 ± 4.5) fs	66.2 µm
200 µs	13.5 µm	Xe^+	(15.9 ± 1.0) fs	(63.6 ± 4.0) fs	245.3 µm
199 µs	13.7 µm	Kr^+	(16.2 ± 1.1) fs	(64.8 ± 4.4) fs	42.6 µm
198 µs	13.3 µm	Xe^+	(15.7 ± 1.0) fs	(62.8 ± 4.0) fs	140.5 µm
196 µs	13.5 µm	Xe^+	(16.0 ± 1.0) fs	(64.0 ± 4.0) fs	82.3 µm
194 µs	13.4 µm	Xe^+	(15.8 ± 1.0) fs	(63.2 ± 4.0) fs	52.3 µm

Table 6.2: The measured fifth-harmonic second-order autocorrelation width shows no dependence on the pulsed gas valve opening time (Parker Iota One indication). This result is verified, using both Kr^+ and Xe^+ as non-linear targets in the same experimental run.

The IAC width however, shows no observable influence, keeping a constant value for the complete valve opening time range, that remains within the experimental uncertainty interval. While the number of ions scales linearly with the applied pressure, it is expected to scale quadratically with the applied intensity in a two-photon transition: $N_{\text{ions}} \propto N_{\text{atoms}} \sigma^{(2)} I^2$. An additional series of measurements has been performed, varying the VUV pulse energy by reducing the IR HHG driving pulse energy in the same manner as in the measurement presented in Fig. 5.6. The IAC data have been analyzed following the same procedure as described above and the corresponding results are summarized in Table 6.3.
A minor increase in the IAC width is observed, although it does not show any clear sign of charge-repulsion origin. As the pulse energy is increased by a factor of 4.7, the number of Kr^+ ions should increase by an order of magnitude and thus charge-repulsion effects on ion imaging should manifest themselves in this dataset. In the same way as in the data shown in Table 6.2, the ion distribution radial width is increasing continuously with higher pulse energy on target. Performing the same measurement using a single optical branch, shows a similar increase in the ion channel radial width as presented here and in Fig. 6.4.

5^{th} H. Pulse Energy (nJ)	IAC FWHM Spatial Ext.	Adopted Delay Scale 5^{th} H. Duration	Exp. Delay Scale 5^{th} H. Duration	Radial Width FWHM
52.14 nJ ± 4.9 nJ	11.9 µm	(14.1 ± 1.0) fs	(56.4 ± 4.0) fs	22.6 µm
109.5 nJ ± 5.8 nJ	12.8 µm	(15.1 ± 1.1) fs	(64.8 ± 4.4) fs	32.1 µm
140.9 nJ ± 6.3 nJ	13.2 µm	(15.6 ± 1.0) fs	(62.4 ± 4.0) fs	54.8 µm
215.8 nJ ± 5.8 nJ	13.5 µm	(15.9 ± 1.0) fs	(63.6 ± 4.0) fs	96.9 µm
246.5 nJ ± 4.9 nJ	13.4 µm	(15.8 ± 1.0) fs	(63.2 ± 4.0) fs	141.1 µm

Table 6.3: Dependence of the measured second-order autocorrelation spatial width on the 5^{th} harmonic pulse energy: Although the generated number of ions follows this change quadratically, no significant deviations are observed on the autocorrelation data.

Both datasets depict a counter-intuitive behavior of the ion imaging system. While the ion channel radial width shows an increase connected with a higher ion yield, either when higher gas density or higher pulse energy are used, the IAC width remains invariant and always approximately 4 times larger than the FRIAC width in all comparative measurements.
An additional measurement has been performed, comparing datasets obtained either with the pulsed gas valve or the gas dosing valve, otherwise in the exact experimental conditions, observing a stable IAC width even when the number of ions per shot was dramatically decreased. The measurement results are shown in Fig. 6.5.

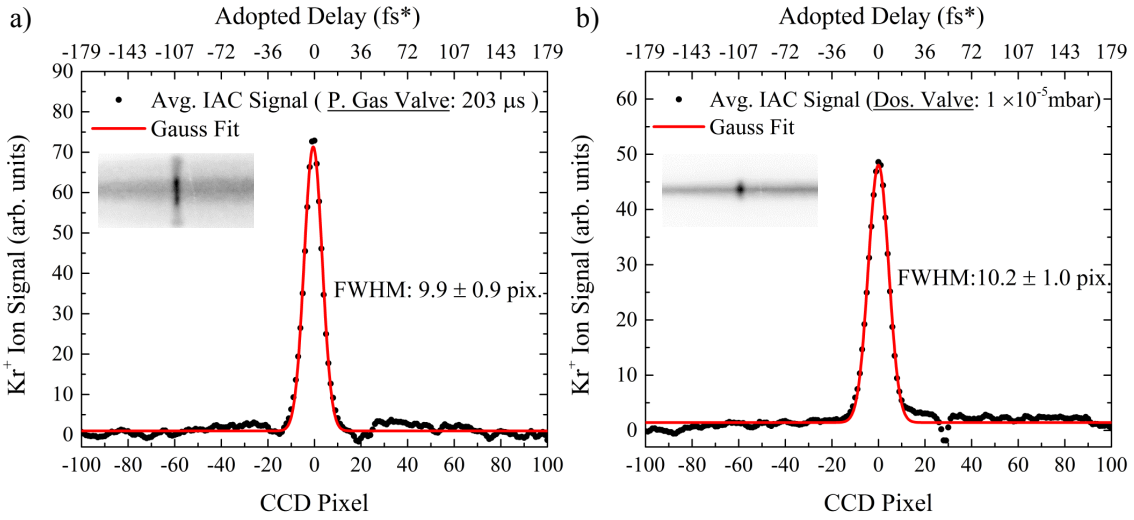

Figure 6.5: Counter-propagating pulse IAC FWHM pressure dependence: The averaged IAC FWHM spatial extent remains constant in a very broad pressure range. The experimental Kr^+ IAC trace obtained either with a) the pulsed gas valve at a long opening time (203 µs), or b) by introducing the gas target using a precision dosing valve and increasing the ambient pressure in the chamber, shows no difference in the obtained IAC width.

The invariance of the IAC width over this broad pressure range, shows that the IAC measurement result is independent of the effects that cause broadening in the radial width of the ion distribution. The dataset obtained with the gas dosing valve is in a range ($1 \cdot 10^{-5}$ mbar) that no radial width broadening has been observed [here 10.5 µm FWHM, see also Fig. 4.16], whereas the pulsed gas valve dataset utilizes an opening time (203 µs) that results in a considerably increased radial width (62.4 µm FWHM, not shown here). The constant broadening factor in the IAC width might result from ion imaging aberrations that either have a space-charge origin, or an unidentified effect that is experimentally relevant, although observationally inaccessible and not apparent in the simulation results presented in Ch. 4.3.
Not being able to identify the origin of this counter-intuitive effect from the comparative experimental investigations, a dedicated SIMION simulation, utilizing the embedded Coulomb repulsion mode, has been performed. The simulation parameters were adapted to the experimental parameters and a number of benchmark simulations have been performed in advance using few ions.

Including a larger number of ions and the ion microscope electric fields, results in computationally exhaustive simulations, lasting several days for realistic ion distributions.
Although a large set of different simulations has been performed by varying the corresponding initial conditions, the origin of the experimentally observed behavior could not be identified. The main simulation used a cylindrical ion distribution with a radius of R=5 µm, separated into two Kr^+ ion groups. The first group simulates the IAC temporal overlap region, having a length of 3.8 µm and the second group the remaining ion distribution with a length of 730 µm corresponding to the detector size divided by the ion microscope magnification. The second group is assigned with 1000 ions, limited by the computation time needed for more particles, while the number of ions in the IAC temporal overlap group is varied between 10 and 300 ions in successive runs. In the experimental data, the number of events forming the temporal overlap region in most single-shot images amounts to approximately 70-80, corresponding to approximately 150 ions taking into account the detection efficiency of approximately 50%, justifying the parameter range used here.
The simulation results were evaluated in a similar manner as in Ch. 4.3. When charge repulsion is neglected, the width of the ion image corresponding to the IAC temporal overlap group extends to 93.1 µm on the detector, as expected by the ion microscope magnification 3.8 µm×24.5=93.1 µm. When charge repulsion is enabled, the imaged ion channel width and IAC ion group extent appear broader on the detector surface. Already when using 10 ions in the IAC temporal overlap group, the IAC ion image gets 3.4 times broader, while with 150 ions the image of the IAC width appears 8.8 times larger than expected on the detector, in disagreement with the experimental results. The simulation predicts a continuous increase both in the width of the ion channel and the IAC width with a growing number of particles. Although intuitive, this result is in disagreement with the experimental observations and an additional effect, of undefined origin, needs to be taken into account in the simulation.
In summary, after excluding a temporal origin for the broader than expected IAC width, the influence of charge-particle imaging distortions has been experimentally investigated by increasing the number of generated ions in the interaction region. This has been accomplished both by increasing the local gas density, as well as the VUV pulse intensity. Although the ion channel radial size grows both with increased gas density and 5^{th} harmonic intensity, the spatial extent of the intensity autocorrelation width is not influenced, remaining constant. Autocorrelation measurements performed at pressure conditions where few ions per shot were produced, result in the same IAC temporal overlap spatial extent as in high gas density IAC measurements obtained using the pulsed gas valve. An additional SIMION simulation unfortunately did not provide insight in the origin of this effect. Nevertheless, all the comparative measurements performed so far, by using the fringe-resolved interferometric autocorrelation results as a benchmark, show a remarkably stable ratio between the obtained autocorrelation widths of approximately 4, compared in different experimental conditions and with different gas targets. Despite the fact that the exact origin of this behavior has not been experimentally accessible, the cross-calibration of the delay-time axis using the fringe-resolved interferometric autocorrelation width, has shown to be consistent with all the measurements that have been performed so far.

In view of these results, the use of a cross-calibrated adopted time-delay scale is justified, as the IAC temporal width is invariant to all different experimental conditions. Furthermore when utilizing a fixed calibration factor for the time-delay scale, the obtained results have been consistent with the FRIAC measurement results in all comparative measurements that have been performed within the timescale of the presented work. Although not self-contained in this case, the IAC measurement results deliver the same 5^{th} harmonic pulse duration measured by the FRIAC setup with use of a constant calibration factor in all the attempted comparative measurements.

6.2 Free-Electron Laser Experiments

The single-shot intensity autocorrelation approach presented in this thesis, although versatile and statistically efficient for use in laboratory-based experiments, it is mainly intended to temporally characterize light sources that exhibit strong shot-to-shot temporal fluctuations. Free-electron lasers (FEL) generating intense VUV-XUV pulses based on self-amplified spontaneous emission belong in this category, delivering pulses that exhibit fluctuations in almost all of their parameters. However, FEL pulses reach unsurpassed intensity levels in the VUV-XUV regime and therefore they are the most suitable light sources to perform XUV pump-probe experiments.

The experimental attempts reported in this section have been realized prior to the 162 nm experiments and the characterization studies described above, taking advantage of the individual pulse-ID data tagging functionality of the experimental apparatus. Both the acquired ion image and TOF spectrum were tagged with the individual pulse-ID number available at both facilities. The data acquisition synchronization has been verified prior to the experiment in both cases. The low level of the attainable non-linear signal needed for the autocorrelation measurement, prohibited a successful autocorrelation measurement in both experimental attempts. This section is intended to give a very brief overview of the attained results and the limitations encountered in both experiments.

The first experiment has taken place at the beamlines BL3 and BL2 at FLASH in Hamburg [20], using FEL pulses at 44 eV (28.2 nm) in combination with the experimental scheme and optical component set described in Ch. 3.2. Two-photon, double ionization of He has been chosen as the non-linear process to deliver an intensity autocorrelation signal in this case, also previously utilized at FLASH for a multi-shot, delay-scanning, intensity autocorrelation [215].

A single optical branch of the 44 eV experimental setup [Ch. 3.2] has been used to verify the ion signal non-linearity. The ion TOF signal was dominated by a saturated He^+ peak, in contrast to a barely visible He^{2+} peak. Unfortunately, the large amount of He^+ ion yield does not provide any temporal information, yet it is expected to increase charge repulsion effects. A typical experimental ion time-of-flight spectrum is shown in Fig. 6.6. The He^{2+} ion signal was not present in every shot, exhibiting large variations, as anticipated by a non-resonant multiphoton process strongly depending on the varying pulse temporal profile. A reduction of the gas density or the FEL beam intensity, in order to avoid space-charge effects in the ion imaging resulted in a dramatic decrease in the He^{2+} ion signal.

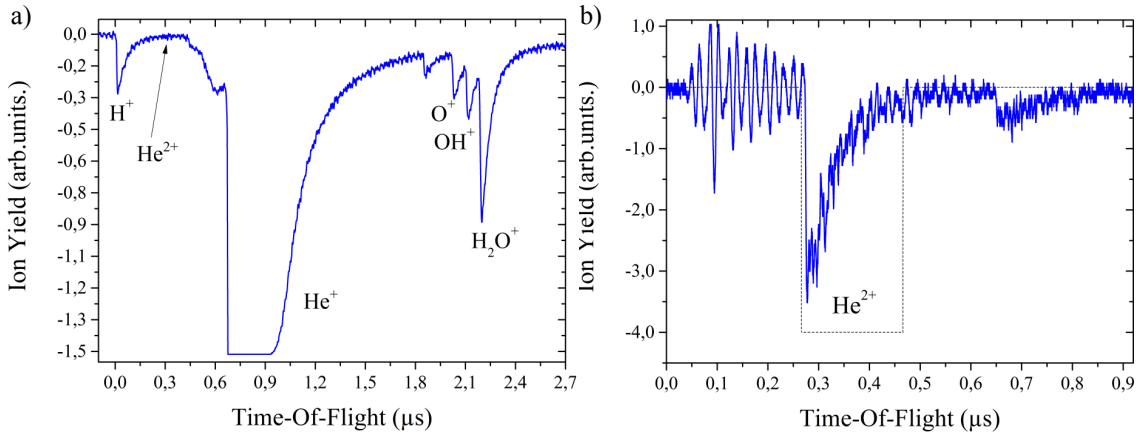

Figure 6.6: a) Averaged ion time-of-flight spectrum obtained at FLASH with a 44 eV photon energy pulse. While the He^+ ion signal is in saturation the He^{2+} ion peak is barely visible in the same scale. b) TOF-Gated He^{2+} ion peak in the same conditions. Few ions were present, not in every shot. The dashed grey line depicts the MCP detector gain time-gate.

Since the pulse temporal shape is not reproduced in every shot [33], obtaining a reliable intensity dependence is not a trivial task. For this reason, the measurement integrated over a large number of shots, in order to statistically reduce this variation as much as possible. The ion TOF spectrum has been acquired for a few hundred-thousand shots, by attenuating the FEL beam using a series of combinations of thin-metallic filters available at the BL3 beamline and taking advantage of the intrinsic pulse intensity fluctuations. The obtained ion TOF data were sorted and subsequently averaged according to the FEL pulse energy, using the pulse-ID tagged gas monitor detector data [296] available at FLASH. The corresponding results are presented in Fig. 6.7.

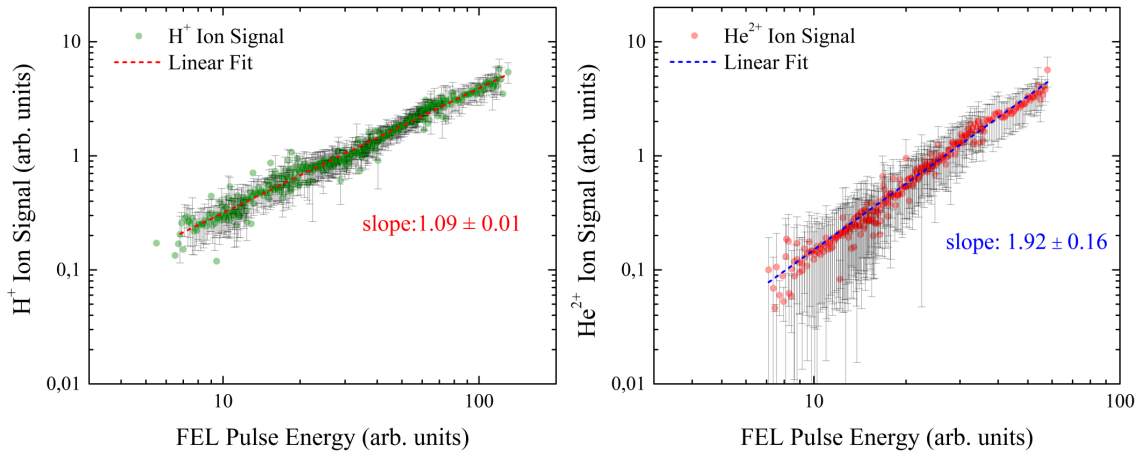

Figure 6.7: Two-photon, double-ionization of He at the Free-Electron Laser FLASH in Hamburg: The ion signal intensity dependence has been measured using a single branch of the counter-propagating pulse optical setup. Double ionization at 44 eV proceeds via non-resonant two-photon absorption, verified by the measured slope in a double-logarithmic scale. The measured slope of singly-ionized H, obtained in parallel serves as a benchmark measurement.

The He^{2+} ion signal plotted as a function of the FEL pulse energy, can be fitted with a slope of 2 in a double-logarithmic scale, denoting a direct two-photon absorption process according to the discussion in Ch. 3.2. In order to verify the consistency of this measurement, the H^+ peak obtained in the same experimental run, resulting from single-photon dissociation of residual H_2O in the experimental chamber has been processed in the same manner, showing a linear increase in a double-logarithmic scale, validating the presented results.
Having verified that the He^{2+} ion signal originates from direct two-photon absorption and thus it is suitable to obtain an intensity autocorrelation measurement, the second counter-propagating pulse has been introduced to the interaction region. Unfortunately, the attainable He^{2+} signal was too low to allow even a multi-shot measurement. A combined image of the He^{2+} ion distribution has been obtained by adding a large number of ion images and shown in Fig. 6.8a. The He^{2+} ion channel width, measured here 5.8 µm FWHM, cannot be safely assigned to the actual beam width in the focus, due to the low-count statistics combined with severe beam pointing instabilities observed during the experiment. It should be additionally noted, that the experimental setup was pre-aligned prior to the XUV experiment using the available Ti:Sa laser system used at FLASH for XUV-IR pump-probe experiments. The IR pulse at 800 nm propagated over the XUV-dedicated reflective components to generate a high-order intensity autocorrelation signal using Xe^+ ions as a non-linear medium. The intensity dependence of the Xe^+ ion signal has not been measured at FLASH due to time restrictions and therefore the IR pulse duration cannot be extracted by deconvolution as the corresponding multiplicative factor is unknown. The intensity autocorrelation FWHM is spatially encoded to a 22.25 µm width at FWHM, corresponding to an equivalent multi-photon intensity autocorrelation FWHM of 148.4 fs.

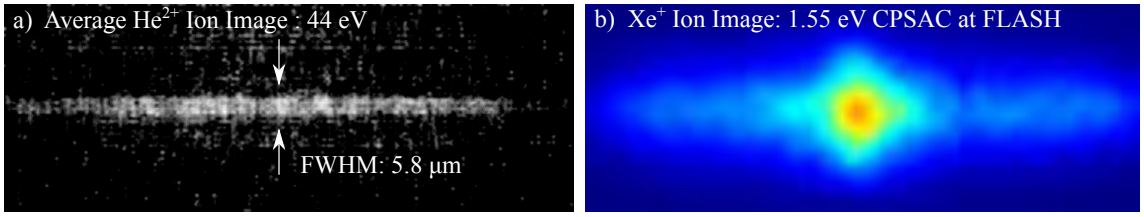

Figure 6.8: a. TOF Gated, multi-shot, combined He^{2+} ion image in the counter-propagating pulse common focus at FLASH (44 eV). b. Multi-photon IR counter-propagating pulse autocorrelation at FLASH using the facility's Ti:Sa pump-probe laser and Xe^+ ion signal as a non-linear target. Both images were obtained utilizing the 1:1 imaging relay-optics as shown in Fig. 4.1.

The appearance of the Xe^+ ion signal (I.P. : 12.13 eV) points to a high non-linearity considering the IR pulse photon energy of 1.55 eV. Although it is possible that the interaction does not lie within the perturbative regime, at least 8 photons are needed in this case for ionization. Considering this fact, the generation of Xe^+ ions is confined at the most intense part of the laser beam and in this way it provides the possibility to achieve a high-precision spatial and temporal beam overlap.
The second experiment took place at FERMI in Trieste [21] using a seeded-FEL pulse centered at 62 nm (20 eV). The experimental scheme used at FERMI is described in detail in Ch. 3.2.

Two-photon single ionization of He constitutes the non-linear autocorrelation process, avoiding an additional competing ionization channel, minimizing possible space-charge issues. An ion TOF spectrum obtained at FERMI operating at 62 nm is shown below.

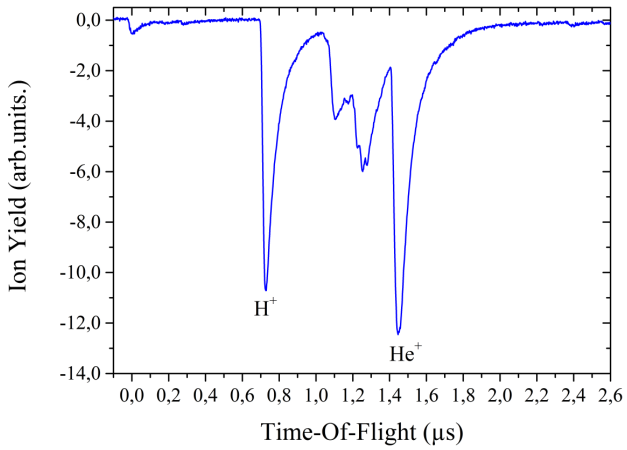

Figure 6.9: Averaged ion time-of-flight spectrum obtained at FERMI at 62 nm (20 eV). The amount of He^+ ions resulting from direct two-photon ionization is comparable to that from residual gas.

A pre-alignment experiment was not possible in this case and the available experimental time has been limited. Most of this time has been used in order to align the counter-propagating pulse spatial and temporal overlap under vacuum conditions. Unfortunately, no sign of an established temporal overlap was available by the end of this short experimental run. The amount of He^+ signal was limited, and the large divergence of the 62 nm FEL beam did not allow unrestricted propagation in the FEL beamline and the experimental setup.
Operating in a TOF-gated mode a series of He^+ as well as Xe^+ ion distribution images were acquired in the counter-propagating pulse common focus, shown in Fig. 6.10. Although the generation of a He^+ ion requires a two-photon absorption process, Xe is singly ionized with the absorption of a single photon at 20 eV. According to the discussion in Ch. 2.1, a signal proportional to the n^{th} power of the intensity will appear with a waist $\sqrt{n}$ narrower than the actual beam waste assuming a Gaussian profile $I^n(r,z) \propto \mathrm{Exp}\left[-2nr^2/w^2(z)\right]$.

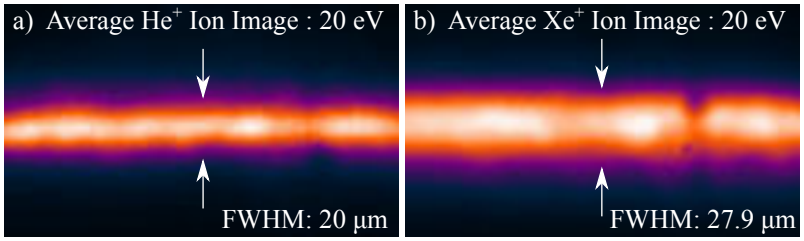

Figure 6.10: a. TOF Gated, multi-shot, combined He^+ ion image in the counter-propagating pulse common focus at FERMI (20 eV). b. TOF Gated, multi-shot, combined Xe^+ ion image in the counter-propagating pulse common focus at FERMI (20 eV). Both images were obtained utilizing the 1:1 imaging relay-optics as shown in Fig. 4.1.

This relation was indeed confirmed by the acquired ion distribution images shown in Fig. 6.10. The He^+ ion distribution shows an approximately $\sqrt{2}$ narrower waist than the Xe^+ ion distribution. Since the actual experimental parameters were not determined, a useful comparison between measured and calculated beam size cannot be attempted. The dark line observed in both images on the right side is attributed to a minor MCP crack as previously mentioned.

In summary, the extension of the counter-propagating pulse intensity autocorrelation technique in the XUV has been attempted both at FLASH and FERMI, at photon energies of 44 eV and 20 eV respectively. In both cases the small amount of non-linear ion signal, chosen to serve as an intensity autocorrelation signal, did not permit a successful measurement. Additionally, beam pointing instabilities and poor statistics did not allow the observation of a pulse temporal overlap in the common focus, although the experimental setup has been pre-aligned using an IR Ti:Sa laser pulse in the first experiment. Improvements in the intensity throughput and a robust pre-alignment may in principle deliver a multi-shot measurement. The possibility of single-shot operation still needs to be evaluated. The high-charge density commonly experienced in the focus of an FEL pulse will compromise the ion imaging quality, as observed in the VUV spectral region. Effective measures to minimize this effect include an appropriate gas target choice and a short FEL pulse favoring the desirable direct multi-photon ionization channel while significantly reducing the sequential single-photon ion yield.

7 Single-Shot Pump-Probe Experiments in the Vacuum Ultraviolet

The delay encoding principle employed in this counter-propagating pulse metrology technique can enable a single-shot pump-probe measurement and give access to time-constants associated with molecular dynamics in the VUV-XUV range. Obtaining an intensity autocorrelation measurement prior to a pump-probe dataset in the same apparatus, enables disclosing dynamics evolving at the same or even shorter timescale than the VUV pulse length [Fig. 2.7].
Gaining confidence from the invariance of the counter-propagating pulse intensity autocorrelation width as a function of all different experimental parameters that could be changed, in addition to the CaF_2 dispersion characterization measurement results, an experiment employing this single-shot VUV-pump/VUV-probe concept and investigating ultrafast dissociation dynamics of O_2 at 161.8 nm, has been carried out.
Here, the adopted delay-time scale has been employed for data analysis, delivering meaningful results, that are in excellent agreement with results obtained performing the same experiment with the fringe-resolved intensity autocorrelation (FRIAC) setup, using the same light source [222]. In addition to this, the results from both measurements are compliant with results obtained at the same wavelength and previously reported in the literature [30, 45]. The utilized delay-time scale is essentially provided by calibrating the delay-time axis of the counter-propagating pulse measurement [Fig. 6.1] using the FRIAC measurement results [Fig. 5.7] as mentioned before.
Although the technique is not self-contained in this way, depending on this cross-calibration, the excellent agreement of the obtained pump-probe results with those obtained in experiments employing different techniques justifies the use of this calibrated delay-time scale.

7.1 Ultrafast Dissociation Dynamics of O_2 at 162 nm

Utilizing the 5^{th} harmonic pulse and taking advantage of the counter-propagating pulse delay encoding principle, in combination with mass/charge state selective ion microscopy, a single-shot VUV-pump/VUV-probe experiment has been performed, investigating ultrafast dissociation of molecular oxygen excited in the Schumann-Runge continuum at 161.8 nm.
Absorption in the UV-VUV spectral region leading to predissociation and photodissociation of O_2 plays an important environmental role, leading to the formation of ozone and atomic oxygen in the stratosphere.

Exciting molecular oxygen well above the dissociation threshold in the first fully allowed excited state $B^3\Sigma_u^-$, gives rise to the Schumann-Runge continuum (176 nm - 100 nm) resulting in dissociation to neutral atomic oxygen (O^3P+O^1D) [279, 297].
Photodissociation in this spectral region is expected to be complete within few-tens of fs and has been investigated using ultrashort pulses in the VUV, utilizing single or two-color pump-probe schemes [30, 45, 52]. In these studies a VUV pulse is used to excite the molecule into the $B^3\Sigma_u^-$ state repulsive barrier, followed by a probing pulse leading to molecular ionization. Observation of the molecular ion signal versus the delay between the pump and probe pulses provides information on the wavepacket dynamics leading to molecular dissociation.
Here, exploiting the high intensity content of the VUV pulse along with its short duration, we attempted tracing the dissociation dynamics of molecular oxygen on a single-shot basis by selectively imaging the O_2^+ ion distribution in the common VUV pulse-pair focus. In the same delay encoding principle as described before, each of the partial beams excites O_2 molecules on each side of the focal volume while propagating towards the focal point, where the two pulses arrive at the same time. Subsequently, the role of the two pulses is exchanged, acting as a probe on the opposite side beyond the focal point. Their respective delay is encoded on the propagation axis as described above [Eq. 3.1] and selective-imaging of the O_2^+ ions delivers the complete pump-probe dataset in every shot. The respective ion TOF spectra associated with the observed O_2^+ ion distributions were previously shown in Fig. 4.14. The VUV-pump/VUV-probe experiment has been performed for different VUV pulse intensities on target, ranging between 120 nJ - 270 nJ, with no result deviations observed within the experimental uncertainty margin.

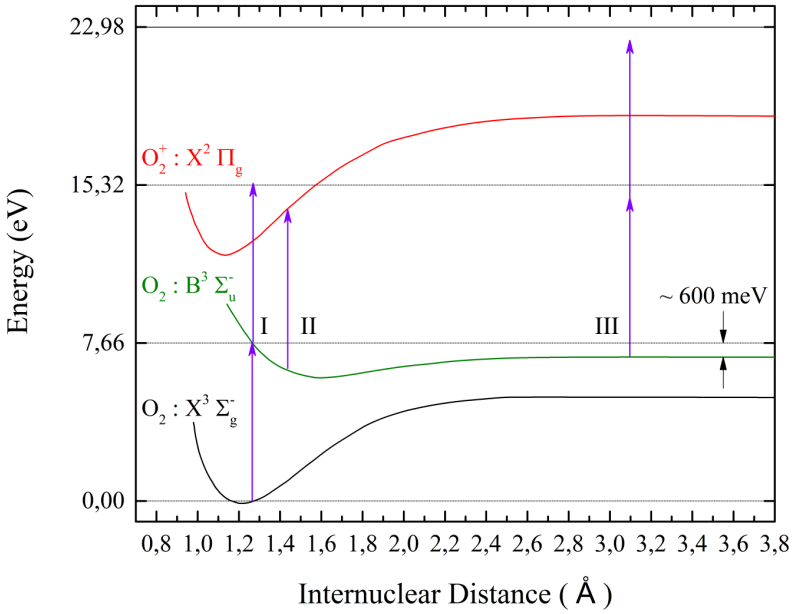

Figure 7.1: O_2 VUV-pump/VUV-probe excitation schematic at 161.8 nm. The violet arrows correspond to the 5^{th} harmonic pulse energy (7.66 eV). I: simultaneous absorption of two VUV photons - delay-time = 0, II: Molecular O_2 ionization window limit, III: Dissociation and two-photon atomic oxygen ionization. The potential energy curve data are adapted from [279].

The dynamics is initiated with the absorption of a pump-photon at 161.8 nm, exciting O_2 approximately 0.58 eV above the dissociation limit [279]. In a second step, the delayed 161.8 nm probe pulse leads to ionization, generating O_2^+ ions. The O_2^+ pump-probe signal is evaluated with prior knowledge of the finite instrument response function, which in this case corresponds to the measured intensity autocorrelation function. The O_2 time-constant, assigned to the dynamics within the ionization widow, is obtained by deconvolution assuming an exponential decay [Eq.2.65], justified in that case as in [45, and references therein].
By comparing the fitted curves, corresponding to the Kr^+ ion distribution and the O_2^+ ion distribution, a distinct broadening attributed to the corresponding wavepacket dynamics in the $B^3\Sigma_u^-$ state leading to dissociation is observed [Fig. 7.2]. This broadening corresponds to a ratio between the pump-probe and autocorrelation trace widths, of approximately $\tau_{\text{p-p}}/\tau_{\text{IAC}} = 1.24$, having been reproduced over several measurements conducted during different days.
When the adopted delay timescale is used, this corresponds to an exponential decay rate of $\tau_{O_2} = 7.3 \pm 2.7$ fs. The same measurement has been performed using the FRIAC setup by T. Gebert and presented in [222], disclosing an exponential decay rate of $\tau_{O_2} = 6.6 \pm 1.7$ fs, extracted in the same manner as here.

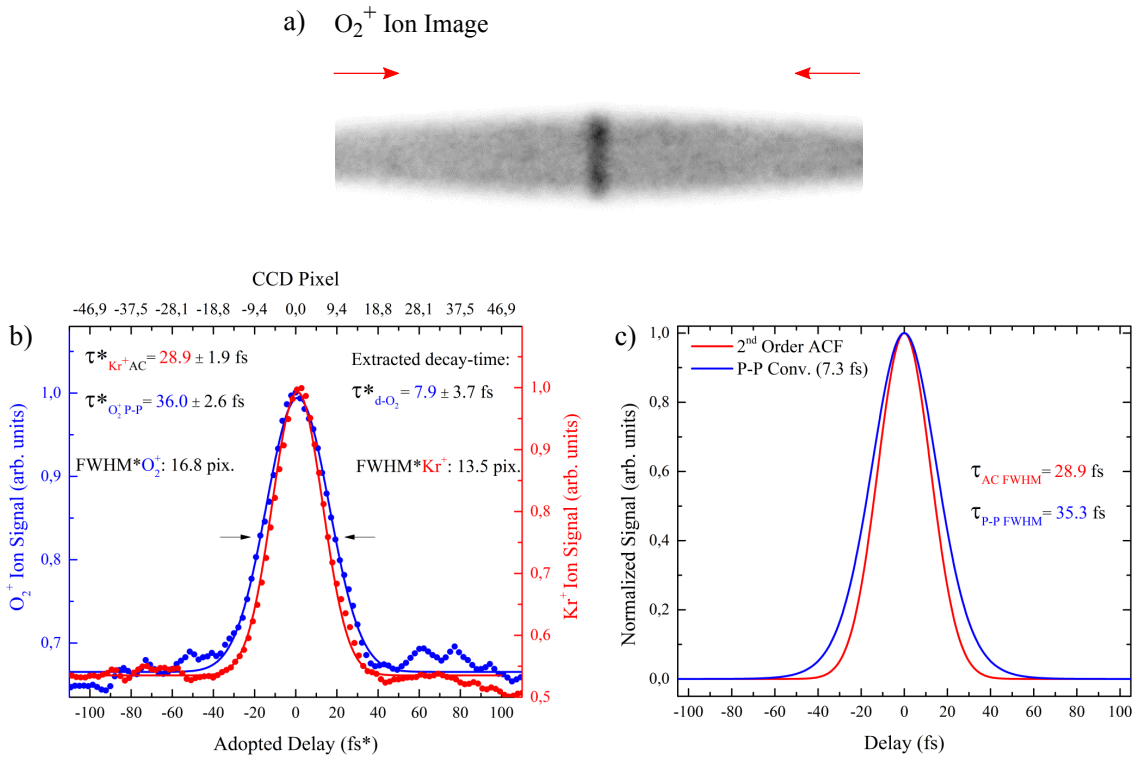

Figure 7.2: VUV-pump/VUV-probe data at 161.8 nm investigating ultrafast dissociation of O_2^+. a) Average O_2^+ measurement over 130 shots, b) Image-integrated signal profile along with the Kr^+ autocorrelation dataset, c) Simulated signal in correspondence to the experimental data shown in 4b.

This very good agreement between the two results, justifies the use of the delay-time calibrated scale for analyzing the counter-propagating pulse data. It additionally indicates that the 5^{th} harmonic pulse cannot be longer in the counter-propagating pulse experiment. If this would have been the case, it would be impossible to observe a temporal broadening in the convolution signal. The measured Kr^+ autocorrelation trace width corresponds to 115.6 fs FWHM, as converted using the CCD pixel size (binning: 2×) and a measured ion imaging magnification of 11.57 ± 0.5, resulting in a 8.53 fs/pixel conversion factor. For an exponential decay time of $\tau_{O_2} = 6.6$ fs, the obtained convolution, or pump-probe signal in this case, would result in a FWHM of 117.5 fs [Eq. 2.65]. Compared to the intensity autocorrelation width of 115.6 fs FWHM, this broadening would be unobservable as the temporal resolution is given by the 8.53 fs/pixel factor and as a result, both the intensity autocorrelation and pump-probe traces should appear identical.

It should be noted that the decay time reflects the wavepacket dynamics in the $B^3\Sigma_u^-$ state, as long as the probe transition can lead to an ionic signal. The final state reached by the probe pulse, that is a bound molecular O_2^+ state, defines the observation window in such a pump-probe measurement as mentioned before [30] and it is specific to the investigated system and the probe-pulse wavelength. Ideally, a fixed pump and a tunable probe wavelength can investigate the complete dissociation dynamics.

The presence of O^+ ion signal along the complete focal volume verifies an additional 2 photon absorption, as it can only occur either after the dissociation of O_2^+, or by two-photon direct ionization of neutral oxygen atoms resulting from the neutral O_2 dissociation. In the first case, a third VUV photon is necessary to reach O_2^+ excited dissociative states lying well above a 1+1 photon transition at 161.8 nm resulting in one ionized atomic oxygen fragment in addition to a neutral oxygen atom [279]. In the second case direct two-photon absorption is required, either from the $O(^3P)$ atomic ground state or the $O(^1D)$ excited state. Discrimination between the two possible pathways is possible by measuring the kinetic energy release which is expected to differ in the two different excitation pathways. This information has been indeed obtained in a previous study using the same wavelength as in this work for the pump pulse [45]. The recoil energy was recorded as the difference in the time-of-flight between forward and backward ejected ionic fragments, corresponding to a total kinetic energy release of 600 meV in good agreement with the energy difference between the excitation energy and the dissociation limit.

In this study, the momentum-sensitive imaging mode of the ion microscope has been utilized in order to measure the atomic oxygen fragment recoil energy and verify the excitation pathway. By detuning the electrostatic lens voltage ratio required for achromatic imaging, ions with an initial momentum vector parallel to the light polarization vector are imaged on the detector plane as two separate ion channel images as described in Ch. 4.3. For a minor voltage detuning in the order of 0.5% of its initial value ($V_{LENS}/V_{REP} = 0.3737 \pm 0.0010$), the two ion channel images retain their spatial characteristics, while they are mutually displaced by a definite distance which scales with their initial kinetic energy in a well-defined predictable manner.

The obtained O^+ ion image is shown in Fig. 7.3a. The image corresponds to an average measurement over a few hundred shots and shows the anticipated behavior with two distinct ion channel images mutually displaced from the detector center with a peak-to-peak distance of 325.6 µm±14 µm.

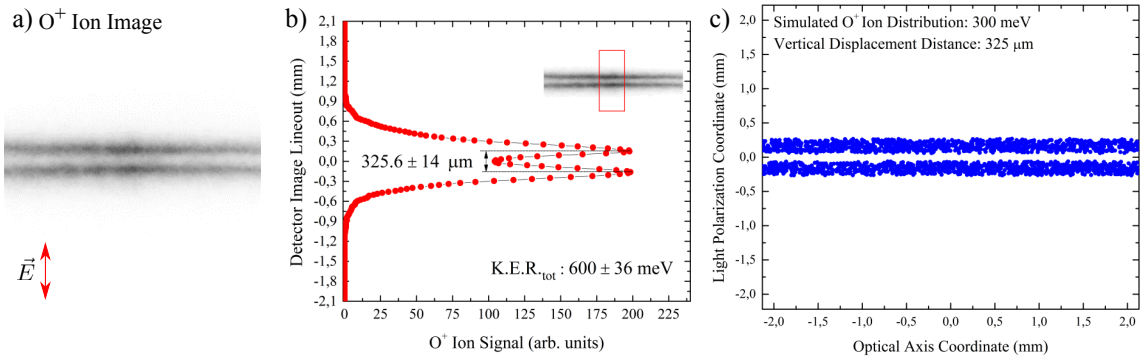

Figure 7.3: O^+ Ion Signal: Kinetic energy release following O_2 dissociation imaged with the ion microscope: 7.3a) Experimental O^+ Ion Signal., 7.3b) O^+ ion image profile (red box enclosed integrated area plotted) showing a peak-to-peak distance of 325.6 µm±14 µm in excellent agreement with the simulated value in 7.3c), 7.3c) Simulated O^+ ion distribution taking into account the experimental parameters and 300 meV initial kinetic energy per fragment in the light polarization vector direction.

This result is in excellent agreement with a simulated displacement value of 325 µm for a total recoil energy of 600 meV. The simulated displacement of 325 µm is predicted for two groups of O^+ ions, starting from a common cylindrical focal volume, with an equally shared initial kinetic energy of 600 meV and momentum vectors pointing along the two directions defined by the light polarization vector respectively.
The simulated ion distribution image on the detector, taking into account the current experimental parameters is shown in Fig. 7.3c along with the experimentally obtained ion distribution image Fig. 7.3a and the corresponding profile plot, showing the peak-to-peak distance in Fig. 7.3b. The same result is also observed when one of the counter-propagating pulses is blocked and the excitation is driven by a single VUV pulse. This finding verifies the hypothesis that the O^+ fragments, are generated by direct two-photon absorption after molecular dissociation in the $B^3\Sigma_u^-$ state in accordance to the result reported in [45] although with a different probing scheme.
In summary, it has been shown that the counter-propagating pulse delay encoding principle, combined with mass/charge selective ion imaging can be used to deliver an individual-shot VUV-pump/VUV-probe dataset. Utilizing a cross calibrated delay-time scale the experimental outcome is in very good agreement with the results obtained using the FRIAC experimental setup for the same measurement [222]. Ultrafast dissociation dynamics of O_2 after excitation in the Schumann-Runge continuum have been followed within the ionization window. Although not commonly available, but conceivable, a wavelength tunable, sub-20 fs VUV pulse would constitute an ideal probe, providing the possibility to follow the molecular dissociation process as long as the ionic ground state potential curve permits. Furthermore, operated in a momentum-resolving mode, the ion microscope can record kinetic energy release for the oxygen atomic fragments and identify the excitation pathway. The experimentally observed ion channel separation is in very good agreement with the simulated values. The lack of temporal evolution in the atomic oxygen ion signal, points at a post-ionization of the atomic fragments at a large internuclear distance.

8 Conclusions and Outlook

In this thesis, a set of experimental techniques and the corresponding instrumentation have been established, facilitating individual pulse temporal metrology in the VUV-XUV spectral range.

In order to enable multi-photon time-resolved spectroscopy in the VUV, a light source based on high-harmonic generation, delivering intense 162 nm pulses, has been implemented, optimized and characterized. An intense driving IR pulse supports a loose-focusing geometry, allowing efficient phase-matched harmonic generation in a long Ar gas cell. The optimal generation conditions have been investigated, using Ar or Xe as a generating medium. It was concluded that when using Ar the 5^{th} harmonic pulse intensity follows a continuous increasing trend and can be further scaled by higher laser energies or gas densities, in contrast to the case where Xe is employed as a generation medium.

The 5^{th} harmonic pulse reaches up to 1.1 µJ/pulse corresponding to 9×10^{11} photons/pulse and a conversion efficiency of 10^{-4}. Its high intensity content has been verified by the observation of non-resonant two- and three-photon absorption in the focus of a long focal-length focusing mirror. The attainable high peak intensity overcomes low-cross section limitations and enables versatile multi-photon excitation schemes in the VUV. Additionally, the high pulse energy permits the use of large focal dimensions that result in an exceptional signal-to-noise ratio. The experimental setup is designed in a way, that all the relevant generation parameters can be varied while performing the experiment, providing the possibility to efficiently optimize the output by monitoring the pulse parameters with the implemented instrumentation. As a future development, a wavelength tunable HHG driving pulse, originating from an optical parametric amplifier, seeded by the 15 mJ IR pulse, can be used alternatively. In this way, wavelength-tunable, ultrashort harmonic pulses can be generated, providing the possibility to perform two-color VUV-XUV pump-probe experiments with adjustable wavelength.

In order to extend single-shot nonlinear autocorrelation methodology to the VUV-XUV spectral range, an all-reflective counter-propagating pulse setup has been designed and experimentally realized. Three different spectral variants of this setup have been implemented and used in separate experiments. The optical geometry and the optical components have been optimized in all cases, in order to satisfy transmission and multiphoton signal constraints in each spectral regime. Additionally, multi-photon processes that can deliver an autocorrelation measurement have been identified for each case and their experimental feasibility has been evaluated. In this approach, the delay between two pulse replicas is encoded on their common propagation axis. The complete autocorrelation measurement is performed during each shot by spatially resolving the resulting nonlinear signal with an imaging detector.

The delay-encoding principle has been experimentally established and verified in ambient conditions, employing a NIR pulse and non-resonant two-photon fluorescence in CdSe quantum dots as an autocorrelation non-linear process. The extracted pulse duration is in good agreement with the laser system manufacturer's specifications. Moreover this experimental implementation allowed a very good degree of pre-alignment of the VUV-XUV optical setups.

An instantaneous non-linear signal, necessary for obtaining an intensity autocorrelation measurement in the VUV-XUV can be provided by direct multiphoton ionization. An ion-imaging time-of-flight spectrometer has been set-up and characterized, providing a mass/charge state-selective magnified image of the ion distribution in the counter-propagating pulse common focus. A set of simulations has been performed in advance, in order to determine the corresponding ion-imaging specifications. The simulated ion image magnification and time-of-flight specifications are reproduced in all experimental datasets, providing confidence in the simulation results. Experimentally, charge-repulsion effects become obvious at an increased ion density, resulting either from higher gas pressure or pulse energy. In this case, it was found that ion imaging is influenced, resulting in an increasingly 'broader' ion distribution image with increased ion density.

In combination with the dedicated counter-propagating optical setup, a single-shot intensity autocorrelation measurement of the 5^{th} harmonic pulse could be obtained. Non-resonant, two-photon ionization of Kr or Xe has been used as a second-order intensity autocorrelation process, providing the same results in consecutive measurements.

The resulting autocorrelation temporal width is found to be broader than expected and previously measured in the same laboratory using the same 5^{th} harmonic generation conditions, with a fringe-resolved intensity autocorrelation setup [220, 222, 294]. A complete series of characterization measurements has been therefore performed, in order to identify the origin of this broadening. In a first step, temporal distortions induced by the optical components were excluded and the validity of the delay encoding principle has been verified with the VUV setup. Varying the ion density in the focal volume by tuning the gas pressure or the VUV pulse energy, results in a constant autocorrelation width for a very broad experimental parameter range. Furthermore, space-charge induced distortions or gain saturation effects originating from the position-sensitive detector have been experimentally excluded.

Retaining a constant behavior under any parameter variation, the broadening effect appears to be a constant systematic imperfection and therefore the intensity autocorrelation can be cross-calibrated using the FRIAC result obtained under the same conditions. The intensity autocorrelation width shows a remarkable invariance to the ion density in the interaction region. Moreover, it has been verified that the utilized calibration factor does not vary in any measurement performed under different experimental conditions or using different gas targets. During the period of several months, no discrepancy has been found between the measurements obtained by the two experimental setups, within the experimental uncertainty, using a fixed calibration factor. This result validates the use of a calibrated time-delay scale for the reported experiments.

Extending the scope of the presented single-shot metrology approach, a single-shot VUV-pump/VUV-probe experiment has been performed, using the same delay-encoding concept. As a proof of principle experiment, the few-femtosecond dissociation dynamics of O_2, excited in the Schumann-Runge continuum at 162 nm, are investigated on a shot-to-shot basis. Combining the intensity autocorrelation information with that obtained by the VUV-pump/VUV-probe experiment, ultrafast dissociation dynamics of O_2 after excitation in the Schumann-Runge continuum can be followed within the ionization window. The extracted time-constant is in excellent agreement with that obtained when performing the same experiment using the FRIAC experimental setup, providing an additional verification of the utilized calibration factor.
Operated in a momentum-resolving mode, the ion microscope reveals the kinetic energy release of the oxygen atomic fragments resulting from molecular dissociation, being in very good agreement with the simulation results.
Results obtained at two free-electron laser experiments and the corresponding experimental limitations that have been encountered are also discussed in detail. The limited amount of multi-photon signal did not permit a single-shot operation in both cases.
Finally, it has been verified that the experimental approach is applicable in the VUV spectral range, delivering meaningful results. A cross-calibration experiment delivers a time-delay calibration factor which has been found to be robust in all the experiments performed. The experimental setup can be adapted in order to accommodate pulses in the XUV range, or a bi-color combination within the DUV-XUV. This enables a variety of one or two-color pump-probe experiments that require high temporal resolution in the few-fs timescale. The long delay range encoded in the focal region, offers additionally the possibility for investigating dynamics evolving over a long timescale. Utilizing the extended delay-range, this approach is advantageous for high-resolution spectroscopic techniques where the spectral resolution relies on the time-delay extent. Such approaches based on quantum interference metrology and linear or nonlinear Fourier-transform spectroscopy have already been demonstrated in the VUV-XUV range [15, 16, 298–300] and in combination with intense broad continuum VUV-XUV light-sources are expected to reach unprecedented spectral resolution. The high data collection efficiency of this counter-propagating pulse setup provides an advantageous alternative for such schemes, avoiding optical misalignment and operation stability restrictions, commonly present over the long delay scan range.

Bibliography

[1] A. H. Zewail. Laser Femtochemistry. *Science*, **242** (1988), 1645. doi:10.1126/science.242.4886.1645.

[2] A. H. Zewail. Femtochemistry. Past, present, and future. *Pure Appl. Chem.*, **72** (2000), 2219. doi:10.1351/pac200072122219.

[3] W. Demtröder. Laser Spectroscopy (Springer-Verlag, Berlin, Heidelberg, New York, 2003), third edition. ISBN 978-3-642-53858-2. doi:10.1007/978-3-642-53859-9.

[4] I. V. Hertel & W. Radloff. Ultrafast dynamics in isolated molecules and molecular clusters. *Reports on Progress in Physics*, **69** (2006), 1897.

[5] A. McPherson, G. Gibson, H. Jara, U. Johann, T. S. Luk, I. A. McIntyre, K. Boyer, & C. K. Rhodes. Studies of multiphoton production of vacuum-ultraviolet radiation in the rare gases. *J. Opt. Soc. Am. B*, **4** (1987), 595. doi:10.1364/JOSAB.4.000595.

[6] M. Ferray, A. L'Huillier, X. F. Li, L. a. Lompre, G. Mainfray, & C. Manus. Multiple-harmonic conversion of 1064 nm radiation in rare gases. *J. Phys. B At. Mol. Opt. Phys.*, **21** (1988), L31. doi:10.1088/0953-4075/21/3/001.

[7] M. Protopapas, C. H. Keitel, & P. L. Knight. Atomic physics with super-high intensity lasers. *Reports Prog. Phys.*, **60** (1997), 389. doi:10.1088/0034-4885/60/4/001.

[8] M. Drescher, M. Hentschel, R. Kienberger, G. Tempea, C. Spielmann, G. A. Reider, P. B. Corkum, & F. Krausz. X-ray pulses approaching the attosecond frontier. *Science*, **291** (2001), 1923. doi:10.1126/science.1058561.

[9] P. M. Paul, E. S. Toma, P. Breger, G. Mullot, F. Auge, P. Balcou, H. G. Muller, & P. Agostini. Observation of a train of attosecond pulses from high harmonic generation. *Science*, **292** (2001), 1689. doi:10.1126/science.1059413.

[10] M. Drescher, M. Hentschel, R. Kienberger, M. Uiberacker, V. Yakovlev, A. Scrinzi, T. Westerwalbesloh, U. Kleineberg, U. Heinzmann, & F. Krausz. Time-resolved atomic inner-shell spectroscopy. *Nature*, **419** (2002), 803. doi:10.1038/nature01143.

[11] P. Agostini & L. F. DiMauro. The physics of attosecond light pulses. *Reports Prog. Phys.*, **67** (2004), 813. doi:10.1088/0034-4885/67/6/R01.

[12] K. Midorikawa, Y. Nabekawa, & A. Suda. XUV multiphoton processes with intense high-order harmonics. *Prog. Quantum Electron.*, **32** (2008), 43. doi: 10.1016/j.pquantelec.2008.04.001.

[13] F. Krausz & M. Ivanov. Attosecond physics. *Rev. Mod. Phys.*, **81** (2009), 163. doi:10.1103/RevModPhys.81.163.

[14] E. Skantzakis, P. Tzallas, J. E. Kruse, C. Kalpouzos, O. Faucher, G. D. Tsakiris, & D. Charalambidis. Tracking autoionizing-wave-packet dynamics at the 1-fs temporal scale. *Phys. Rev. Lett.*, **105** (2010), 043902. doi:10.1103/PhysRevLett.105.043902.

[15] T. Okino, Y. Furukawa, T. Shimizu, Y. Nabekawa, K. Yamanouchi, & K. Midorikawa. Nonlinear Fourier transformation spectroscopy of small molecules with intense attosecond pulse train. *J. Phys. B At. Mol. Opt. Phys.*, **47** (2014), 124007. doi: 10.1088/0953-4075/47/12/124007.

[16] P. A. Carpeggiani, P. Tzallas, A. Palacios, D. Gray, F. Martín, & D. Charalambidis. Disclosing intrinsic molecular dynamics on the 1-fs scale through extreme-ultraviolet pump-probe measurements. *Phys. Rev. A*, **89** (2014), 023420. doi:10.1103/PhysRevA.89.023420.

[17] E. Constant, D. Garzella, P. Breger, E. Mével, C. Dorrer, C. Le Blanc, F. Salin, & P. Agostini. Optimizing High Harmonic Generation in Absorbing Gases: Model and Experiment. *Physical Review Letters*, **82** (1999), 1668. doi:10.1103/PhysRevLett.82.1668.

[18] E. Takahashi, Y. Nabekawa, M. Nurhuda, & K. Midorikawa. Generation of high-energy high-order harmonics by use of a long interaction medium. *J. Opt. Soc. Am. B*, **20** (2003), 158. doi:10.1364/JOSAB.20.000158.

[19] W. Boutu, T. Auguste, J. P. Caumes, H. Merdji, & B. Carré. Scaling of the generation of high-order harmonics in large gas media with focal length. *Physical Review A*, **84** (2011), 053819. doi:10.1103/PhysRevA.84.053819.

[20] W. Ackermann, G. Asova, V. Ayvazyan, A. Azima, N. Baboi, J. Bähr, V. Balandin, B. Beutner, A. Brandt, A. Bolzmann, R. Brinkmann, O. I. Brovko, M. Castellano, P. Castro, L. Catani, E. Chiadroni, S. Choroba, A. Cianchi, J. T. Costello, D. Cubaynes, J. Dardis, W. Decking, H. Delsim-Hashemi, A. Delserieys, G. Di Pirro, M. Dohlus, S. Düsterer, A. Eckhardt, H. T. Edwards, B. Faatz, J. Feldhaus, K. Flöttmann, J. Frisch, L. Fröhlich, T. Garvey, U. Gensch, C. Gerth, M. Görler, N. Golubeva, H. Grabosch, M. Grecki, O. Grimm, K. Hacker, U. Hahn, J. H. Han, K. Honkavaara, T. Hott, M. Hüning, Y. Ivanisenko, E. Jaeschke, W. Jalmuzna, T. Jezynski, R. Kammering, V. Katalev, K. Kavanagh, E. T. Kennedy, S. Khodyachykh, K. Klose, V. Kocharyan, M. Körfer, M. Kollewe, W. Koprek, S. Korepanov, D. Kostin, M. Krassilnikov, G. Kube, M. Kuhlmann, C. L. S. Lewis, L. Lilje, T. Limberg, D. Lipka, F. Löhl, H. Luna, M. Luong, M. Martins, M. Meyer,

P. Michelato, V. Miltchev, W. D. Möller, L. Monaco, W. F. O. Müller, O. Napieralski, O. Napoly, P. Nicolosi, D. Nölle, T. Nuñez, A. Oppelt, C. Pagani, R. Paparella, N. Pchalek, J. Pedregosa-Gutierrez, B. Petersen, B. Petrosyan, G. Petrosyan, L. Petrosyan, J. Pflüger, E. Plönjes, L. Poletto, K. Pozniak, E. Prat, D. Proch, P. Pucyk, P. Radcliffe, H. Redlin, K. Rehlich, M. Richter, M. Roehrs, J. Roensch, R. Romaniuk, M. Ross, J. Rossbach, V. Rybnikov, M. Sachwitz, E. L. Saldin, W. Sandner, H. Schlarb, B. Schmidt, M. Schmitz, P. Schmüser, J. R. Schneider, E. A. Schneidmiller, S. Schnepp, S. Schreiber, M. Seidel, D. Sertore, A. V. Shabunov, C. Simon, S. Simrock, E. Sombrowski, A. A. Sorokin, P. Spanknebel, R. Spesyvtsev, L. Staykov, B. Steffen, F. Stephan, F. Stulle, H. Thom, K. Tiedtke, M. Tischer, S. Toleikis, R. Treusch, D. Trines, I. Tsakov, E. Vogel, T. Weiland, H. Weise, M. Wellhöfer, M. Wendt, I. Will, A. Winter, K. Wittenburg, W. Wurth, P. Yeates, M. V. Yurkov, I. Zagorodnov, & K. Zapfe. Operation of a free-electron laser from the extreme ultraviolet to the water window. *Nat. Photonics*, **1** (2007), 336. doi:10.1038/nphoton.2007.76.

[21] E. Allaria, R. Appio, L. Badano, W. Barletta, S. Bassanese, S. Biedron, A. Borga, E. Busetto, D. Castronovo, P. Cinquegrana, S. Cleva, D. Cocco, M. Cornacchia, P. Craievich, I. Cudin, G. D'Auria, M. Dal Forno, M. Danailov, R. De Monte, G. De Ninno, P. Delgiusto, A. Demidovich, S. Di Mitri, B. Diviacco, A. Fabris, R. Fabris, W. Fawley, M. Ferianis, E. Ferrari, S. Ferry, L. Froehlich, P. Furlan, G. Gaio, F. Gelmetti, L. Giannessi, M. Giannini, R. Gobessi, R. Ivanov, E. Karantzoulis, M. Lonza, A. Lutman, B. Mahieu, M. Milloch, S. Milton, M. Musardo, I. Nikolov, S. Noe, F. Parmigiani, G. Penco, M. Petronio, L. Pivetta, M. Predonzani, F. Rossi, L. Rumiz, A. Salom, C. Scafuri, C. Serpico, P. Sigalotti, S. Spampinati, C. Spezzani, M. Svandrlik, C. Svetina, S. Tazzari, M. Trovo, R. Umer, A. Vascotto, M. Veronese, R. Visintini, M. Zaccaria, D. Zangrando, & M. Zangrando. Highly coherent and stable pulses from the FERMI seeded free-electron laser in the extreme ultraviolet. *Nat. Photonics*, **6** (2012), 699. doi:10.1038/nphoton.2012.233.

[22] P. Emma, R. Akre, J. Arthur, R. Bionta, C. Bostedt, J. Bozek, A. Brachmann, P. Bucksbaum, R. Coffee, F.-J. Decker, Y. Ding, D. Dowell, S. Edstrom, A. Fisher, J. Frisch, S. Gilevich, J. Hastings, G. Hays, P. Hering, Z. Huang, R. Iverson, H. Loos, M. Messerschmidt, A. Miahnahri, S. Moeller, H.-D. Nuhn, G. Pile, D. Ratner, J. Rzepiela, D. Schultz, T. Smith, P. Stefan, H. Tompkins, J. Turner, J. Welch, W. White, J. Wu, G. Yocky, & J. Galayda. First lasing and operation of an ångstrom-wavelength free-electron laser. *Nat. Photonics*, **4** (2010), 641. doi:10.1038/nphoton.2010.176.

[23] T. Ishikawa, H. Aoyagi, T. Asaka, Y. Asano, N. Azumi, T. Bizen, H. Ego, K. Fukami, T. Fukui, Y. Furukawa, S. Goto, H. Hanaki, T. Hara, T. Hasegawa, T. Hatsui, A. Higashiya, T. Hirono, N. Hosoda, M. Ishii, T. Inagaki, Y. Inubushi, T. Itoga, Y. Joti, M. Kago, T. Kameshima, H. Kimura, Y. Kirihara, A. Kiyomichi, T. Kobayashi, C. Kondo, T. Kudo, H. Maesaka, X. M. Maréchal, T. Masuda, S. Matsubara, T. Matsumoto, T. Matsushita, S. Matsui, M. Nagasono, N. Nariyama, H. Ohashi, T. Ohata, T. Ohshima, S. Ono, Y. Otake, C. Saji, T. Sakurai, T. Sato, K. Sawada, T. Seike,

K. Shirasawa, T. Sugimoto, S. Suzuki, S. Takahashi, H. Takebe, K. Takeshita, K. Tamasaku, H. Tanaka, R. Tanaka, T. Tanaka, T. Togashi, K. Togawa, A. Tokuhisa, H. Tomizawa, K. Tono, S. Wu, M. Yabashi, M. Yamaga, A. Yamashita, K. Yanagida, C. Zhang, T. Shintake, H. Kitamura, & N. Kumagai. A compact X-ray free-electron laser emitting in the sub-ångström region. *Nat. Photonics*, **6** (2012), 540. doi: 10.1038/nphoton.2012.141.

[24] N. Miyamoto, M. Kamei, D. Yoshitomi, T. Kanai, T. Sekikawa, T. Nakajima, & S. Watanabe. Observation of Two-Photon Above-Threshold Ionization of Rare Gases by xuv Harmonic Photons. *Phys. Rev. Lett.*, **93** (2004), 83903. doi:10.1103/PhysRevLett.93.083903.

[25] E. P. Benis, D. Charalambidis, T. N. Kitsopoulos, G. D. Tsakiris, & P. Tzallas. Two-photon double ionization of rare gases by a superposition of harmonics. *Phys. Rev. A*, **74** (2006), 051402. doi:10.1103/PhysRevA.74.051402.

[26] M. Meyer, D. Cubaynes, J. Dardis, P. Hayden, P. Hough, V. Richardson, E. Kennedy, J. Costello, S. Düsterer, W. Li, P. Radcliffe, H. Redlin, J. Feldhaus, S. Strakhova, E. Gryzlova, A. Grum-Grzhimailo, R. Taïeb, & A. Maquet. Two-color experiments in the gas phase at FLASH. *J. Electron Spectros. Relat. Phenomena*, **181** (2010), 111. doi:10.1016/j.elspec.2010.05.015.

[27] A. Rudenko, Y. H. Jiang, M. Kurka, K. U. Kühnel, L. Foucar, O. Herrwerth, M. Lezius, M. F. Kling, C. D. Schröter, R. Moshammer, & J. Ullrich. Exploring few-photon, few-electron reactions at FLASH: from ion yield and momentum measurements to time-resolved and kinematically complete experiments. *J. Phys. B At. Mol. Opt. Phys.*, **43** (2010), 194004. doi:10.1088/0953-4075/43/19/194004.

[28] B. Rudek, S.-K. Son, L. Foucar, S. W. Epp, B. Erk, R. Hartmann, M. Adolph, R. Andritschke, A. Aquila, N. Berrah, C. Bostedt, J. Bozek, N. Coppola, F. Filsinger, H. Gorke, T. Gorkhover, H. Graafsma, L. Gumprecht, A. Hartmann, G. Hauser, S. Herrmann, H. Hirsemann, P. Holl, A. Hömke, L. Journel, C. Kaiser, N. Kimmel, F. Krasniqi, K.-U. Kühnel, M. Matysek, M. Messerschmidt, D. Miesner, T. Möller, R. Moshammer, K. Nagaya, B. Nilsson, G. Potdevin, D. Pietschner, C. Reich, D. Rupp, G. Schaller, I. Schlichting, C. Schmidt, F. Schopper, S. Schorb, C.-D. Schröter, J. Schulz, M. Simon, H. Soltau, L. Strüder, K. Ueda, G. Weidenspointner, R. Santra, J. Ullrich, A. Rudenko, & D. Rolles. Ultra-efficient ionization of heavy atoms by intense X-ray free-electron laser pulses. *Nat. Photonics*, **6** (2012), 858. doi: 10.1038/nphoton.2012.261.

[29] Y. Hikosaka, M. Fushitani, A. Matsuda, T. Endo, Y. Toida, E. Shigemasa, M. Nagasono, K. Tono, T. Togashi, M. Yabashi, T. Ishikawa, & A. Hishikawa. Five-photon sequential double ionization of He in intense extreme-ultraviolet free-electron laser fields. *Phys. Rev. A*, **90** (2014), 053403. doi:10.1103/PhysRevA.90.053403.

[30] A. Peralta Conde, J. Kruse, O. Faucher, P. Tzallas, E. P. Benis, & D. Charalambidis. Realization of time-resolved two-vacuum-ultraviolet-photon ionization. *Phys. Rev. A*, **79** (2009), 061405. doi:10.1103/PhysRevA.79.061405.

[31] H. Tao, T. K. Allison, T. W. Wright, A. M. Stooke, C. Khurmi, J. van Tilborg, Y. Liu, R. W. Falcone, A. Belkacem, & T. J. Martínez. Ultrafast internal conversion in ethylene. I. The excited state lifetime. *J. Chem. Phys.*, **134** (2011), 244306. doi:10.1063/1.3604007.

[32] A. González-Castrillo, A. Palacios, H. Bachau, & F. Martín. Clocking Ultrafast Wave Packet Dynamics in Molecules through UV-Induced Symmetry Breaking. *Phys. Rev. Lett.*, **108** (2012), 063009. doi:10.1103/PhysRevLett.108.063009.

[33] E. Saldin, E. Schneidmiller, & M. Yurkov. Statistical properties of the radiation from VUV FEL at DESY operating at 30nm wavelength in the femtosecond regime. *Nucl. Instruments Methods Phys. Res. Sect. A Accel. Spectrometers, Detect. Assoc. Equip.*, **562** (2006), 472. doi:10.1016/j.nima.2006.02.166.

[34] M. Drescher, U. Frühling, M. Krikunova, T. Maltezopoulos, & M. Wieland. Time-diagnostics for improved dynamics experiments at XUV FELs. *J. Phys. B At. Mol. Opt. Phys.*, **43** (2010), 194010. doi:10.1088/0953-4075/43/19/194010.

[35] Z. Huang & K.-J. Kim. Review of x-ray free-electron laser theory. *Phys. Rev. Spec. Top. - Accel. Beams*, **10** (2007), 034801. doi:10.1103/PhysRevSTAB.10.034801.

[36] U. Frühling, M. Wieland, M. Gensch, T. Gebert, B. Schütte, M. Krikunova, R. Kalms, F. Budzyn, O. Grimm, J. Rossbach, E. Plönjes, & M. Drescher. Single-shot terahertz-field-driven X-ray streak camera. *Nat. Photonics*, **3** (2009), 523. doi:10.1038/nphoton.2009.160.

[37] B. Schütte, U. Frühling, M. Wieland, A. Azima, & M. Drescher. Electron wave packet sampling with laser-generated extreme ultraviolet and terahertz fields. *Opt. Express*, **19** (2011), 18833. doi:10.1364/OE.19.018833.

[38] I. Grguraš, a. R. Maier, C. Behrens, T. Mazza, T. J. Kelly, P. Radcliffe, S. Düsterer, a. K. Kazansky, N. M. Kabachnik, T. Tschentscher, J. T. Costello, M. Meyer, M. C. Hoffmann, H. Schlarb, & a. L. Cavalieri. Ultrafast X-ray pulse characterization at free-electron lasers. *Nat. Photonics*, **6** (2012), 852. doi:10.1038/nphoton.2012.276.

[39] E. Goulielmakis, M. Uiberacker, R. Kienberger, A. Baltuska, V. Yakovlev, A. Scrinzi, T. Westerwalbesloh, U. Kleineberg, U. Heinzmann, M. Drescher, & F. Krausz. Direct measurement of light waves. *Science*, **305** (2004), 1267. doi:10.1126/science.1100866.

[40] E. Cormier, I. A. Walmsley, E. M. Kosik, A. S. Wyatt, L. Corner, & L. F. DiMauro. Self-Referencing, Spectrally, or Spatially Encoded Spectral Interferometry for the

Complete Characterization of Attosecond Electromagnetic Pulses. *Phys. Rev. Lett.*, **94** (2005), 033905. doi:10.1103/PhysRevLett.94.033905.

[41] Y. Mairesse, O. Gobert, P. Breger, H. Merdji, P. Meynadier, P. Monchicourt, M. Perdrix, P. Salières, & B. Carré. High Harmonic XUV Spectral Phase Interferometry for Direct Electric-Field Reconstruction. *Phys. Rev. Lett.*, **94** (2005), 173903. doi:10.1103/PhysRevLett.94.173903.

[42] G. Kolliopoulos, P. Tzallas, B. Bergues, P. A. Carpeggiani, P. Heissler, H. Schröder, L. Veisz, D. Charalambidis, & G. D. Tsakiris. Single-shot autocorrelator for extreme-ultraviolet radiation. **31** (2014), 926.

[43] K. Kosma, S. A. Trushin, W. Fuss, & W. E. Schmid. Ultrafast Dynamics and Coherent Oscillations in Ethylene and Ethylene- d 4 Excited at 162 nm. *J. Phys. Chem. A*, **112** (2008), 7514. doi:10.1021/jp803548c.

[44] S. A. Trushin, W. E. Schmid, & W. Fuß. A time constant of 1.8 fs in the dissociation of water excited at 162nm. *Chem. Phys. Lett.*, **468** (2009), 9. doi:10.1016/j.cplett.2008.11.093.

[45] S. A. Trushin, W. E. Schmid, & W. Fuß. Time-resolved photodissociation of oxygen at 162 nm. *J. Phys. B At. Mol. Opt. Phys.*, **44** (2011), 165602. doi:10.1088/0953-4075/44/16/165602.

[46] T. K. Allison, H. Tao, W. J. Glover, T. W. Wright, A. M. M. Stooke, C. Khurmi, J. van Tilborg, Y. Liu, R. W. Falcone, T. J. Martínez, & A. Belkacem. Ultrafast internal conversion in ethylene. II. Mechanisms and pathways for quenching and hydrogen elimination. *J. Chem. Phys.*, **136** (2012), 124317. doi:10.1063/1.3697760.

[47] B. R. Beck, J. A. Becker, P. Beiersdorfer, G. V. Brown, K. J. Moody, J. B. Wilhelmy, F. S. Porter, C. A. Kilbourne, & R. L. Kelley. Energy Splitting of the Ground-State Doublet in the Nucleus ^{229}Th. *Phys. Rev. Lett.*, **98** (2007), 142501. doi:10.1103/PhysRevLett.98.142501.

[48] X. Zhao, Y. N. Martinez de Escobar, R. Rundberg, E. M. Bond, A. Moody, & D. J. Vieira. Observation of the Deexcitation of the ^{229}Th Nuclear Isomer. *Phys. Rev. Lett.*, **109** (2012), 160801. doi:10.1103/PhysRevLett.109.160801.

[49] G. A. Kazakov, A. N. Litvinov, V. I. Romanenko, L. P. Yatsenko, A. V. Romanenko, M. Schreitl, G. Winkler, & T. Schumm. Performance of a 229 Thorium solid-state nuclear clock. *New J. Phys.*, **14** (2012), 083019. doi:10.1088/1367-2630/14/8/083019.

[50] W. G. Rellergert, D. DeMille, R. R. Greco, M. P. Hehlen, J. R. Torgerson, & E. R. Hudson. Constraining the Evolution of the Fundamental Constants with a Solid-State Optical Frequency Reference Based on the ^{229}Th Nucleus. *Phys. Rev. Lett.*, **104** (2010), 200802. doi:10.1103/PhysRevLett.104.200802.

[51] P. Farmanara, V. Stert, & W. Radloff. Ultrafast internal conversion and fragmentation in electronically excited C2H4 and C2H3Cl molecules. *Chem. Phys. Lett.*, **288** (1998), 518. doi:10.1016/S0009-2614(98)00312-1.

[52] P. Farmanara, O. Steinkellner, M. T. Wick, M. Wittmann, G. Korn, V. Stert, & W. Radloff. Ultrafast internal conversion and photodissociation of molecules excited by femtosecond 155 nm laser pulses. *J. Chem. Phys.*, **111** (1999), 6264. doi:10.1063/1.479932.

[53] M. Göppert-Mayer. Über Elementarakte mit zwei Quantensprüngen. *Ann. Phys.*, **401** (1931), 273. doi:10.1002/andp.19314010303.

[54] T. H. Maiman. Stimulated Optical Radiation in Ruby. *Nature*, **187** (1960), 493. doi:10.1038/187493a0.

[55] P. W. Langhoff, S. T. Epstein, & M. Karplus. Aspects of Time-Dependent Perturbation Theory. *Rev. Mod. Phys.*, **44** (1972), 602. doi:10.1103/RevModPhys.44.602.

[56] B. Bransden & C. Joachain. Physics of Atoms and Molecules (Longman Scientific & Technical, 1983), second edition. ISBN 0-582-44401-2.

[57] F. H. M. Faisal. Introduction to Atomic Dynamics in Intense Light Fields. In K. Yamanouchi, (Ed.) Proc. Natl. Acad. Sci., volume 94 of *Springer Series in Chemical Physics*, 1–40 (Springer Berlin Heidelberg, Berlin, Heidelberg, 2010). ISBN 978-3-540-95943-4. doi:10.1007/978-3-540-95944-1_1.

[58] G. Laplanche, A. Durrieu, Y. Flank, M. Jaouen, & A. Rachman. The infinite summations of perturbation theory in atomic multiphoton ionization. *J. Phys. B At. Mol. Phys.*, **9** (1976), 1263.

[59] F. H. M. Faisal. Multiple absorption of laser photons by atoms. *J. Phys. B At. Mol. Phys.*, **6** (1973), L89. doi:10.1088/0022-3700/6/4/011.

[60] G. Mainfray & G. Manus. Multiphoton ionization of atoms. *Reports Prog. Phys.*, **54** (1991), 1333. doi:10.1088/0034-4885/54/10/002.

[61] L. A. Lompré, G. Mainfray, C. Manus, & J. Thebault. Multiphoton ionization of rare gases by a tunable-wavelength 30-psec laser pulse at 1.06 μm. *Phys. Rev. A*, **15** (1977), 1604. doi:10.1103/PhysRevA.15.1604.

[62] F. Fabre, G. Petite, P. Agostini, & M. Clement. Multiphoton above-threshold ionisation of xenon at 0.53 and 1.06 μm. *J. Phys. B At. Mol. Phys.*, **15** (1982), 1353. doi:10.1088/0022-3700/15/9/012.

[63] L. A. Lompré, A. L'Huillier, G. Mainfray, & C. Manus. Laser-intensity effects in the

energy distributions of electrons produced in multiphoton ionization of rare gases. *J. Opt. Soc. Am. B*, **2** (1985), 1906. doi:10.1364/JOSAB.2.001906.

[64] P. Lambropoulos. Mechanisms for Multiple Ionization of Atoms by Strong Pulsed Lasers. *Phys. Rev. Lett.*, **55** (1985), 2141. doi:10.1103/PhysRevLett.55.2141.

[65] S. Speiser & J. Jortner. The 3/2 power law for high order multiphoton processes. *Chem. Phys. Lett.*, **44** (1976), 399. doi:10.1016/0009-2614(76)80692-6.

[66] T. D. S. Uiterwaal & C. J. G. J. Simulating the focal volume effect: a quantitative analysis. *Laser Phys.*, **23** (2013), 125302. doi:10.1088/1054-660X/23/12/125302.

[67] J. T. Verdeyen. Laser Electronics (Prentice Hall, New Jersey, 1995), third edition. ISBN 0-13-706666-X.

[68] J. E. Muffett, C. G. Wahlstrom, & M. H. R. Hutchinson. Numerical modelling of the spatial profiles of high-order harmonics. *J. Phys. B At. Mol. Opt. Phys.*, **27** (1994), 5693. doi:10.1088/0953-4075/27/23/013.

[69] S. Augst, D. D. Meyerhofer, D. Strickland, & S. L. Chint. Laser ionization of noble gases by Coulomb-barrier suppression. *J. Opt. Soc. Am. B*, **8** (1991), 858. doi:10.1364/JOSAB.8.000858.

[70] P. Hansch, M. Walker, & L. Van Woerkom. Spatially dependent multiphoton multiple ionization. *Phys. Rev. A*, **54** (1996), R2559. doi:10.1103/PhysRevA.54.R2559.

[71] N. B. Delone & V. P. Krainov. Multiphoton Processes in Atoms, volume 50 (Springer Berlin Heidelberg, Berlin, Heidelberg, 2000). ISBN 978-3-642-62969-3. doi:10.1007/978-3-642-57208-1.

[72] P. Agostini, F. Fabre, G. Mainfray, G. Petite, & N. K. Rahman. Free-Free Transitions Following Six-Photon Ionization of Xenon Atoms. *Phys. Rev. Lett.*, **42** (1979), 1127. doi:10.1103/PhysRevLett.42.1127.

[73] P. Kruit, J. Kimman, H. G. Muller, & M. J. van der Wiel. Electron spectra from multiphoton ionization of xenon at 1064, 532, and 355 nm. *Phys. Rev. A*, **28** (1983), 248. doi:10.1103/PhysRevA.28.248.

[74] P. H. Bucksbaum, R. R. Freeman, M. Bashkansky, & T. J. McIlrath. Role of the ponderomotive potential in above-threshold ionization. *J. Opt. Soc. Am. B*, **4** (1987), 760. doi:10.1364/JOSAB.4.000760.

[75] G. G. Paulus, W. Nicklich, F. Zacher, P. Lambropoulos, & H. Walther. High-order above-threshold ionization of atomic hydrogen using intense, ultrashort laser pulses. *J. Phys. B At. Mol. Opt. Phys.*, **29** (1996), L249. doi:10.1088/0953-4075/29/7/002.

[76] B. W. Shore & P. L. Knight. Enhancement of high optical harmonics by excess-photon ionisation. *J. Phys. B At. Mol. Phys.*, **20** (1987), 413. doi:10.1088/0022-3700/20/2/021.

[77] A. D. Bandrauk. Photodissociation in intense laser fields: Predissociation analogy. *J. Chem. Phys.*, **74** (1981), 1110. doi:10.1063/1.441217.

[78] X. Tang, A. Lyras, & P. Lambropoulos. Dynamics of resonances rapidly shifting under short laser pulses. *Phys. Rev. Lett.*, **63** (1989), 972. doi:10.1103/PhysRevLett.63.972.

[79] P. H. Bucksbaum, A. Zavriyev, H. G. Muller, & D. W. Schumacher. Softening of the H_2^+ Molecular Bond in Intense Laser Fields. *Phys. Rev. Lett.*, **64** (1990), 1883. doi:10.1103/PhysRevLett.64.1883.

[80] A. Zavriyev, P. Bucksbaum, J. Squier, & F. Saline. Light-induced vibrational structure in H_2^+ and D_2^+ in intense laser fields. *Phys. Rev. Lett.*, **70** (1993), 1077. doi:10.1103/PhysRevLett.70.1077.

[81] L. Frasinski, J. Posthumus, J. Plumridge, K. Codling, P. Taday, & A. Langley. Manipulation of Bond Hardening in H_2^+ by Chirping of Intense Femtosecond Laser Pulses. *Phys. Rev. Lett.*, **83** (1999), 3625. doi:10.1103/PhysRevLett.83.3625.

[82] I. R. Solá, B. Y. Chang, J. Santamaría, V. S. Malinovsky, & J. L. Krause. Selective Excitation of Vibrational States by Shaping of Light-Induced Potentials. *Phys. Rev. Lett.*, **85** (2000), 4241. doi:10.1103/PhysRevLett.85.4241.

[83] B. Y. Chang, I. R. Solá, J. Santamaría, V. S. Malinovsky, & J. L. Krause. Transferring vibrational population between electronic states of diatomic molecules via light-induced-potential shaping. *J. Chem. Phys.*, **114** (2001), 8820. doi:10.1063/1.1368130.

[84] J. H. Posthumus. The dynamics of small molecules in intense laser fields. *Reports Prog. Phys.*, **67** (2004), 623. doi:10.1088/0034-4885/67/5/R01.

[85] L. V. Keldysh. Ionization in the field of a strong electromagnetic wave. *Sov. Phys. JETP*, **20** (1965), 1307. doi:10.1234/12345678.

[86] V. S. Popov. Tunnel and multiphoton ionization of atoms and ions in a strong laser field (Keldysh theory). *Physics-Uspekhi*, **47** (2004), 855. doi:10.1070/PU2004v047n09ABEH001812.

[87] P. Lambropoulos & G. M. Nikolopoulos. Multiple ionization under strong XUV to X-ray radiation. *Eur. Phys. J. Spec. Top.*, **222** (2013), 2067. doi:10.1140/epjst/e2013-01987-7.

[88] P. Heissler, A. Barna, J. M. Mikhailova, G. Ma, K. Khrennikov, S. Karsch, L. Veisz,

I. B. Földes, & G. D. Tsakiris. Multi-μJ harmonic emission energy from laser-driven plasma. *Appl. Phys. B*, **118** (2015), 195. doi:10.1007/s00340-014-5968-x.

[89] T. Brabec & F. Krausz. Intense few-cycle laser fields: Frontiers of nonlinear optics. *Rev. Mod. Phys.*, **72** (2000), 545. doi:10.1103/RevModPhys.72.545.

[90] T. Pfeifer, C. Spielmann, & G. Gerber. Femtosecond x-ray science. *Reports Prog. Phys.*, **69** (2006), 443. doi:10.1088/0034-4885/69/2/R04.

[91] P. B. Corkum. Plasma perspective on strong field multiphoton ionization. *Phys. Rev. Lett.*, **71** (1993), 1994. doi:10.1103/PhysRevLett.71.1994.

[92] M. Lewenstein, P. Balcou, M. Y. Ivanov, A. L' Huillier, & P. B. Corkum. Theory of high-harmonic generation by low-frequency laser fields. *Phys. Rev. A*, **49** (1994), 2117. doi:10.1103/PhysRevA.49.2117.

[93] K. S. Budil, P. Salières, A. L'Huillier, T. Ditmire, & M. D. Perry. Influence of ellipticity on harmonic generation. *Phys. Rev. A*, **48** (1993), R3437. doi:10.1103/PhysRevA.48.R3437.

[94] N. H. Burnett, C. Kan, & P. B. Corkum. Ellipticity and polarization effects in harmonic generation in ionizing neon. *Phys. Rev. A*, **51** (1995), R3418. doi:10.1103/PhysRevA.51.R3418.

[95] Y. Liang, M. V. Ammosov, & S. L. Chin. High-order harmonic generation in argon by elliptically polarized picosecond dye laser pulses. *J. Phys. B At. Mol. Opt. Phys.*, **27** (1994), 1269. doi:10.1088/0953-4075/27/6/024.

[96] T. Hänsch. A proposed sub-femtosecond pulse synthesizer using separate phase-locked laser oscillators. *Opt. Commun.*, **80** (1990), 71. doi:10.1016/0030-4018(90)90509-R.

[97] G. Farkas & C. Tóth. Proposal for attosecond light pulse generation using laser induced multiple-harmonic conversion processes in rare gases. *Phys. Lett. A*, **168** (1992), 447. doi:10.1016/0375-9601(92)90534-S.

[98] P. Tzallas, D. Charalambidis, N. a. Papadogiannis, K. Witte, & G. D. Tsakiris. Direct observation of attosecond light bunching. *Nature*, **426** (2003), 267. doi:10.1038/nature02091.

[99] Y. Kobayashi, T. Sekikawa, Y. Nabekawa, & S. Watanabe. 27-fs extreme ultraviolet pulse generation by high-order harmonics. *Opt. Lett.*, **23** (1998), 64. doi:10.1364/OL.23.000064.

[100] G. Sansone, L. Poletto, & M. Nisoli. High-energy attosecond light sources. *Nat. Photonics*, **5** (2011), 655. doi:10.1038/nphoton.2011.167.

[101] M. Chini, K. Zhao, & Z. Chang. The generation, characterization and applications of broadband isolated attosecond pulses. *Nat. Photonics*, **8** (2014), 178. doi:10.1038/nphoton.2013.362.

[102] A. L'Huillier, K. J. Schafer, & K. C. Kulander. Theoretical aspects of intense field harmonic generation. *J. Phys. B At. Mol. Opt. Phys.*, **24** (1991), 3315. doi:10.1088/0953-4075/24/15/004.

[103] R. J. Jones, K. D. Moll, M. J. Thorpe, & J. Ye. Phase-Coherent Frequency Combs in the Vacuum Ultraviolet via High-Harmonic Generation inside a Femtosecond Enhancement Cavity. *Phys. Rev. Lett.*, **94** (2005), 193201. doi:10.1103/PhysRevLett.94.193201.

[104] R. T. Zinkstok, S. Witte, W. Ubachs, W. Hogervorst, & K. S. Eikema. Frequency comb laser spectroscopy in the vacuum-ultraviolet region. *Phys. Rev. A*, **73** (2006), 061801. doi:10.1103/PhysRevA.73.061801.

[105] D. C. Yost, T. R. Schibli, J. Ye, J. L. Tate, J. Hostetter, M. B. Gaarde, & K. J. Schafer. Vacuum-ultraviolet frequency combs from below-threshold harmonics. *Nat. Phys.*, **5** (2009), 815. doi:10.1038/nphys1398.

[106] J. A. Hostetter, J. L. Tate, K. J. Schafer, & M. B. Gaarde. Semiclassical approaches to below-threshold harmonics. *Phys. Rev. A*, **82** (2010), 023401. doi:10.1103/PhysRevA.82.023401.

[107] E. P. Power, A. M. March, F. Catoire, E. Sistrunk, K. Krushelnick, P. Agostini, & L. F. DiMauro. XFROG phase measurement of threshold harmonics in a Keldysh-scaled system. *Nat. Photonics*, **4** (2010), 352. doi:10.1038/nphoton.2010.38.

[108] W.-H. Xiong, J.-W. Geng, J.-Y. Tang, L.-Y. Peng, & Q. Gong. Mechanisms of Below-Threshold Harmonic Generation in Atoms. *Phys. Rev. Lett.*, **112** (2014), 233001. doi:10.1103/PhysRevLett.112.233001.

[109] P.-C. Li, Y.-L. Sheu, C. Laughlin, & S.-I. Chu. Dynamical origin of near- and below-threshold harmonic generation of Cs in an intense mid-infrared laser field. *Nat. Commun.*, **6** (2015), 7178. doi:10.1038/ncomms8178.

[110] R. W. Boyd. Nonlinear Optics (Academic Press, 2008), third edition. ISBN 978-0123694706.

[111] P. Balcou, P. Saliéres, A. L'Huillier, & M. Lewenstein. Generalized phase-matching conditions for high harmonics: The role of field-gradient forces. *Phys. Rev. A*, **55** (1997), 3204. doi:10.1103/PhysRevA.55.3204.

[112] M. B. Gaarde, F. Salin, E. Constant, P. Balcou, K. J. Schafer, K. C. Kulander, &

A. L' Huillier. Spatiotemporal separation of high harmonic radiation into two quantum path components. *Phys. Rev. A*, **59** (1999), 1367. doi:10.1103/PhysRevA.59.1367.

[113] M. B. Gaarde & K. J. Schafer. Quantum path distributions for high-order harmonics in rare gas atoms. *Phys. Rev. A*, **65** (2002), 031406. doi:10.1103/PhysRevA.65.031406.

[114] R. W. Boyd. Intuitive explanation of the phase anomaly of focused light beams. *J. Opt. Soc. Am.*, **70** (1980), 877. doi:10.1364/JOSA.70.000877.

[115] P. Saliéres & I. Christov. Strong Field Laser Physics, volume 134 of *Springer Series in Optical Sciences*, chapter Macroscopic Effects in High-Order Harmonic Generation, 261–280 (Springer New York, New York, NY, 2009). ISBN 978-0-387-40077-8. doi: 10.1007/978-0-387-34755-4.

[116] E. Takahashi, Y. Nabekawa, & K. Midorikawa. Generation of 10- μJ coherent extreme-ultraviolet light by use of high-order harmonics. *Opt. Lett.*, **27** (2002), 1920. doi:10.1364/OL.27.001920.

[117] E. J. Takahashi, Y. Nabekawa, & K. Midorikawa. Low-divergence coherent soft x-ray source at 13 nm by high-order harmonics. *Appl. Phys. Lett.*, **84** (2004), 4. doi:10.1063/1.1637949.

[118] W. Diels, Rudolph. Ultrashort Laser Pulse Phenomena (Academic Press, 2006), second edition. ISBN 978-0-12-215493-5.

[119] C. Rulliere & Others. Femtosecond Laser Pulses, volume 2 of *Advanced Texts in Physics* (Springer New York, New York, NY, 2005). ISBN 978-0-387-01769-3. doi: 10.1007/b137908.

[120] F. Kärtner, (Ed.) Few-Cycle Laser Pulse Generation and Its Applications, volume 95 (Springer, 2004). ISBN 3-540-10192-6.

[121] T. Brabec, (Ed.) Strong Field Laser Physics, volume 134 of *Springer Series in Optical Sciences* (Springer New York, New York, NY, 2009). ISBN 978-0-387-40077-8. doi:10.1007/978-0-387-34755-4.

[122] T. Udem, R. Holzwarth, & T. W. Hänsch. Optical frequency metrology. *Nature*, **416** (2002), 233. doi:10.1038/416233a.

[123] S. Cundiff & J. Ye. Colloquium: Femtosecond optical frequency combs. *Rev. Mod. Phys.*, **75** (2003), 325. doi:10.1103/RevModPhys.75.325.

[124] S. Kane & J. Squier. Grism-pair stretcher-compressor system for simultaneous second- and third-order dispersion compensation in chirped-pulse amplification. *J. Opt. Soc. Am. B*, **14** (1997), 661. doi:10.1364/JOSAB.14.000661.

[125] R. Szipocs, K. Ferencz, C. Spielmann, & F. Krausz. Chirped multilayer coatings for broadband dispersion control in femtosecond lasers. *Opt. Lett.*, **19** (1994), 201. doi:10.1364/OL.19.000201.

[126] F. X. Kärtner, N. Matuschek, T. Schibli, U. Keller, H. A. Haus, C. Heine, R. Morf, V. Scheuer, M. Tilsch, & T. Tschudi. Design and fabrication of double-chirped mirrors. *Opt. Lett.*, **22** (1997), 831. doi:10.1364/OL.22.000831.

[127] V. Pervak, C. Teisset, A. Sugita, S. Naumov, F. Krausz, & A. Apolonski. High-dispersive mirrors for femtosecond lasers. *Opt. Express*, **16** (2008), 10220. doi:10.1364/OE.16.010220.

[128] P. Tournois. Acousto-optic programmable dispersive filter for adaptive compensation of group delay time dispersion in laser systems. *Opt. Commun.*, **140** (1997), 245. doi:10.1016/S0030-4018(97)00153-3.

[129] A. M. Weiner. Femtosecond pulse shaping using spatial light modulators. *Rev. Sci. Instrum.*, **71** (2000), 1929. doi:10.1063/1.1150614.

[130] A. Monmayrant, S. Weber, & B. Chatel. A newcomer's guide to ultrashort pulse shaping and characterization. *J. Phys. B At. Mol. Opt. Phys.*, **43** (2010), 103001. doi:10.1088/0953-4075/43/10/103001.

[131] E. Treacy. Optical pulse compression with diffraction gratings. *IEEE J. Quantum Electron.*, **5** (1969), 454. doi:10.1109/JQE.1969.1076303.

[132] M. Daimon & A. Masumura. High-accuracy measurements of the refractive index and its temperature coefficient of calcium fluoride in a wide wavelength range from 138 to 2326 nm. *Appl. Opt.*, **41** (2002), 5275. doi:10.1364/AO.41.005275.

[133] V. Wong & I. a. Walmsley. Linear filter analysis of methods for ultrashort-pulse-shape measurements. *J. Opt. Soc. Am. B*, **12** (1995), 1491. doi:10.1364/JOSAB.12.001491.

[134] Hamamatsu Photonics. Guide to Streak Cameras. Technical report (2008).

[135] P. A. Jaanimagi. Breaking the 100-fs barrier with a streak camera. In R. O. Tatchyn, Z. Chang, J.-C. Kieffer, & J. B. Hastings, (Eds.) Proc. SPIE, volume 5194, 171–182 (2004). doi:10.1117/12.512747.

[136] P. M. Morse & H. Feshbach. Methods of Theoretical Physics, Part I (Mc Graw Hill Book Company Inc., 1953). ISBN 978-0070433168.

[137] E. W. Weisstein. "Delta Function." From MathWorld–A Wolfram Web Resource. http://mathworld.wolfram.com/DeltaFunction.html.

[138] F. Träger. Springer Handbook of Lasers and Optics, volume 72 (Springer New York, New York, NY, 2007). ISBN 978-0-387-95579-7. doi:10.1007/978-0-387-30420-5.

[139] R. J. Glauber. The Quantum Theory of Optical Coherence. *Phys. Rev.*, **130** (1963), 2529. doi:10.1103/PhysRev.130.2529.

[140] R. Loudon. The Quantum Theory of Light (Oxford University Press, 2000), Third edition. ISBN 978-0-19-850176-3.

[141] R. J. Glauber. Quantum Theory of Optical Coherence (Wiley-VCH Verlag GmbH & Co. KGaA, Weinheim, Germany, 2006). ISBN 9783527610075. doi:10.1002/9783527610075.

[142] L. Mandel & E. Wolf. Optical coherence and quantum optics (Cambridge University Press, Cambridge, 1995). ISBN 9781139644105. doi:10.1017/CBO9781139644105.

[143] P. Lambropoulos. Field-Correlation Effects in Two-Photon Processes. *Phys. Rev.*, **168** (1968), 1418. doi:10.1103/PhysRev.168.1418.

[144] G. S. Agarwal. Field-Correlation Effects in Multiphoton Absorption Processes. *Phys. Rev. A*, **1** (1970), 1445. doi:10.1103/PhysRevA.1.1445.

[145] E. W. Weisstein. "Convolution." From MathWorld–A Wolfram Web Resource. http://mathworld.wolfram.com/Convolution.html.

[146] J. C. Diels, J. J. Fontaine, I. C. McMichael, & F. Simoni. Control and measurement of ultrashort pulse shapes (in amplitude and phase) with femtosecond accuracy. *Appl. Opt.*, **24** (1985), 1270. doi:10.1364/AO.24.001270.

[147] K. Naganuma, K. Mogi, & H. Yamada. General method for ultrashort light pulse chirp measurement. *IEEE J. Quantum Electron.*, **25** (1989), 1225. doi:10.1109/3.29252.

[148] Jung-Ho Chung & A. Weiner. Ambiguity of ultrashort pulse shapes retrieved from the intensity autocorrelation and the power spectrum. *IEEE J. Sel. Top. Quantum Electron.*, **7** (2001), 656. doi:10.1109/2944.974237.

[149] H. Mashiko, A. Suda, & K. Midorikawa. All-reflective interferometric autocorrelator for the measurement of ultra-short optical pulses. *Appl. Phys. B*, **76** (2003), 525. doi:10.1007/s00340-003-1148-0.

[150] P. Tzallas, D. Charalambidis, N. a. Papadogiannis, K. Witte, & G. D. Tsakiris. Second-order autocorrelation measurements of attosecond XUV pulse trains. *J. Mod. Opt.*, **52** (2005), 321. doi:10.1080/09500340412331301533.

[151] H. Mashiko, A. Suda, & K. Midorikawa. Second-order autocorrelation functions

for all-reflective interferometric autocorrelator. *Appl. Phys. B*, **87** (2007), 221. doi: 10.1007/s00340-006-2574-6.

[152] H. Weber. Comments on the pulse width measurement with two-photon excitation of fluorescence. *Phys. Lett. A*, **27** (1968), 321. doi:10.1016/0375-9601(68)90728-7.

[153] J. R. Klauder, M. A. Duguay, J. A. Giordmaine, & S. L. Shapiro. Correlation Effects In The Display Of Picosecond Pulses By Two-Photon Techniques. *Appl. Phys. Lett.*, **13** (1968), 174. doi:10.1063/1.1652558.

[154] A. A. Grütter, H. P. Weber, & R. Dändliker. Imperfectly Mode-Locked Laser Emission and Its Effects on Nonlinear Optics. *Phys. Rev.*, **185** (1969), 629. doi: 10.1103/PhysRev.185.629.

[155] D. Auston. Higher order intensity correlations of optical pulses. *IEEE J. Quantum Electron.*, **7** (1971), 465. doi:10.1109/JQE.1971.1076835.

[156] M. Rhodes, G. Steinmeyer, & R. Trebino. Standards for ultrashort-laser-pulse-measurement techniques and their consideration for self-referenced spectral interferometry. *Appl. Opt.*, **53** (2014), D1. doi:10.1364/AO.53.0000D1.

[157] E. I. Blount & J. R. Klauder. Recovery of Laser Intensity from Correlation Data. *J. Appl. Phys.*, **40** (1969), 2874. doi:10.1063/1.1658092.

[158] S. Luan, M. H. R. Hutchinson, R. a. Smith, & F. Zhou. High dynamic range third-order correlation measurement of picosecond laser pulse shapes. *Meas. Sci. Technol.*, **4** (1993), 1426. doi:10.1088/0957-0233/4/12/018.

[159] D. Kane & R. Trebino. Characterization of arbitrary femtosecond pulses using frequency-resolved optical gating. *IEEE J. Quantum Electron.*, **29** (1993), 571. doi:10.1109/3.199311.

[160] K. W. DeLong, R. Trebino, J. Hunter, & W. E. White. Frequency-resolved optical gating with the use of second-harmonic generation. *J. Opt. Soc. Am. B*, **11** (1994), 2206. doi:10.1364/JOSAB.11.002206.

[161] R. Trebino, K. W. DeLong, D. N. Fittinghoff, J. N. Sweetser, M. a. KrumbuÌ?gel, B. a. Richman, & D. J. Kane. Measuring ultrashort laser pulses in the time-frequency domain using frequency-resolved optical gating. *Rev. Sci. Instrum.*, **68** (1997), 3277. doi:10.1063/1.1148286.

[162] D. J. Kane. Principal components generalized projections: a review [Invited]. *J. Opt. Soc. Am. B*, **25** (2008), A120. doi:10.1364/JOSAB.25.00A120.

[163] R. Barakat & G. Newsam. Necessary conditions for a unique solution to two-dimensional phase recovery. *J. Math. Phys.*, **25** (1984), 3190. doi:10.1063/1.526089.

[164] R. P. Millane. Phase retrieval in crystallography and optics. *J. Opt. Soc. Am. A*, **7** (1990), 394. doi:10.1364/JOSAA.7.000394.

[165] C. Iaconis & I. A. Walmsley. Spectral phase interferometry for direct electric-field reconstruction of ultrashort optical pulses. *Opt. Lett.*, **23** (1998), 792. doi:10.1109/CLEO.1998.676573.

[166] C. Dorrer & I. a. Walmsley. Accuracy criterion for ultrashort pulse characterization techniques: application to spectral phase interferometry for direct electric field reconstruction. *J. Opt. Soc. Am. B*, **19** (2002), 1019. doi:10.1364/JOSAB.19.001019.

[167] T. Sekikawa, T. Kanai, & S. Watanabe. Frequency-Resolved Optical Gating of Femtosecond Pulses in the Extreme Ultraviolet. *Phys. Rev. Lett.*, **91** (2003), 103902. doi:10.1103/PhysRevLett.91.103902.

[168] F. Quéré, J. Itatani, G. L. Yudin, & P. B. Corkum. Attosecond Spectral Shearing Interferometry. *Phys. Rev. Lett.*, **90** (2003), 073902. doi:10.1103/PhysRevLett.90.073902.

[169] Y. Mairesse & F. Quéré. Frequency-resolved optical gating for complete reconstruction of attosecond bursts. *Phys. Rev. A*, **71** (2005), 011401. doi:10.1103/PhysRevA.71.011401.

[170] A. Kosuge, T. Sekikawa, X. Zhou, T. Kanai, S. Adachi, & S. Watanabe. Frequency-resolved optical gating of isolated attosecond pulses in the extreme ultraviolet. *Phys. Rev. Lett.*, **97** (2006), 263901. doi:10.1103/PhysRevLett.97.263901.

[171] J. Gagnon, E. Goulielmakis, & V. Yakovlev. The accurate FROG characterization of attosecond pulses from streaking measurements. *Appl. Phys. B*, **92** (2008), 25. doi:10.1007/s00340-008-3063-x.

[172] P. Heissler, P. Tzallas, J. M. Mikhailova, K. Khrennikov, L. Waldecker, F. Krausz, S. Karsch, D. Charalambidis, & G. D. Tsakiris. Two-photon above-threshold ionization using extreme-ultraviolet harmonic emission from relativistic laser-plasma interaction. *New J. Phys.*, **14** (2012), 043025. doi:10.1088/1367-2630/14/4/043025.

[173] C. Bourassin-Bouchet & M.-E. Couprie. Partially coherent ultrafast spectrography. *Nat. Commun.*, **6** (2015), 6465. doi:10.1038/ncomms7465.

[174] G. De Ninno, D. Gauthier, B. Mahieu, P. R. Ribič, E. Allaria, P. Cinquegrana, M. B. Danailov, A. Demidovich, E. Ferrari, L. Giannessi, G. Penco, P. Sigalotti, & M. Stupar. Single-shot spectro-temporal characterization of XUV pulses from a seeded free-electron laser. *Nat. Commun.*, **6** (2015), 8075. doi:10.1038/ncomms9075.

[175] J. Itatani, F. Quéré, G. L. Yudin, M. Y. Ivanov, F. Krausz, & P. B. Corkum.

Attosecond Streak Camera. *Phys. Rev. Lett.*, **88** (2002), 173903. doi:10.1103/PhysRevLett.88.173903.

[176] R. Kienberger, E. Goulielmakis, M. Uiberacker, A. Baltuska, V. Yakovlev, F. Bammer, A. Scrinzi, T. Westerwalbesloh, U. Kleineberg, U. Heinzmann, M. Drescher, & F. Krausz. Atomic transient recorder. *Nature*, **427** (2004), 817. doi:10.1038/nature02277.

[177] U. Frühling. Light-field streaking for FELs. *J. Phys. B At. Mol. Opt. Phys.*, **44** (2011), 243001. doi:10.1088/0953-4075/44/24/243001.

[178] A. Maquet & R. Taïeb. Two-colour IR + XUV spectroscopies: the "soft-photon approximation". *J. Mod. Opt.*, **54** (2007), 1847. doi:10.1080/09500340701306751.

[179] R. Taïeb, A. Maquet, & M. Meyer. Two-color photoionization in XUV-FEL and laser fields. *J. Phys. Conf. Ser.*, **141** (2008), 012017. doi:10.1088/1742-6596/141/1/012017.

[180] Y. Mairesse, A. de Bohan, L. J. Frasinski, H. Merdji, L. C. Dinu, P. Monchicourt, P. Breger, M. Kovacev, R. Taïeb, B. Carre, H. G. Muller, P. Agostini, & P. Salieres. Attosecond Synchronization of High-Harmonic Soft X-rays. *Science (80-.).*, **302** (2003), 1540. doi:10.1126/science.1090277.

[181] P. Radcliffe, S. Düsterer, A. Azima, H. Redlin, J. Feldhaus, J. Dardis, K. Kavanagh, H. Luna, J. P. Gutierrez, P. Yeates, E. T. Kennedy, J. T. Costello, A. Delserieys, C. L. S. Lewis, R. TaiÌ?eb, A. Maquet, D. Cubaynes, & M. Meyer. Single-shot characterization of independent femtosecond extreme ultraviolet free electron and infrared laser pulses. *Appl. Phys. Lett.*, **90** (2007), 131108. doi:10.1063/1.2716360.

[182] S. Düsterer, P. Radcliffe, C. Bostedt, J. Bozek, a. L. Cavalieri, R. Coffee, J. T. Costello, D. Cubaynes, L. F. DiMauro, Y. Ding, G. Doumy, F. Grüner, W. Helml, W. Schweinberger, R. Kienberger, a. R. Maier, M. Messerschmidt, V. Richardson, C. Roedig, T. Tschentscher, & M. Meyer. Femtosecond x-ray pulse length characterization at the Linac Coherent Light Source free-electron laser. *New J. Phys.*, **13** (2011), 093024. doi:10.1088/1367-2630/13/9/093024.

[183] P. Radcliffe, M. Arbeiter, W. B. Li, S. Düsterer, H. Redlin, P. Hayden, P. Hough, V. Richardson, J. T. Costello, T. Fennel, & M. Meyer. Atomic photoionization in combined intense XUV free-electron and infrared laser fields. *New J. Phys.*, **14** (2012), 043008. doi:10.1088/1367-2630/14/4/043008.

[184] R. Morita, M. Hirasawa, N. Karasawa, S. Kusaka, N. Nakagawa, K. Yamane, L. Li, A. Suguro, & M. Yamashita. Sub-5 fs optical pulse characterization. *Meas. Sci. Technol.*, **13** (2002), 1710. doi:10.1088/0957-0233/13/11/307.

[185] J. E. Kruse, P. Tzallas, E. Skantzakis, C. Kalpouzos, G. D. Tsakiris, & D. Charalam-

bidis. Inconsistencies between two attosecond pulse metrology methods: A comparative study. *Phys. Rev. A*, **82** (2010), 021402. doi:10.1103/PhysRevA.82.021402.

[186] T. Witting, F. Frank, W. a. Okell, C. a. Arrell, J. P. Marangos, & J. W. G. Tisch. Sub-4-fs laser pulse characterization by spatially resolved spectral shearing interferometry and attosecond streaking. *J. Phys. B At. Mol. Opt. Phys.*, **45** (2012), 074014. doi:10.1088/0953-4075/45/7/074014.

[187] F. Hache, T. J. Driscoll, M. Cavallari, & G. M. Gale. Measurement of ultrashort pulse durations by interferometric autocorrelation: influence of various parameters. *Appl. Opt.*, **35** (1996), 3230. doi:10.1364/AO.35.003230.

[188] C. Dorrer. Influence of the calibration of the detector on spectral interferometry. *J. Opt. Soc. Am. B*, **16** (1999), 1160. doi:10.1364/JOSAB.16.001160.

[189] L. Xu, E. Zeek, & R. Trebino. Simulations of frequency-resolved optical gating for measuring very complex pulses. *J. Opt. Soc. Am. B*, **25** (2008), A70. doi:10.1364/JOSAB.25.000A70.

[190] M. Rhodes, G. Steinmeyer, J. Ratner, & R. Trebino. Pulse-shape instabilities and their measurement. *Laser Photon. Rev.*, **7** (2013), 557. doi:10.1002/lpor.201200102.

[191] J. M. Mikhailova, A. Buck, A. Borot, K. Schmid, C. Sears, G. D. Tsakiris, F. Krausz, & L. Veisz. Ultra-high-contrast few-cycle pulses for multipetawatt-class laser technology. *Opt. Lett.*, **36** (2011), 3145. doi:10.1364/OL.36.003145.

[192] A. Baltuska, M. Pshenichnikov, & D. Wiersma. Second-harmonic generation frequency-resolved optical gating in the single-cycle regime. *IEEE J. Quantum Electron.*, **35** (1999), 459. doi:10.1109/3.753651.

[193] R. Harrach. Effects of partial mode-locking on contrast ratios in two-photon excitation of fluorescence. *Phys. Lett. A*, **28** (1968), 393. doi:10.1016/0375-9601(68)90453-2.

[194] J. Janszky, G. Corradi, & R. Gyuzalian. On a possibility of analysing the temporal characteristics of short light pulses. *Opt. Commun.*, **23** (1977), 293. doi:10.1016/0030-4018(77)90365-0.

[195] J. A. Giordmaine, P. M. Rentzepis, S. L. Shapiro, & K. W. Wecht. Two-Photon Excitation Of Fluorescence By Picosecond Light Pulses. *Appl. Phys. Lett.*, **11** (1967), 216. doi:10.1063/1.1755105.

[196] Y. Takagi, T. Kobayashi, K. Yoshihara, & S. Imamura. Multiple- and single-shot autocorrelator based on two-photon conductivity in semiconductors. *Opt. Lett.*, **17** (1992), 658. doi:10.1364/OL.17.000658.

[197] D. Panasenko & Y. Fainman. Interferometric Correlation of Infrared Femtosecond

Pulses with Two-Photon Conductivity in a Silicon CCD. *Appl. Opt.*, **41** (2002), 3748. doi:10.1364/AO.41.003748.

[198] D. M. Rayner, P. a. Hackett, & C. Willis. Ultraviolet laser, short pulse-width measurement by multiphoton ionization autocorrelation. *Rev. Sci. Instrum.*, **53** (1982), 537. doi:10.1063/1.1136978.

[199] P. Simon, H. Gerhardt, & S. Szatmari. A single-shot autocorrelator for UV femtosecond pulses. *Meas. Sci. Technol.*, **1** (1990), 637. doi:10.1088/0957-0233/1/7/017.

[200] F. Salin, P. Georges, G. Roger, & A. Brun. Single-shot measurement of a 52-fs pulse. *Appl. Opt.*, **26** (1987), 4528. doi:10.1364/AO.26.004528.

[201] a. Brun, P. Georges, G. L. Saux, & F. Salin. Single-shot characterization of ultrashort light pulses. *J. Phys. D. Appl. Phys.*, **24** (1991), 1225. doi:10.1088/0022-3727/24/8/001.

[202] D. J. Kane, A. J. Taylor, R. Trebino, & K. W. DeLong. Single-shot measurement of the intensity and phase of a femtosecond UV laser pulse with frequency-resolved optical gating. *Opt. Lett.*, **19** (1994), 1061. doi:10.1364/OL.19.001061.

[203] M. Campbell, T. Bensky, & R. Jones. Single-shot detection of wavepacket evolution. *Opt. Express*, **1** (1997), 197. doi:10.1364/OE.1.000197.

[204] S. Pedersen & A. H. Zewail. Femtosecond real time probing of reactions XXII. Kinetic description of probe absorption fluorescence depletion and mass spectrometry. *Mol. Phys.*, **89** (1996), 1455. doi:10.1080/002689796173291.

[205] Y. H. Jiang, A. Rudenko, J. F. Pérez-Torres, O. Herrwerth, L. Foucar, M. Kurka, K. U. Kühnel, M. Toppin, E. Plésiat, F. Morales, F. Martín, M. Lezius, M. F. Kling, T. Jahnke, R. Dörner, J. L. Sanz-Vicario, J. van Tilborg, A. Belkacem, M. Schulz, K. Ueda, T. J. M. Zouros, S. Düsterer, R. Treusch, C. D. Schröter, R. Moshammer, & J. Ullrich. Investigating two-photon double ionization of D_2 by XUV-pump-XUV-probe experiments. *Phys. Rev. A*, **81** (2010), 051402. doi:10.1103/PhysRevA.81.051402.

[206] K. Meyer, C. Ott, P. Raith, A. Kaldun, Y. Jiang, A. Senftleben, M. Kurka, R. Moshammer, J. Ullrich, & T. Pfeifer. Noisy Optical Pulses Enhance the Temporal Resolution of Pump-Probe Spectroscopy. *Phys. Rev. Lett.*, **108** (2012), 098302. doi:10.1103/PhysRevLett.108.098302.

[207] P. M. Rentzepis & M. A. Duguay. Picosecond Light Pulse Display Using Two Different Optical Frequencies. *Appl. Phys. Lett.*, **11** (1967), 218. doi:10.1063/1.1755106.

[208] M. Duguay, J. Hansen, & S. Shapiro. Study of the Nd: Glass laser radiation. *IEEE J. Quantum Electron.*, **6** (1970). doi:10.1109/JQE.1970.1076349.

[209] M. H. R. Hutchinson, I. a. McIntyre, G. N. Gibson, & C. K. Rhodes. Measurement of 248-nm, subpicosecond pulse durations by two-photon fluorescence of xenon excimers. *Opt. Lett.*, **12** (1987), 102. doi:10.1364/OL.12.000102.

[210] N. Sarukura, M. Watanabe, A. Endoh, & S. Watanabe. Single-shot measurement of subpicosecond KrF pulse width by three-photon fluorescence of the XeF visible transition. *Opt. Lett.*, **13** (1988), 996. doi:10.1364/OL.13.000996.

[211] C. Xu, J. Guild, W. Webb, & W. Denk. Determination of absolute two-photon excitation cross sections by in situ second-order autocorrelation. *Opt. Lett.*, **20** (1995), 2372. doi:10.1364/OL.20.002372.

[212] R. Fischer, D. N. Neshev, S. M. Saltiel, A. a. Sukhorukov, W. Krolikowski, & Y. S. Kivshar. Monitoring ultrashort pulses by transverse frequency doubling of counterpropagating pulses in random media. *Appl. Phys. Lett.*, **91** (2007), 031104. doi:10.1063/1.2751583.

[213] Y. Nabekawa, T. Shimizu, T. Okino, K. Furusawa, H. Hasegawa, K. Yamanouchi, & K. Midorikawa. Interferometric Autocorrelation of an Attosecond Pulse Train in the Single-Cycle Regime. *Phys. Rev. Lett.*, **97** (2006), 153904. doi:10.1103/PhysRevLett.97.153904.

[214] S.-i. Zaitsu, Y. Miyoshi, F. Kira, S. Yamaguchi, T. Uchimura, & T. Imasaka. Interferometric characterization of ultrashort deep ultraviolet pulses using a multiphoton ionization mass spectrometer. *Opt. Lett.*, **32** (2007), 1716. doi:10.1364/OL.32.001716.

[215] R. Mitzner, A. A. Sorokin, B. Siemer, S. Roling, M. Rutkowski, H. Zacharias, M. Neeb, T. Noll, F. Siewert, W. Eberhardt, M. Richter, P. Juranic, K. Tiedtke, & J. Feldhaus. Direct autocorrelation of soft-x-ray free-electron-laser pulses by time-resolved two-photon double ionization of He. *Phys. Rev. A*, **80** (2009), 025402. doi:10.1103/PhysRevA.80.025402.

[216] Y. Miyoshi, S. Zaitsu, & T. Imasaka. In situ third-order interferometric autocorrelation of a femtosecond deep-ultraviolet pulse. *Appl. Phys. B*, **103** (2011), 789. doi:10.1007/s00340-010-4324-z.

[217] R. Hörlein, Y. Nomura, P. Tzallas, S. G. Rykovanov, B. Dromey, J. Osterhoff, Z. Major, S. Karsch, L. Veisz, M. Zepf, D. Charalambidis, F. Krausz, & G. D. Tsakiris. Temporal characterization of attosecond pulses emitted from solid-density plasmas. *New J. Phys.*, **12** (2010), 043020. doi:10.1088/1367-2630/12/4/043020.

[218] R. Moshammer, T. Pfeifer, A. Rudenko, Y. H. Jiang, L. Foucar, M. Kurka, K. U. Kühnel, C. D. Schröter, J. Ullrich, O. Herrwerth, M. F. Kling, X.-J. Liu, K. Motomura, H. Fukuzawa, A. Yamada, K. Ueda, K. L. Ishikawa, K. Nagaya, H. Iwayama, A. Sugishima, Y. Mizoguchi, S. Yase, M. Yao, N. Saito, A. Belkacem, M. Nagasono, A. Higashiya, M. Yabashi, T. Ishikawa, H. Ohashi, H. Kimura, & T. Togashi.

Second-order autocorrelation of XUV FEL pulses via time resolved two-photon single ionization of He. *Opt. Express*, **19** (2011), 21698. doi:10.1364/OE.19.021698.

[219] E. J. Takahashi, P. Lan, O. D. Mücke, Y. Nabekawa, & K. Midorikawa. Attosecond nonlinear optics using gigawatt-scale isolated attosecond pulses. *Nat. Commun.*, **4** (2013), 2691. doi:10.1038/ncomms3691.

[220] T. Gebert, D. Rompotis, M. Wieland, F. Karimi, A. Azima, & M. Drescher. Michelson-type all-reflective interferometric autocorrelation in the VUV regime. *New Journal of Physics*, **16** (2014), 073047. doi:doi:10.1088/1367-2630/16/7/073047.

[221] O. Faucher, P. Tzallas, E. P. Benis, J. Kruse, a. Peralta Conde, C. Kalpouzos, & D. Charalambidis. Four-dimensional investigation of the 2nd order volume autocorrelation technique. *Appl. Phys. B Lasers Opt.*, **97** (2009), 505. doi:10.1007/s00340-009-3559-z.

[222] T. Gebert. Messung ultrakurzer molekularer Zeitkonstanten mit nichtlinearer interferometrischer Autokorrelation bei 160 nm Wellenlänge. Ph.D. thesis, University of Hamburg (2015).

[223] A. H. Carim, M. M. Dovek, C. F. Quate, R. Sinclair, & C. Vorst. High-resolution electron microscopy and scanning tunneling microscopy of native oxides on silicon. *Science*, **237** (1987), 630. doi:10.1126/science.237.4815.630.

[224] D. L. Windt. IMD Software for modeling the optical properties of multilayer films. *Computers in Physics*, **12** (1998), 360. doi:http://dx.doi.org/10.1063/1.168689.

[225] ISO 21348. Space environment (natural and artificial). Process for determining solar irradiances. Technical report (2007). doi:10.3403/30109606.

[226] A. A. Sorokin, M. Wellhöfer, S. V. Bobashev, K. Tiedtke, & M. Richter. X-ray-laser interaction with matter and the role of multiphoton ionization: Free-electron-laser studies on neon and helium. *Phys. Rev. A*, **75** (2007), 051402. doi:10.1103/PhysRevA.75.051402.

[227] V. Richardson, J. T. Costello, D. Cubaynes, S. Düsterer, J. Feldhaus, H. W. van der Hart, P. Juranić, W. B. Li, M. Meyer, M. Richter, a. a. Sorokin, & K. Tiedke. Two-Photon Inner-Shell Ionization in the Extreme Ultraviolet. *Phys. Rev. Lett.*, **105** (2010), 013001. doi:10.1103/PhysRevLett.105.013001.

[228] P. Tzallas, E. Skantzakis, & D. Charalambidis. Direct two-XUV-photon double ionization in xenon. *J. Phys. B At. Mol. Opt. Phys.*, **45** (2012), 074007. doi:10.1088/0953-4075/45/7/074007.

[229] P. Lambropoulos, L. a. a. Nikolopoulos, M. G. Makris, & A. Mihelič. Direct versus

sequential double ionization in atomic systems. *Phys. Rev. A*, **78** (2008), 055402. doi:10.1103/PhysRevA.78.055402.

[230] T. Nakajima & L. A. A. Nikolopoulos. Use of helium double ionization for autocorrelation of an xuv pulse. *Phys. Rev. A*, **66** (2002), 041402. doi:10.1103/PhysRevA.66.041402.

[231] T. Sekikawa, T. Ohno, T. Yamazaki, Y. Nabekawa, & S. Watanabe. Pulse Compression of a High-Order Harmonic by Compensating the Atomic Dipole Phase. *Phys. Rev. Lett.*, **83** (1999), 2564. doi:10.1103/PhysRevLett.83.2564.

[232] P. Schmüser, M. Dohlus, & J. Rossbach. Ultraviolet and Soft X-Ray Free-Electron Lasers, volume 229 of *Springer Tracts in Modern Physics* (Springer Berlin Heidelberg, Berlin, Heidelberg, 2009). ISBN 978-3-540-79571-1. doi:10.1007/978-3-540-79572-8.

[233] G. Geloni, E. Saldin, E. Schneidmiller, & M. Yurkov. Exact solution for second harmonic generation in XFELs. *Opt. Commun.*, **271** (2007), 207. doi:10.1016/j.optcom.2006.10.019.

[234] W. R. Hunter, D. W. Angel, & R. Tousey. Thin Films and Their Uses for the Extreme Ultraviolet. *Appl. Opt.*, **4** (1965), 891. doi:10.1364/AO.4.000891.

[235] F. R. Powell, P. W. Vedder, J. F. Lindblom, & S. F. Powell. Thin film filter performance for extreme ultraviolet and x-ray applications. *Opt. Eng.*, **29** (1990), 614. doi:10.1117/12.55641.

[236] K. Tiedtke, A. Azima, N. von Bargen, L. Bittner, S. Bonfigt, S. Düsterer, B. Faatz, U. Frühling, M. Gensch, C. Gerth, N. Guerassimova, U. Hahn, T. Hans, M. Hesse, K. Honkavaar, U. Jastrow, P. Juranic, S. Kapitzki, B. Keitel, T. Kracht, M. Kuhlmann, W. B. Li, M. Martins, T. Núñez, E. Plönjes, H. Redlin, E. L. Saldin, E. a. Schneidmiller, J. R. Schneider, S. Schreiber, N. Stojanovic, F. Tavella, S. Toleikis, R. Treusch, H. Weigelt, M. Wellhöfer, H. Wabnitz, M. V. Yurkov, & J. Feldhaus. The soft x-ray free-electron laser FLASH at DESY: beamlines, diagnostics and end-stations. *New J. Phys.*, **11** (2009), 023029. doi:10.1088/1367-2630/11/2/023029.

[237] Y. Nabekawa, H. Hasegawa, E. J. Takahashi, & K. Midorikawa. Production of Doubly Charged Helium Ions by Two-Photon Absorption of an Intense Sub-10-fs Soft X-Ray Pulse at 42 eV Photon Energy. *Phys. Rev. Lett.*, **94** (2005), 1. doi:10.1103/PhysRevLett.94.043001.

[238] M. A. Kornberg & P. Lambropoulos. Photoelectron energy spectrum in 'direct' two-photon double ionization of helium. *J. Phys. B At. Mol. Opt. Phys.*, **32** (1999), L603. doi:10.1088/0953-4075/32/20/106.

[239] L. A. A. Nikolopoulos & P. Lambropoulos. Multichannel theory of two-photon single

and double ionization of helium. *J. Phys. B At. Mol. Opt. Phys.*, **34** (2001), 545. doi:10.1088/0953-4075/34/4/304.

[240] L. A. A. Nikolopoulos & P. Lambropoulos. Helium double ionization signals under soft-x-ray coherent radiation. *J. Phys. B At. Mol. Opt. Phys.*, **39** (2006), 883. doi:10.1088/0953-4075/39/4/012.

[241] E. Foumouo, G. L. Kamta, G. Edah, & B. Piraux. Theory of multiphoton single and double ionization of two-electron atomic systems driven by short-wavelength electric fields: An ab initio treatment. *Phys. Rev. A*, **74** (2006), 063409. doi:10.1103/PhysRevA.74.063409.

[242] E. Foumouo, P. Antoine, B. Piraux, L. Malegat, H. Bachau, & R. Shakeshaft. Evidence for highly correlated electron dynamics in two-photon double ionization of helium. *J. Phys. B At. Mol. Opt. Phys.*, **41** (2008), 051001. doi:10.1088/0953-4075/41/5/051001.

[243] J. Feist, S. Nagele, R. Pazourek, E. Persson, B. I. Schneider, L. a. Collins, & J. Burgdörfer. Nonsequential two-photon double ionization of helium. *Phys. Rev. A - At. Mol. Opt. Phys.*, **77** (2008), 1. doi:10.1103/PhysRevA.77.043420.

[244] X. Guan, K. Bartschat, & B. I. Schneider. Dynamics of two-photon double ionization of helium in short intense xuv laser pulses. *Phys. Rev. A*, **77** (2008), 043421. doi:10.1103/PhysRevA.77.043421.

[245] L. Malegat, H. Bachau, B. Piraux, & F. Reynal. A novel estimate of the two-photon double-ionization cross section of helium. *J. Phys. B At. Mol. Opt. Phys.*, **45** (2012), 175601. doi:10.1088/0953-4075/45/17/175601.

[246] L. Argenti, R. Pazourek, J. Feist, S. Nagele, M. Liertzer, E. Persson, J. Burgdörfer, & E. Lindroth. Photoionization of helium by attosecond pulses: Extraction of spectra from correlated wave functions. *Phys. Rev. A*, **87** (2013), 053405. doi:10.1103/PhysRevA.87.053405.

[247] H. Hasegawa, E. J. Takahashi, Y. Nabekawa, & K. Midorikawa. Nonlinear Multiphoton Process of He at 42 eV by High-Order Harmonics. *Laser Phys.*, **15** (2005), 812.

[248] M. Nagasono, E. Suljoti, A. Pietzsch, F. Hennies, M. Wellhöfer, J.-T. Hoeft, M. Martins, W. Wurth, R. Treusch, J. Feldhaus, J. R. Schneider, & A. Föhlisch. Resonant two-photon absorption of extreme-ultraviolet free-electron-laser radiation in helium. *Phys. Rev. A*, **75** (2007), 051406. doi:10.1103/PhysRevA.75.051406.

[249] A. Rudenko, L. Foucar, M. Kurka, T. Ergler, K. U. Kühnel, Y. H. Jiang, A. Voitkiv, B. Najjari, A. Kheifets, S. Lüdemann, T. Havermeier, M. Smolarski, S. Schössler, K. Cole, M. Schöffler, R. Dörner, S. Düsterer, W. Li, B. Keitel, R. Treusch, M. Gensch, C. D. Schröter, R. Moshammer, & J. Ullrich. Recoil-Ion Momentum Distributions for

Two-Photon Double Ionization of He and Ne by 44 eV Free-Electron Laser Radiation. *Phys. Rev. Lett.*, **101** (2008), 073003. doi:10.1103/PhysRevLett.101.073003.

[250] M. Kurka, J. Feist, D. A. Horner, A. Rudenko, Y. H. Jiang, K. U. Kühnel, L. Foucar, T. N. Rescigno, C. W. McCurdy, R. Pazourek, S. Nagele, M. Schulz, O. Herrwerth, M. Lezius, M. F. Kling, M. Schöffler, A. Rudenko, S. Düsterer, R. Treusch, B. I. Schneider, L. A. Collins, J. Burgdörfer, C. D. Schröter, R. Moshammer, & J. Ullrich. Differential cross sections for non-sequential double ionization of He by 52 eV photons from the Free Electron Laser in Hamburg, Flash. *New J. Phys.*, **12** (2010). doi:10.1088/1367-2630/12/7/073035.

[251] H. Takenaka, S. Ichimaru, T. Ohchi, & E. M. Gullikson. Soft-X-ray reflectivity and heat resistance of SiC/Mg multilayer. *J. Electron Spectros. Relat. Phenomena*, **144-147** (2005), 1047. doi:10.1016/j.elspec.2005.01.227.

[252] A. Aquila, F. Salmassi, Y. Liu, & E. Gullikson. Tri-material multilayer coatings with high reflectivity and wide bandwidth for 25 to 50 nm extreme ultraviolet light. *Opt. Express*, **17** (2009), 22102. doi:10.1364/OE.17.022102.

[253] M. Fernández-Perea, R. Soufli, J. C. Robinson, L. R. De Marcos, J. a. Méndez, J. I. Larruquert, & E. M. Gullikson. Triple-wavelength, narrowband Mg/SiC multilayers with corrosion barriers and high peak reflectance in the 25-80 nm wavelength region. *Opt. Express*, **20** (2012), 24018. doi:10.1364/OE.20.024018.

[254] R. Soufli, M. Fernández-Perea, S. L. Baker, J. C. Robinson, J. Alameda, & C. C. Walton. Spontaneously intermixed Al-Mg barriers enable corrosion-resistant Mg/SiC multilayer coatings. *Appl. Phys. Lett.*, **101** (2012), 043111. doi:10.1063/1.4737649.

[255] R. Soufli. Private communication (2013).

[256] N. Peyghambarian, B. Fluegel, D. Hulin, A. Migus, M. Joffre, A. Antonetti, S. Koch, & M. Lindberg. Femtosecond optical nonlinearities of CdSe quantum dots. *IEEE J. Quantum Electron.*, **25** (1989), 2516. doi:10.1109/3.40636.

[257] C. a. Leatherdale, W.-K. Woo, F. V. Mikulec, & M. G. Bawendi. On the Absorption Cross Section of CdSe Nanocrystal Quantum Dots. *J. Phys. Chem. B*, **106** (2002), 7619. doi:10.1021/jp025698c.

[258] L. a. Padilha, J. Fu, D. J. Hagan, E. W. Van Stryland, C. L. Cesar, L. C. Barbosa, C. H. B. Cruz, D. Buso, & A. Martucci. Frequency degenerate and nondegenerate two-photon absorption spectra of semiconductor quantum dots. *Phys. Rev. B*, **75** (2007), 075325. doi:10.1103/PhysRevB.75.075325.

[259] Y. B. Kyung, S. Lee, H. Oh, I. An, & H. Lee. Determination of the Optical Functions of Various Liquids by Rotating Compensator Multichannel Spectroscopic Ellipsometry. *Bull. Korean Chem. Soc.*, **26** (2005), 947. doi:10.5012/bkcs.2005.26.6.947.

[260] Light Conversion Ltd. PHAROS Model 06-200-PP Service Report 24.02.2015.

[261] M. Wagner & H. Schröder. A novel four grid ion reflector for saturation of laser multiphoton ionization yields in a time of flight mass spectrometer. *Int. J. Mass Spectrom. Ion Process.*, **128** (1993), 31. doi:10.1016/0168-1176(93)87014-J.

[262] M. Walker, P. Hansch, & L. Van Woerkom. Intensity-resolved multiphoton ionization: Circumventing spatial averaging. *Phys. Rev. A*, **57** (1998), R701. doi:10.1103/PhysRevA.57.R701.

[263] R. Bredy, H. a. Camp, H. Nguyen, T. Awata, B. Shan, Z. Chang, & B. D. DePaola. Three-dimensional spatial imaging in multiphoton ionization rate measurements. *J. Opt. Soc. Am. B*, **21** (2004), 2221. doi:10.1364/JOSAB.21.002221.

[264] M. Schultze, B. Bergues, H. Schröder, F. Krausz, & K. L. Kompa. Spatially resolved measurement of ionization yields in the focus of an intense laser pulse. *New J. Phys.*, **13** (2011). doi:10.1088/1367-2630/13/3/033001.

[265] T. Kock. Aufbau und Charakterisierung eines Ionenmikroskops zur nichtinvasiven Messung eines Lichtfokus. Master thesis, University of Hamburg (2010).

[266] D. A. Dahl. SIMION for the personal computer in reflection. *Int. J. Mass Spectrom.*, **200** (2000), 3. doi:10.1016/S1387-3806(00)00305-5.

[267] J. Ladislas Wiza. Microchannel plate detectors. *Nucl. Instruments Methods*, **162** (1979), 587. doi:10.1016/0029-554X(79)90734-1.

[268] Hamamatsu technical information MCP assembly. Technical report.

[269] J. Oberheide, P. Wilhelms, & M. Zimmer. New results on the absolute ion detection efficiencies of a microchannel plate. *Meas. Sci. Technol.*, **8** (1999), 351. doi:10.1088/0957-0233/8/4/001.

[270] G. Fraser. The ion detection efficiency of microchannel plates (MCPs). *Int. J. Mass Spectrom.*, **215** (2002), 13. doi:10.1016/S1387-3806(01)00553-X.

[271] Marketech International - Scintillator Crystal Data Table: https://mkt-intl.com/uploads/pdf/ScintillatorsData.pdf.

[272] W. Graves & E. Johnson. A high resolution electron beam profile monitor. *Proc. 1997 Part. Accel. Conf. (Cat. No.97CH36167)*, **2** (1997). doi:10.1109/PAC.1997.751084.

[273] P. Schauer & J. Bok. Study of spatial resolution of YAG:Ce cathodoluminescent imaging screens. *Nucl. Instruments Methods Phys. Res. Sect. B Beam Interact. with Mater. Atoms*, **308** (2013), 68. doi:10.1016/j.nimb.2013.05.006.

[274] D. Heddle. Electrostatic Lens Systems (Institute of Physics Publishing, Bristol, 2000), second edition. ISBN 0 7503 0697 1.

[275] F. H. Read. Accurate calculations of double-aperture electrostatic immersion lenses. *J. Phys. E.*, **2** (2002), 165. doi:10.1088/0022-3735/2/2/311.

[276] H. Liebl. Applied charged particle optics (2008). ISBN 9783540719243. doi:10.1007/978-3-540-71925-0.

[277] F. Hinterberger. Ion optics with electrostatic lenses. *CAS, Cern Accel. Sch. small Accel. Proc. Zeegse, Netherlands, 24 May-2 June 2005*, (2006), 27. doi:10.5170/CERN-2006-012.27.

[278] K. Luria, W. Christen, & U. Even. Generation and Propagation of Intense Supersonic Beams. *J. Phys. Chem. A*, **115** (2011), 7362. doi:10.1021/jp201342u.

[279] P. H. Krupenie. The Spectrum of Molecular Oxygen. *J. Phys. Chem. Ref. Data*, **1** (1972), 423. doi:10.1063/1.3253101.

[280] A. T. J. B. Eppink & D. H. Parker. Velocity map imaging of ions and electrons using electrostatic lenses: Application in photoelectron and photofragment ion imaging of molecular oxygen. *Rev. Sci. Instrum.*, **68** (1997), 3477. doi:10.1063/1.1148310.

[281] Atomic Data for Krypton, Handbook of Basic Atomic Spectroscopic Data, NIST.

[282] Leybold Vacuum. Ionivac ITR 90 Operation Manual - GA 09.420/3.02.

[283] T. Kanai, T. Kanda, T. Sekikawa, S. Watanabe, T. Togashi, C. Chen, C. Zhang, Z. Xu, & J. Wang. Generation of vacuum-ultraviolet light below 160 nm in a kbbf crystal by the fifth harmonic of a single-mode ti:sapphire laser. *Journal of the Optical Society of America B: Optical Physics*, **21** (2004), 370. doi:10.1364/JOSAB.21.000370.

[284] M. Wittmann, M. Wick, O. Steinkellner, P. Farmanara, V. Stert, W. Radloff, G. Korn, & I. Hertel. Generation of femtosecond {VUV} pulses and their application to time resolved spectroscopy in the gas phase. *Optics Communications*, **173** (2000), 323 . doi:http://dx.doi.org/10.1016/S0030-4018(99)00607-0.

[285] P. Tzankov, O. Steinkellner, J. Zheng, M. Mero, W. Freyer, A. Husakou, I. Babushkin, J. Herrmann, & F. Noack. High-power fifth-harmonic generation of femtosecond pulses in the vacuum ultraviolet using a Ti:sapphire laser. *Opt. Express*, **15** (2007), 6389. doi:10.1364/OE.15.006389.

[286] M. Beutler, M. Ghotbi, & F. Noack. Generation of intense sub-20-fs vacuum ultraviolet pulses compressed by material dispersion. *Optics Letters*, **36** (2011), 3726. doi:10.1364/OL.36.003726.

[287] K. Kosma, S. A. Trushin, W. E. Schmid, & W. Fuß. Vacuum ultraviolet pulses of 11 fs from fifth-harmonic generation of a Ti:sapphire laser. *Optics Letters*, **33** (2008), 723. doi:10.1364/OL.33.000723.

[288] D. Strickland & G. Mourou. Compression of amplified chirped optical pulses. *Optics Communications*, **56** (1985), 219. doi:http://dx.doi.org/10.1016/0030-4018(85)90120-8.

[289] P. F. Moulton. Spectroscopic and laser characteristics of Ti:Al2O3. *Journal of the Optical Society of America B: Optical Physics*, **3** (1986), 125. doi:10.1364/JOSAB.3.000125.

[290] A. Stingl, R. Szipöcs, M. Lenzner, C. Spielmann, & F. Krausz. Sub-10-fs mirror-dispersion-controlled ti:sapphire laser. *Optics Letters*, **20** (1995), 602. doi:10.1364/OL.20.000602.

[291] G. Cheriaux, B. Walker, L. F. Dimauro, P. Rousseau, F. Salin, & J. P. Chambaret. Aberration-free stretcher design for ultrashort-pulse amplification. *Opt. Lett.*, **21** (1996), 414. doi:10.1364/OL.21.000414.

[292] E. Gullikson, R. Korde, L. Canfield, & R. Vest. Stable silicon photodiodes for absolute intensity measurements in the VUV and soft X-ray regions. *Journal of Electron Spectroscopy and Related Phenomena*, **80** (1996), 313 . doi:http://dx.doi.org/10.1016/0368-2048(96)02983-0. Proceedings of the 11th International Conference on Vacuum Ultraviolet Radiation Physics.

[293] F. Karimi. Spectrometer for diagnostics of lower orders of HHG XUV-pulses. Master's thesis, University of Hamburg (2013).

[294] D. Rompotis, T. Gebert, M. Wieland, F. Karimi, & M. Drescher. Efficient generation of below-threshold harmonics for high-fidelity multi-photon physics in the VUV spectral range. *Optics Letters*, **40** (2015), 1675. doi:10.1364/OL.40.001675.

[295] J. Burnett, Z. Levine, & E. Shirley. Intrinsic birefringence in calcium fluoride and barium fluoride. *Phys. Rev. B*, **64** (2001), 241102. doi:10.1103/PhysRevB.64.241102.

[296] K. Tiedtke, J. Feldhaus, U. Hahn, U. Jastrow, T. Nunez, T. Tschentscher, S. V. Bobashev, A. A. Sorokin, J. B. Hastings, S. Möller, L. Cibik, A. Gottwald, A. Hoehl, U. Kroth, M. Krumrey, H. Schöppe, G. Ulm, & M. Richter. Gas detectors for x-ray lasers. *J. Appl. Phys.*, **103** (2008), 094511. doi:10.1063/1.2913328.

[297] D. H. Parker. Laser Photochemistry of Molecular Oxygen. *Acc. Chem. Res.*, **33** (2000), 563. doi:10.1021/ar980012d.

[298] S. Witte, R. T. Zinkstok, W. Ubachs, W. Hogervorst, & K. S. E. Eikema. Deep-

Ultraviolet Quantum Interference Metrology with Ultrashort Laser Pulses. *Science (80-.).*, **307** (2005), 400. doi:10.1126/science.1106612.

[299] I. Liontos, S. Cavalieri, C. Corsi, R. Eramo, S. Kaziannis, A. Pirri, E. Sali, & M. Bellini. Ramsey spectroscopy of bound atomic states with extreme-ultraviolet laser harmonics. *Opt. Lett.*, **35** (2010), 832.

[300] P. Tzallas, E. Skantzakis, L. A. A. Nikolopoulos, G. D. Tsakiris, & D. Charalambidis. Extreme-ultraviolet pump-probe studies of one-femtosecond-scale electron dynamics. *Nat. Phys.*, **7** (2011), 781. doi:10.1038/nphys2033.

A Autocorrelation Theoretical Aspects

A.1 Field Autocorrelation - Spectral Intensity Correspondence

The Fourier transform of the field autocorrelation signal, obtains the the spectral intensity distribution of the pulse and thus a linear autocorrelation measurement is not sufficient for determining the pulse temporal profile.
This result is mathematically described by the Wiener-Khinchin theorem, also known as Khinchin-Kolmogorov theorem.
As a reminder, the field autocorrelation signal, commonly obtained at the output of a Michelson interferometer with a detection system exhibiting a linear response to the input light intensity, reads:

$$S_{FAC}(\tau) \propto 2 \cdot \int_{-\infty}^{+\infty} |E(t)|^2 \, dt - 2 \cdot \mathrm{Re} \int_{-\infty}^{+\infty} E(t)E^*(t-\tau)dt$$

The last term represents the first-order correlation function of the light field and it is the quantity of interest. The first term is delay independent and thus a measurement constant for a time-integrating detector.
A simple proof will be provided for an arbitrary time dependent signal, described by the time-dependent function $f(t)$ as follows. The Fourier transform of the corresponding autocorrelation function can be written as:

$$\mathscr{F}\left\{\int_{-\infty}^{+\infty} f(t)f^*(t-\tau)dt\right\} = \int_{-\infty}^{+\infty}\int_{-\infty}^{+\infty} f(t)f^*(t-\tau)dte^{-i\omega\tau}d\tau =$$

$$= \int_{-\infty}^{+\infty} f(t)\int_{-\infty}^{+\infty} f^*(t-\tau)e^{-i\omega\tau}d\tau dt = \int_{-\infty}^{+\infty} f(t)\left[\int_{-\infty}^{+\infty} f(t-\tau)e^{i\omega\tau}d\tau\right]^* dt =$$

$$\overset{\tau' = -\tau}{=} \int_{-\infty}^{+\infty} f(t)\left[\int_{-\infty}^{+\infty} f(\tau'+t)e^{-i\omega\tau'}d\tau'\right]^* dt = \int_{-\infty}^{+\infty} f(t)\left[F(\omega)e^{i\omega t}\right]^* dt =$$

$$= \int_{-\infty}^{+\infty} f(t)e^{-i\omega t}dtF^*(\omega) = F(\omega)F^*(\omega) = |F(\omega)|^2$$

A.2 Second-Order Interferometric Autocorrelation

This section is devoted to the complete expansion of the second-order interferometric autocorrelation signal:

$$S^{(2)}_{\mathrm{FRAC}}(\tau) = \int_{-\infty}^{+\infty} \left|[E(t) + E(t-\tau)]^2\right|^2 dt =$$

$$= \int_{-\infty}^{+\infty} \left[E^2(t) + E^2(t-\tau) + 2E(t)E(t-\tau)\right]\left[E^{*2}(t) + E^{*2}(t-\tau) + 2E^*(t)E^*(t-\tau)\right] dt$$

$$= \int_{-\infty}^{+\infty} \Big\{\left|E^2(t)\right|^2 + E^2(t)E^{*2}(t-\tau) + 2E^2(t)E^*(t)E^*(t-\tau) +$$

$$+ 2E(t)E(t-\tau)E^{*2}(t) + 2E(t)E(t-\tau)E^{*2}(t-\tau + 4\left|E(t)\right|^2\left|E(t-\tau)\right|^2\Big\} dt$$

Using the fact that the pulse intensity corresponds to $I(t) \equiv |E(t)|^2$ we obtain:

$$S^{(2)}_{\mathrm{FRAC}}(\tau) = \int_{-\infty}^{+\infty} \Big\{I^2(t) + E^2(t)E^{*2}(t-\tau) + 2I(t)E^*(t)E^*(t-\tau) +$$

$$+E^2(t-\tau)E^{*2}(t) + I^2(t-\tau) + 2I(t-\tau)E^*(t)E(t-\tau) -$$

$$- 2I(t)E^*(t)E(t-\tau) + 2I(t-\tau)E(t)E^*(t-\tau) + 4I(t-\tau)I(t)\Big\} dt$$

Which results in:

$$S^{(2)}_{\mathrm{FRAC}}(\tau) = \int_{-\infty}^{+\infty} \left|[E(t) + E(t-\tau)]^2\right|^2 dt =$$

$$= \int_{-\infty}^{+\infty} I^2(t) + I^2(t-\tau) dt$$

$$+ 4 \cdot \int_{-\infty}^{+\infty} I(t)I(t-\tau) dt$$

$$+ 2 \cdot \int_{-\infty}^{+\infty} \left[I(t) + I(t-\tau)\right] E(t)E^*(t-\tau) dt + \text{c.c.}$$

$$+ 2 \cdot \int_{-\infty}^{+\infty} E^2(t)E^{*2}(t-\tau) dt + \text{c.c.}$$

B Two-Photon Fluorescence Autocorrelation: Magnification Measurement

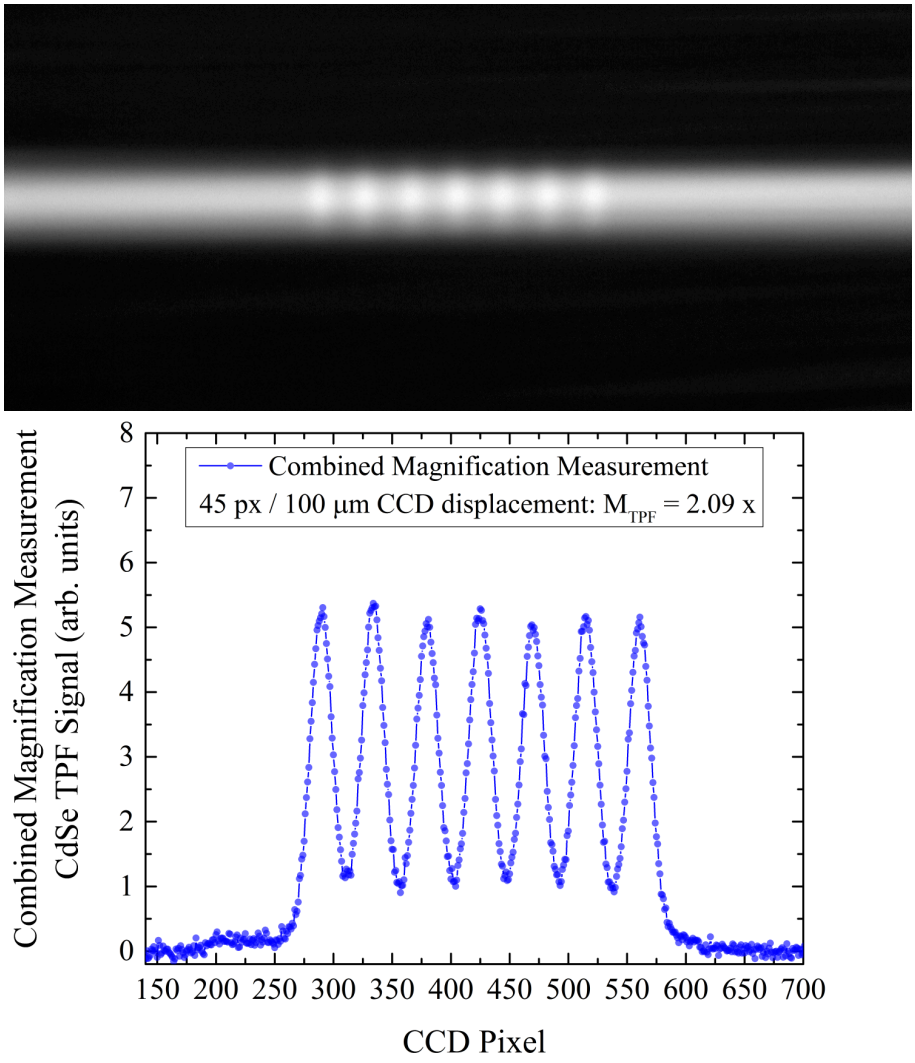

Figure B.1: Optical magnification measurement using the temporal overlap two-photon fluorescence signal as a reference. The CCD camera is translated along the axis parallel to the beam propagation axis using a high-precision linear translation stage. The stage is translated in 100 µm steps and the magnification is evaluated from the combined image. The temporal overlap displacement corresponds to an average of 45 pixels / 100 µm. Taking into account the pixel size (4.65 µm/pixel) the resulting magnification corresponds to $M_{TPF} = 2.09\times$.

C Ion Microscope: Supplementary Information and Simulation Results

C.1 Ion Microscope: Experimental Implementation

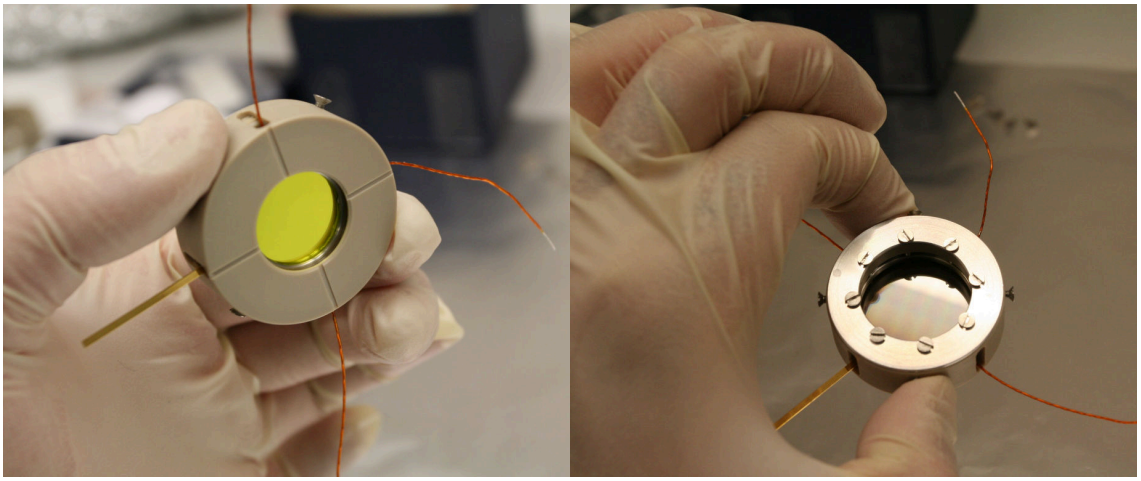

Figure C.1: Assembled position-sensitive detector before installation on the instrument.

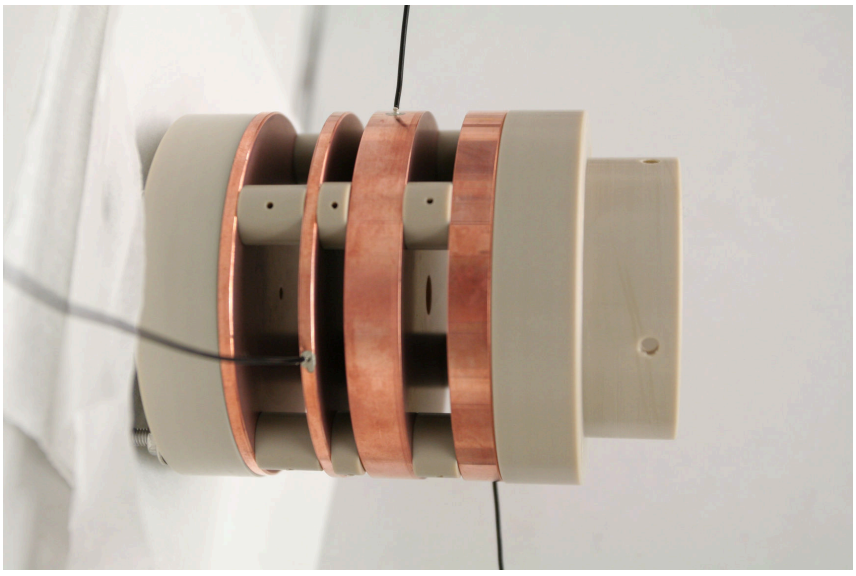

Figure C.2: The detachable ion optics assembly before being mount on the flight tube.

C.2 Supplemental SIMION Simulation Results

C.2.1 Ion Imaging: Ion Optics Focal Plane Properties

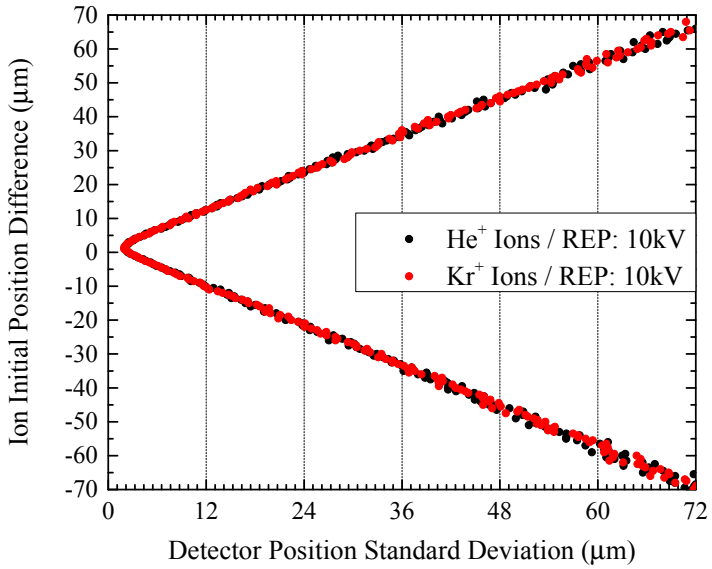

Figure C.3: Ion imaging focal properties simulation results for both Kr^+ and He^+ ions using the exact simulation parameters (as in 4.7). The simulation results show no mass dependence.

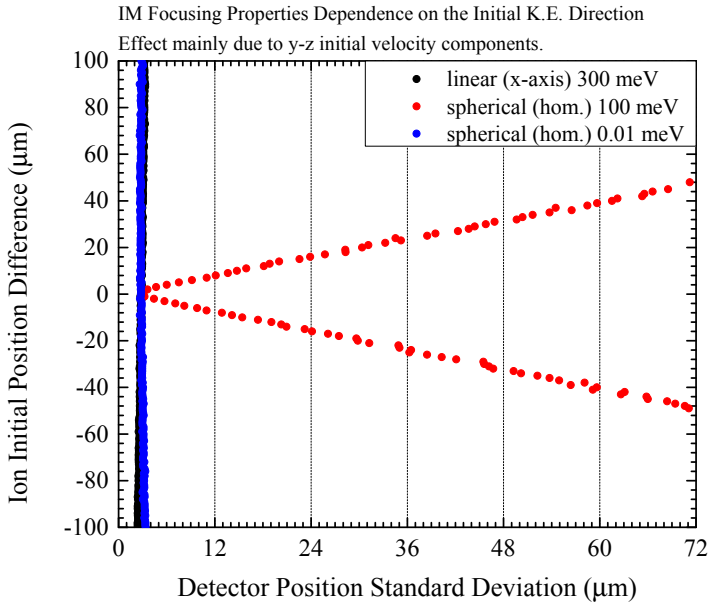

Figure C.4: The ion microscope depth-of-focus strongly depends on the ions initial velocity direction and magnitude. A homogeneous initial spherical distribution clearly shows a dependence on the absolute value of the kinetic energy as shown also in Fig. 4.7. However when the velocity vector is pointing along the ion optical axis (x-direction) even a higher initial kinetic energy shows no x-axis starting position dependence.

C.2.2 Ion Imaging: Simulated Ion Optics Aberrations

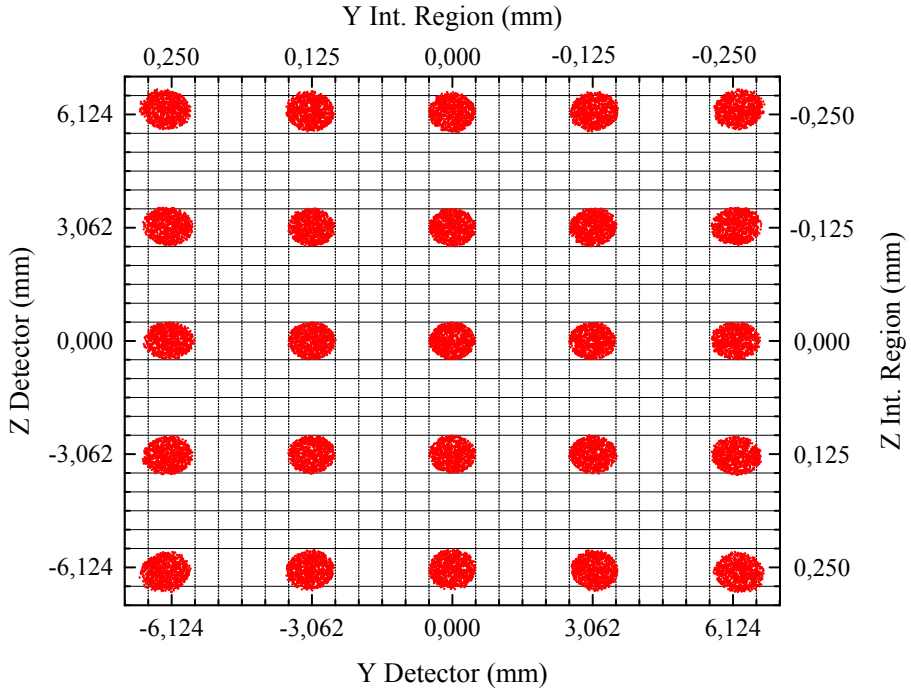

Figure C.5: Simulated ion detector image using a grid of equally spaced (125 µm) Kr^+ ion cylinders at REP=10kV and $V_{LENS}/V_{REP} = 0.3717$. The cylinder axis matches the x-axis, the length of the cylinder is 10 µm and the radius 50 µm. The grid lines depict the ideal imaging scale, indicating the expected ion disk location and size. As mentioned before, pincushion-like imaging distortion is observable at the image edges although it is not expected to restrict the detection scope of the instrument.

C.2.3 Ion Optical System Spatial Resolution Study: Initial Kinetic Energy Dependence

Ion Initial Kinetic Energy	Radial 1 µm Spatial Resolution Extent
10^{-5} meV	± 55 µm
0.01 meV	± 55 µm
10 meV	± 50 µm
100 meV	± 40 µm

Table C.1: Simulated ion optical system spatial resolution (1 µm separated ion disk-pairs) as a function of the ions initial kinetic energy. The simulation parameters are identical to those in Fig. 4.9. The initial ion velocity vector directions are homogeneously distributed over a spherical pupil with R=5 µm.

D Time-Delay Scale Calibration

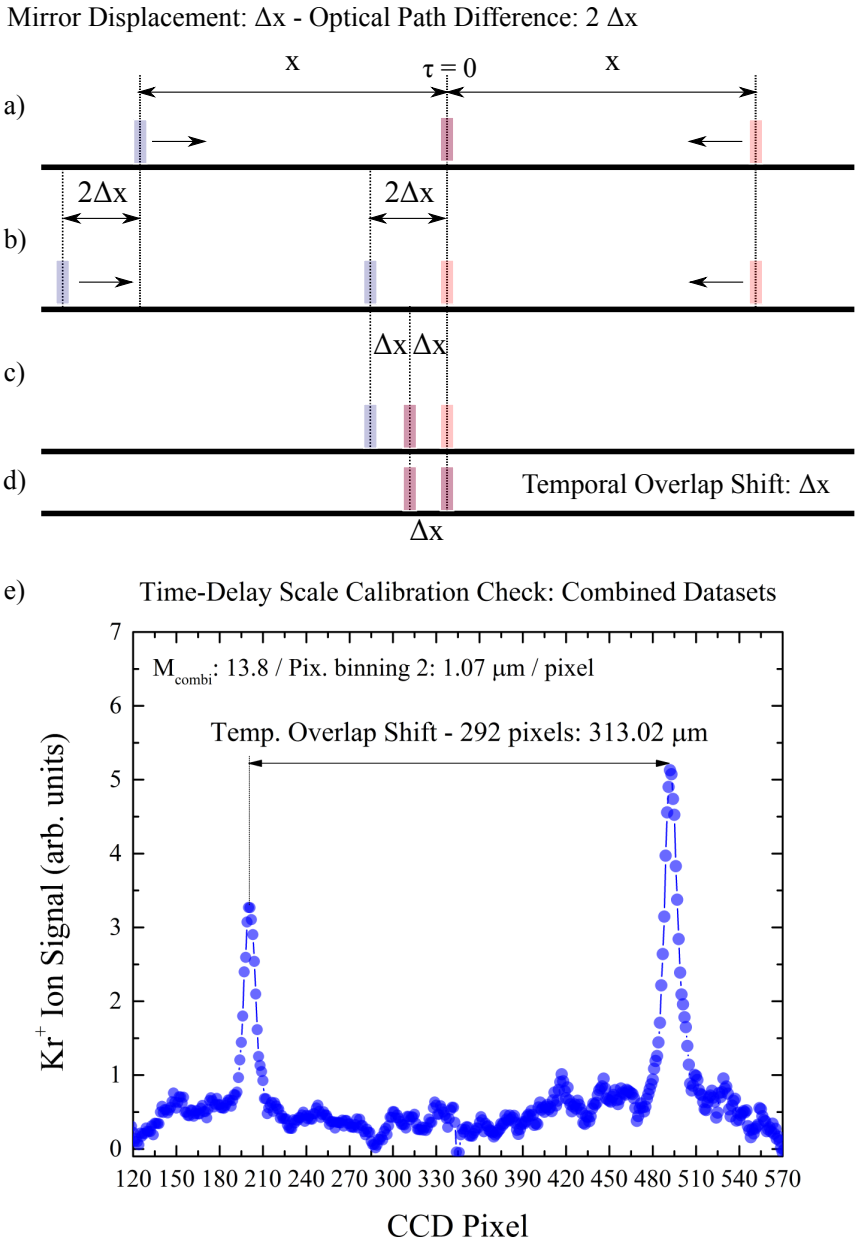

Figure D.1: Delay scale verification measurement: a) Prior to the mirror displacement the two pulses encounter each other in the center of symmetry of the optical arrangement. b) A spherical mirror displacement by Δx results in an optical path difference of 2Δx as the beam travels twice the path. When the pulse on the right side (red) arrives at the previous overlap position the pulse on the left side (blue) is in a distance of 2Δx. c) The two counter-propagating pulses subsequently bridge this distance, meeting in the middle. d) As a result, the new temporal overlap position is found in a distance Δx away from the temporal overlap position prior to the mirror displacement as shown in a). e) Measured temporal overlap shift for one revolution of the picomotor actuator thread (80 tpi - Δx=317.5 µm/revolution). The observed IAC trace peak decrease results due to focus mismatch between the two counter-propagating pulses.

E Acknowledgments

I would like to express my gratitude to a number of people that supported me and assisted to successfully complete the work presented in this thesis.
First of all, I would like to thank Prof. Dr. Markus Drescher for giving me the opportunity to work in this very exciting and challenging topic, for his excellent supervision, as well as for his continuous support, motivation and advice.
I am really grateful to Dr. Marek Wieland for his endless support and encouragement over all these years. The stimulating discussions and his positive approach and feedback were instrumental for the completion of this work.
A major part of the laboratory experimental work presented in this thesis has been accomplished in close collaboration with Dr. Thomas Gebert. Working and discussing with him has always been inspiring and motivating and I would like to thank him for his support and constructive comments.
I would also like to thank Dr. Theophilos Maltezopoulos for his assistance with the data acquisition part of the experiment, his constant aid and for his detailed look and feedback on this manuscript.
For his endless support during the FEL experiments and his advice in many technical issues, I also would like to thank Oliver Becker.
I am grateful to Dr. Michael Meyer for his interest in this work and for accepting to evaluate this thesis as a referee, as well as to Prof. Dr. Peter Schmelcher, Prof. Dr. Ulrike Frühling and Prof. Dr. Thorsten Uphues for accepting to be members of the examination committee.
The mechanical workshop under the guidance of Stephan Fleig and the electrical workshop under the guidance of Armin Spikofsky fabricated a large number of parts for the experimental setup, always being very helpful and effective. The excellent work of Klaudia Hagemann from DESY resulted in very precisely manufactured ion microscope electrodes that really made a difference.
Valuable advice and practical support has been provided by Dr. Regina Soufli and Dr. David L. Windt on the selection and design of the utilized XUV multilayer optics.
Valuable assistance has been offered numerous times from Dr. Elke Plönjes-Palm, Dr. Marion Kuhlmann, Dr. Barbara Keitel, Dr. Stefan Düsterer, Dr. Günter Brenner, Dr. N. Schirmel and permanent personel at FLASH in Hamburg during our FEL experimental campaigns. I would like to thank Dr. Luca Giannessi, Dr. Marco Zangrando, Dr. Lorenzo Raimondi, Dr. Cristian Svetina, Dr. Nicola Mahne and the permanent personnel at FERMI in Trieste for their assistance before and during our experiment in Italy.

E Acknowledgments

I am really grateful to Prof. Dr. Peter Lambropoulos for numerous enlightening discussions, as well as to Dr. Paraskevas Tzallas and Prof. Dr. Dimitris Charalambidis for their valuable advice.
I am also grateful to Dr. Oriol Vendrell Romagosa for our discussion and the insight to ultrafast molecular dynamics.
A short stay at the Max Born Institut für Nichtlineare Optik und Kurzzeit-Spektroskopie has been particularly instructive for me and I would like to thank Prof. Dr. Marc Vrakking for giving me this opportunity.
I would also like to thank all my colleagues at the *DynamiX* group for the nice atmosphere in the laboratory, as well as outside. A special mention goes to Arne Baumann and Oliver Schepp who continue the efforts and pursue similar research objectives as those that this work has focused on.
I am grateful to the organizing and fellow members of the Marie Curie ATTOFEL ITN Network for providing me with excellent educational opportunities and the ATTOFEL ITN Network as well as the German Ministry for Education and Research, for financial support during this work.
A special thanks goes to Evangelos Karamatskos, Antonia Karamatskou and Dr. Julian Hirscht for being very encouraging and positive at the right moment.
Finally I would like thank all the good friends in Hamburg, Crete, Athens and around the world for their unending support and love and most importantly my family for always standing by my side.

F Declaration On Oath

I hereby declare, on oath, that I have written the present dissertation by my own and have not used other than the acknowledged resources and aids.

Hamburg, October 26, 2015

Dimitrios Rompotis